Two-Dimensional Structures and Order of Nano-Objects on the Surface of Water:

Synchrotron X-ray Scattering Studies

A thesis presented

by

Masafumi Fukuto

to

The Department of Physics

in partial fulfillment of the requirements
for the degree of
Doctor of Philosophy
in the subject of

Physics

Harvard University
Cambridge, Massachusetts
May 2001

Masafumi Fukuto

Two-Dimensional Structures and Order of Nano-Objects on the Surface of Water:

Synchrotron X-ray Scattering Studies

Advisor: Peter S. Pershan

Abstract

Surface-sensitive synchrotron x-ray scattering techniques have been used to study the microscopic two-dimensional (2D) structures of Langmuir monolayers (LMs) formed by various nano-meter sized macromolecules on water at room temperature.   The molecules studied are: sphere-like fullerene-propylamine adduct (C60-PA); rod-like α-helical polypeptide poly(γ-benzyl-L-glutamate) (PBLG); hairy-rod polypeptide poly(γ-4-(hexadecyloxy)benzyl α,L-glutamate) (C16-O-PBLG); and sphere-like gold nano-particles derivatized with carboxylic acid-terminated alkylthiol chains (AuSC16). PBLG and C16-O-PBLG rods lie down parallel to the interface and align locally with neighboring rods within the monolayer plane.

The observations of broad grazing incidence diffraction (GID) peaks indicate that the C60-PA and AuSC16 monolayers are 2D amorphous solids that are consistent with local hexagonal packing. They possess only short-range positional order with lateral correlations extending over no more than a few nearest-neighbor distances. The large number of electrons contained in the molecules makes the observations of liquid-like 2D x-ray structure factors possible.

The surface pressure versus area isotherm and specular reflectivity (XR) measurements confirm that both the LMs of rod-like PBLG and sphere-like AuSC16 undergo a first-order monolayer/bilayer transition upon lateral compression. In both cases, off-specular diffuse scattering (XOSDS) intensities from compressed monolayers

are consistent with the presence of capillary waves on the surface and the lateral homogeneity of the films. However, both PBLG and AuSC16 bilayers exhibit excess off-specular scattering above the predicted capillary contribution, indicating that the bilayers are microscopically inhomogeneous. The results demonstrate the utility of XOSDS techniques for probing inhomogeneities on liquid surfaces.

Due to the additional long alkyl side chains, the monolayers of hairy rod C16-O-PBLG sustain much higher surface pressures than PBLG and the monolayer/bilayer transition is suppressed. In C16-O-PBLG LM, hydrophobic side chains are segregated towards the film/gas interface, while the PBLG cores reside closer to the water/film interface. The two high-angle GID peaks observed at high surface pressures are consistent with a common packing mode of alkyl chains known as the herringbone (HB) packing. One of the peaks is absent at low surface pressures, suggesting that the HB order is first established by the side chains that are confined one-dimensionally between aligned PBLG cores.

their technical support at the beamline. I also thank Prof. Moshe Deutsch of Bar-Ilan University for his friendship with our group and his encouragements at the beamline.

As for the members of the Harvard X-ray Group, I have had the privilege of working directly with two postdocs. First of all, I owe very special thanks to Ralf Heilmann for the great teamwork and many helpful discussions we had, his support and encouragements, and most of all his friendship. Most of the work presented in this thesis resulted from our measurements together and would not have been possible without him. I also thank his successor Oleg Gang, who has always been ready to help, give advice, and have friendly chats and a nice cup of coffee. Both Ralf and Oleg have been my unofficial advisors with whom I can always exchange ideas and it has been fun to work. Besides Peter and Ralf, three former group members, namely, Holger Tostmann, Konstantin Penanen, and Mike Regan deserve special thanks for the particularly strong influence they have had on my graduate career, both as unofficial mentors and as friends. I also thank the other current or former group members whom I had the pleasure of knowing and working indirectly with: They are (in order of appearance) Seth Kosowsky, Bill Foster, Mingchih Shih, C. Chou, Oleg Shpyrko, Elizabeth Fabbroni, Patrick Huber, and Kyle Alvine. My deep appreciation also goes to Frank Molea of McKay Lab for his friendly jokes and encouragements over the past several years.

I would also like to acknowledge my undergraduate research advisor Prof. David C. Johnson of the University of Oregon for giving me the very first opportunity to do experimental research and experience the joy of doing science.

On the personal side, I would first like to thank my best friend and my significant other Hana Sugimoto for being there for me and for having helped me stay positive throughout the writing of this thesis (we did it!). I am extremely grateful to my "American parents" Mary and Gene Milbrath; their warm friendship, encouragements and faith in me since my high school days have had a lot to do with my choosing this path and finally reaching this goal. I thank my grandparents Kiminori and Mitsuko

Somyo and my late grandparents Noriaki and Chiyoko Fukuto for their wisdom, advice, and support. My younger brothers Hiro and Yas Fukuto have been my greatest comrades in arms whom I can count on both in good times as well as when things get tough. Finally and most importantly, this thesis is dedicated to my parents Nobuo and Noriko Fukuto; I cannot express in words how grateful I am to you for everything you have been and done for me and my brothers.

Contents

List of Figures

List of Tables

To my parents

Chapter 1
Introduction

1.1 Synchrotron X-ray Studies of Liquid Surfaces

The first experimental confirmations or observations of many interesting phenomena that we now know occur at the free surface of liquid resulted from structural studies based on scattering of intense synchrotron-generated x-rays. These phenomena include surface-induced semectic ordering at the free surface of nematic liquid crystals [1], surface freezing of alkanes [2], atomic layering at the free surface of liquid metals [3-5], and thermally induced, long-wavelength fluctuations of liquid surfaces, also known as capillary waves [6-10]. These studies demonstrated that three surface-sensitive x-ray scattering techniques are particularly useful for probing liquid surface structures. They are: x-ray specular reflectivity (XR) [11-13], grazing incidence diffraction (GID) [12, 14], and off-specular diffuse scattering [7-10].

These three techniques probe different aspects of interfacial structures and are therefore complementary to each other. XR is sensitive mostly to the gradient of electron density profile across an interface and can be used to elucidate the structure normal to the surface, such as layering. GID is a two-dimensional (2D) analogue of ordinary diffraction and is useful for identifying the in-plane structure of a surface phase at the intermolecular length scales. Off-specular diffuse scattering probes long-wavelength density fluctuations parallel to the surface, where the lateral length scales involved are typically on the order of 100 Å to 1 μm. The studies presented in this thesis utilize all three of these techniques to investigate the microscopic structures of various Langmuir monolayers formed at the gas/water interface.

1

1.2 Langmuir Monolayers

A Langmuir monolayer (LM) is a one-molecule thick film formed at a liquid/vapor interface, with water being the most common choice for the liquid subphase. The most conventional LM system consists of simple long-chain surfactant molecules that possess a hydrophilic head and hydrophobic tail(s). Such an "amphiphilic" character of these molecules certainly plays an important role in stabilizing these molecules at the water surface. However, the amphiphicity is not a requirement for the formation of a stable monolayer. In fact none of the LMs studied in this thesis consist of amphiphilic molecules. Molecules that interact too strongly with water would result in dissolution, whereas those with too strong an attraction to themselves would lead to three-dimensional aggregation. It appears therefore that so long as neither of the molecule-subphase and molecule-molecule interactions dominates too strongly, the molecules may form a LM.

The LMs have been studied over a century [14, 15]. However, the level of interest in LMs has been growing particularly strongly over the past two decades, to which several different developments in various scientific fields contributed simultaneously. For example, in the late 1970s, a 2D melting theory (the "KTHNY" theory) was proposed that predicted the existence of a 2D hexatic phase and transformation from 2D solid to hexatic and then to isotropic liquid through unbinding of dislocation and disclination pairs [16-20]. It was followed by a number of experimental studies in 2D physics [21-23], and LMs were recognized as one of the real physical systems that might be suitable for that purpose.

During the same period, two types of experimental techniques were developed that are now in widespread use for studying LMs. One corresponds to the microscopy techniques that allow in-situ imaging of LM films on the water surface, namely, fluorescence microscopy and Brewster-angle microscopy (BAM) [24-27]. The other is the development of synchrotron x-ray scattering techniques described above. In fact, it is

only within the last ten to fifteen years that the applications of these techniques allowed detailed molecular-level descriptions of the LM structures to emerge [12, 14, 24-26]. In the most studied case of fatty acid monolayers, most of the 2D crystalline and liquid crystalline phases (at least eight in total) that appear in the ordered part of the generalized surface pressure-temperature phase diagram have now been characterized both optically and structurally [14, 26].

In recent years, the growing interests in nanotechnology have led to significant progress in both syntheses of nano-meter sized macromolecules and constructions of monolayer or multilayer films of these nano-objects through Langmuir-Blodgett (LB) deposition techniques [28-32]. However, direct structural characterizations of their LM states on water prior to LB deposition, such as may be accomplished by the synchrotron x-ray measurements, have received limited attention so far.

In the studies presented in this thesis, we probed 2D structures of LMs formed by some of these macromolecules using surface-sensitive x-ray scattering techniques. These molecules are shaped either like spheres or rods and their dimensions range from ~10 Å to > 100 Å. Our choice of these materials stems partly from our interest in studying phase transitions between ordered and disordered 2D phases. The LMs of simple long-chain surfactants have proven to be extremely interesting systems with many different ordered 2D phases; however, one drawback is that such molecules are too small for their liquid 2D phases to produce measurable GID intensities. On the other hand, the molecules we studied are much larger and contain a greater number of electrons per molecule. We will show that the quantitative characterizations of non-crystalline or amorphous 2D structures of these large molecules are possible.

However, it should be noted that so far we have not been able to find a LM system of nano-objects that exhibits a 2D phase transformation. Due to the large size of these molecules, mutual attractions between them are relatively strong. This leads to 2D aggregation of these molecules such that the local structure initially formed upon

spreading on the surface is already fairly close packed and solid-like. If these or other nano-meter sized molecules can be laterally dispersed or somehow "fluidized" in future, they may serve as useful candidates for x-ray scattering studies of 2D order-disorder transitions.
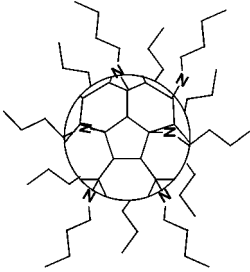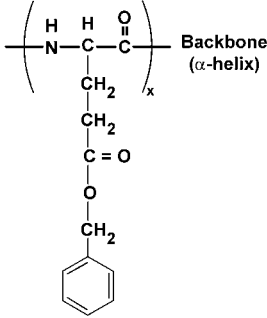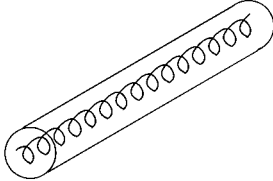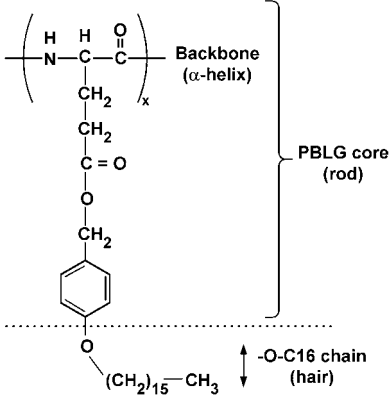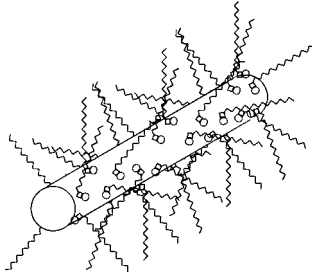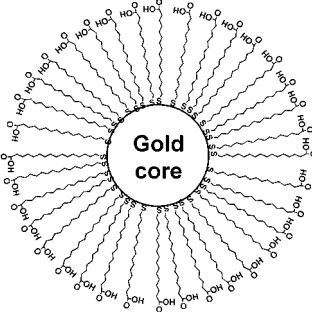
1.3 Overview

The following provides a brief overview of the studies contained in this thesis. The chemical formulas or structures and pictorial representations of the molecules used in these studies are listed in Table 1.1.

Chapter 2 presents a study of LMs formed by fullerene-propylamine adduct (C60-PA) molecules. The C60-PA molecule is shaped like a sphere. The main result of this study is that a very broad GID peak has been observed that is consistent with 2D hexagonal close packing of these molecules but with only short-range order. The lateral positional correlations extend no more than a few intermolecular distances. To the best of our knowledge, this was one of the first observations of 2D x-ray structure factor from a disordered Langmuir monolayer.

Chapter 3 is devoted to a study of LMs of α-helical polypeptide poly(γ-benzyl L-glutamate) (PBLG). The molecule is rod-like and its long axis lie parallel to the water surface. This LM system undergoes a first-order monolayer/bilayer transition upon compression. GID results show that rods are locally aligned with their neighbors. The bilayer exhibits two GID peaks that are consistent with two layers being incommensurate. The off-specular diffuse scattering (XOSDS) measurements show that the monolayer is laterally homogeneous. On the other hand, the bilayer exhibits extra off-specular scattering in excess of what the capillary wave (CW) model predicts, indicating that the bilayer is laterally inhomogeneous. A condensed version of this XOSDS study is provided in Appendix A, which also discusses how the thermal diffuse scattering arising from CWs can be calculated theoretically.

Table 1.1: Abbreviated names, chemical structures, and pictorial representations of the molecules used to form Langmuir monolayers on water. The chapter that describes each type of monolayers is indicated after the name.

Abbreviated Name	Chemical formula or structure	Pictorial representation
C60-PA (Chp. 2)	C_{60}-$[NH_2$-$(CH_2)_2$-$CH_3]_{12}$	
PBLG (Chp. 3)		
C16-O-PBLG (Chp. 4)		
AuSC16 (Chp. 5)	Au_x-$[S$-$(CH_2)_{15}$-$COOH]_y$ $x = 300 \sim 500$ $y = 70 \sim 130$	

In Chapter 4, LMs of another α-helical polypeptide poly(γ-4-(hexadecyloxy) benzyl α,L-glutamate) (C16-O-PBLG) is studied. The molecule can be regarded as a "hairy rod," which consists of attachments of hydrocarbon chains (-O-C16) to PBLG cores. The stability of C16-O-PBLG monolayers at high surface pressure Π is evident in their Π-A isotherms, indicating that the monolayer/bilayer transition is suppressed in this system. The hydrophobicity of the extra –O-C16 chains result in internal segregation of the monolayer, with the chains segregated at the film/gas interface and PBLG cores sitting parallel to and near the water/film interface. Due to the presence of these extra chains, inter-helix distance between aligned C16-O-PBLG rods is larger than that between bare PBLG rods. Compression of the film to high surface pressure enhances lateral packing order of –O-C16 chains, which appears to be the reason for the stability of this monolayer. The two GID peaks observed at high Π are consistent with a common packing mode of alkyl chains known as the herringbone (HB) packing. One of the peaks is absent at low Π, which suggests that even when the external pressure is absent, the ordered fraction of the –O-C16 chains are packed one-dimensionally. We will propose a possible model to explain these observations.

Chapter 5 presents a study of LMs formed by gold nanoparticles derivatized with carboxylic acid-terminated alkylthiols (AuSC16). The AuSC16 molecule is shaped like a sphere although it is also hairy due to the attachment of long alkyl chains. This system also exhibits a monolayer/bilayer transition when compressed. The large number of electrons contained in gold cores results in a very strong lowest-order GID peak even though the lateral order is short range. The GID results are consistent with local 2D hexagonal packing with correlations extending over only 3 ~ 4 nearest-neighbor distances. The limited range of lateral correlations appears to be a consequence of polydispersity in the size of cores. XOSDS measurements again indicate that the monolayer is laterally homogeneous whereas the bilayer is less so. Due to the presence of high-density AuSC16 layer on the surface, the description of x-ray scattering based on

the Born (or kinematic) approximation fails over a larger range of scattering angles than the case with low density layers. Therefore, the analysis of XR and XOSDS data from AuSC16 LMs required an improvement upon the Born approximation. The details on this issue are addressed separately in Appendix B.

References for Chapter 1

[1] P. S. Pershan, *Structure of Liquid Crystal Phases* (World Scientific, Singapore, 1988).

[2] B. M. Ocko, X. Z. Wu, E. B. Sirota, S. K. Sinha, O. Gang and M. Deutsch, *Phys. Rev. E* **55,** 3164 (1997).

[3] O. M. Magnussen, B. M. Ocko, M. J. Regan, K. Penanen, P. S. Pershan and M. Deutsch, *Phys. Rev. Lett.* **74,** 4444 (1995).

[4] M. J. Regan, E. H. Kawamoto, S. Lee, P. S. Pershan, N. Maskil, M. Deutsch, O. M. Magnussen, B. M. Ocko and L. E. Berman, *Phys. Rev. Lett.* **75,** 2498 (1995).

[5] H. Tostmann, E. DiMasi, P. S. Pershan, B. M. Ocko, O. G. Shpyrko and M. Deutsch, *Phys. Rev. B* **59,** 783 (1999).

[6] A. Braslau, P. S. Pershan, G. Swislow, B. M. Ocko and J. Als-Nielsen, *Phys. Rev. A* **38,** 2457 (1988).

[7] S. K. Sinha, E. B. Sirota, S. Garoff and H. B. Stanley, *Phys. Rev. B* **38,** 2297 (1988).

[8] D. K. Schwartz, M. L. Schlossman, E. H. Kawamoto, G. J. Kellogg, P. S. Pershan and B. M. Ocko, *Phys. Rev. A* **41,** 5687 (1990).

[9] M. K. Sanyal, S. K. Sinha, K. G. Huang and B. M. Ocko, *Phys. Rev. Lett.* **66,** 628 (1991).

[10] P. S. Pershan, *Colloids and Surfaces* **A171,** 149 (2000).

[11] J. Als-Nielsen and H. Möwald, in *Handbook of Synchrotron Radiation*, Vol. 4, edited by S. Ebashi, E. Rubenstein and M. Koch (North Holland, Amsterdam, 1991), pp. 1.

[12] J. Als-Nielsen, D. Jacquemain, K. Kjaer, F. Leveiller, M. Lahav and L. Leiserowitz, *Physics Reports* **246,** 251 (1994).

[13] P. S. Pershan and J. Als-Nielsen, *Phys. Rev. Lett.* **52 ,** 759 (1984).

[14] V. M. Kaganer, H. Möwald and P. Dutta, *Rev. Mod. Phys.* **71,** 779 (1999).

[15]   G. L. Gaines, *Insoluble Monolayers at a Liquid Gas Interface* (Wiley and Sons, New York, 1966).

[16] B. I. Halperin and D. R. Nelson, *Phys. Rev. Lett.* **41,** 121 (1978).

[17]   C. Y. Young, R. Pindak, N. A. Clark and R. B. Meyer, *Phys. Rev. Lett.* **40,** 773 (1978).

[18] D. R. Nelson and B. I. Halperin, *Phys. Rev. B* **19,** 2456 (1979).

[19]   D. R. Nelson, in *Phase Transitions and Critical Phenomena*, Vol. 7, edited by C. Domb and J. L. Lebowitz (Academic, New York, 1983), pp. 1.

[20] K. J. Strandburg, *Rev. Mod. Phys.* **60,** 161 (1988).

[21] S. K. Sinha, Ed., *Ordering in Two Dimensions* (North-Holland, Amsterdam, 1980).

[22] R. J. Birgeneau and P. M. Horn, *Science* **232,** 329 (1986).

[23] J. D. Brock, R. J. Birgeneau, J. D. Litster and A. Aharony, *Physics Today* **July,** 52 (1989).

[24] H. Möhwald, *Annu. Rev. Phys. Chem.* **41,** 441 (1990).

[25] C. M. Knobler, *Adv. Chem. Phys.* **77,** 397 (1990).

[26] C. M. Knobler and R. C. Desai, *Annu. Rev. Phys. Chem.* **43,** 207 (1992).

[27] S. Henon and J. Meunier, *Rev. Sci. Instrum.* **62,** 936 (1991).

[28] G. Wegner, *Thin Solid Films* **216,** 105 (1992).

[29] G. Wegner and K. Mathauer, *Mat. Res. Soc. Symp. Proc.* **247,** 767 (1992).

[30] D. Neher, *Adv. Mater.* **7,** 691 (1995).

[31] J. H. Fendler and F. C. Meldrum, *Adv. Mater.* **7,** 607 (1995).

[32] J. R. Heath, C. M. Knobler and D. V. Leff, *J. Phys. Chem. B.* **101,** 189 (1997).

Chapter 2
C_{60}-propylamine Adduct Monolayers at the Gas/Water Interface

Abstract

Brewster angle microscopy (BAM), x-ray specular reflectivity and grazing-incidence x-ray diffraction (GID) studies of C_{60}-propylamine adduct monolayers at the gas/water interface are reported. At large molecular areas ($A > \sim 150$ Å^2/molecule), BAM images reveal macroscopic heterogeneity in the film, consisting of the coexistence between regions covered with uniform solid-like monolayer and bare water surface. After compression to a limiting molecular area of 150 Å^2/molecule, the film is observed to be homogeneous, with the uniform monolayer covering the entire available surface. Both the x-ray reflectivity results and the GID patterns are consistent with the formation of a uniform monolayer at $A \sim 150$ Å^2/molecule, while the little dependence that the GID patterns have on the molecular area for $A > \sim 150$ Å^2/molecule is consistent with the heterogeneity in the film. Upon further compression to higher densities ($A < \sim 120$ Å^2/molecule), the x-ray reflectivity results suggest the formation of a partial layer either at the molecule/gas interface or at the molecule/water interface. In this high density regime, the shift in the observed GID pattern with molecular area is much smaller than would be expected if the film were to remain a homogeneous monolayer, also consistent with the formation of an inhomogeneous partial layer. The analysis of the broad GID pattern observed from a uniform monolayer in terms of a model 2D radial distribution function, implies a short range positional correlation, extending to only a few

molecular distances. The average nearest neighbor distance ($d \sim 13$ Å), extracted from the GID analysis, is consistent with the limiting molecular area ($A \sim 150$ Å^2/molecule) assuming local hexagonal packing. These results together with the sharp facets observed in the BAM images demonstrate that the monolayer when uniform is a two-dimensional amorphous solid.

2.1 Introduction

One of the principal motivations behind many modern theoretical, computational and experimental studies of surface and interfacial phenomena is to understand the effects of physical dimension on statistical physics [1-3]. A challenge in this general area of physics has been to identify real, well defined physical systems that are suitable for experimental studies. Examples of two- or quasi-two-dimensional (2D) systems that have been investigated for this purpose in recent years include rare gases adsorbed on solid substrates [3-6], freely suspended thin liquid crystal films [7-10], and Langmuir monolayers of simple long-chain molecules such as fatty acids, alcohols, esters, etc. [11-15]. Related statistical phenomena at surfaces and interfaces that have been often studied for more practical motivations include wetting [16-18], pre-melting and reconstruction of crystalline surfaces [19-22], and surface induced order at liquid surfaces [23-26]. The experimental techniques that have been applied to these various systems are as diverse as the types of systems that have been studied. It is therefore not very surprising that one of the principal applications of the synchrotron based x-ray scattering techniques has been to probe the structure and phase transitions of both interfaces and monolayers.

The relative magnitude of the atomic cross section for elastic x-ray scattering, in comparison with the various inelastic or absorptive processes, has given unique advantages to x rays for studying the bulk structures of varieties of condensed matter. Singularly important for these purposes is the fact that with typical x-ray wavelengths, λ = 1 ~ 2 Å, it is practical to probe structures at atomic or molecular length scales. The

possibility of using x-rays to study surface physics followed in recent times from the combination of these advantages with the enhanced intensity, high collimation and small beam size of synchrotron generated x-rays [27, 28].Nevertheless, the scattering length for x-rays is typically many orders of magnitude larger than typical interatomic distances. Consequently, the scattering length is also many orders of magnitude larger than the thicknesses of interfacial regions, and the cross section for x-ray scattering from surfaces is small. As a result of all this, most of the observed x-ray scattering from surfaces, to date, has been from ordered phases, for which coherent addition of scattering from many atoms or molecules gives rise to relatively sharp intense peaks that can be separated from the diffuse background scattering from other sources [14, 21]. To the best of our knowledge, there are only four exceptions for which x-ray scattering can be said to have been observed from interfacial, or two-dimensional, systems with only short-range order.

The first exception is that of phase transitions involving gases adsorbed within the internal atomic planes of exfoliated graphite [5, 6]. Several systems that have been studied exhibit a rich variety of phase transitions and critical phenomena that have been extensively modeled; however, phase transitions for these systems are complicated by the presence of the periodic graphite substrate [1, 29]. For example, the submonolayer behavior of Kr on graphite [5] as well as the order-disorder transition for He on graphite at a near monolayer coverage [4] can be described by 'lattice gas' models, where the localized lattice gas sites reflect the long range order of the substrate. The second class of exceptions corresponds to observation of x-ray scattering peaks from hexatic phases of Langmuir monolayers, i.e., phases with long range bond-orientational order but only exponentially decaying positional order [30-32]. The observed half widths of these peaks are broader than the resolution limited Bragg peaks observed from crystalline phases; however, the widths are still narrower than what one expects from simple liquids, for which the bond-orientational order is also short range [33-35]. The third example is a recent report of liquid-like order in a monolayer of Bi adsorbed on the surface of liquid

11

Ga [36]. Finally, there are the numerous studies of phase transitions and quasi-long range correlations in thin films of various smectic liquid crystals [7, 34, 35, 37, 38]. These are amongst the more important measurements of the structural correlations for 2D statistical systems; however, only the very thinnest films are strictly two-dimensional.

We present here a combination of optical and x-ray scattering studies of a Langmuir monolayer (LM) formed by fullerene-propylamine adduct (abbreviated as C60-PA) molecules [39]. The C60-PA molecule consists of a C_{60} molecule and twelve propylamine ($NH_2(CH_2)_2CH_3$) chains attached to it. The unique feature of the C60-PA system is that the number of electrons scattering coherently from any one molecule is large enough to allow quantitative measurements of x-ray structure factor from a 2D structure with only short-range order. We will show that the C60-PA monolayer, both as-deposited and at low surface pressures, is a relatively incompressible solid that is either a 2D amorphous glass or a 2D microcrystalline solid. Although this is in itself an interesting observation, even more important is its implication that if some fullerene derivatives that form liquid, rather than solid, Langmuir monolayers could be developed, x-ray scattering studies of both 2D solidification and vaporization would be practical.

Obeng and Bard [40] were amongst the first to report formation of a LM of pure C_{60} at the H_2O/air interface. Although Maliszewskyj et al. [41] support Obeng and Bard, others [39, 42-46] found that the strong mutual attraction of the C_{60} molecules caused them to cluster, thereby destabilizing the LM. Nevertheless, Vaknin and coworkers were able to demonstrate the utility of covalent modification of C_{60} as a method for reducing the strong attractive interactions between clusters [39, 46]. The modification of C_{60} in this case consisted of attachment of multiple alkyl chains through the formation of C_{60}-amine adducts. The peripheral alkyl chains reduce cluster-cluster interactions and enable the formation of homogeneous monolayers.

Vaknin and coworkers reported both the surface pressure/area (Π-A) isotherm of LM of the fullerene-propylamine adduct (C60-PA) mentioned above as well as x-ray

reflectivity from the LM as a function of the area density [39, 46]. They observed that the reflectivity was consistent with well-defined monolayers that appeared to thicken when the LM was compressed and the surface pressure started to rise. The present measurements extend that work as follows: (i) We report Brewster angle microscopy (BAM) studies that allow visualization of the macroscopic morphology of the monolayer, both as spread and under varying degrees of compression. In fact, for specific area greater than ~150 Å^2/molecule the water surface is inhomogeneously covered by the LM. The LM covered regions are themselves homogeneous, having boundaries with rigid faceted edges that are indicative of a solid-like film. (ii) Whereas the original x-ray reflectivity measurements of Vaknin and associates used a laboratory x-ray source, we have extended the reflectivity measurements to larger angles using synchrotron radiation. These measurements allow for a quantitative improvement in the extracted models for the surface profile. (iii) We report the results of grazing incidence x-ray diffraction measurements. The observation of a broad GID peak indicates that the solid LM-coated regions viewed by the BAM are either 2D amorphous solid or 2D microcrystalline. As judged by the angular dependence of the scattered intensity, it appears as though the local structure of the amorphous solid changes only slightly under macroscopic compression by a factor of more than two.

The organization of this chapter is as follows: In Sec. 2.2, the experimental details concerning the x-ray scattering techniques, BAM, and the Π-A isotherm measurements are described briefly. In Sec. 2.3, the experimental results of Π-A isotherm, BAM, and x-ray scattering measurements on the C60-PA LM are presented and discussed. In the x-ray scattering part, the results and analysis of specular reflectivity and grazing incidence diffraction and rod scans are discussed separately. Finally, a summary is given in Sec. 2.4, and the main conclusions from this study are highlighted.

2.2 Experimental Details

2.2.1 X-ray techniques

The x-ray scattering measurements reported in this chapter were conducted at the Beamline X22B of the National Synchrotron Light Source, Brookhaven National Laboratory. A detailed description of the Harvard/BNL liquid surface spectrometer has been given previously [47]. In the following, x-ray specular reflectivity and grazing incidence diffraction techniques are discussed briefly.

The kinematics for the specular reflectivity technique is illustrated in Fig. 2.1(a). Highly collimated monochromatic x-rays of wavelength λ are incident at an angle α to the surface. For specular reflection, the scattered x-rays make an equal angle ($\beta = \alpha$) to the surface within the plane of incidence, and the reflected intensity is measured as a function of the z-component of the wave vector transfer $q_z = (4\pi/\lambda)\sin(\alpha)$. The component of the wave vector parallel to the surface is zero: $q_{xy} = 0$. The critical angle α_c for total reflection is typically on the order of $0.15°$ for water and $\lambda \sim 1.5$ Å, and for $\alpha > 4 \sim 5 \ \alpha_c$, the reflectivity $R(q_z)$ is approximately given by [14, 32, 48]

$$\frac{R(q_z)}{R_F(q_z)} \cong \left| \frac{1}{\rho_\infty} \int_{-\infty}^{\infty} dz \ \frac{d\langle \rho(z) \rangle}{dz} e^{iq_z z} \right|^2 \qquad (2.1)$$

In the above formula, $<\rho(z)>$ is the average electron density at some height z along the surface normal, $R_F(q_z)$ is the theoretical Fresnel reflectivity from an ideally flat, abrupt interface, and ρ_∞ is the electron density in the bulk liquid. As described in the literature, measurements of $R(q_z)$ can be interpreted in terms of model profiles, $<\rho(z)>$, that describe the average electron density of the interface along the surface normal. For a homogeneous LM on the surface of water the models yield surprisingly accurate measures of the thickness of the monolayer and the average electron density [14, 32]. On the other hand, without an independent determination that the surface is homogeneous, such as can be provided by the BAM technique, it could be difficult to interpret the model profile.

Within the last several years application of grazing incidence x-ray diffraction (GID) techniques has provided detailed information on the microscopic structure of a number of 2D phases [11-15, 19-21]. Except for a few cases where hexatic order was observed, most of these phases exhibited resolution-limited Bragg peaks characteristic of 2D crystalline phases. Fig. 2.1(b) illustrates the kinematics for the GID experiment. Highly collimated monochromatic x-rays are incident on the surface at an angle α that is smaller than the critical angle α_c, so that the incident beam only penetrates the bulk evanescently, decaying into the bulk exponentially. Consequently for $\alpha < \alpha_c$ the scattering from the bulk is suppressed significantly, and given the enhanced incident flux provided by a synchrotron source, the ratio of scattering from the surface to that of the bulk is sufficient to study surface phenomena.

(a)   (b)
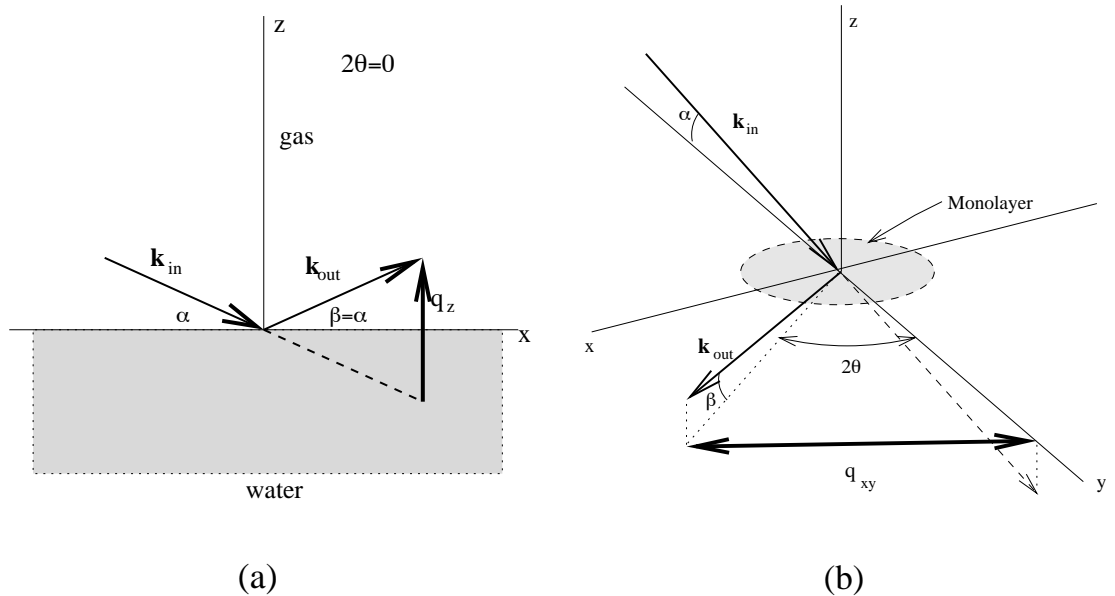
Figure 2.1: Scattering geometry for (a) specular reflectivity and (b) GID.

For GID, the detector makes an angle β to the surface, and 2θ is the angle between

the vertical plane containing the detected ray and the plane of incidence. In this geometry, the wavevector transfer between incident and detected radiation has components

$$q_z = \frac{2\pi}{\lambda}\left(\sin\alpha + \sin\beta\right)$$

$$q_{xy} = \frac{2\pi}{\lambda}\sqrt{\cos^2\alpha + \cos^2\beta - 2\cos\alpha\cos\beta\cos 2\theta}$$

(2.2)

For a 2D liquid monolayer of molecules with form factor $f(q_z, q_{xy})$ and 2D particle density of $n(r)$, the scattering amplitude for GID is proportional to [49]

$$S\left(q_{xy}, q_z\right) \propto \left|f\left(q_{xy}, q_z\right)\right|^2 \int \left\langle\left[n(0) - n_0\right]\left[n(r) - n_0\right]\right\rangle \exp\left(-i\vec{q}_{xy}\cdot\vec{r}\right)d^2r$$

$$\propto \left|f\left(q_{xy}, q_z\right)\right|^2 \int \left[\left\langle n(0)n(r)\right\rangle - n_0^2\right] J_0\left(q_{xy}r\right)rdr$$

(2.3)

where J_0 is the Bessel function of zeroth order and $n_0 = <n>$. The difference between liquid and crystalline powder has to do with the long range order in the 2D particle-particle correlation function, $<n(0)n(r)> - n_0^2$. For the 2D crystalline powder $S(q_{xy}, q_z)$ consists of a series of sharp circles at radii $q_{xy} = 2\pi/d_{h,k}$ where $d_{h,k}$ are the d-spacings for the 2D lattice [50]. Radial scans that measure intensity as a function of 2θ, or alternatively of q_{xy}, result in sharp peaks. In a typical *rod* scan, the scattered intensity is measured along q_z with q_{xy} held fixed at the GID peak position. For a monolayer, the only structure in the intensity along a rod results from the molecular form factor, $f(q_{xy}, q_z)$. For small molecules, or longer ones that are normal to the surface, this is typically peaked at $q_z = 0$ and varies slowly on the scale of $1/L$, where L is the molecular length projected on the surface normal.

For many of the 2D crystalline systems that have been studied experimentally, the molecular form factor $f(q_{xy}, q_z)$ and the Debye-Waller factor combine so that only the lowest-order Bragg peaks are observed. This is particularly true for the LM films. For 2D liquids or hexatic phases, with finite positional correlation lengths ξ, these peaks

16

should be both broader and weaker. Since the peak-height and peak width are proportional to ξ^2 and $1/\xi$, respectively, for liquid-like monolayers with $\xi \sim 3$ or 4 molecular radii, the peak intensity becomes vanishingly small. Although broadened peaks have been observed from 2D hexatic phases of freely suspended thin liquid crystal films [7, 35, 37], the evidence that they have been observed for LM is ambiguous [51-53].

2.2.2 Brewster angle microscope (BAM)

In principle GID measurements provide the most direct information of the microscopic order of 2D phases. However, microscopic information can often provide indirect evidence for a phase, or phase transition. For example, using Brewster angle microscopy and fluorescence microscopy, Knobler et al. have observed the macroscopic structure of both crystalline domains and macroscopic strain patterns surrounding microscopic defects [11, 54]. Analysis of these has often yielded information on both the microscopic structure of the phases and the nature of phase transitions. Microscopic observation to establish that the monolayer is homogeneous is a necessary prerequisite to quantitative interpretation of x-ray specular reflectivity.

The Brewster angle microscope [55] used in the present study is identical to the one described by Foster et al. [56, 57]. A p-polarized, argon-ion laser light ($\lambda = 488$ nm) is incident on the monolayer at the Brewster angle for water $\theta = 53.3°$ relative to the surface normal. The size of the illuminated sample area was approximately 5mm × 8.6mm. The presence of the monolayer on the water surface destroys the Brewster condition thereby causing non-zero reflected intensity, which makes the imaging of the illuminated monolayer surface possible. The images were focused by an achromatic lens of focal length f = 175 mm and were captured by a CCD camera, located approximately 1450 mm from the focusing lens. This set-up provided a magnification of 7.3 and a resolution of 20 μm, and the dimensions of the images captured by the CCD camera corresponded approximately to a surface area of 0.86mm × 1.1mm on the

monolayer.

2.2.3 Langmuir trough

The C60-PA LM sample [39] was prepared on a teflon Langmuir trough with a Wilhelmy pressure sensor, all of which were sealed in an aluminum enclosure filled with N_2 gas, as described by Schwartz et al. [47]. Millipore Milli-Q Plus water was used as the subphase. All of the measurements reported in this chapter were carried out at room temperature, typically at 22 ~ 23 °C. Before each spreading of a monolayer, the cleanliness of the water surface was tested by performing a quick compression isotherm on the water surface. If the surface pressure change over a compression ratio of 4 was less than 0.1 dynes/cm, the surface was considered to be clean enough for use. A monolayer was prepared by spreading a chloroform solution of C60-PA (0.28 mg/ml) on water at a specific area equal to or larger than 200 Å^2/molecule. Typically, the volume of the solution spread was about 80 µl. From estimated uncertainties in the concentration and the added volume of the solution and from the small variation in the available water surface area with the water height, the uncertainty in the area/molecule is estimated to be less than 4%. After the spreading of the film, a low flow of N_2 gas was maintained for about 30 min. to remove the evaporated chloroform and refill the enclosure with N_2 gas. Then, before starting any measurements, the N_2 flow was stopped, and the film was left undisturbed for about 30 min. for equilibration.

We used two different methods for the Π-A isotherm measurements in this study. In *relaxation* isotherms [47, 56, 57], the monolayer was allowed to relax after each step of compression by a small area change, typically ΔA ~ 2.5 Å^2/molecule. While the film was being relaxed at a given fixed specific area, the surface pressure was measured every minute. When the change in the surface pressure over five successive measurements, i.e. over 5 min., was less than 0.05 dynes/cm, a final measurement of surface pressure was made at that area/molecule, and the next compression step was taken. In *continuous*

isotherms, the monolayer was compressed at the rate of 2 (Å^2/molecule)/min. and the surface pressure was measured immediately after every 1 Å^2 change in the area/molecule.

During the x-ray measurements, the temperature of the water subphase and the C60-PA film was held at 22°C. The same procedure was followed for the preparation of the monolayer, except that high-purity He gas was used in place of N_2 gas in order to reduce the background scattering from the gas above the interface. The high degree of relaxation in the high-density part of the isotherm was taken into account by compressing the film in the following way. Up to the specific area at which the x-ray measurement was conducted, the film was compressed in steps of $\Delta A \cong 2.5 \ \text{Å}^2$/molecule, and after each compression step, the film was relaxed for 3 minutes. Once the specific area of interest was reached, the film was allowed to relax more fully. The x-ray measurement was started only after the surface pressure dropped to the value given by the relaxation isotherm. At the given specific area, the measurement was repeated at least once to make sure that there was no structural change with time.

2.3 Results and Discussion

2.3.1 Π-A isotherm

A typical isotherm taken at $T = 22$°C for each type of isotherm is shown in Fig. 2.2, with the open circles and the solid line corresponding to the relaxation isotherm and the continuous isotherm, respectively. While the entire continuous scan took slightly over one hour, the relaxation scan took nearly two days due to the long relaxation time in the high density region. The shape of the continuous Π-A curve is nearly identical to the measurements reported by Vaknin et al. [39]. As shown in the figure, the shapes of the two isotherms are only qualitatively similar. For specific area $A > 150 \sim 160 \ \text{Å}^2$/molecule, the surface pressure remains close to zero, although the
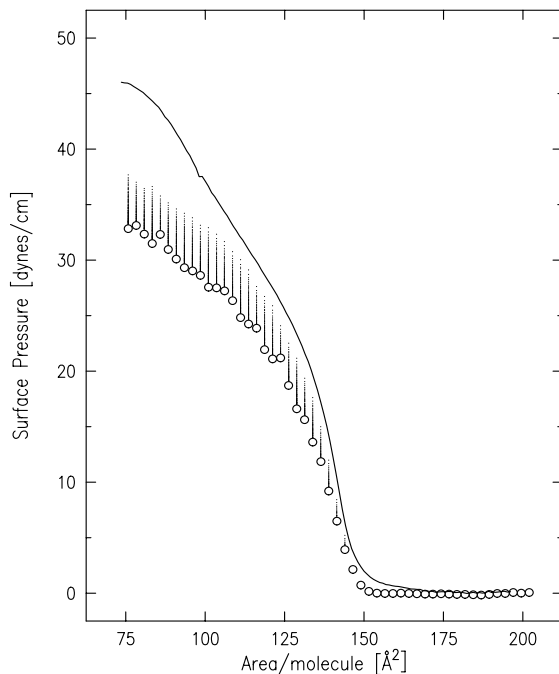
Figure 2.2: Π-A isotherms taken on C_{60}-propylamine films at $T = 22°C$. The solid curve (——) is a continuous isotherm, in which the film was compressed continuously at the rate of 2 ($Å^2$/molecule)/min. The open circles ($\bigcirc$) correspond to the relaxation isotherm, in which the film was allowed to relax at a given fixed area/molecule until the surface pressure variation over 5 min. was less than 0.05 dynes/cm.. The dots ($\cdot$) are for the intermediate surface pressure measurements during relaxation.

continuous isotherm shows a gradual increase in the surface pressure as A approaches 150 $Å^2$/molecule. Compression past $A \approx 150$ $Å^2$/molecule results initially in a steep increase in the surface pressure, with a very low compressibility that is constant over $\Delta A \sim 20$ $Å^2$. The value of the limiting area/molecule at the onset of the rise in Π and the slope of the Π-A curve in this region are both well reproducible for each of the isotherms. The high degree of incompressibility in the region just below 150 $Å^2$/molecule suggests that the molecules become closely packed around 150 $Å^2$/molecule. This value of

20

specific area agrees well with the expected cross-sectional area of one C_{60}-$[NH_2(CH_2)_2CH_3]_{12}$ molecule and gives strong evidence that (i) the deposited film is a monolayer and (ii) that the monolayer is uniform at 150 Å^2/molecule. One explanation that is consistent with the fact that the surface pressure remains nearly zero for specific area greater than the limiting value, is that at low densities the monolayer is macroscopically heterogeneous and coexists with either bare water surface or a low-density 2D gas. As will be described later, the inferences made above are consistent with the BAM and reflectivity results.

In both isotherms, further compression into the high-density region ($A < 130$ Å^2/molecule) results in a surface pressure increase with a smaller slope, where the cross-over between the two compressibilities occurs around $A = 125 \sim 135$ Å^2/molecule. This indicates that the film is more compressible at higher densities. A likely explanation is that in this region, compression forces the molecules out of the monolayer plane. Since the molecules have already become closely packed, a further reduction in the specific area can only be achieved either through the deformation of molecules themselves or by sending some molecules into the third dimension. The comparison between the continuous and relaxation isotherms gives a clear indication that the degree of relaxation is quite high in the high-density regimes. Although we cannot prove that the relaxed monolayer is in thermal equilibrium, it is clear that the unrelaxed monolayer is not.

2.3.2 Surface imaging by BAM

The BAM images taken from the C60-PA monolayer at various specific areas are summarized in Fig. 2.3. Fig. 2.3(a) illustrates the nature of an as-deposited monolayer at specific area $A = 280 \pm 11$ Å^2/molecule. The coexistence of bright and dark regions is evident. At this specific area, one often finds a large uniformly bright region, which indicates a homogeneous monolayer. However, it is not difficult to find varying degrees
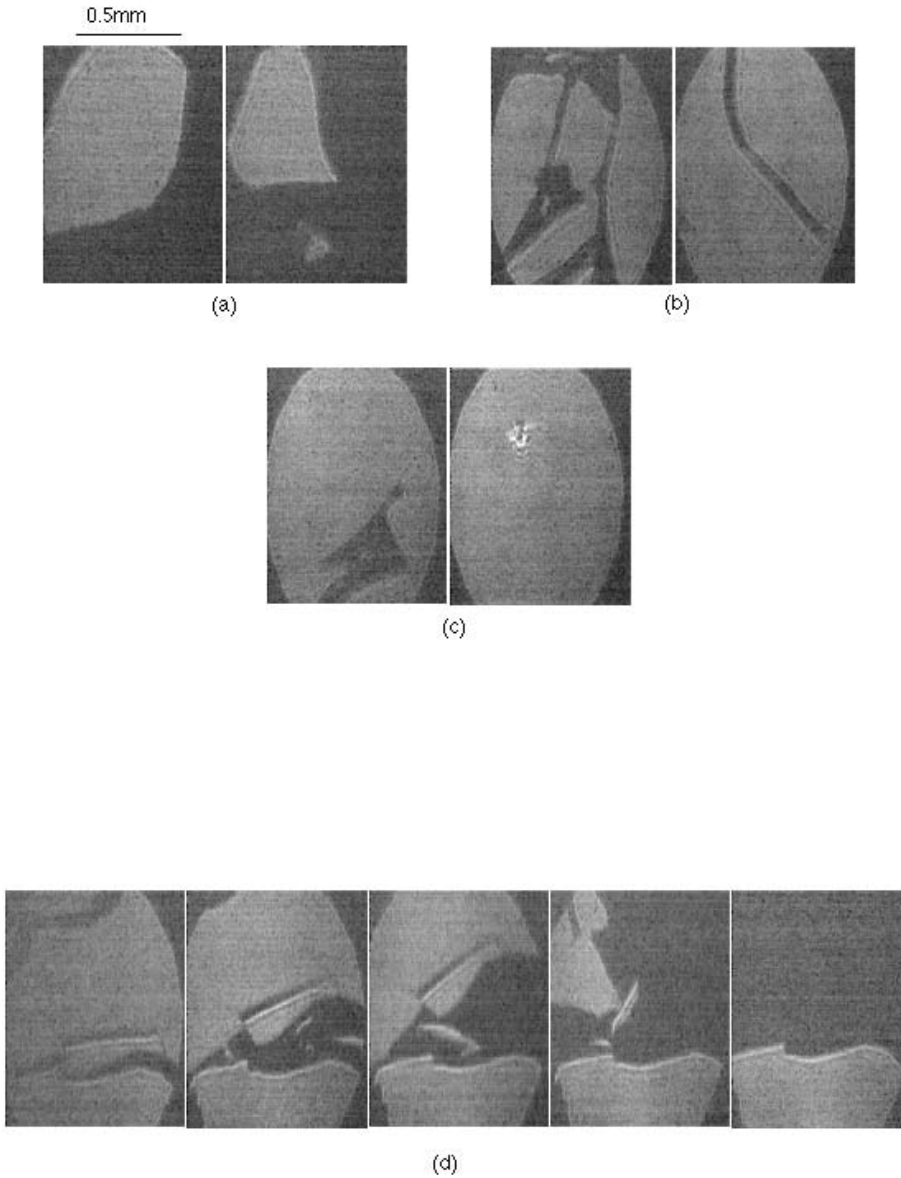
Figure 2.3:   BAM images taken at A = (a) 280 ± 11 Å^2/molecule, (b) 190 ± 8 Å^2/molecule, and (c) 165 ± 7 Å^2/molecule in a compression cycle. BAM images in (d) were taken at A = 245 ± 10 Å^2/molecule in the expansion cycle, at t = 0, 4, 10, 11, and 13 seconds. The film was first compressed to 165 ± 7 Å^2/molecule and then expanded, where the rate of compression/expansion was ~0.05 Å^2/sec.

of dark areas, which indicate either bare, uncovered water surfaces or 2D gas of C60-PA molecules at very low density. Two images in Fig. 2.3(a) illustrate the varying degrees of surface coverage at this specific area. The relatively sharp cusp ($40° \pm 5°$) formed by the boundary between the covered and bare surface is one indication that the monolayer is solid.

Upon compression, the fraction of time that the viewed area appears to be covered with a homogeneous monolayer increases. The images shown in Fig. 2.3(b) were taken after the LM was compressed continuously to a specific area of 190 ± 8 Å^2/molecule at the rate of ~ 0.05 Å^2/molecule-sec. At this specific area, homogeneous fields of view are most common. However, images like those shown in Fig. 2.3(b) are easy to obtain. Here too, the boundaries of the monolayer covered regions are most often straight, meeting at sharp angles that would not be expected if the monolayer were fluid.

Compression at the same rate to 165 ± 7 Å^2/molecule yields a monolayer for which it is very difficult to find any dark regions. Fig. 2.3(c) illustrates two typical views of the few non-uniform regions that can be located at this specific area. Aside from being rarer, the dark regions are smaller when found. At $A \sim 150$ Å^2/molecule, it is almost impossible to locate any dark regions and, as might be implied by the isotherm, we believe that at this specific area the C60-PA LM has fully coated the surface of the trough.

According to this interpretation, further compression can only be achieved either by reducing the molecular area while maintaining an intact monolayer or by forcing some of the fullerene molecules out of the plane to form a bilayer or other multilayer structures. Although the reflected optical intensity does increase systematically with further compression, we were not able to observe any well defined contrasting regions that might have indicated macroscopically formed bilayers, or other multilayers. Such regions, if they form, must be smaller than the resolution ~ 20 µm of the BAM for weakly contrasting domains.

Figure 2.3(d) illustrates the process by which the uniform monolayer breaks upon expansion. This monolayer had been compressed to 165 Å^2/molecule and then expanded at ~ 0.05 Å^2/molecule-sec to 245±10 Å^2/molecule, at which the images shown were observed at t = 0, 4, 10, 11, 13 seconds. The shape of the boundaries when the monolayer breaks gives another strong evidence that the monolayer is solid-like.

2.3.3 X-ray reflectivity

In Fig. 2.4, the measured reflectivity data normalized to the theoretical Fresnel reflectivity of an ideally flat water surface, $R(q_z)/R_F(q_z)$, are shown for the C_{60}-propylamine film at five different specific areas. From the variation of the $R(q_z)/R_F(q_z)$ curves with the specific area, it is clear that the film grows thicker with increasing density. In fitting the measured reflectivities, only the simplest models for the electron density profiles are justified because of the limited range of the q_z values in the data. The models we used for the average electron density profile along the surface normal are single-layer and double-layer "box" models in which each interface is smeared out with a Gaussian roughness. A *single-layer* model contains four free parameters and is defined as

$$\frac{\langle\rho(z)\rangle_{1-box}}{\rho_{water}} = 1 + (h-1)\frac{1}{2}\left(1 + erf\left(\frac{z+d}{\sqrt{2}\sigma_1}\right)\right) - h\frac{1}{2}\left(1 + erf\left(\frac{z}{\sqrt{2}\sigma_0}\right)\right), \qquad (2.4)$$

where d is the thickness of the monolayer, h is the electron density in the layer normalized with respect to that of water (ρ_{water} = 0.334 electrons/Å^3), and σ_0 and σ_1 are the roughness for the gas/monolayer interface and for the monolayer/water interface, respectively. In a *double-layer* model, another layer is added to the single-layer model. However, in order to keep the number of parameters small, we assumed a common thickness d for both of the two layers and a common roughness σ for all of the three interfaces. Consequently, the double-layer model also has only four free parameters and
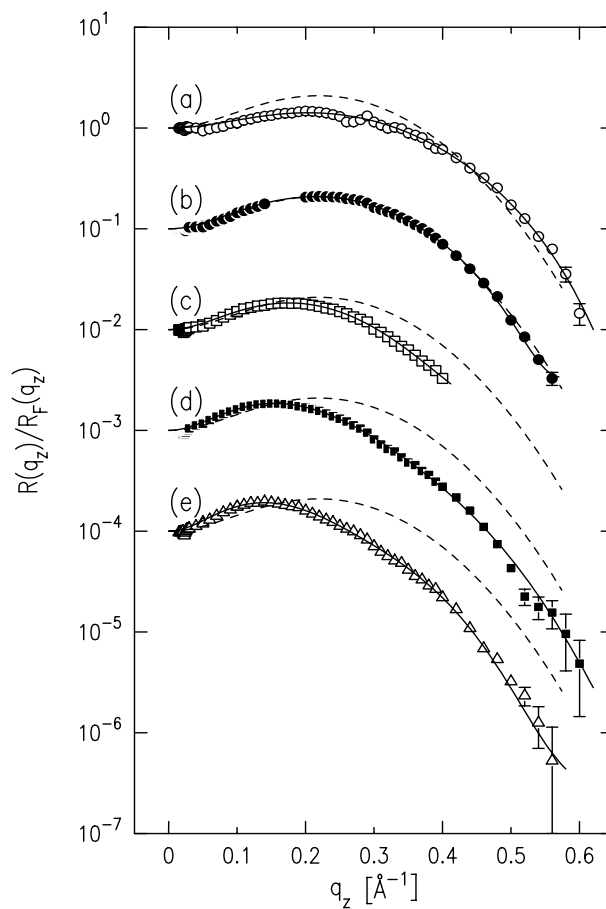
Figure 2.4: Measured reflectivity normalized by the Fresnel reflectivity of an ideally flat and sharp water/gas interface, taken at $A = 189 \pm 8$ Å^2/molecule (a,$\bigcirc$), 147 ± 6 Å^2/molecule (b,$\bullet$), 126 ± 5Å^2/molecule (c,$\square$), 105 ± 4Å^2/molecule (d,$\blacksquare$), and 84 ± 3Å^2/molecule (e, open triangle). For each, solid curve is the best fit by the box model, corresponding to the average electron density profile shown in Fig. 2.5. The dashed curves are all identical and correspond to the best fit to the 147 ± 6Å^2 data that is based on the model of average electron density profile given by the solid curve in Fig. 2.12(c).

25
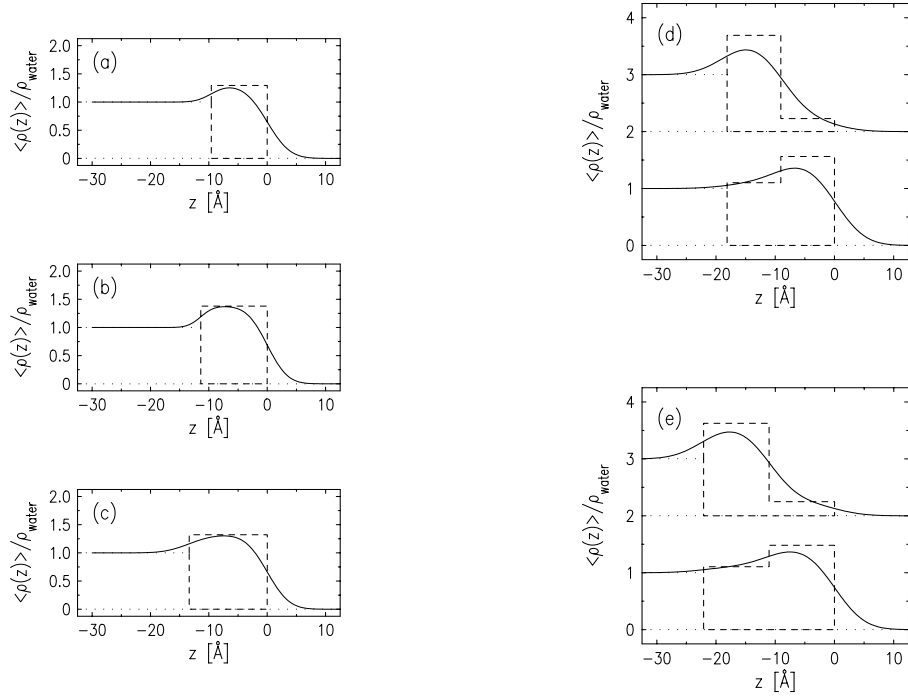
Figure 2.5: The box models for the average electron density along the surface normal, normalized to the bulk density in water, all corresponding to the best fit. (a) $A = 189 \pm 8$ Å^2/molecule, (b) 147 ± 6 Å^2/molecule, (c) 126 ± 5 Å^2/molecule, (d) 105 ± 4 Å^2/molecule, and (e) 84 ± 3Å^2/molecule. The boxes in the models are indicated by the dashed lines. The dotted lines refer to the zeros and the bulk value of the electron density.

is defined as

$$
\begin{aligned}
\frac{\langle \rho(z) \rangle_{2-box}}{\rho_{water}} = 1 &+ (h_1 - 1)\frac{1}{2}\left(1 + erf\left(\frac{z + 2d}{\sqrt{2}\sigma}\right)\right) \\
&+ (h_2 - h_1)\frac{1}{2}\left(1 + erf\left(\frac{z + d}{\sqrt{2}\sigma}\right)\right) - h_2 \frac{1}{2}\left(1 + erf\left(\frac{z}{\sqrt{2}\sigma}\right)\right)
\end{aligned}
\tag{2.5}
$$

where h_1 and h_2 are the normalized electron densities in the layer just above water and in the layer just below the gas, respectively.

The nonlinear least-squares fitting to the measured $R(q_z)/R_F(q_z)$ was done using the Born approximation (Eq. (2.1)) and the box models just described. Since the Born

Table 2.1: The list of best-fit parameters used to fit the measured R/R_F data, where the fits are based on gaussian-smeared "box" models for the average electron density profile $<\rho(z)>$ across the water/LM/gas interface. (a) Single-box model. The thickness of and the excess electron density (relative to the bulk electron density ρ_{water}) in the monolayer are given respectively by d and h. The roughness σ_0 is for the monolayer/gas interface, and σ_1 is for the water/monolayer interface. (b) and (c) Double-layer box models. Each of the two layers is assumed to have the same thickness d, and each of the three interfaces is assumed to have the same roughness σ. The relative electron densities h_1 and h_2 are respectively for the bottom layer (in contact with water) and for the top layer (in contact with vapor). The second, less dense layer is introduced as the bottom layer in part (b) and as the top layer in part (c).

(a) Single-box model

$A^\dagger$ (Å^2/molec.)	$h = \rho_{box}/\rho_{water}$	d (Å)	σ_0 (Å)	σ_1 (Å)
189±8	1.29±0.07	9.6±0.9	3.07±0.4	2.09±0.7
147±6	1.38±0.05	11.4±0.8	2.76±0.3	1.78±0.5
126±5	1.32±0.09	13.4±1.8	2.99±0.5	3.33±0.7

(b) Double-layer box model with the second layer _below_ the monolayer.

$A^\dagger$ (Å^2/molec.)	h_1	h_2	d (Å)	σ (Å)
105±4	1.10±0.05	1.56±0.07	9.1±1.2	4.05±0.14
84±3	1.105±0.024	1.483±0.036	11.1±1.0	4.03±0.12

(c) Double-layer box model with the second layer _above_ the monolayer.

$A^\dagger$ (Å^2/molec.)	h_1	h_2	d (Å)	σ (Å)
105±4	1.69±0.09	0.23±0.09	9.1±1.2	4.05±0.14
84±3	1.63±0.05	0.25±0.04	11.1±1.0	4.02±0.12

† Note that the area/molecule A is *not* a fitting parameter.

approximation is valid only for $q_z > 4\sim5q_c$ ($q_c = 0.0218$ Å^{-1} for water), only the data for $q_z \geq 0.1$ Å^{-1} were fitted. The best fits to $R(q_z)/R_F(q_z)$ are given by the solid curves in Fig. 2.4, and the corresponding average electron density profiles are shown in Figs. 2.5(a)-(e) for the five specific areas. Note that for the higher density monolayers in Figs. 2.5(d)-(e),

the data can be equally well represented by the two different profiles [58]. As indicated by the boxes (dashed lines in Fig. 2.5(a)-(e)) shown along with the density profiles, the data for $A = 189\pm8$, 147 ± 6, and 126 ± 5 Å^2/molecule were fitted by the single-layer model, while the double-layer models were necessary to obtain a good fit to the data for $A = 105\pm4$ and 84 ± 3 Å^2/molecule. The parameters obtained in the fitting are summarized in Table 2.1; however, since the BAM results clearly indicate that the monolayer is inhomogeneous at 189 Å^2/molecule, ascribing a physical meaning to the parameters for this density is questionable.

The carbon cage radius of a C_{60} molecule is 3.55 Å [59, 60], and the end-to-end length of the tetrahedrally-bonded N-C-C-C unit in a propylamine chain is about 4 Å. If each of the twelve N-C_{60} bonds is assumed to be about 1.5 Å long and to point in the radial direction, the diameter of one C60-PA molecule is estimated to be about 16 Å. However, when the electron density of one such molecule is projected onto a z-axis, more than 90% of the electrons are concentrated within $|z| < 5 \sim 6$ Å. Therefore, if the film is a monolayer, the thickness d of the layer obtained from the average electron density profile is expected to be $10 \sim 12$ Å. As listed in Table 2.1, the single-layer model gives $d \approx 9.6$ Å at $A = 189$ Å^2/molecule and $d \approx 11.4$ Å at $A = 147$ Å^2/molecule, and it is clear that the film is a monolayer at these specific areas. This result is consistent with the isotherm studies, and agrees with the earlier reflectivity study on the same system by Vaknin et al. [39]. Also note that the roughnesses σ_0 and σ_1 are smaller and the excess electron density h is higher at 147 Å^2/molecule than at 189 Å^2/molecule. Both the reduction in the roughnesses and the enhancement in the excess electron density, upon compression from 189 to 147 Å^2/molecule, are consistent with the BAM observation that the monolayer is macroscopically inhomogeneous at $A \sim 190$ Å^2/molecule and also suggest the formation of a uniform monolayer around 150 Å^2/molecule. At $A = 126$ Å^2/molecule, the data can still be fitted by the single-layer model, but both the roughness and the thickness of the film are slightly greater than those at 147 Å^2/molecule.

The film thickness $d \approx 13.7$ Å is still consistent with the film being a monolayer at this specific area. However, the increased thickness and roughness may also suggest that some molecules are probably starting to be forced out of the monolayer plane.

At $A = 105$ and 84 Å^2/molecule, the film is no longer a monolayer, and the fitting at these specific areas requires the introduction of a second layer. We have considered both models in which the second layer is introduced *above* the original monolayer and with the second layer being *below* the first layer. The data at each specific area can be fitted equally well by the two models, whether the second layer is introduced above or below the monolayer, and it is not possible from these data to determine which corresponds to the actual situation. Nonetheless, it is evident from both models, as indicated by the boxes in Figs. 2.5(d) and 2.5(e), that the film consists of two layers at these specific areas, and the average total thickness of the film is about twice that of a monolayer. The roughness $\sigma \approx 4$ Å at these densities is greater than the monolayer values by ~ 30%, and this may be an indication that the second layer formed is inhomogeneous.

Since all electrons, whether from water or from C60-PA molecules, contribute to specular reflectivity in the same way in the x-ray regime, it is not strictly possible to determine the exact location of the water/film interface from the reflectivity data. However, it is reasonable, especially in the single-layer models, to use the size of the "boxes," shown in Figs. 2.5(a)-(e), as an estimate for the contribution from the C60-PA molecules to the average electron density. More specifically, the number of electrons from the C60-PA molecules per unit area parallel to the interface should be roughly equal to the electron density ρ_{water} in water times the integrated area in the box, namely $h \cdot d$ for the single-layer model and $h_1 \cdot d + h_2 \cdot d$ for the double-layer model with the second layer *above* the monolayer. In the case of the double-layer model with the second layer being *below* the first layer, the contribution to the box area from the C60-PA molecule should only be $x \cdot h_2 \cdot d + h_2 \cdot d$, where $x = (h_1-1)/(h_2-1)$ and h_2 is for the complete monolayer in this case. In Fig. 2.6, the surface electron density of the film calculated this way using the

best-fit values is plotted as a function of specific area. Also shown in the figure (solid curve) is the "theoretical" surface electron density of the film, given by the ratio of the known number of electrons per C60-PA molecule and area/molecule, which is a quantity completely independent of the reflectivity results. The surface electron densities in the film calculated by the two independent methods agree quite well for the monolayers at $A = 189$, 147, and 125 Å^2/molecule, indicating that the values of the layer thicknesses and excess electron densities obtained from the reflectivity results are physically reasonable. However, the values of the surface electron density based on the double-layer models are
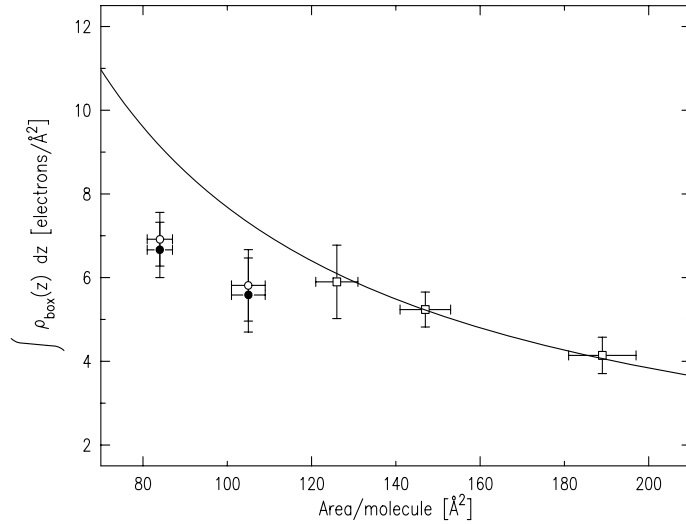
Figure 2.6: The surface density of electrons from the C$_{60}$-propylamine film as a function of specific area. The "measured" values are given by $\rho_{water} = 0.334$ electrons/Å^3 times the area of the boxes in the models in Fig. 2.5 that corresponds to the contribution from the C60-PA molecules. The open squares ($\square$) correspond to the single-layer models, and the circles are for the double-layer model with the second layer being *above*($\bigcirc$) and *below*($\bullet$) the monolayer. The solid curve (—) is the theoretical value, given by the number of electrons per molecule (768) divided by the specific area.

lower than the expected theoretical values. This is probably an indication that at high

densities, part of the molecules that are in excess of the number needed for the complete monolayer, are collected around the barrier and edges of the trough and/or form small aggregates, although the rest of the extra molecules are forced out to a second layer as indicated by the reflectivity results.

2.3.4 GID and rod scans

The most important result of the GID study on the C60-PA monolayer is the observation of the x-ray scattering factor from an amorphous or liquid-like structure in two dimensions. Fig. 2.7 illustrates typical raw GID scans of the C60-PA monolayer, clean water surface, and He gas above the monolayer. For the scans in Fig. 2.7(a), a single set of crossed slits of width 3 mm and height 20 mm, located at distance of 605 mm from the sample, were used in front of the detector. Taking into account the size of the x-ray-illuminated footprint on the film (36 mm × 0.4 mm), the q_{xy} resolution with these slits varied from $\delta q_{xy} = 0.02$ to $0.03\ \text{Å}^{-1}$ in the range where the scans were taken. The scans shown in Fig. 2.7(b) were collected using Soller slits that had a horizontal acceptance angle of 3×10^{-3} radians, corresponding to a resolution of $\delta q_{xy} < 0.012\ \text{Å}^{-1}$. In addition to those shown in the figure, scans with finer steps were taken to make certain that there was no sharp resolution-limited peak. The contribution from the C60-PA molecules to the scattered intensity is given by the difference between the raw scan on the film and that on the water surface. The result of this subtraction is shown in Fig. 2.8 for three specific areas, 105±4, 147±6, and 189±8 Å^2/molecule. At all the specific areas studied, the scans from the film exhibited a broad peak which was centered at $q_{xy} = 0.42 \sim 0.45\ \text{Å}^{-1}$ and had a full width of $\Delta q_{xy} \approx 0.2\ \text{Å}^{-1}$. The comparison between Figs. 2.7(a) and 2.7(b) demonstrates that the peak width is much broader than and hence independent of the two detector resolutions. Consequently, the subsequent measurements were made using the coarser resolution (i.e. the regular crossed slits).
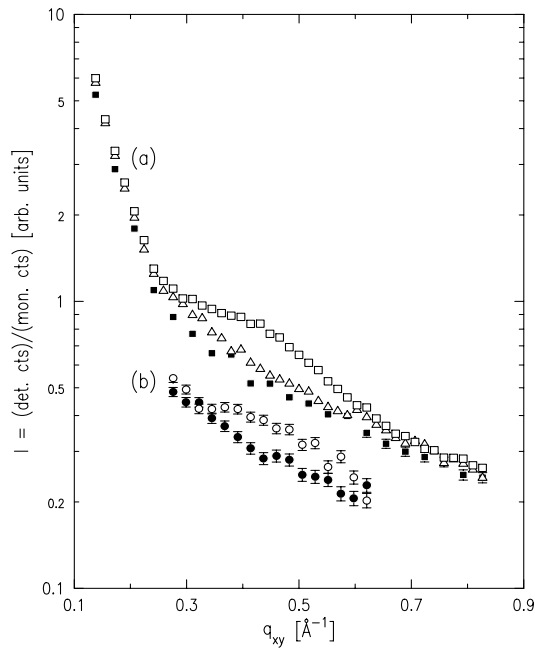
Figure 2.7: (a) Typical raw GID scans taken with a set of cross slits at the detector. The three scans shown correspond to a C60-PA monolayer (□), water (open triangle), and He background above the film (■). (b) Typical raw GID scans taken with Soller slits. The two scans shown are for a C60-PA monolayer (○) and He background above the film (●).

Figure 2.8 clearly indicates that the background subtracted GID patterns shown all have a broad peak of width $\Delta q_{xy} \approx 0.2 \text{ Å}^{-1}$. The position of the peak center at $q^0_{xy} \sim 0.42 \text{ Å}^{-1}$ for $A = 189$ and 147 Å^2/molecule roughly corresponds to a characteristic length of $2\pi/q^0_{xy} \sim 15 \text{ Å}$, which is comparable to the diameter of a C60-PA molecule. Since the instrumental resolution, being one order of magnitude smaller than Δq_{xy}, is negligible, the broadness of the peak is evidence that the positional correlation of the molecules in the film is of short-range [61]. As discussed earlier, the reflectivity results have demonstrated that the film is a monolayer at $A = 189$ and 147 Å^2/molecule. Therefore, at these specific areas, the monolayer is a 2D amorphous phase, which the

32
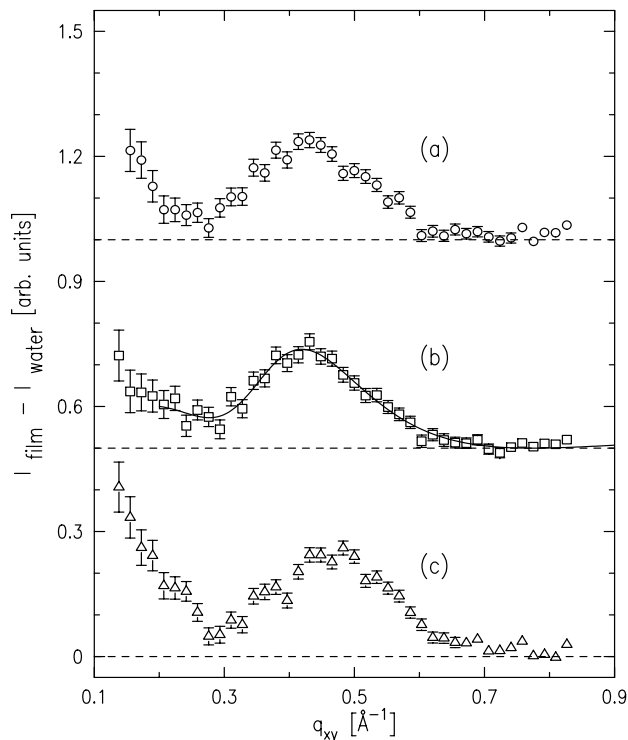
Figure 2.8: The measured net GID patterns from the C_{60}-propylamine film, after the water+He background has been subtracted off, for A = (a) 189 ± 8 Å^2/molecule, (b) 147 ± 6 Å^2/molecule, and (c) 105 ± 4 Å^2/molecule. The solid curve in (b) is the best fit at A = 147 ± 6 Å^2/molecule, based on the molecular form factor calculated from the spherical model of the C60-PA molecule described in Fig. 2.9 and the model 2D radial distribution function shown in Fig. 2.10.

BAM images have suggested is solid-like. The fact that the GID patterns at A = 189 and 147 Å^2/molecule are nearly identical, is consistent with the BAM observation that the monolayer does not fill the entire available trough area at large specific areas. Rather it consists of large "islands" which only come together to form a uniform, complete monolayer at around 150 Å^2/molecule.

The GID pattern for A = 105 Å^2/molecule is nearly identical to the other two

33

except for the peak position, $q^0_{xy} \sim 0.45$ Å^{-1}. This small shift is a clear indication that unlike at low densities, the compression actually pushes molecules against each other in the high-density regime, as evidenced by the increase in the surface pressure. However, the shift in the peak is much smaller than would be expected if the film were to remain homogeneous and one-molecule thick. If the compression only forced the molecules closer together in the monolayer plane, the reduction of the specific area from 147 to 105 Å^2/molecule would correspond to the change in the average intermolecular distance by ~18%, and the center of the peak at $A = 105$ Å^2/molecule would be at $q^0_{xy} \sim 0.50$ Å^{-1}. The fact that the dependence of the GID peak position on the specific area is only slight at high densities, is consistent with the reflectivity observation that below ~120 Å^2/molecule, some molecules are forced out of the monolayer plane. The explanation for the similarity of the GID patterns, aside from the slight shift in the peak position, is probably that the second layer is inhomogeneous and the observed scattered intensity comes almost entirely from the short-range positional correlation of the molecules in the first layer.

More quantitative analysis of the GID pattern has been carried out as follows. In the absence of long-range correlation, the extent of the molecular positional order in a *homogeneous* monolayer is characterized by a 2D radial distribution function, $g(r)$, which is defined so that $n_0 g(r) d^2 r_{xy}$ gives the probability for finding a molecular center in $d^2 r_{xy}$ at distance $r = [x^2 + y^2]^{1/2}$ *given that* there is another molecule at the origin. The 2D average molecular density in the homogeneous monolayer is given by $n_0 = \langle n(0) \rangle$. The 2D radial distribution function $g(r)$ goes to 0 as $r \to 0$ due to hard core repulsion, and approaches 1 as $r \to \infty$ since the probability is equal to the average density in the absence of correlation. The normalization condition on $g(r)$ is given by

$$n_0 \int_{\text{footprint}} g(r) 2\pi r \, dr = N - 1 \quad (\approx N), \tag{2.6}$$

34

where N is the number of molecules in the plane that are illuminated. In terms of the 2D radial distribution function, the scattering function for the GID patterns can be expressed as [49, 62]

$$S(\vec{q}) = S_0 \left| f\left(q_{xy}, q_z\right) \right|^2 \left\{ 1 + 2\pi n_0 \int_0^\infty \left(g(r) - 1\right) J_0\left(q_{xy} r\right) r dr \right\}, \qquad (2.7)$$

where the terms that contribute only to the scattering in the plane of incidence are omitted in the above expression [62, 63]. The first term on the right-hand side of Eq. (2.7) corresponds to the uncorrelated sum of scattering from individual molecules, and the second term to the interference between the scattered waves. Apart from the number of molecules illuminated, the proportionality factor S_0 depends only on the incident angle α, which is a fixed quantity for GID scans. Because of the normalization condition Eq. (2.6), the scattering function, as given by Eq. (2.7), must vanish at $q_{xy} = 0$; that is, $S(q_{xy} = 0, q_z) = 0$.

When the entire film is a *homogeneous monolayer*, the 2D average molecular density n_0 appearing in Eq. (2.7) is given by the inverse of the specific area A. Therefore, the use of Eq. (2.7) with the substitution $n_0 = 1/A$ to fit the GID pattern is appropriate for the specific area $A = 147$ Å^2/molecule, at which we know that the film is a uniform monolayer. Ideally, the extraction of the 2D radial distribution function $g(r)$ from the data would involve taking the relative difference, or residual, between the observed GID pattern and the molecular form factor $|f(q_{xy}, q_z)|^2$ and inverse-Hankel transforming the result. However, in the present case, the limited range of the GID data and the fact that the molecular form factor for a C60-PA molecule is not well defined, make it less practical to attempt this direct method. Instead, the fitting of the GID pattern with Eq. (2.7) was done by modeling both $g(r)$ and a spherically-symmetric average electron density $\rho_1(r)$ in a C60-PA molecule, which gives $f(q_{xy}, q_z)$ through Fourier transformation. Since the limited q_{xy} range of the GID data makes the fitting insensitive to any detailed

structures, simple models are used here.

Our model for the radial distribution function is given by

$$
g(r) = \begin{cases} h \exp\left(-\dfrac{(r-d)^2}{\sigma^2} \right) & \text{for } r \le d \\[3mm] 1 + (h-1)\exp\left(-\dfrac{r-d}{\xi} \right)\cos(\kappa(r-d)) & \text{for } r \ge d \end{cases}
\tag{2.8}
$$

The increase of $g(r)$ from the origin to the nearest neighbors is modeled by a Gaussian centered at an average nearest neighbor distance d. We have assumed that the width σ of the Gaussian is sufficiently smaller than d, and neglected the fact that a small value of $g(r)$ at $r = 0$ given by the model is not strictly zero. The results would not be significantly changed if the model were modified to make $g(0)$ identical to zero. In order to include the correlation with the next neighbors with the smallest number of parameters, an exponentially decaying cosine is used for $r \ge d$, where we have assumed that the positional correlation extends only a few intermolecular distances and the exact periodicity of the cosine function is not essential. Although there are five parameters (d, h, σ, ξ, κ) in the model, only four of them are independent due to the normalization condition Eq. (2.6) on $g(r)$. Using the equivalent condition $S(q_{xy} = 0, q_z) = 0$, the parameter h can be expressed in terms of the other four parameters:

$$
h = \frac{1}{I_1 + I_2}\left\{ I_2 + \frac{1}{2}d^2 - \frac{1}{2\pi n_0} \right\}
\tag{2.9a}
$$

where

$$
\begin{cases} I_1 = \dfrac{\sigma^2}{2}\left\{ \dfrac{\sqrt{\pi}d}{\sigma}\, erf\left(\dfrac{d}{\sigma} \right) + \exp\left(-\dfrac{d^2}{\sigma^2} \right) - 1 \right\} \\[5mm] I_2 = \left(\dfrac{\xi}{1+\kappa^2\xi^2} \right)^2 \left\{ 1 + \dfrac{d}{\xi} + \kappa^2\xi^2\left(\dfrac{d}{\xi} - 1 \right) \right\} \end{cases}
\tag{2.9b}
$$
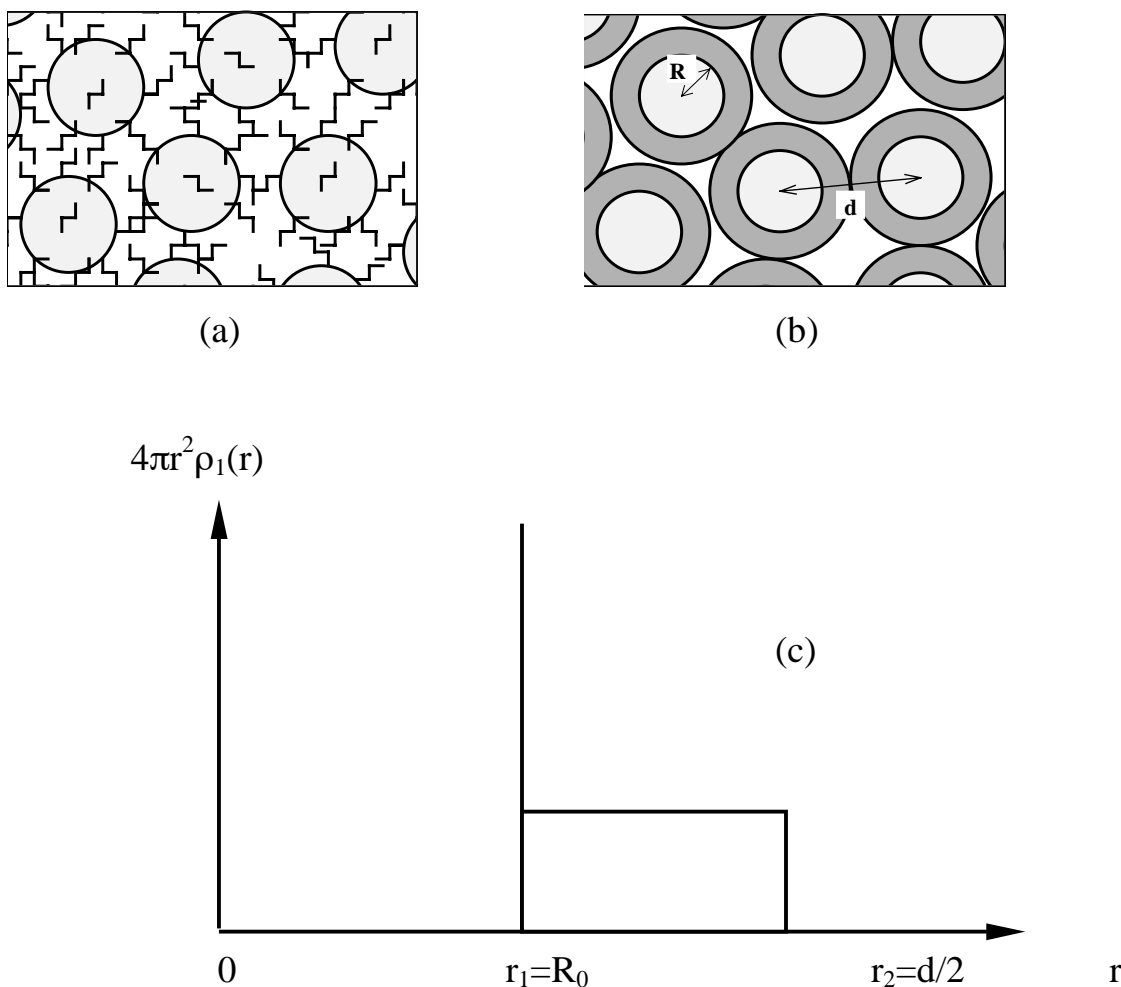
Figure 2.9: (a) Illustration of a closed-packed, 2D arrangement of C_{60}-propylamine adduct molecules on water surface. (b) Illustration for the spherically-symmetric shell model, in which the distribution of electrons in each C60-PA molecule is separated into two parts: one for the electrons from the pure C_{60} molecule and the other for those from the propylamine chains. (c) The model electron density within a C60-PA molecule, as a function of radius r. The model consists of (i) a delta function at $r_1 = R_0 = 3.55$ Å for the C_{60} molecule and (ii) a spherical shell of inner radius $r_1 = R_0$ and outer radius $r_2 = d/2$ for the propylamine chains, in which electrons are distributed so that the number in each spherical shell of width dr is constant.

The distribution of electrons within a C60-PA molecule consists of two parts: 360 electrons from the C_{60} molecule and 408 electrons from the twelve propylamine ($NH_2(CH_2)_2CH_3$) chains. Since the molecules in the monolayer are closely packed at $A = 147$ $Å^2$/molecule, the propylamine chains from neighboring molecules may be intertwined, each chain may be oriented in various ways with respect to the C_{60} molecule it is attached to, or some chains may not be stretched out, as illustrated in Fig. 2.9(a). However, the observed GID data are not very sensitive to these detailed configurations, except for the number of electrons and an average size of the distribution of these electrons within one molecule. We have approximated the electron density within a molecule as spherically symmetric and consisting of two parts. The electron density corresponding to the C_{60} molecule is modeled as 360 electrons uniformly distributed at radius $r_1 = R_0 = 3.55$ Å, the known carbon-cage radius of the C_{60} molecule. The chains are modeled as 408 electrons distributed between $r_1 = R_0 = 3.55$ Å and $r_2 = d/2$, one half of the average nearest-neighbor distance introduced in the model $g(r)$, in such a way that the number of electrons in each spherical shell of width dr is the same. This model is depicted in Fig. 2.9(b) and (c), and is given by

$$\rho_1(r) = \begin{cases} \dfrac{360}{4\pi R_0^2}\delta(r - R_0) + \dfrac{408}{d/2 - R_0}\dfrac{1}{4\pi r^2} & \text{for } r \in [R_0, d/2] \\ 0 & \text{otherwise} \end{cases} \tag{2.10}$$

where $R_0 = 3.55$ Å. There are no additional parameters introduced in this model. By taking the Fourier transform of Eq. (2.10), the molecular form factor with this model is given by

$$f(q_{xy}, q_z) = 360\frac{\sin(qR_0)}{qR_0} + 408\frac{Si(qd/2) - Si(qR_0)}{q(d/2 - R_0)}, \tag{2.11}$$

where

$$\begin{cases} q = \sqrt{q_{xy}^2 + q_z^2} \\ Si(x) = \int_0^x dt\,\dfrac{\sin t}{t} \end{cases}$$

The non-linear least-squares fitting of the GID pattern for $A = 147$ Å^2/molecule has been carried out using the models Eqs. (2.8) and (2.11) in the expression (2.7), with the constraint given by the condition (2.9). Since the q_z component of the momentum transfer vector $\mathbf{q}$ is negligible for the GID scans, we have set $q = q_{xy}$ in the form factor Eq. (2.11). There are a total of five parameters in the fitting: the four independent parameters (d, σ, ξ, κ) from the model $g(r)$, and an additional parameter for the proportionality constant S_0 in Eq. (2.7). The best fit to the GID pattern for $A = 147$ Å^2/molecule is given by the solid curve shown in Fig. 2.8(b), and the five parameters corresponding to the best fit are summarized in Table 2.2. The model $g(r)$ using these parameters is shown in Fig. 2.10.
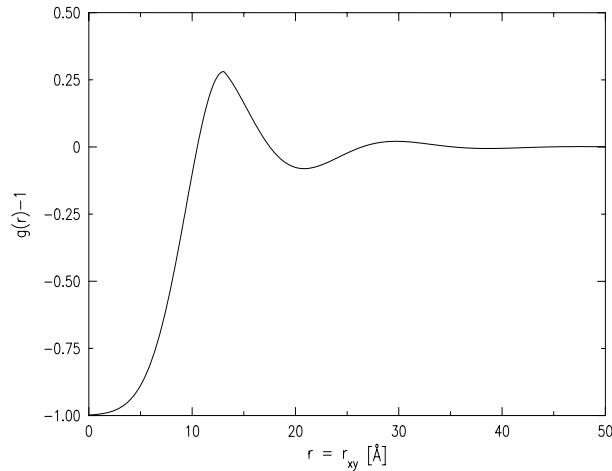
Figure 2.10: The model for $g(r) - 1$ as a function of $r = r_{xy} = [x^2 + y^2]^{1/2}$, corresponding to the best fit to the GID pattern at $A = 147 \pm 6$Å^2/molecule (see Fig. 2.8(b)). $g(r)$ is the 2D radial distribution function. The average nearest-neighbor distance is at $d = 13.1 \pm 0.4$ Å. In the model, the $r < d$ part of $g(r)$ is approximated by a gaussian centered at d and the $r > d$ part is approximated by an exponentially decaying cosine that approaches 1 as r increases to infinity.

Table 2.2: The list of best-fit parameters used to fit the GID pattern at $A = 147$ Å^2/molecule. The parameter S_0 is the proportionality factor between the observed GID intensity and the 2D structure factor. The four parameters d, σ, ξ, and κ are defined in the model 2D radial distribution function $g(r)$ used in this chapter. In the model, the increase from $g(0) \sim 0$ to $g(d) > 1$ (at an average nearest-neighbor distance d) is approximated as a gaussian of width σ centered at $r = d$, and the approach of $g(r)$ to 1 with increasing r is modeled as an exponentially decaying cosine, with decay length ξ and angular frequency κ.

$A = 1/n_0$ (Å^2/molec.)	S_0 (arb.)	d (Å)	σ (Å)	ξ (Å)	κ (Å^{-1})
147 [†]	1.474×10^{-6}	13.07	5.17	6.66	0.353
	$\pm 0.045 \times 10^{-6}$	± 0.38	± 0.35	± 0.62	± 0.026

[†] Held fixed in the fitting.

As evident in Fig. 2.10, the positional correlation of the molecules is of short range and extends only up to the next-nearest neighbors, which demonstrates that the monolayer is indeed amorphous. The best fit gives the value of the average nearest-neighbor distance at $d = 13.1 \pm 0.4$ Å, which is comparable to the thickness of the monolayer obtained from the reflectivity measurement. It is slightly larger than the intermolecular distance of 10 Å in the fcc crystal of pure C_{60} [59, 60], but this is expected due to the presence of propylamine chains. The obtained value for an average intermolecular distance, d, provides an independent measure for the average molecular density, or the specific area, within the uniform monolayer. Assuming that the C60-PA molecules are *locally* arranged by hexagonal packing, the area/molecule is given by $A = (\sqrt{3}/2)d^2$. Using the value $d = 13.1 \pm 0.4$ Å obtained from the best fit, the specific area based on the GID measurement is given by $A_{GID} = 149 \pm 6$ Å^2/molecule, which is in an excellent agreement with the value $A_{trough} = 147$ Å^2/molecule, based on the trough measurement. This result is consistent with the BAM and isotherm observations that the monolayer consists of islands at low densities and it becomes uniform at ~150 Å^2/molecule, where the molecules become closely packed over the whole available surface and the surface pressure begins to increase.
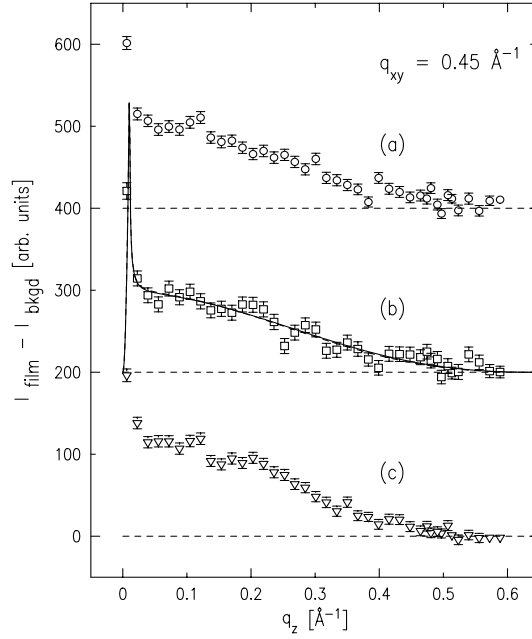
Figure 2.11: Measured rod scans at $q_{xy} = 0.45$ Å^{-1} (fixed) as a function of q_z, taken at $A =$ (a) 189 ± 8 Å^2/molecule, (b) 147 ± 6Å^2/molecule, and (c) 105 ± 4Å^2/molecule. The solid curve in (b) is the best fit at $A = 147 \pm 6$Å^2/molecule, assuming that the molecular form factor is given by the spherical model of the C60-PA molecule described in Fig. 2.9. The dashed line, which is nearly indistinguishable from the solid line, is the result of the fitting when the outer radius r_2 of the C60-PA molecule is fixed at the value $r_2 = 6.54$ Å extracted from the GID analysis.

In order to obtain an independent measure for the molecular form factor, rod scans [14] were carried out. In the rod scans, scattered intensity was scanned along the angle β in Fig. 2.1(b), while keeping the angle 2θ fixed near the maximum of the GID peak. In terms of the momentum transfer vector, the procedure corresponded to scanning along q_z while q_{xy} was held fixed at 0.45 Å^{-1}. The same scans were performed on C60-PA film and He gas above the film. The difference between the scans on the water and He background was negligibly small compared to that between the film and the He background. Fig. 2.11 shows the intensity along the rod for three specific areas

41

$A = 105\pm4$, 147 ± 6, and 189 ± 8 Å^2/molecule, after subtracting the corresponding contribution from the He background. As expected for spherically symmetric molecules, the rods are centered about $q_z = 0$.

The scattering function for the rod scan corresponds to the q_z dependence of the scattering function of the GID scan with q_{xy} held fixed at a peak position. Taking into account the surface enhancement factor $T(\alpha)T(\beta)$ where $T(\alpha) = (2\alpha/\alpha_c)^2 \sqrt{R_F(\alpha)}$ [64, 65], and noting that the incident angle is fixed,

$$S_{Rod}(q_z) = S_1 T(\beta)\left|f\left(q_{xy}^0, q_z\right)\right|^2, \tag{2.12}$$

where $q_{xy}^0 = 0.45$ Å^{-1} and S_1 is a proportionality constant. The data for $A = 147\pm6$ Å^2/molecule has been fitted using Eqs. (2.11) and (2.12), with S_1 and d as the only parameters. The best fit to the observed rod scan is given by the solid curve in Fig. 2.11(b). The fit gives the value of the outer radius in the $\rho_1(r)$ model at $r_2 = d/2 = 6.17\pm0.6$ Å, or $d = 12.4\pm1.2$ Å, which agrees fairly well with the value obtained in the GID analysis. The dashed line, which is almost completely covered by the solid line, corresponds to the fit with the outer radius fixed at the GID based value $r_2 = d/2 = 6.54$ Å.

2.3.5 Application of the spherical model to the fitting of reflectivity data

Finally, we show here that the above spherical model of the C60-PA molecules can also be applied to the fitting of the reflectivity data, by constructing a model electron density profile based on the spherical model and using it to fit the reflectivity result at $A = 147$ Å^2/molecule. The electron densities shown in Fig. 2.12(a)-(c) summarize the basic ideas behind this particular model. First, the electron density in one C60-PA molecule, assuming the spherical model with the outer radius $r_2 = d/2 = 6.54$ Å, was projected onto the z-axis by integrating over (x, y). Since the monolayer covers the trough surface uniformly and the molecules are closely packed at this specific area, we
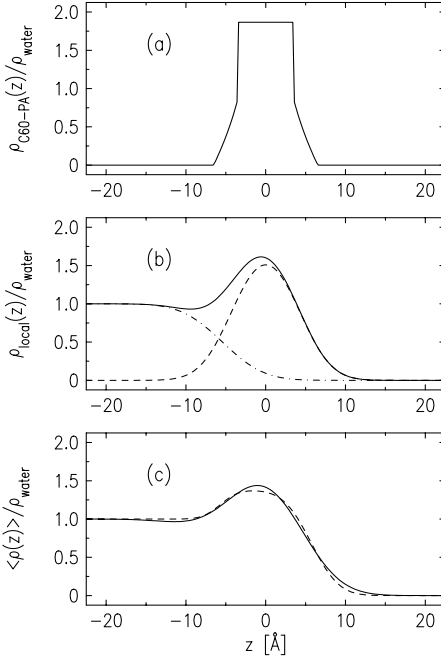
Figure 2.12: A model of electron density profile based on the spherical C60-PA model (see Fig. 2.9). All the profiles correspond to the best fit to the reflectivity data at 147 ± 6 Å^2/molecule. (a) The projection onto the z-axis of the model electron density within one C60-PA molecule, normalized to the bulk density in water, assuming the GID-based value $r_2 = 6.54$ Å for the outer radius of the C60-PA molecule. (b) Models for the *local* electron density profile of the C60-PA monolayer (-----), and of water ($-\cdot-\cdot-$), and of the total local electron density (——). The model for the monolayer is the convolution of the result (a) with a gaussian of width σ_{LM}. (c) The solid line is the average electron density profile, given by the convolution of the total local electron density in part (b) with a gaussian of roughness σ due to thermally excited capillary waves. The dashed curve is the result of the single-box model at 147 ± 6Å^2/molecule, shown here for comparison.

can attribute a column with hexagonal cross sectional area $A = (\sqrt{3}/2)d^2$ to each molecule. The contribution from the C60-PA molecule to the electron density in this column is given by dividing the projected one-molecule density by $(\sqrt{3}/2)d^2$, which is denoted as $\rho_{C60\text{-}PA}(z)$ in Fig. 2.12(a). Now assuming that the *local* distribution for the heights of molecular centers is gaussian with a characteristic width σ_{LM}, the contribution from the monolayer to the *local* electron density is given by the convolution of $\rho_{C60\text{-}PA}(z)$

43

with this gaussian distribution. This is shown by the dashed curve in Fig. 2.12(b). The contribution from the water to the local density was modeled with a simple error function, located at distance -l into the bulk and having a width σ_{water}. The sum of the two contributions gives the total *local* electron density, which is shown by the solid curve in Fig. 2.12(b). Finally, the local electron density was convoluted with the roughness σ due to the thermally excited capillary waves [65, 66], to obtain the average electron density profile, shown by the solid curve in Fig. 12(c). Since the surface pressure at this specific area is close to zero, we have set the roughness at the value $\sigma = 2.60$ Å of the clean bare water surface, which was measured with the same experimental resolution prior to the spreading of the monolayer. With this model, the only free parameters in the fitting are σ_{LM}, σ_{water}, and l. The best fit to the reflectivity data at $A = 147$ Å^2/molecule is given by the dashed curves in Fig. 2.4. The density profiles shown as solid lines in Fig. 2.12 correspond to the best-fit values of the three parameters, which are listed in Table 2.3.

The average electron density profile obtained with the above spherical model for the C60-PA molecule is in a qualitative agreement with the one obtained earlier by the single-box model. The thickness and the height of the excess electron density in the monolayer are similar in the two models, as compared in Fig. 2.12(c). This again shows that the film at this specific area is a homogeneous monolayer with density just right to cover the entire available surface with closely-packed molecules. On the other hand, we also note a small difference in the shapes of the two profiles. The detailed features in the profiles are highly dependent on the models used, and it is difficult to distinguish the two models simply from the reflectivity results because of the limited range and accuracy in the data. This is an example of the limitation on the extent over which any detailed features can be extracted from a given reflectivity result.

Table 2.3: The list of best-fit parameters used to fit the R/R_F data measured at $A = 147$ Å^2/molecule, where the fitting is based on a model average electron density profile $<\rho(z)>$ calculated assuming a spherically symmetric electron density within the

C$_{60}$-propylamine adduct molecule. The outer radius r_2 of the C60-PA molecule was held fixed at one half of the average nearest neighbor distance d extracted from the GID analysis. The model assumes that the local height distribution of the C60-PA molecules is gaussian of width σ_{LM}, and that the water/monolayer interface has a width σ_{water} and is located at distance $-l$ below the average height of molecular centers. Since the surface pressure is close to zero at $A = 147$ Å^2/molecule, the roughness σ due to thermally excited capillary waves was held fixed at the value measured for clean water surface.

r_2 (Å)	σ_{LM} (Å)	σ_{water} (Å)	$-l$ (Å)	σ (Å)
6.54 [†]	3.08±0.12	4.09±0.45	-5.42±0.23	2.60 [†]

[†] Held fixed in the fitting.

2.4. Summary

Using Brewster angle microscopy and x-ray scattering techniques, both the macroscopic and microscopic structure of C$_{60}$-propylamine adduct monolayers on water have been studied at various surface densities. At low densities ($A > \sim 150$ Å^2/molecule), the monolayer is macroscopically heterogeneous, with the surface consisting of regions covered with a uniform solid like monolayer and regions of bare water surface. The compression at these densities only reduces the area of uncovered surface, until the monolayer becomes macroscopically uniform at $A \sim 150$ Å^2/molecule. This behavior is evidenced by (i) the BAM images and the following results: (ii) the surface pressure remains zero until it begins to increase at $A \sim 150$ Å^2/molecule, (iii) both the reflectivity and GID results are consistent with the formation of a closely packed, uniform monolayer at $A \sim 150$ Å^2/molecule, and finally (iv) the GID patterns at low densities are essentially identical to the one at $A \sim 150$ Å^2/molecule. For high densities ($A < \sim 120$ Å^2/molecule), the compression forces out of the monolayer plane those molecules that are in excess of the number needed for a complete monolayer, with some of the molecules forming 3D aggregates and/or collected around the barrier and edges of the trough and the rest going to a second layer above or below the original monolayer. The main evidences for this

behavior are (i) the model electron density profiles obtained from the reflectivity results at high densities and (ii) the fact that the shift in the position of the GID peak at high densities is much smaller than would be expected if the film were to remain a homogeneous monolayer at high densities.

The most important result of this study on the C_{60}-propylamine adduct monolayer on water is the experimental observation of x-ray scattering factor from a 2D structure with only a short-range positional order. By constructing a model 2D radial distribution function $g(r)$ and utilizing it to fit the observed GID pattern at $A = 147$ Å^2/molecule, we have shown that the positional correlation of the molecules in the uniform monolayer extends only over a few molecular distances. While this result is interesting in its own right, it is also important to note that the observation of such a 2D amorphous structure was made possible mainly by the large number of electrons contained in each scattering unit, the C_{60}-propylamine adduct molecule in the present case. To the best knowledge of the authors, the x-ray GID studies of Langmuir monolayers have so far been limited to hexatic phases and crystalline structures with quasi-long range positional order. Considering this, the results of the present study have an important implication that if other C_{60} derivatives can be developed that (i) form stable monolayers on water and (ii) have an order-disorder transition with a liquid as the disordered phase, then, it may be possible to study both sides of these transitions with the x-ray scattering techniques.

References for Chapter 2

[1] D. R. Nelson, in *Phase Transitions and Critical Phenomena*, Vol. 7, edited by C. Domb and J. L. Lebowitz (Academic, New York, 1983), pp. 1.

[2] K. J. Strandburg, *Rev. Mod. Phys.* **60,** 161 (1988).

[3] S. K. Sinha, Ed., *Ordering in Two Dimensions* (North-Holland, Amsterdam, 1980).

[4] R. Marx, *Physics Reports* **125,** 1 (1985).

[5] R. J. Birgeneau and P. M. Horn, *Science* **232,** 329 (1986).

[6] K. Knorr, *Physics Reports* **214,** 113 (1992).

[7] P. S. Pershan, *Structure of Liquid Crystal Phases* (World Scientific, Singapore, 1988).

[8] J. D. Brock, R. J. Birgeneau, J. D. Litster and A. Aharony, *Physics Today* **July,** 52 (1989).

[9] B. D. Swanson, H. Stragier, D. J. Tweet and L. B. Sorensen, *Phys. Rev. Let.* **62,** 909 (1989).

[10] C. Bahr, *Int. J. Mod. Phys. B* **8,** 3051 (1994).

[11] C. M. Knobler, in *Advances in Chemical Physics*, Vol. 77, edited by S. Rice and I. Prigogine (1990), pp. 397.

[12] C. M. Knobler and R. C. Desai, *Annu. Rev. Phys. Chem.* **43,** 207 (1992).

[13] H. Möhwald, *Annu. Rev. Phys. Chem.* **41,** 441 (1990).

[14] J. Als-Nielsen, D. Jacquemain, K. Kjaer, F. Leveiller, M. Lahav and L. Leiserowitz, *Physics Reports* **246,** 251 (1994).

[15] V. M. Kaganer, H. Möwald and P. Dutta, *Rev. Mod. Phys.* **71,** 779 (1999).

[16] P. G. de Gennes, *Rev. Mod. Phys.* **57,** 827 (1985).

[17] M. Schick, in *Liquids at Interfaces*, Vol. XLVIII, edited by J. Charvolin, J. F. Joanny and J. Zinn-Justin (Elsevier, Amsterdam, 1990), pp. 419.

[18] E. M. Blokhuis and B. Widom, *Curr. Opin. in Coll. and Interf.m Sci.* **1,** 424 (1996).

[19] R. A. Cowley, in *Equilibrium structure and properties of surfaces and interfaces*, edited by A. Gonis and G. M. Stocks (Plenum, New York, 1992), pp. 1.

[20] H. Dosch, *Int. J. Mod. Phys.* **6,** 2773 (1992).

[21] I. K. Robinson and D. J. Tweet, *Rep. Prog. Phys.* **55,** 599 (1992).

[22] J. G. Dash, H. Fu and J. S. Wettlaufer, *Reports on Prog. in Physics* **58,** 115 (1994).

[23] B. M. Ocko, X. Z. Wu, E. B. Sirota, S. K. Sinha, O. Gang and M. Deutsch, *Phys. Rev. E* **55,** 3164 (1997).

[24] O. M. Magnussen, B. M. Ocko, M. J. Regan, K. Penanen, P. S. Pershan and M. Deutsch, *Phys. Rev. Lett.* **74,** 4444 (1995).

[25] M. J. Regan, E. H. Kawamoto, S. Lee, P. S. Pershan, N. Maskil, M. Deutsch, O. M. Magnussen, B. M. Ocko and L. E. Berman, *Phys. Rev. Lett.* **75,** 2498 (1995).

[26] N. Lei, Z. Huang and S. A. Rice, *J. Chem. Phys.* **104,** 4802 (1996).

[27] D. Raoux, in *Neutron and synchrotron radiation for condensed matter studies*, Vol. 1, edited by J. Baruchel, J.-L. Hodeau, M. S. Lehmann, J.-R. Regnard and C. Schlenker (Springer-Verlag, New York, 1993), pp. 37.

[28] H. Winick, *Synchrotron Radiation Sources: A Primer* (World Scientific, Sinapore, 1994).

[29] B. I. Halperin, in *Symmetries and Broken Symmetries in Condensed Matter Physics. Proceedings of the Colloque Pierre Curie*, edited by N. Boccara (IDSET, Paris, France, 1981).

[30] B. Berge, O. Konovalov, J. Lajzerowicz, A. Renault, J. P. Rieu, M. Vallade, J. Als-Nielsen, G. Grubel and J. F. Legrand, *Phys. Rev. Lett.* **73,** 1652 (1994).

[31] K. Kjaer, J. Als-Nielsen, C. A. Helm, L. A. Laschuber and H.Möhwald, *Phys. Rev. Lett.* **58,** 2224 (1987).

[32] J. Als-Nielsen and H. Möwald, in *Handbook of Synchrotron Radiation*, Vol. 4, edited by S. Ebashi, E. Rubenstein and M. Koch (North Holland, Amsterdam, 1991), pp. 1.

[33] E. B. Sirota, J. Collett, P. S. Pershan and L. B. Sorensen, *Phys. Rev. Lett.* **55,** 2039 (1985).

[34] S. Amador, P. S. Pershan, H. Stragier, B. D. Swanson, D. J. Tweet, L. B. Sorensen, E. B. Sirota, G. E. Ice and A. Habenschuss, *Phys. Rev* **A39,** 2703 (1989).

[35] C.-F. Chou, J. T. Ho, S. W. Hui and V. Surendranth, *Phys. Rev. Lett.* **76,** 4556 (1996).

[36] N. Lei, Z. Huang and S. A. Rice, *J. Chem. Phys.* **105,** 9615 (1996).

[37] J. D. Brock, A. Aharony, R. J. Birgeneau, K. W. Evans-Lutterodt, J. D. Litster, P. M. Horn, G. B. Stephenson and A. R. Tajbakhsh, *Phys. Rev. Lett.* **57,** 98 (1986).

[38] J. D. Shindler, E. A. L. Mol, A. Shalaginov and W. H. d. Jeu, *Phys. Rev. Lett.* **74,**

722 (1995).

[39] D. Vaknin, J. Y. Wang and R. A. Uphaus, *Langmuir* **11,** 1435 (1995).

[40] Y. S. Obeng and A. J. Bard, *J. Am. Chem. Soc.* **113,** 6279 (1991).

[41] N. C. Maliszewskyj, P. A. Heiney, D. R. Jones, R. M. Strongin, M. A. Cichy and I. Smith, Amos B., *Langmuir* **9,** 1439 (1993).

[42] R. Back and R. B. Lennox, *J. Phys. Chem.* **96,** 8149 (1992).

[43] J. Guo, Y. Xu, Y. Li, Y. Yao, D. Zhu and C. Bai, *Chem. Phys. Lett.* **195,** 625 (1992).

[44] J. Milliken, D. D. Dominguez, H. H. Nelson and W. R. Barger, *Chem. Mater.* **4,** 252 (1992).

[45] Y. Tomioka, M. Ishibashi, H. Kajiyama and Y. Taniguchi, *Langmuir* **9,** 32 (1993).

[46] J. Y. Wang, D. Vaknin, R. A. Uphaus, K. Kjær and M. Lösche, *Thin Solid Flims* **242,** 40 (1994).

[47] D. K. Schwartz, M. L. Schlossman and P. S. Pershan, *J. Chem. Phys.* **96,** 2356 (1992).

[48] P. S. Pershan and J. Als-Nielsen, *Phys. Rev. Lett.* **52 ,** 759 (1984).

[49]   P. M. Chaikin and T. C. Lubensky, *Principles of condensed matter physics* (Cambridge University Press, New York, 1995).

[50] Strictly speaking, statistical fluctuations destroy the long-range positional order in 2D crystals; however, unless special procedures are invoked it is difficult to distinguish between the singular "power law" line shape of a 2D crystal and the superposition of a resolution limited Bragg peak on a thermal background, as is observed in 3D. See Berge et al. Phys. Rev. Lett. 73, 1652 (1994).

[51] T. M. Fischer, R. F. Bruinsma and C. M. Knobler, *Phys. Rev. E* **50,** 413 (1994).

[52] S. Garoff, H. W. Deckman, J. H. Dunsmuir and M. S. Alvarez, *J. Physique* **47,** 701 (1986).

[53] J. Ruiz-Garcia, X. Qiu, M.-W. Tsao, G. Marshall, C. M. Knobler, G. A. Overbeck and D. Mobius, *J. Phys. Chem.* **97,** 6955 (1993).

[54] C. M. Knobler, *J. Phys. Condensed Matter* **3,** 1 (1991).

[55] S. Henon and J. Meunier, *Rev. Sci. Instrum.* **62,** 936 (1991).

[56] G. M. Bommarito, W. J. Foster, P. S. Pershan and M. L. Schlossman, *J. Chem.*

Phys. **105,** 5265 (1996).

[57] W. J. Foster, M. C. Shih and P. S. Pershan, *J. Chem. Phys.* **105,** 3307 (1996).

[58] P. S. Pershan, *Phys. Rev. E* **50,** 2369 (1994).

[59] M. S. Dresselhaus, G. Dresselhaus and P. C. Eklund, *Science of fullerenes and carbon nanotubes* (Academic Press, San Diego, 1996).

[60] W. Kratschmer, L. D. Lamb, K. Fostiropoulos and D. R. Huffman, *Nature* **347,** 354 (1990).

[61] G. S. Cargill III, in *Solid State Physics*, Vol. 30, edited by H. Ehrenreich, F. Seitz and D. Turnbull (Academic Press, New York, 1975), pp. 227.

[62] P. A. Egelstaff, *An Introduction to the Liquid State* (Academic, New York, 1967).

[63] B. E. Warren, *X-ray Diffraction* (Addison Wesley, Reading, 1969).

[64] S. K. Sinha, E. B. Sirota, S. Garoff and H. B. Stanley, *Phys. Rev. B* **38,** 2297 (1988).

[65] D. K. Schwartz, M. L. Schlossman, E. H. Kawamoto, G. J. Kellogg, P. S. Pershan and B. M. Ocko, *Phys. Rev. A* **41,** 5687 (1990).

[66] A. Braslau, P. S. Pershan, G. Swislow, B. M. Ocko and J. Als-Nielsen, *Phys. Rev. A* **38,** 2457 (1988).

Chapter 3

Structure of poly(γ-benzyl-L-glutamate) Monolayers at the Gas/Water Interface

Abstract

This chapter reports Brewster angle microscopy (BAM), x-ray specular reflectivity (XR), grazing incidence diffraction (GID) and off-specular diffuse scattering (XOSDS) measurements of Langmuir monolayers formed on water by both mono- and polydisperse samples of α-helical poly(γ-benzyl L-glutamate) (PBLG) as a function of area/monomer A. The microscopic behavior does not exhibit any discernible effects due to differing dispersity. At low surface densities ($A > \sim 21$ Å^2/monomer, surface pressure $\Pi = 0$), BAM images reveal partial surface coverage by solid-like monolayer islands. GID measurements show an inter-helix peak corresponding to a local parallel alignment of rod-like PBLG molecules, indicating their tendency to aggregate laterally without external pressure. Compression to $A <$ 21 Å^2/monomer first leads to full and uniform surface coverage by the monolayer, followed by a steep rise in Π that is accompanied by a decrease in the inter-helix distance. Further compression results in a plateau of constant Π in the Π-A isotherm ($\sim 11.5 < A < \sim 18.5$ Å^2/monomer, $\Pi \sim 9$ dyn/cm), which has previously been attributed to a first-order monolayer-bilayer transition. The interfacial electron density profiles determined by the XR measurements on both sides of the coexistence plateau provide direct evidence for this transition. On the basis of x-ray scattering results, the film on the high density side of the plateau is shown to consist of a newly formed incomplete and incommensurate second layer that sits on top of and has lower

average density than a homogeneous first layer. GID measurements indicate that the second layer can be characterized by larger inter-helix d-spacing than the first layer, while XOSDS measurements on the bilayer suggest that the second layer is microscopically inhomogeneous. For both mono- and bilayers, the analysis of observed GID peak widths indicates that the extent of lateral positional correlations between parallel PBLG rods ranges from a few to no more than ~15 inter-helix distances, implying short-range order.

3.1 Introduction

Langmuir monolayers (LMs) provide one example of real physical systems in which an experimental study of two-dimensional (2D) physics should be possible [1-3]. Macroscopic physical chemistry of LMs has been studied for the better part of this century; however, it is only within the most recent 10 to 15 years that the availability of synchrotron generated x rays made it possible to directly characterize their microscopic structures [4, 5]. A considerable number of synchrotron x-ray scattering experiments have now been conducted on LMs, especially those formed by simple surfactant molecules like fatty acids, fatty alcohols, and phospholipids.

Grazing incidence x-ray diffraction (GID) [4, 5] studies demonstrated that these 'long chain' amphiphilic molecules form close packed 2D crystalline and liquid crystalline structures on water in which the chains are oriented either normal to the surface or at relatively small angles to the surface normal. Compression- and temperature-induced phase transformations between ordered LM phases involve changes in the amplitude and direction of the chain tilt [2, 5]. By and large the different 2D crystalline structures observed in the LMs of simple long chain molecules are similar to the various tilted and untilted phases of both thin freely-suspended liquid crystal films and bulk smectic liquid crystals [2, 6, 7]. One unfortunate aspect of all of these studies is that the number of electrons contained in such simple amphiphilic molecules is often too

small to produce measurable scattering from their noncrystalline 2D phases [8, 9]. As a result the elucidation of microscopic structures through x-ray scattering was mostly limited to ordered phases for these LM systems.

This chapter describes optical and x-ray scattering studies of LMs formed by polypeptides in the α-helical conformation [10-26]. These rigid rod-like molecules lie down flat on the water surface with 2D nematic like structures. As such they differ from the aforementioned more conventional amphiphilic LMs and liquid crystal films in that the director **n**, or principal axis of the molecules, lies within the monolayer plane rather than pointing away from it. Another important difference is that these polypeptide molecules are larger than the simpler amphiphilic molecules studied previously. As a result, the constructive interference in the GID patterns that can be used to characterize the intermolecular packing occurs at smaller angles with larger amplitudes. The combination of this and the one to two orders of magnitude greater number of electrons per molecule has the important consequence that broad GID peaks can be observed from disordered LM phases. For example, a recent GID experiment on a LM formed by C_{60}-propylamine adduct molecules [27] demonstrated that a quantitative measurement of a liquid-like 2D structure factor due to short-range positional correlations is possible when the number of electrons per scattering unit (i.e. molecule) is sufficiently large. The hope is that as a result of the increased scattering power provided by large molecules, it might be possible to characterize the structural changes in the noncrystalline part of 2D phase diagrams.

Another potential advantage for studies using α-helical polypeptides is that without compromising the rigidity of the helical backbones, their intermolecular interactions within the LM plane may be controlled by chemically altering the side chain groups and through copolymerization of different peptide monomer units. Such chemical modifications have already been shown to influence the formation of 3D liquid crystalline phases [28-33].

The interest in LMs of α-helical polypeptides also arises from the fact that many of them can be transferred onto solid substrates as multilayers using the Langmuir-Blodgett (LB) technique. In recent years, various α-helical poly(L-glutamates) have been studied both as LMs on water [23, 25, 26, 34-37] and as LB films on solid substrates [26, 34, 37-49]. In most of these studies the primary objective has been to achieve good-quality LB films that possess technologically important properties [50], such as lateral homogeneity [23, 45], thermal [37, 44, 47, 49] and mechanical [45, 48] stability, low defect density [38, 45], and optical anisotropy [38, 39, 42]; in addition, potential applications [50, 51], for example, as optical waveguides [38, 41, 42], optical data storage media [43, 44], and photoresists [37] have also been suggested. However, despite the high activity in this research area, direct structural characterizations at the intermolecular level have been limited mostly to transferred LB films, as opposed to their LM counterparts, partly due to experimental difficulties involved with studying liquid surfaces [23]. As Motschmann *et al.* [23] pointed out, the elucidation of LM structures as the state immediately prior to LB-deposition is an important step that may provide additional insights on controlling LB multilayer structures.

We report here the results of Brewster angle microscopy (BAM) and extensive x-ray scattering studies conducted *in-situ* on LMs formed by both monodisperse and polydisperse poly(γ-benzyl L-glutamate) (PBLG) [12, 13, 18, 25], emphasizing the changes in their microscopic structures with lateral compression. The principal results are as follows: (i) Direct microscopic characterization of the first-order monolayer-bilayer transition. This transition was originally inferred from the presence of a plateau region of constant Π in the surface pressure (Π) vs. area/monomer (A) isotherms of the PBLG LM [11, 12, 18]. Further indirect evidence was provided by Takenaka *et al.* [18], who LB-deposited the same number of PBLG layers onto solid substrates from both the "bilayer" and "monolayer" regions in the isotherm and found the ratio of their measured total thicknesses to be approximately 1.7. In the present study, x-ray specular reflectivity

(XR) was employed to directly measure the average electron density profiles across the water/PBLG LM/gas interface for both of the regions. The results show that the numbers of molecules per unit area in the two layers of a bilayer are not the same. (ii) The in-plane arrangement of these PBLG rods parallel to the water surface was probed by the GID technique. Evidence for a partial alignment of these rods within the LM plane is provided by observation of a relatively broad peak at a scattered wave vector ($\sim 2\pi/d$) that is consistent with the expected d-spacing between neighboring parallel α-helices. In this connection, the dependence of the inter-helix distance on Π and A, the limited extent of in-plane positional correlations, as well as the incommensurability of the two layers in the bilayer are discussed. (iii) Microscopic lateral inhomogeneities within both PBLG monolayers and bilayers were studied using an x-ray off-specular diffuse scattering (XOSDS) technique. The XOSDS intensities observed from the bilayer have been found to exceed the values theoretically expected for a homogeneous bilayer with thermal capillary-wave fluctuations. The excess scattering is explained quantitatively in terms of inhomogeneities in the newly-formed second layer.

Finally, one of the issues that motivated the present study is concerned with the effect of sample dispersity on PBLG LM structures. The lyotropic liquid crystalline behavior of conventional polydisperse PBLG in 3D has been known since the late 1950s [28, 52-59]; in particular, in addition to the usual cholesteric phase [28, 52-56, 58, 59], the observations of nematic [53, 54, 60] and columnar [57] phases have been reported. Recently, Tirrell *et al.* [61] demonstrated that unlike the polydisperse case, the monodisperse PBLG in both bulk solutions and solution cast films exhibits a smectic-like liquid crystalline order. Their x-ray diffraction results clearly indicated that the smectic layers had a thickness close to the length of these rod-like molecules, and this has been attributed to the narrow size distribution in the monodisperse sample [61]. The present study extends the investigation of such dispersity effects into 2D. In contrast to the 3D case, both XR and GID results on LMs show very little dependence on the sample

dispersity; in particular, no evidence for smectic layering has been found for monodisperse PBLG LMs.

The organization of this chapter is as follows: Sec. 3.2 describes the experimental methods used. The XOSDS subsection provides a more detailed discussion elucidating a recently developed analysis procedure used to quantitatively distinguish homogeneous and inhomogeneous liquid surfaces. In Sec. 3.3, the experimental results of the Π-A isotherm, BAM, XR, GID, and XOSDS measurements are presented and discussed. In Sec. 3.4, the main conclusions from this study are summarized.

3.2 Experimental Details and Analysis Methods

3.2.1 Sample, Langmuir trough, and Π-A isotherms

The polydisperse sample of PBLG [MW 26,000 (vis); DP 119, PDI 1.5] was purchased from Sigma Chemical Co. The monodisperse sample [MW 16,700; DP 76] was synthesized using the recombinant DNA method described in Yu *et al.* [61]. The PBLG molecule, due to its α-helix conformation, resembles a rigid rod-like structure, whose rod diameter is approximately 13 Å [61]. The length of the PBLG rod is about 115 Å for the monodisperse sample [61] and on the order of 150 Å for the polydisperse case.

The Langmuir troughs and the film deposition and compression methods used have been described previously [27, 62, 63]. Both the trough and the moveable barrier are made of teflon, and the surface pressure Π is measured with a Wilhelmy balance. For all of the measurements, pure water subphase (Milli-Q quality) was used, and the temperature was maintained at 22-23 °C. For the Π-A isotherm measurements, the sealed aluminum box enclosing the trough assembly was filled with high purity N_2 gas. During the x-ray measurements, high purity He gas was used instead of N_2 to reduce background scattering. A PBLG monolayer was prepared by spreading a pure chloroform or 3%-trifluoroacetic acid/97%-chloroform mixture (% by volume) solution of PBLG on water

at a specific area equal to or larger than 23 Å^2/monomer [64]. The PBLG concentration in the spreading solutions used ranged from 0.1 to 0.5 mg/mL, and the volume of the solution spread ranged from 50 to 200 μL.   No significant dependence on the concentration and the spread volume was found in any of the measurements performed during this study.

Π-A isotherms were measured using both continuous and relaxation methods [27, 62, 63]. The two methods differ on whether or not the film is allowed to relax after each compression step. During a relaxation scan, the surface pressure was monitored every minute while the film relaxed at a given fixed area/monomer A.   When the surface pressure change over five minutes was less than 0.05 dyn/cm, a final surface pressure measurement was recorded, and the next compression step was taken. In a continuous scan, the film was compressed at a constant rate, and the surface pressure was measured immediately after each compression step. The barrier speeds used in both compression methods corresponded to compression rates ranging from 0.005 to 0.01 Å^2/monomer-sec. During x-ray experiments, the continuous method was used for compression from one area of interest to the next, but the film was allowed to relax after the target area/monomer was reached.

3.2.2 Brewster-angle microscope (BAM)

The BAM setup used has been described previously [27, 63]. A p-polarized laser beam (argon-ion laser, $\lambda = 488$ nm) strikes the LM surface at the Brewster condition for the bare water surface (an incident angle of 53.3° from the surface normal). The non-zero reflected intensity caused by the presence of a monolayer was used to image the LM coated surface. The reflected beam was passed though an achromatic lens with a focal length of 175 mm, and the image was recorded by a CCD camera, placed approximately at 1450 mm from the lens. With this setup, a surface area of approximately 0.86 mm × 1.1 mm on the illuminated LM surface was captured in each image at a magnification of

7.3 and a resolution of 20 μm.

3.2.3 X-ray scattering techniques

The x-ray scattering experiments were carried out using the Harvard/BNL liquid surface spectrometer [62] at Beamline X22B, National Synchrotron Light Source, Brookhaven National Laboratory. The general scattering geometry is illustrated in Fig. 3.1. Highly collimated monochromatic x rays of wavelength $\lambda = 1.55$ Å and incident wave vector $\mathbf{k}_{in}$ strike the LM surface at an incident angle α. The scattered x rays are characterized by an output wave vector $\mathbf{k}_{out}$, an angle β to the surface and an angle 2θ to the plane of incidence. The difference between the incident and output wave vectors defines the wave vector transfer, $\mathbf{q} = \mathbf{k}_{out} - \mathbf{k}_{in}$. The Cartesian components of $\mathbf{q}$ are

$$
\begin{aligned}
q_z &= k\left[\sin(\alpha) + \sin(\beta)\right] \\
q_x &= k\cos(\beta)\sin(2\theta) \\
q_y &= k\left[\cos(\beta)\cos(2\theta) - \cos(\alpha)\right]
\end{aligned}
\tag{3.1}
$$
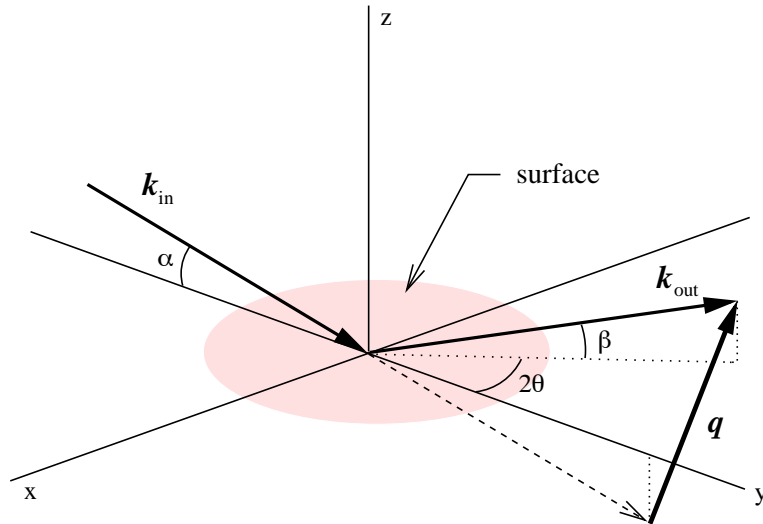
Figure 3.1: General x-ray scattering geometry. The surface lies in the x-y plane.

where $k = 2\pi/\lambda$. In particular, the component parallel to the LM surface is equal to

$$q_{xy} = \sqrt{q_x^2 + q_y^2} = k\sqrt{\cos^2(\alpha) + \cos^2(\beta) - 2\cos(\alpha)\cos(\beta)\cos(2\theta)} . \qquad (3.2)$$

The following scattering techniques were used.

X-ray specular reflectivity (XR).

In XR, the specularly reflected intensity I is measured as a function of the incident angle α or wave vector transfer $q_z = (4\pi/\lambda)\sin(\alpha)$ along the surface normal while maintaining the specular reflection condition given by $\beta = \alpha$ and $2\theta = 0$ or equivalently $q_{xy} = 0$. A pair of crossed Huber slits of width $W = 3$ mm and height $H = 2.5$ mm, located approximately $L \sim 620$ mm from the sample center, were placed in front of a NaI scintillation detector to define its angular acceptance $\delta\beta \sim H/L \sim 0.23°$ and $\delta(2\theta) \sim W/L \sim 0.28°$. The background due to bulk scattering from the subphase and scattering from sample cell windows and gas in the beam path was accounted for by subtracting the intensities measured at $\beta = \alpha$ with 2θ offsets of $\pm 0.3°$. The result of the subtraction , i.e. $\Delta I(\alpha) = I(\alpha, 2\theta = 0) - (1/2)[I(\alpha, +0.3°) + I(\alpha, -0.3°)]$, was normalized to the incident beam intensity I_0 to obtain the measured specular reflectivity $R(q_z)$.

For water as the subphase, the critical wave vector for total reflection is equal to $q_c = 0.0218$ Å^{-1}, and the corresponding critical angle of incidence is $\alpha_c = 0.154°$ for $\lambda = 1.55$ Å. For $q_z/q_c > 4 \sim 5$ ($q_z > \sim 0.1$ Å^{-1} for water), the specular reflectivity $R(q_z)$ from a macroscopically homogeneous surface is well described by the Born approximation expression [4, 5, 65]

$$\frac{R(q_z)}{R_F(q_z)} \cong \left| \int_{-\infty}^{+\infty} dz \frac{d}{dz} \left[\frac{\langle \rho(z) \rangle}{\rho_\infty} \right] e^{-iq_z z} \right|^2 , \qquad (3.3)$$

where $\langle \rho(z) \rangle$ is the *average* electron density profile ('average' over the appropriate coherence lengths in the x-y plane) across the interface at height z along the surface

normal, and ρ_∞ is the electron density in the bulk subphase ($\rho_\infty = 0.334$ electrons/Å^3 for water). $R_F(q_z)$ is the Fresnel reflectivity expected from an ideally flat and sharp bulk/gas interface, which can be expressed as

$$R_F\left(q_z\right) \cong \left| \frac{q_z - \sqrt{q_z^2 - q_c^2}}{q_z + \sqrt{q_z^2 - q_c^2}} \right|^2 . \tag{3.4}$$

For $q_z \leq q_c$, Eq. (3.4) results in total external reflection ($R_F(q_z) = 1$), and for $q_z \gg q_c$, it decays algebraically as $R_F(q_z) \approx (q_c/2q_z)^4$.

Grazing incidence diffraction (GID).

For GID, x rays are incident on the surface at an angle $\alpha < \alpha_c$, such that the total reflection condition is maintained. This results in an evanescent wave on the bulk side of the interface and thereby suppresses the scattering from the bulk relative to the surface. The scattered intensity is measured as a function of 2θ (or q_{xy}) while maintaining $\beta \sim 0$ (or $q_z \sim 0$). Structures periodic in the surface plane with a repeat distance d result in a diffraction peak at $q_{xy} = 2\pi/d$. Most of the GID data were collected using a fixed incident angle of $\alpha = 0.12°$ and Soller slits in front of the NaI scintillator detector. The Soller slits had a horizontal angular acceptance of $\delta(2\theta) \sim 0.16°$, corresponding to an in-plane FWHM resolution of $\delta q_{xy} \sim 0.012$ Å^{-1}. The vertical opening of the Soller slits (limited to 18 mm) corresponded to the integration of scattered signals over $\Delta\beta \sim 1.7°$ or $\Delta q_z \sim 0.12$ Å^{-1}.

As a result of the finite width of the horizontal detector opening ($W = 6$ mm) and the narrow 2θ resolution of the Soller slits, when 2θ is large enough, the detector only views a fraction of the illuminated path ($L_f \sim 40$ mm) along the LM surface. For $2\theta > W/L_f \sim 8.6°$ (or $q_{xy} > \sim 0.6$ Å^{-1}), this fraction varies as $1/\sin(2\theta)$, yielding a measured intensity proportional to $q_{xy}^{-1} \times$ (2D structure factor). In addition to the specularly reflected signal, there is also a background due to scattering of the incident and totally

reflected beams by the entrance and exit Kapton windows of the sample cell (separated by $L_w = 16.5$ cm along the beam) as well as from the gas in the beam path. Fortunately, for $2\theta > W/L_w = 2.1°$ (or $q_{xy} > 0.15$ Å^{-1}), the detector resolution screens out the scattering from the two windows and the observed background is almost entirely due to the He gas and water vapor above the surface. The measured intensity from this also varies roughly as q_{xy}^{-1} due to the decrease in the length of the beam path viewed by the detector.

For rod scans [5], the q_{xy} (or 2θ) position of the detector is held at the center of a GID peak, and the scattered intensities along q_z (or β), which depend on molecular scale density correlations *normal to the surface*, are measured. However, unlike XR, they are sensitive only to the in-plane ordered regions of the surface that give rise to the GID peak. For a LM with no molecular tilt, the intensity falls slowly with q_z on the scale of l^{-1}, where l is the molecular length along the surface normal. In the rod scan experiment, the data were collected using a Braun position-sensitive linear detector with a quartz wire along the β-direction. The background, which was nearly all due to scattering from the He gas and water vapor, was eliminated by subtracting similar scans that only differed in that the LM surface was lowered to 2 mm below the incident beam.

X-ray off-specular diffuse scattering (XOSDS) from liquid surfaces.

In a typical small-angle XOSDS experiment, the intensity scattered from a given surface is measured within the plane of incidence ($2\theta = 0$ or $q_x = 0$) at non-specular conditions, i.e. $\alpha \neq \beta$ or $q_y \neq 0$. The non-zero q_y component of the wave vector transfer *parallel to* the surface typically ranges from 10^{-5} to 10^{-2} Å^{-1}, which is limited by the detector resolution and low counting rates, respectively. Therefore, XOSDS is sensitive to lateral density fluctuations over the surface on submicron length scales, including interfacial height fluctuations.

In this study, a β-scan method was used in which the scattered intensity $I(\alpha, \beta, 2\theta = 0)$ was measured as a function of β at constant α. Since q_z is varied simultaneously

with q_y, β-scans are also sensitive to the density profile along the surface normal. The experimental setup was identical to that for XR except that a vertical detector slit size of $H = 1.0$ mm was used. This setup provided angular detector resolutions of $\delta\beta = H/L = 0.092°$ and $\delta(2\theta) = W/L = 0.28°$, which are related to reciprocal space resolutions through $\delta q_y \sim (2\pi/\lambda)\sin(\beta)\delta\beta$ and $\delta q_x \sim (2\pi/\lambda)\delta(2\theta)$. As in XR, background intensities measured with 2θ offsets of $\pm 2\theta_b = \pm 0.3°$ were subtracted from the intensity measured at $2\theta = 0$ and the same (α, β). The result was normalized to the incident beam intensity I_0 to obtain the measured normalized intensity difference:

$$\frac{\Delta I(\alpha,\beta)}{I_0} = \frac{1}{I_0}\left\{ I(\alpha,\beta,2\theta = 0) - \frac{1}{2}\left[I(\alpha,\beta,2\theta = +2\theta_b) + I(\alpha,\beta,2\theta = -2\theta_b) \right] \right\}.$$

(3.5)

A characteristic feature of liquid surfaces, including LM systems, is the presence of capillary waves, that is, thermally excited fluctuations in the liquid-vapor interfacial height $h(r_{xy})$, which give rise to thermal diffuse scattering (TDS). The capillary waves cause the interfacial height-height correlation function $g(r_{xy}) = <[h(r_{xy}) - h(0)]^2>$ to vary logarithmically with the distance r_{xy} along the surface [66-68] for r_{xy} smaller than a gravitationally imposed cutoff (~ mm) and large compared to the molecular size d (~ Å). Consequently, for $\eta = (k_B T/2\pi\gamma)q_z^2 < 2$, where γ is the surface tension, the scattering cross section is characterized by an algebraic singularity of the form $1/q_{xy}^{2-\eta}$, without a true specular term [~ $\delta^{(2)}(\mathbf{q}_{xy})$] [66, 67]. Because of this power-law behavior, the capillary wave TDS is a primary source of small-angle XOSDS from liquid surfaces. Therefore, in order to probe non-capillary lateral inhomogeneities occurring in a LM film, their contribution to the XOSDS intensities needs to be quantitatively separable from the capillary-wave TDS.

A given LM is laterally homogeneous if the heights of all interfaces (water/layer, layer/gas, etc.) are conformal with the capillary fluctuations and if there is no density

variation within the surface. In such cases, the local electron density $\rho_{T=0}(\mathbf{r}_{xy}, z')$, which can be defined conceptually by considering a non-uniform frame in which capillary fluctuations are absent [i.e. $z' = z - h(r_{xy})$], is equal to its lateral average $<\rho_{T=0}(z')>$. This average "intrinsic" or local electron density profile $<\rho_{T=0}(z')>$ is to be distinguished from the total average density profile $<\rho(z)>$ defined in Eq.(3.3), which is obtained from the convolution of $<\rho_{T=0}(z')>$ with the capillary wave height distribution $\{h(r_{xy})\}$. It has recently been shown that for small-angle scattering from a homogeneous liquid surface, a properly normalized form of the differential cross section is given by [69, 70]

$$\frac{1}{A_0}\left(\frac{d\sigma}{d\Omega}\right)_{hmg} \approx \frac{1}{16\pi^2}\left(\frac{q_c}{2}\right)^4 \frac{T_F(\alpha)T_F(\beta)}{q_z^2 \sin(\alpha)}\left|\Phi_0(q_z)\right|^2 \frac{2\pi\eta}{q_{xy}^2}\left(\frac{q_{xy}}{q_{max}}\right)^\eta \quad (3.6)$$

for $\eta = (k_B T/2\pi\gamma)q_z^2 < 2$, where A_0 is the cross sectional area of the incident beam, and $T_F(\alpha) = (2\alpha/\alpha_c)^2 \sqrt{R_F(\alpha)}$ is the Fresnel transmission factor [66]. The upper cutoff wave vector q_{max} is determined by the condition that the number of capillary wave modes is on the order of the number of molecules per unit surface area. This is equivalent to fixing $q_{max} \sim 2\pi/d$, where d is on the order of the intermolecular distance. A surface structure factor $\Phi_0(q_z)$ is defined as [69, 70]

$$\Phi_0(q_z) = \int dz \frac{d}{dz}\left[\frac{\langle\rho_{T=0}(z)\rangle}{\rho_\infty}\right]\exp(-iq_z z). \quad (3.7)$$

Therefore, apart from the effect of layering and local interfacial diffuseness contained in $\Phi_0(q_z)$, scattering from a homogeneous LM is still described by the characteristic power law $1/q_{xy}^{2-\eta}$ of the capillary-wave TDS.

If the LM is laterally *inhomogeneous*, the local electron density deviates from the lateral average so that $\delta\rho_{T=0}(\mathbf{r}_{xy}, z') \equiv \rho_{T=0}(\mathbf{r}_{xy}, z') - <\rho_{T=0}(z')> \neq 0$, and there will be additional scattering in excess of Eq. (3.6). This leads to a non-zero *second term* in the differential cross section, whose general form is given by

$$\frac{1}{A_0}\left(\frac{d\sigma}{d\Omega}\right)_{inhmg} = \frac{1}{16\pi^2}\left(\frac{q_c}{2}\right)^4 \frac{1}{A_0}\left|\int d^3\mathbf{r}\exp(-i\mathbf{q}\cdot\mathbf{r})\exp\left(-iq_z h\left(r_{xy}\right)\right)\frac{\delta\rho_{T=0}(\mathbf{r})}{\rho_\infty}\right|^2.$$

(3.8)

In general, the normalized intensity I/I_0 is equal to the convolution of the differential cross section with an appropriate instrumental resolution function Ξ:

$$\frac{I(\alpha,\beta,2\theta)}{I_0} = \int d\beta'\int d(2\theta')\Xi_\Omega(\beta-\beta';2\theta-2\theta')\frac{1}{A_0}\frac{d\sigma}{d\Omega}(\alpha,\beta',2\theta'),$$ (3.9a)

or equivalently, using the approximation $d\Omega \approx d\beta d(2\theta) \approx d^2\mathbf{q}_{xy}/[k^2\sin(\beta)]$,

$$\frac{I(\mathbf{q})}{I_0} = \int \frac{d^2\mathbf{q}'_{xy}}{k^2\sin(\beta)}\Xi_q\left(\mathbf{q}_{xy} - \mathbf{q}'_{xy}\right)\frac{1}{A_0}\frac{d\sigma}{d\Omega}\left(\mathbf{q}'_{xy}\right).$$ (3.9b)

For $\alpha \gg \alpha_c$, the physical size of the detector opening is much larger than the projection of the illuminated sample area onto the plane of the detector. Therefore, the simple and reasonable choice for Ξ is a rectangular resolution function whose center and area correspond to the nominal detector position and the angular acceptance defined by the detector slits, respectively:

$$\Xi_\Omega\left(\Delta\beta;\Delta(2\theta)\right) = \begin{cases}1 & \text{if } |\Delta\beta| \leq \delta\beta/2, |\Delta(2\theta)| \leq \delta(2\theta)/2 \\ 0 & \text{otherwise}\end{cases},$$ (3.10a)

or equivalently,

$$\Xi_q\left(\Delta q_x,\Delta q_y\right) = \begin{cases}1 & \text{if } |\Delta q_x| \leq \delta q_x/2, |\Delta q_y| \leq \delta q_y/2 \\ 0 & \text{otherwise}\end{cases}.$$ (3.10b)

By substituting Eq. (3.6) in (3.9), carrying out the convolution with the slit-defined resolution function from Eq. (3.10) numerically, and taking the same intensity difference as in Eq. (3.5), one can calculate the homogeneous capillary-wave contribution $[\Delta I(\alpha, \beta)/I_0]_{hmg}$ to the normalized XOSDS intensity difference $\Delta I(\alpha, \beta)/I_0$ [69-71]. The physical parameters (T, γ) and detector resolutions are known, and q_{max} can be estimated

from the size of the LM forming molecules. Moreover, since Eq.(3.6) is also valid for XR, the factor $\Phi_0(q_z)$, or the intrinsic profile $\langle\rho_{\Gamma=0}(z)\rangle$, can be determined by fitting $[\Delta I(\alpha, \beta = \alpha)/I_0]_{hmg}$ to the measured specular reflectivity $R(q_z)$ [69, 70]. Consequently, the homogeneous contribution $[\Delta I(\alpha, \beta)/I_0]_{hmg}$ can be calculated with no adjustable parameters. It follows that comparison between the theoretical curve $[\Delta I(\alpha, \beta)/I_0]_{hmg}$ and the measured data $\Delta I(\alpha, \beta)/I_0$ provides an unambiguous test of the homogeneity for a given LM.   Any excess scattering $\Delta I/I_0 - [\Delta I/I_0]_{hmg} > 0$ is a measure of surface inhomogeneities $\delta\rho_{\Gamma=0}(r_{xy}, z) \neq 0$, and can be analyzed in terms of the convolution of Eq.(3.8) with the same resolution functions.

X-ray radiation damage.

During the x-ray experiments on PBLG LMs, changes in the scattered intensity were observed when the maximum incident flux (on the order of 10^9 photons/sec) was used. For GID, in which α is small and therefore the incident beam is spread over a larger surface area, radiation-induced changes (often evidenced by the disappearance of a peak) occurred only after exposing the same spot of the film for many hours at full intensity. For XR and XOSDS, at the largest values of α measured, the use of high flux led to changes in the reflected intensities after less than 30 minutes. Subsequently, special care was taken to minimize radiation damage by limiting the x-ray exposure through absorbers and carefully monitoring the scattered signals. There was no indication of film damage in any of the results presented here.

3.3 Results and Discussion

3.3.1 *Π-A* isotherms and surface imaging by BAM

Representative *Π-A* isotherms are shown in Fig. 3.2(a) for polydisperse and in Fig. 3.2(b) for monodisperse PBLG. BAM images obtained from a polydisperse film are summarized in Figs. 3.3 and 3.4. In Fig. 3.2(a), the solid line and the filled circles

correspond to a continuous and a relaxation isotherm, respectively. The solid line in Fig. 3.2(b) is a continuous scan taken during the x-ray scattering experiments. In both figures, the Π-A positions at which x-ray measurements were carried out are indicated with open circles. The shown isotherms are very similar to those obtained previously by others for polydisperse samples [12, 13, 18, 25, 46]. As indicated in Fig. 3.2, the Π-A phase diagram can be divided into four main regions, each exhibiting a different surface pressure variation with compression.
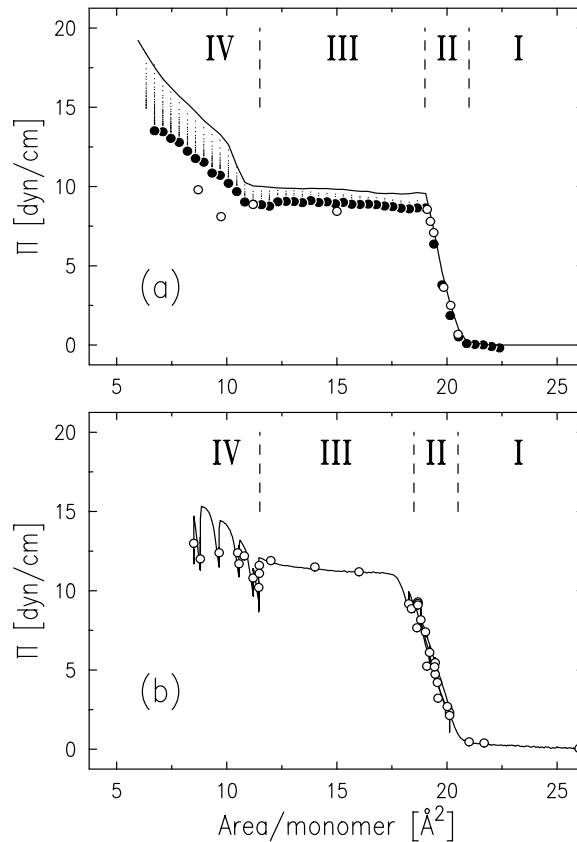
Figure 3.2: Π-A isotherms at T = 23 °C for (a) polydisperse and (b) monodisperse PBLG films. In (a), the solid line (——) is a continuous isotherm, and the filled circles (●) correspond to a relaxation isotherm. The dots (···) show intermediate surface pressures measured during relaxation at fixed *A*. In (b), the solid line (——) is a set of continuous compression/expansion scans taken on Film-1 during the x-ray scattering experiment. In both (a) and (b), the open circles (○) indicate the points at which x-ray scattering measurements were carried out.

0.50 mm

(a)   (b)   (c)   (d)
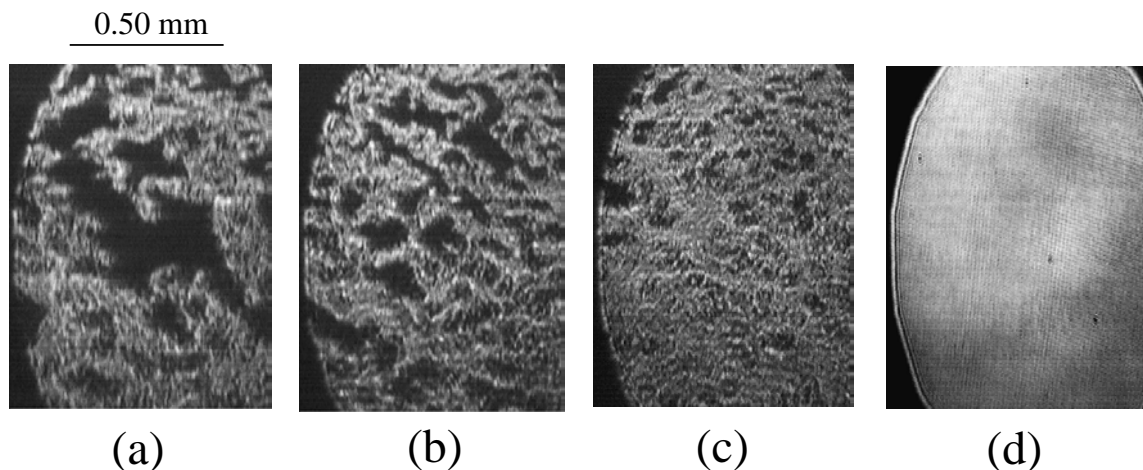
Figure 3.3: BAM images taken at A = (a) 31, (b) 25, (c) 23, and (d) 20 Å^2/monomer. The images (a)-(c) are in Region I of the Π-A isotherm, while (d) is in Region II.

In Region I (A > ~21 Å^2/monomer), the surface pressure remains zero as the film is compressed. This behavior is due to an incomplete surface coverage, which is clearly evident in BAM images from Region I [Fig. 3.3(a)-(c)]. As deposited, LM-coated regions coexist with regions of bare water surface. A typical image Fig. 3.3(a) reveals that a LM-coated region itself consists of a network of PBLG islands (bright) with small gaps of bare water surface in between (dark). In an epifluorescence microscopy study, Lavigne *et al*. also observed an aggregation of PBLG molecules into 2D islands at low surface density [25]. As a result, compression in Region I only leads to a reduction in the area of the gaps between PBLG islands, as illustrated in a series of images Fig. 3.3(a)-(c) taken at A = 31, 25, 23 Å^2/monomer. This type of compression is consistent with the absence of measurable surface pressure since it does not alter the microscopic structure within the islands themselves. Another important BAM observation is that the monolayer is solid like as indicated by the intricate shapes of the island/water boundaries which would not be expected for a fluid monolayer.

Region II (~18.5 Å^2/monomer < A < ~21 Å^2/monomer) is characterized by an increase in the surface pressure above Π ~ 0. Given the PBLG rod diameter of about 13

Å [61] and the α-helix pitch of 1.5 Å/monomer along the rod axis, one expects a limiting area/monomer of $A_{lim} \sim 19.5$ Å^2/monomer for a close packed monolayer of PBLG rods lying down parallel to the water/gas interface [25]. The fact that this A_{lim} value falls into Region II, where the Π increase is observed, provides indirect evidence for both the single molecule thickness of the film in Regions I and II and the parallel-to-surface orientation of the PBLG rods. In Region II, the entire surface is uniformly covered with the PBLG LM. A typical BAM image Fig. 3.3(d), taken at A = 20 Å^2/monomer, also shows that the LM surface has become more or less homogeneous. Since the bare areas observed in Region I are now absent, compression in Region II should result in a microscopic reduction in the intermolecular distance within the 2D plane.

Region III ($\sim$11.5 Å^2/monomer $< A < \sim$18.5 Å^2/monomer) of the isotherm is characterized by a plateau of infinite compressibility ($\chi = - A^{-1} \cdot dA/d\Pi = \infty$), which

0.50 mm

(a)   (b)   (c)
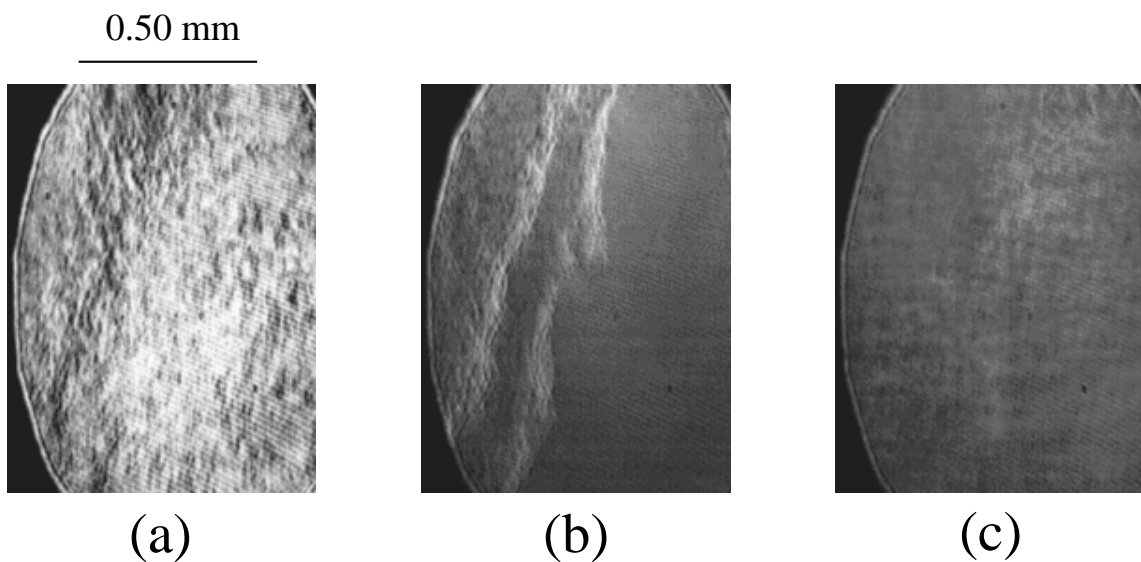
Figure 3.4: BAM images taken at $A = 13.3$ Å^2/monomer in Region III. The moveable barrier and the trough edge on the opposite side, both of which run parallel to the vertical edges of the images, are located approximately 6.5 cm to the left and 5 cm to the right of image (b), respectively. Images (a) and (c) were taken from spots that were less than 1 cm away from the image (b) spot, with (a) being on the barrier side and (c) being on the opposite side. The sensitivity of the CCD camera used here (the same for (a)-(c)) is lower than that in Fig. 3.3.

signifies a first-order phase transition between two coexisting phases. Since the ratio of the area/monomer values at the two ends of this coexistence region is close to two, the second phase coexisting with the monolayer phase has been assumed to be a bilayer [11, 12, 18, 25]. Further compression into Region IV ($A < \sim11.5$ Å^2/monomer) results in a surface pressure increase in the continuous isotherms. However, the relaxation effect is now more significant. When the film is left to relax at a constant area/monomer in this region, surface pressure decreases almost to the plateau value. As indicated by the open circles in Fig. 3.2, x-ray measurements in Region IV were made on relaxed films.

Figure 3.4 shows BAM images taken at $A = 13.3$ Å^2/monomer in Region III. As shown in Fig. 3.4(b), a region of inhomogeneity (confined to less than 1 cm along the compression direction) was found in which ridge or step-like morphologies ran more or less parallel to the moveable barrier (i.e. perpendicular to the compression direction). The images (see Fig. 3.4(c)) taken from the stationary edge side of this inhomogeneous region are very similar to those obtained for the monolayer in Region II. However, the intensity reflected from the moveable barrier side of the surface (see Fig. 3.4(a)) is consistently higher than that from the other side. These observations indicate that the monolayer coexists with a thicker phase in Region III. Moreover, the coexistence is not uniform over the surface. While the stationary edge side of the surface is mostly still a monolayer, the film on the moveable barrier side seems to be dominated by a thicker phase. This suggests that the formation of the second thicker phase starts preferably at the moving barrier and grows parallel to the compression direction [22]. Evidence that this second phase is in fact a bilayer is provided by the XR results to be discussed below.

During the BAM study, birefringence effects were also investigated by placing an analyzing polarizer after the imaging lens. However, no clear evidence was found for optical anisotropy within the PBLG films. This seems to suggest a lack of long-range orientational order and the absence of large oriented domains within the film. However, it may also be due to a relatively small difference between the refractive indices in the

directions parallel and perpendicular to the molecular axes [38, 39, 41, 72].

3.3.2 X-ray specular reflectivity (XR)

Representative reflectivity data are shown in Fig. 3.5(a) for monodisperse and Fig. 3.5(b) for polydisperse PBLG Langmuir films. The three R/R_F curves in each figure correspond to: a low-Π film in Region II, near the I/II boundary (A, A'); a high-Π film in Region II, near the II/III boundary (B, B'); and a film in Region IV, on the high-density side of the coexistence region (C, C'). The results are nearly independent of the sample
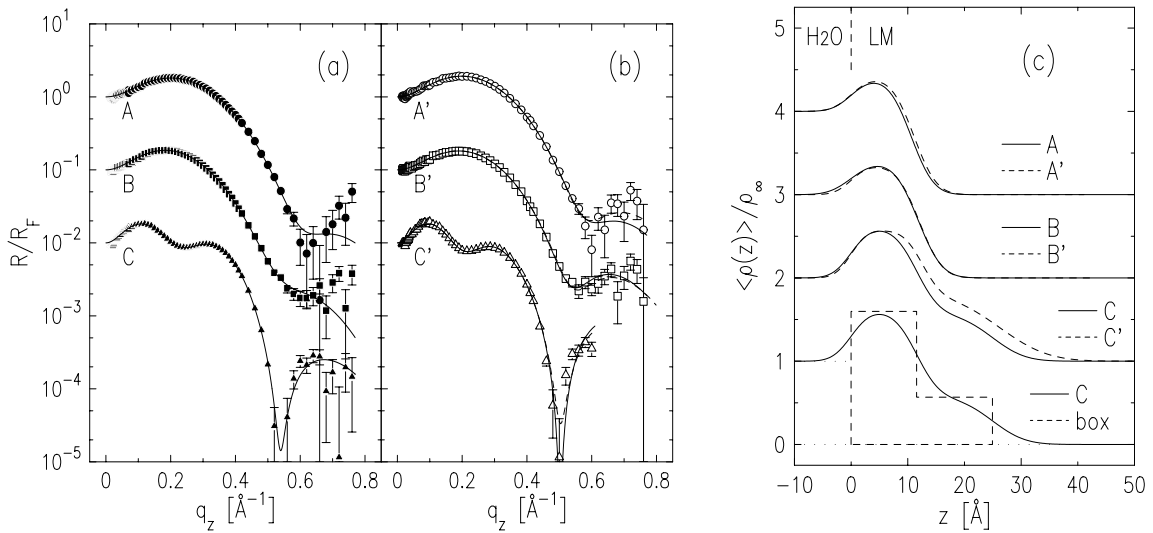
Figure 3.5: Measured specular reflectivity normalized to the Fresnel reflectivity of an ideally flat and sharp water/gas interface for (a) monodisperse and (b) polydisperse PBLG films. In (a), the shown R/R_F data were obtained at A ($\bullet$): 21.7 Å^2/monomer, 0.4 dyn/cm; B ($\blacksquare$): 18.7 Å^2/monomer, 9.3 dyn/cm; C ($\blacktriangle$): 11.5 Å^2/monomer, 11.6 dyn/cm. In (b), the data were obtained at A' ($\bigcirc$): 20.2 Å^2/monomer, 2.5 dyn/cm; B' ($\square$): 19.2 Å^2/monomer, 7.8 dyn/cm; C' ($\triangle$): 9.7 Å^2/monomer, 8.8 dyn/cm. The solid curves (—) in (a) and (b) are best fits given by Eq. (3.3) and the box-model *total* average electron density profiles $\langle\rho(z)\rangle/\rho_\infty$ shown in (c). The dashed lines (---) in (b) for the polydisperse film are best fits based on Eq. (3.6) and the box-model average *local* electron density profiles $\langle\rho_{T=0}(z)\rangle/\rho_\infty$ shown in the insets in Figs. 3.12(a) and 3.13(a).

70

dispersity. The oscillation rate (in q_z) of the R/R_F curves C and C' is higher by about a factor of two than that for the curves A, B, A', and B'. This implies that PBLG films in Region IV are about twice as thick as those in Region II.

Quantitative fitting of each reflectivity curve was done by constructing a simple "box" model [4, 5, 27] for the relative average electron density profile $<\rho(z)>/\rho_\infty$ across the water/PBLG/gas interface. In a single-layer box model, a layer of thickness l_1 and density $\rho_1/\rho_\infty = \phi_1$ is assumed between the bulk subphase below ($\rho/\rho_\infty = 1$) and the gas above ($\rho/\rho_\infty = 0$), and the water/layer and layer/gas interfaces are smeared out with Gaussian roughnesses σ_{w1} and σ_{1g}, respectively. In a double-layer box model, a second layer of thickness l_2 and density $\rho_2/\rho_\infty = \phi_2$ is added on top of the first layer; the Gaussian roughnesses for the layer-1/layer-2 and layer-2/gas interfaces are designated as σ_{12} and σ_{2g}, respectively.

Using these models, the R/R_F data have been fit to the Born approximation expression [Eq. (3.3)] for $q_z \geq 0.1$ Å^{-1}. The single-layer model was used for the PBLG films in Region II (A, B; A', B'), while the double-layer model was necessary to obtain good fits in Region IV (C, C'). The best-fit R/R_F curves are shown as the solid lines in Fig. 3.5(a) and (b). The corresponding density profiles $<\rho(z)>/\rho_\infty$ are shown in Fig. 3.5(c), and the best-fit parameters are listed in Table 3.1. As evident in Fig. 3.5(a) and 3.5(b), the reflectivity data are well described by the simple box models. In some cases, there are small residual deviations between the data and the fits at large q_z (where the error bars are large). Although the use of more sophisticated models or increased number of parameters could further improve the fitting, the improvement would only appear in fine structural details that would not affect the principal physical interpretations.

It is evident from Fig. 3.5(c) and Table 3.1(a) that both the monodisperse and polydisperse PBLG films in Region II (A, B; A', B') are monolayers with their layer thicknesses l_1 being comparable to the PBLG rod diameter of ~ 13 Å, as expected.

Table 3.1: The list of best-fit parameters used to fit the measured R/R_F data, where the fits are based on Gaussian-smeared "box" models for the average electron density profile $\langle\rho(z)\rangle/\rho_\infty$ across the water/PBLG/gas interface. The parameter designations are as follows. (a) Single-layer box model for PBLG monolayers: layer thickness, l_1; relative electron density in the layer, $\phi_1 = \rho_1/\rho_\infty$; water/layer and layer/gas interfacial roughness, σ_{w1}, σ_{1g}. (b) Double-layer box model for PBLG bilayers: layer-1 and layer-2 thickness, l_1, l_2; layer-1 and layer-2 relative electron density, $\phi_1 = \rho_1/\rho_\infty$, $\phi_2 = \rho_2/\rho_\infty$; water/layer-1, layer-1/layer-2, and layer-2/gas interfacial roughness, σ_{w1}, σ_{12}, σ_{2g}.

(a) Single-layer box models for monolayers

	Disp.	A [$\mathring{A}^2$/mon]	$<\Pi>$ [dyn/cm]	$\phi_1 = \rho_1/\rho_\infty$	l_1 [$\mathring{A}$]	σ_{w1} [$\mathring{A}$]	σ_{1g} [$\mathring{A}$]
A	mono	21.7	0.4	1.39 ± 0.09	10.6 ± 1.0	2.67 ± 0.5	3.14 ± 0.5
B	mono	18.7	9.3	1.39 ± 0.06	11.8 ± 0.8	3.12 ± 0.4	3.35 ± 0.23
A'	poly	20.2	2.5	1.40 ± 0.08	11.1 ± 0.9	2.66 ± 0.5	3.14 ± 0.5
B'	poly	19.2	7.8	1.34 ± 0.04	12.1 ± 0.5	2.31 ± 0.4	3.18 ± 0.2

(b) Double-layer box models for bilayers

	Disp.	A [$\mathring{A}^2$]	$<\Pi>$ [dy/cm]	ϕ_1	ϕ_2	l_1 [$\mathring{A}$]	l_2 [$\mathring{A}$]	σ_{w1} [$\mathring{A}$]	σ_{12} [$\mathring{A}$]	σ_{2g} [$\mathring{A}$]
C	mono	11.5	11.6	1.60 ± 0.10	0.57 ± 0.10	11.6 ± 0.6	13.4 ± 0.8	2.61 ± 0.7	3.17 ± 0.9	4.52 ± 1.0
C'	poly	9.7	8.8	1.57 ± 0.04	0.81 ± 0.13	12.5 ± 0.6	13.6 ± 0.6	2.24 ± 0.5	2.64 ± 0.6	6.76 ± 0.9

Theoretically, since the PBLG molecule contains 116 electrons/monomer, one expects the surface density of electrons originating from a PBLG monolayer to increase from 5.4 to 6.3 electrons/$\mathring{A}^2$ as the specific area is reduced from A = 21.5 to 18.5 $\mathring{A}^2$/monomer. Experimentally, the surface electron density is given roughly by the integrated area under the single-layer "box" (i.e. $\sim \rho_\infty \cdot \phi_1 \cdot l_1$). The latter experimentally derived estimates of surface electron densities are within 10% of the theoretically expected values, indicating that the values for the monolayer thickness and density parameters are physically reasonable. As for the roughness parameters, for all of the PBLG monolayers in Region

II, the layer/gas interface (σ_{lg}) is just slightly rougher or more diffuse than the water/layer interface (σ_{w1}). These roughness values are comparable to the capillary-wave roughness of about 2.5 Å for the water/gas interface measured with the same instrumental resolution [73, 74]. Finally, the main effect of compression in Region II (A → B; A' → B') is to thicken the monolayer slightly, which is consistent with both close packing and microscopic compression. The fact that the product $A \times l_1$, which should be constant for a fixed amount of material, varies by about 4 % between scans {A, A'} and {B, B'} is probably a measure of confidence one can have in this very simple model. These results establish that in Region II the PBLG molecules form a stable monomolecular layer on water with their rod axes parallel to the surface.

By contrast, both monodisperse and polydisperse PBLG films in Region IV are no longer monolayers. If the XR results are taken at face value, the conclusion would be that the relaxed film in this region is a bilayer characterized by a low density second layer on top of a dense first layer (Fig. 3.5(c)). In fact, as already mentioned, there is evidence that the film is not homogeneous in this region, and the proper quantitative interpretation of the best fit density profile is not clear. On the other hand, the q_z positions of the minima and maxima of the R/R_F curves depend only on the film thickness and not on the average density. The fact that the reflectivity can be well fit by the double-layer box model does indicate that the thickness of this second layer obtained from the best fits is reliable.

Based on the parameters listed in Table 3.1(b), the following observations can be made: First, the thickness (l_1 or l_2) of each of the two layers is comparable to the PBLG rod diameter of ~ 13 Å. This strongly suggests that the PBLG molecules in the bilayer are confined within one or the other of the two layers and are still oriented parallel to the surface. Secondly, for all the bilayers measured in Region IV, the magnitude of the second layer densities (ϕ_2) was found to be only 30 to 50% of the first layer densities (ϕ_1). This implies that on the average a smaller number of PBLG molecules occupy the top layer than the bottom layer. It is possible that the reflectivity arises from only some

fraction of the film that is a homogeneous bilayer. The remainder could be a monolayer, but it is also possible that a sizeable fraction of the film consists of thicker aggregates that do not reflect. Thirdly, ϕ_1 for the bilayers in Region IV is about 15 % greater than the monolayer densities in Region II. All of these observations together suggest that as the film is compressed through Region III into IV, some of the PBLG molecules are pushed up from the monolayer into the second layer above, with others possibly pushed into even thicker aggregates. At the same time the first layer becomes slightly more packed than the monolayer in Region II. Moreover, throughout this process, the PBLG rods remain parallel to the interfacial plane.

There are a few other points to be made regarding the bilayers in Region IV. First, l_2 is slightly larger (by 1-2 Å) than l_1. Moreover, the roughness σ_{2g} for the second layer/gas interface is greater than those for the other two interfaces by more than 1 Å, giving a more diffuse appearance to the second layer/gas interface in the density profile. Considering that the molecules in the second layer have been pushed out of the monolayer upon compression, it may be possible that not all the PBLG rods in the second layer are located at the same height and some may not be oriented perfectly parallel to the interface. It is also important to note that the less dense second layer may be more susceptible to lateral density fluctuations over the surface. All of these points imply that the bilayer in Region IV is more likely to be microscopically inhomogeneous than the monolayer in Region II. This issue is considered more quantitatively in the XOSDS section below.
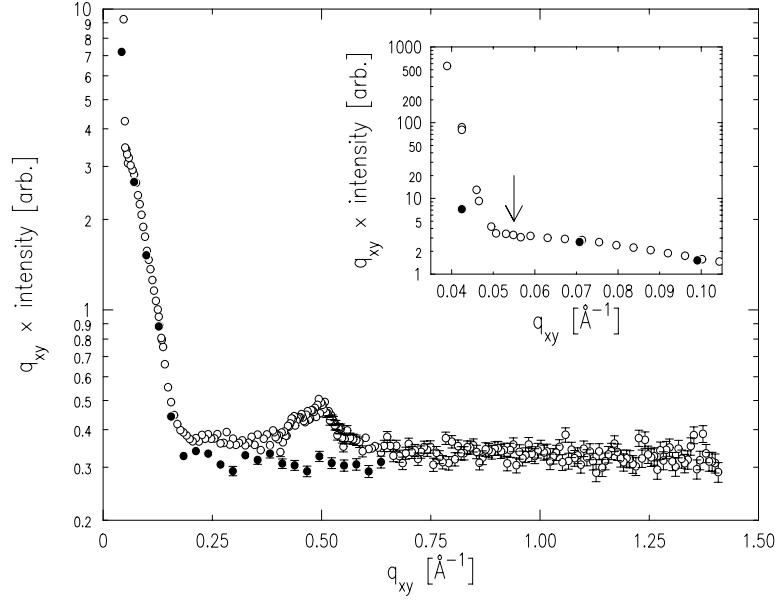
Figure 3.6: The open circles (O) show typical wide-range GID data from a PBLG film. This particular scan was measured on a monodisperse PBLG film at (A, $<\Pi>$) = (11.2 Å^2/monomer, 9.8 dyn/cm). The filled circles (●) show a background scan. The inset is an enlargement of a small q_{xy} portion of the same data, shown with a different vertical scale. The arrow (↓) at $q_{xy} = 0.055$ Å^{-1} indicates where a GID peak would be found if monodisperse PBLG molecules (rod length ~ 115 Å) were to form smectic layers within the film. In the figures, the detected signal (apart from the structure near $q_{xy} = 0.5$ Å^{-1}) is dominated by diffuse scattering from the surface for $q_{xy} <$ ~0.048 Å^{-1}; small-angle scattering from the Kapton windows of the sample cell for ~0.048 $\text{Å}^{-1} < q_{xy} < 0.15$ Å^{-1}; and scattering by gas above the surface for $q_{xy} > 0.15$ Å^{-1}.

3.3.3 Grazing incidence diffraction (GID)

Figure 3.6 is representative of wide GID scans taken on PBLG films. In order to account for the variation in the length of the beam path (i.e. the incident and totally reflected beam) viewed by the detector, the plotted quantity is q_{xy} × intensity. For most values of q_{xy}, the detected signal is attributed almost entirely to the background (filled circles). However, scattering from the film shows a structure around q_{xy} ~ 0.5 Å^{-1} that clearly rises above the background. Its q_{xy} position corresponds to a characteristic lateral

distance of $d \sim 13$ Å, which is close to the nearest-neighbor distance of 12.6 Å observed in the bulk smectic phase of PBLG [61]. This repeat distance is comparable to the rod diameter of the molecule, and its presence indicates parallel alignment of PBLG helices within the LM plane. Rotation of the film about the surface normal showed no indication of variations in the peak intensities, i.e. the scattering from the illuminated sample area viewed by the detector (on the order of 1 mm × 40 mm at $q_{xy} \sim 0.5$ Å^{-1}) corresponded to a powder average with no evidence for large oriented domains [75].

No other diffraction peaks were observed during the GID experiment. In particular, no evidence was found for smectic layering in the monodisperse PBLG films. Given the molecular length of about 115 Å for the monodisperse PBLG [61], the presence of one-dimensional smectic layers within the 2D plane would be signaled by a peak at q_{xy} ~ 0.055 Å^{-1}. No such peak was found in the GID data, as indicated by the arrow in the inset to Fig. 3.6. However, there is a small possibility that a smectic peak was obscured by relatively high background in the small q_{xy} region. Although this cannot be absolutely ruled out, the above result seems to suggest that if there exists monodispersity-induced smectic order as observed in 3D [61], the extent of such ordering must be small in the PBLG LM.

Representative inter-helix peaks around $q_{xy} \sim 0.5$ Å^{-1} from different regions in the Π-A isotherms are shown in Fig. 3.7 for both mono- and polydisperse samples. The same qualitative behavior is observed regardless of sample dispersity. A peak is already present in Region I, without external pressure. In Region II, the peak shifts to larger q_{xy} with increasing Π. In the plateau region (III), little or no shift is observed. Finally, on the denser side of coexistence in Region IV, a weaker and broader *second* peak appears at slightly smaller q_{xy}. Quantitative analysis of these peaks was done by fitting the observed GID patterns to one (Regions I-III) or two (Region IV) Lorentzians with constant and linear background terms. Best fits are shown as solid lines in Fig. 3.7. Integrated intensities (area under the peak) and peak widths do not follow any consistent trend as a
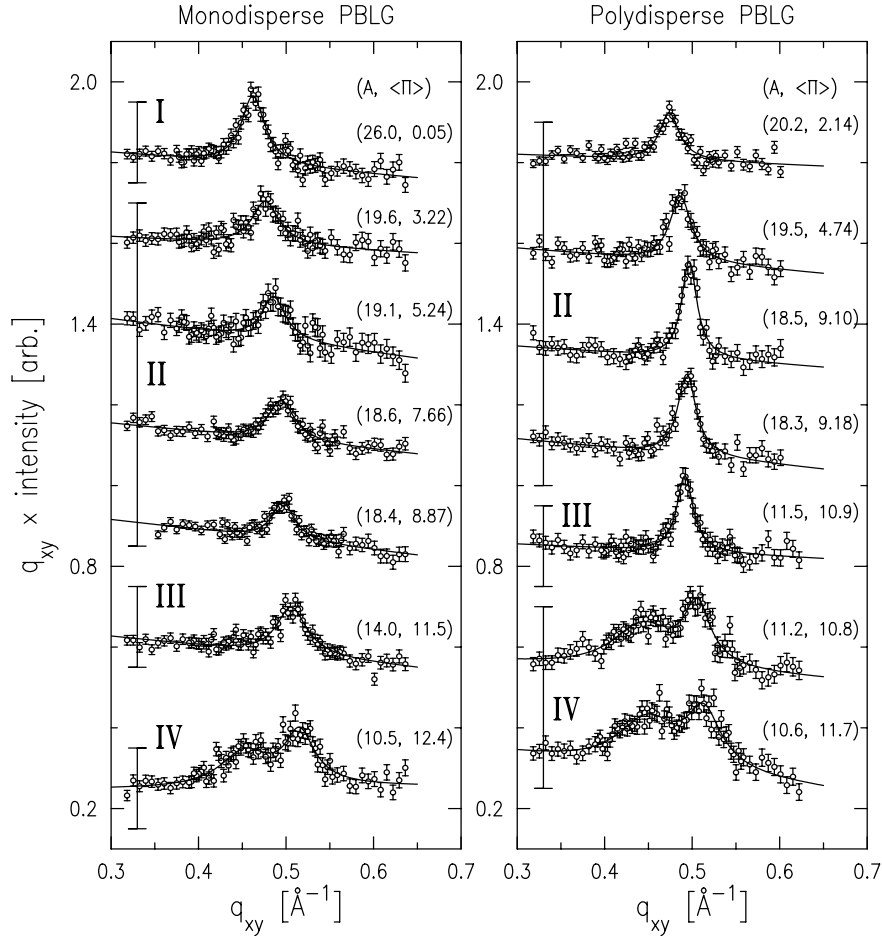
Figure 3.7: Representative inter-helix GID peaks from different regions in the Π-A isotherms, for both monodisperse (left) and polydisperse (right) PBLG films. Area/monomer (A, in Å^2) and surface pressure (Π, in dyn/cm) values for the individual scans are indicated on the right side in each figure. The solid curves (——) are best fits to one (Regions I-III) or two (Region IV) Lorentzians with constant and linear background terms.

function of A or Π. However, the peak positions $q_{xy} = q_0$, and therefore the inter-helix distances $d = 2\pi/q_0 = \lambda/[2\sin(\theta_0)]$, display a distinct behavior in each of the four regions that is quantitatively similar for both mono- and polydisperse PBLG films.

Figure 3.8 and Fig. 3.9 summarize the dependence of the inter-helix d-spacing on both A and Π, obtained from measurements on two separate monodisperse PBLG films.
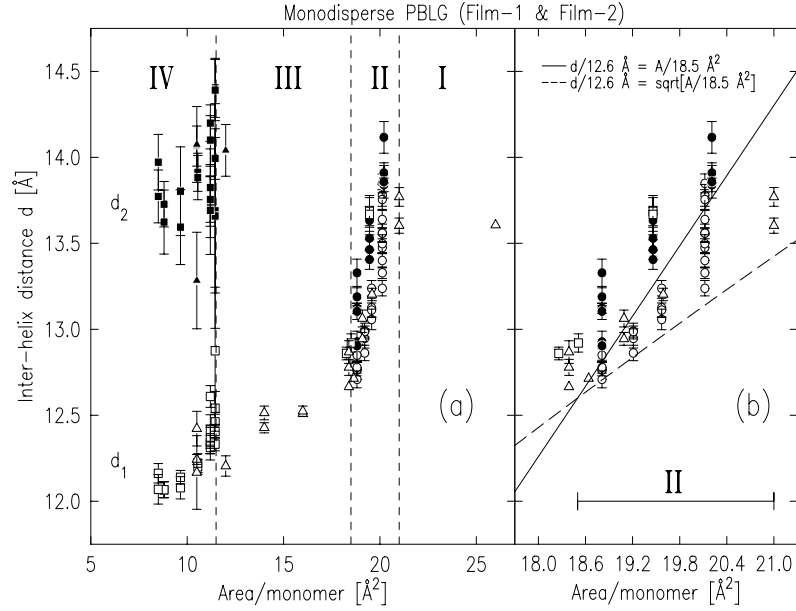
Figure 3.8: (a) Inter-helix d-spacing as a function of area/monomer, obtained from GID scans on two separate monodisperse PBLG films (Film-1 and Film-2). In Region IV, d_1 and d_2 indicate the two sets of d-spacings corresponding to the two GID peaks observed from bilayers. The data from Film-1 are separated into the first compression sequence (O, $A \geq 18.8$ Å^2/monomer), the expansion sequence (●, $18.8 \leq A \leq 20.2$ Å^2/monomer), and the second compression sequence (□ for d_1, ■ for d_2). The data for Film-2, which was compressed without intermediate expansion, are indicated by triangles (△ for d_1, ▲ for d_2). (b) An enlargement of Region II part of (a). The solid line (—) and the dashed curve (---) describe a linear ($A \propto d$) and a quadratic ($A \propto d^2$) relationship between area/monomer and inter-helix d-spacing, respectively, where each curve was assumed to go through the point $(A, d) = (18.5$ Å^2/monomer, 12.6 Å$)$.

Fig. 3.8(b) shows the Region II part of Fig. 3.8(a). The compression/expansion sequence used for each film is as follows: Film-1 was compressed first up to $A = 18.8$ Å^2/monomer (open circles), expanded back to 20.2 Å^2/monomer (filled circles), and then compressed across Region III into IV (squares). Film-2 was compressed from Region I through IV without intermediate expansion (triangles). At a given fixed A, two or more GID scans were typically taken, and the inter-helix distances obtained from all the scans are presented together in Figs. 3.8 and 3.9. A PBLG monolayer (Regions I and II) is characterized by a single d-spacing, while a bilayer (Region IV) is associated with two d-

78

spacings. The latter correspond to the two GID peaks observed and are labeled as d_1 (the first peak) and d_2 (the second peak at smaller q_{xy}).

The observation of a well defined inter-helix distance in Region I ($\Pi = 0$) indicates that after being spread on water, PBLG molecules spontaneously aggregate and align themselves with their near neighbors to form 2D islands. As shown in Fig. 3.8(a), the d-spacing in this region remains almost unchanged at $d \sim 13.6$ Å. This is consistent with the earlier suggestion that due to an incomplete surface coverage, macroscopic compression does not lead to microscopic compression in Region I. The inter-helix distance here is slightly larger than the value of $d = 12.6$ Å observed in the 3D smectic phase [61]. In addition to the absence of external pressure in Region I, this could be due to the smaller number of nearest neighbors in 2D.
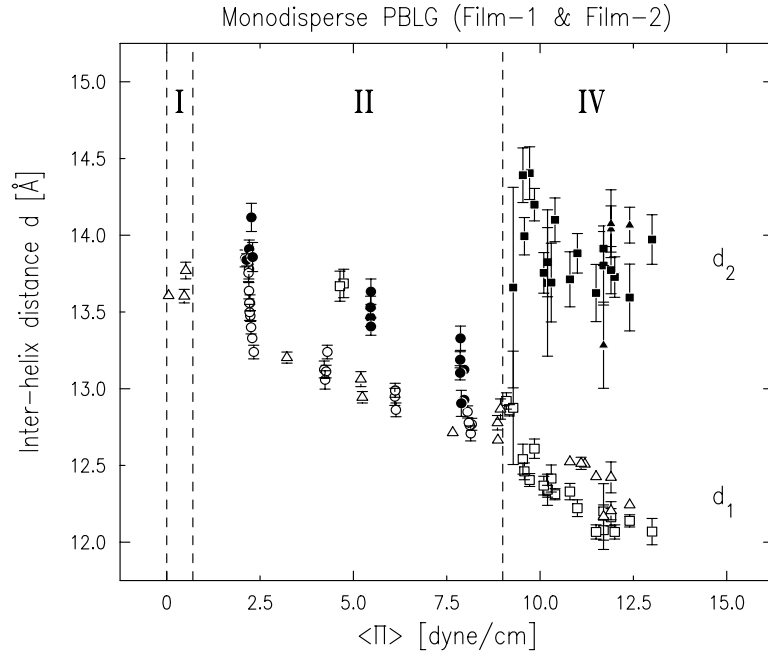
Figure 3.9: Inter-helix d-spacing as a function of surface pressure, obtained from GID scans on two separate monodisperse PBLG films (Film-1 and Film-2). The data from Film-1 are separated into the first compression sequence (O), the expansion sequence (●), and the second compression sequence (□ for d_1, ■ for d_2). The data for Film-2 are indicated by triangles (△ for d_1, ▲ for d_2).

In Region II ($\Pi > 0$), macroscopic compression does result in a microscopic reduction of the inter-helix distance, with the smallest d-spacing of $d \sim 12.6$ Å occurring at the Region II/III boundary. This is consistent with both a macroscopically full surface coverage expected for a closely packed LM (BAM) and a small increase in monolayer thickness l_1 with compression in Region II (XR). In Fig. 3.8(b), the two lines represent two extreme cases for a possible compression mode, assuming that they go through the point $(A, d) = (18.5$ Å^2/monomer, 12.6 Å$)$. The solid line assumes a linear relationship between d and A, such that compression only reduces the inter-helix distance perpendicular to the long axes of the helices; the dashed line assumes isotropic compression, i.e. $d \propto \sqrt{A}$. Unfortunately, the slopes for these two possibilities seem to bracket the data, and it is not possible to distinguish between them. Nevertheless, the molecules appear to remain confined to a monolayer throughout Region II. As for the Π dependence, using the data points from the first compression sequence (open circles and triangles in Fig. 3.9), the average in-plane inter-helix compressibility is estimated to be $\chi = - d^{-1}(\Delta d/\Delta \Pi) \sim 8 \times 10^{-3}$ cm/dyn in Region II.

The Π-A isotherm in Region II shows only small relaxation for Π and is reversible with little hysteresis. However, note that the d vs. A and d vs. Π curves are not perfectly reversible in this region. Fig. 3.8(b) and Fig. 3.9 show that expansion (filled circles) leads to relaxation of the d-spacing to values larger than those during the initial compression. On the other hand, the second compression points (open squares) appear to follow the expansion curve, indicating a smaller hysteresis in the expansion/recompression cycle than in the first compression/expansion cycle. Relaxation effects can also be seen in the time dependence. Fig. 3.10 shows a gradual increase in the d-spacing with time (after the trough barrier was stopped) at two fixed values of A in Region II. One possible explanation for these observations may be that the monolayer initially compressed to Region II contains many "defects" at the intermolecular level. For example, if there were defects such as holes between the ends of helices or between
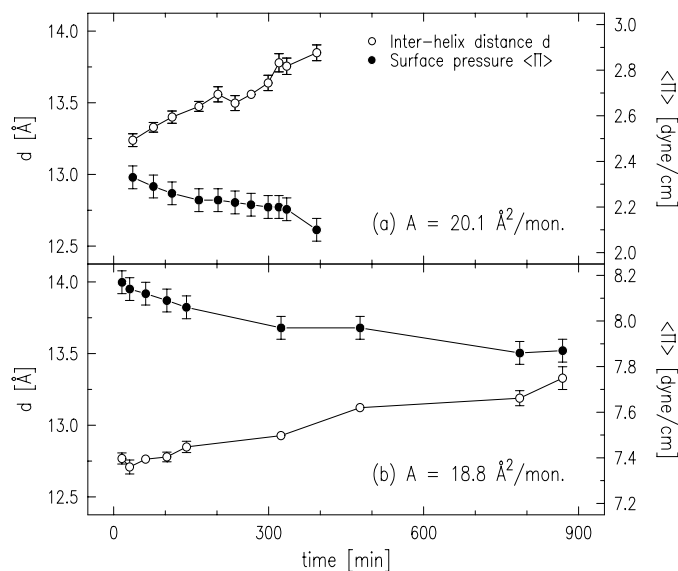
Figure 3.10: Inter-helix d-spacing (O) and surface pressure (●) as a function of time after the end of compression at A = (a) 20.1 Å^2/monomer and (b) 18.8 Å^2/monomer, obtained from measurements on a monodisperse PBLG film (Film-1) during the first compression sequence in Region II.

misaligned domains, the lateral inter-helix compression necessary to attain a given macroscopic area would be greater than in the absence of holes. If this were so, then the relaxation of the inter-helix d-spacing would correspond to the molecules having rearranged their positions to fill in some of these gaps. Alternatively, it is also possible that with time some molecules move out of the monolayer.

In Region III, a single inter-helix distance d_1 (i.e. a monolayer) is observed for the most part, except near the Region III/IV boundary where the second d-spacing d_2 appears (signifying a bilayer). However, unlike in Region II, compression across Region III leaves the value of d_1 more or less unchanged at $d_1 \sim 12.5$ Å (see Fig. 3.8(a)). This suggests that the monolayer part of the coexisting phases in Region III remains similar to the compressed monolayer at the highest Π in Region II. The fact that d_2 is not observed until near the Region III/IV boundary can be explained from a combination of the experimental geometry and the nature of bilayer formation. The footprint of the incident

beam samples a surface area that is closer to the stationary edge of the trough (opposite to the movable barrier) than the barrier position at the beginning of coexistence. Assuming that the second layer preferably starts forming at the moving barrier and grows laterally with twice the barrier speed, the bilayer should enter the illuminated region at $A \sim 12$ to 12.5 Å^2/monomer, just before reaching Region IV. In order to investigate this behavior, specular reflectivity was monitored at constant q_z during compression across Region III. A sudden change was always observed around areas of $A = 11.5$ to 13 Å^2/monomer that signified the entrance of a bilayer region into the illuminated area. This also agrees with the BAM results suggesting that the second layer formation does not initiate everywhere but grows from near the barrier. Probably the moving barrier induces local time-dependent stresses that do not propagate down the length of the film.

As regards the two distinct d-spacings clearly observed for the PBLG bilayer in Region IV, the most likely explanation of their origin is an *incommensurate* structure in which inter-helix distances are different and uncorrelated between the two layers of the bilayer. The XR results have shown that the average of the newly formed second layer is less dense than the first layer below. Moreover, the second GID peak corresponding to d_2 was always weaker than the first peak. These observations suggest that the second d-spacing d_2 corresponds to the inter-helix distance in the second layer, while d_1 comes from the original monolayer underneath. This inference is further supported by the fact that during compression in Region IV, d_2 remains (within the large scatter in the data) close to the value $d = 13.6$ Å observed for the uncompressed monolayer in Region I (see Figs. 3.8(a) and 3.9). Since the second layer is not nearly as tightly packed as the first layer below, the aggregation of nearest-neighbor molecules in the second layer is probably similar to the behavior observed for the molecules in Region I. On the other hand, compression in Region IV leads to a systematic decrease in d_1 for the underlying monolayer. In fact, the Π dependence of d_1 looks like an extrapolation of the behavior observed for the monolayer in Region II. This suggests that once the second layer is

occupied to a certain degree, further upward transfer of molecules from the first layer becomes greatly inhibited. Consequently, compression of the bilayer results in a reduction of d_1 in the close packed first layer to values smaller than the limit of $d \sim 12.6$ Å that can be sustained by the monolayer in Region II.

Analysis of observed inter-helix peaks also provides information about the extent of lateral positional correlations within the film, perpendicular to the PBLG rods. As mentioned already, the peak widths did not show any general trend with A or Π. The FWHM of the inter-helix d_1 peaks (i.e. for monolayers and the first layer of bilayers) ranged from $\Delta q_{xy} \sim 0.025$ to 0.06 Å^{-1} with an average of $\Delta q_{xy} \sim 0.04$ Å^{-1}, while the FWHM for the d_2 peaks (i.e. for the second layer of bilayers) ranged from $\Delta q_{xy} \sim 0.05$ to 0.1 Å^{-1} with an average of $\Delta q_{xy} \sim 0.075$ Å^{-1}. These observed widths are clearly greater than the experimental resolution of $\delta q_{xy} \sim 0.012$ Å^{-1}. Assuming that the FWHM of the peaks arise from the convolution of a Lorentzian experimental resolution and Lorentzian broadening due to a finite lateral correlation length $\xi_\perp$ perpendicular to the helical axes of aligned PBLG molecules, the following relation can be obtained:

$$\frac{\xi_\perp}{d} = \frac{q_0}{\pi[\Delta q_{xy} - \delta q_{xy}]}, \tag{3.11}$$

where the peak center is given by $q_0 = 2\pi/d$. Using Eq. (3.11), the correlation length $\xi_\perp$ can be estimated to be only on the order of 3 to 12 inter-helix distances for the PBLG rods in the monolayer and a few inter-helix distances for those within the second layer of bilayers. Therefore, despite the tendency of PBLG molecules to align with their near neighbors, their lateral *positional* correlations do not extend very far, implying only short-range order. This result indicates that after being spread on water, PBLG molecules aggregate into a 2D glassy phase with only local positional ordering. Moreover, the lack of any systematic variation in $\xi_\perp$ with A or Π suggests that the local order remains "frozen in" during subsequent compression.

One interesting observation is that the inter-helix correlation length $\xi_\perp$ is (and stays) comparable to the linear dimensions of the PBLG molecules used in this study (~100 Å). Although the above GID results do not provide any information about the extent of *orientational* correlations, this observation seems to suggest that a typical size of an aligned domain may be on the order of the molecular length in both directions (parallel and perpendicular to the rod axes). If a PBLG monolayer consists of many such small domains in random orientations, extensive smectic order is not likely to be present even within a monodisperse film. This is consistent with the absence of a smectic layering peak in the GID data.

The absence of smectic-like order in the monodisperse PBLG films studied here is probably due to the strong aggregation tendency of PBLG. In the bulk study of monodisperse PBLG by Yu *et al*., the use of a small amount of trifluoroacetic acid (TFA) in a chloroform solution seemed to play an important role in achieving smectic ordering, presumably by inhibiting the aggregation of PBLG molecules [61, 64]. On the other hand, in the present study of monodisperse LMs on water, the evaporation of spreading solvent (3%-TFA/97%-chloroform) is essentially instantaneous after film deposition. In a solvent-free environment, the formation of a 2D smectic phase (assuming it is possible) is likely to be suppressed by the local aggregation of PBLG molecules that results in glassy 2D domains.

Finally, in order to obtain additional evidence for the incommensurate structure of the PBLG bilayer, the q_z-dependence of the d_1 peaks was probed by rod scans. The Bragg-rods from the d_2 peaks could not be measured due to the lack of sufficient intensity. Fig. 3.11(a) and (b) show the background subtracted Bragg-rod data on the d_1 peak (taken at fixed $q_{xy} = 2\pi/d_1$) from Region II and IV, respectively. The lines in the figure are based on a model in which the electron density along the surface normal of a laterally correlated domain is simply approximated by a box of thickness l, and are described by

$$I_{rod}(q_z) \propto \left[\frac{\sin(q_z l/2)}{q_z l/2} \right]^2 . \qquad (3.12)$$

The comparison between the data and the model curves in Fig. 3.11 shows that whether the PBLG film is a monolayer or a bilayer, the part of laterally correlated domains with inter-helix distance d_1 is confined effectively to a thickness of $l = 8 \sim 10$ Å. This thickness is comparable to but slightly smaller than the total thickness of a PBLG monolayer observed by XR. Therefore, the rod-scan result implies that the d_1 inter-helix peak originates from a single layer even in the case of a bilayer. This conclusion is also consistent with the interpretations given earlier, namely that in Region IV, the d_1 peaks arise only from the bottom layer, and the lateral order is uncorrelated between the two layers of the bilayer.
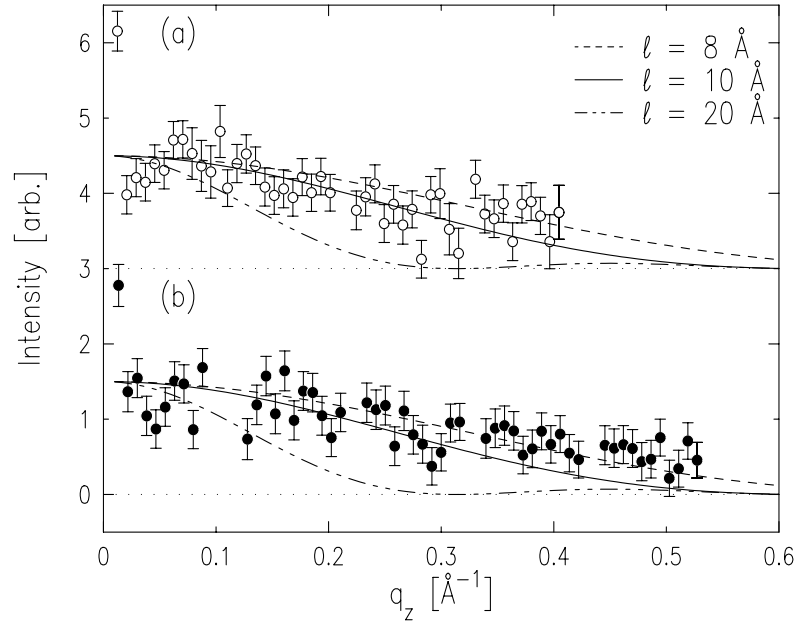
Figure 3.11: Bragg rod along q_z for the inter-helix GID peak at $q_{xy} = 2\pi/d_1$, measured on a monodisperse PBLG film at (a) $A = 19.2$ Å^2/monomer, $q_{xy} = 0.488$ Å^{-1} (O, Region II), and (b) $A = 10.5$ Å^2/monomer, $q_{xy} = 0.502$ Å^{-1} (●, Region IV). In each, the first data point near $q_z = 0$ corresponds to the surface enhancement peak (Yoneda peak) at $\beta = \alpha_c$. The lines are model Bragg rods given by Eq. (3.12) for $l = 8$ Å (---), 10 Å (—), and 20 Å (— -- —), where l is an effective "thickness" of the part of laterally correlated domains that gives rise to the GID peak.
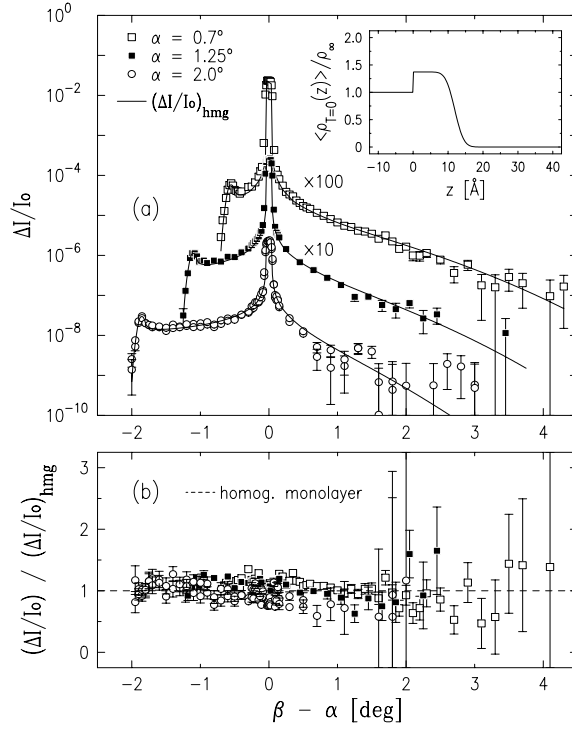
Figure 3.12: (a) β-scans at fixed α from a polydisperse PBLG monolayer at $(A, <\Pi>) = (19.2\ \text{Å}^2/\text{monomer}, 7.8\ \text{dyn/cm})$, shown as normalized intensity difference $\Delta I/I_0$ vs $\beta - \alpha$, where $\Delta I \equiv I(2\theta = 0) - (1/2)[I(+0.3°) + I(-0.3°)]$. The solid curves $[\Delta I(\alpha, \beta)/I_0]_{\text{hmg}}$ (——) theoretically expected for a *homogeneous* monolayer are based on Eq. (3.6), detector resolutions, and the average *local* electron density profile $<\rho_{T=0}(z)>/\rho_\infty$ shown in the inset. The profile $<\rho_{T=0}(z)>/\rho_\infty$ for this monolayer was obtained from a single-layer box model and the fitting of $[\Delta I(\beta = \alpha)/I_0]_{\text{hmg}}$ to the observed specular reflectivity $R(q_z)$, shown by the dashed curve (---) for B' in Fig. 3.5(b). (b) The ratio of the data $\Delta I/I_0$ to the solid line (——), i.e. calculated homogeneous contributions $[\Delta I/I_0]_{\text{hmg}}$, in (a). The ratio should be unity (---) for a homogeneous PBLG monolayer.

3.3.4 Small-angle off-specular diffuse scattering (XOSDS)

The results of β-scans on polydisperse PBLG films, taken at various fixed incident angles α, are summarized in Fig. 3.12(a) for a monolayer in Region II and in Fig. 3.13(a) for an incomplete bilayer in Region IV. These data are from monolayer B' and bilayer C', respectively, whose R/R_F data have already been shown in Fig. 3.5(b). In Figs. 3.12(a) and 3.13(a), the central peaks at $\beta - \alpha = 0$ correspond to specular reflection,

86

and the much smaller peaks at $\beta = \alpha_c$ on the left wings are the Yoneda or surface enhancement peaks, which originate from the Fresnel transmission factor $T_F(\beta)$.

The solid curves in Figs. 3.12(a) and 3.13(a) correspond to the calculated normalized intensity difference $[\Delta I(\alpha, \beta)/I_0]_{hmg}$ expected for *homogeneous* films. The calculation is based on the known temperature and surface tension of each PBLG film and the slit-defined resolution functions, as explained in Sec. 3.2.3. The layering structure factor $\Phi_0(q_z)$ for each film was obtained by using a box model for the average *local* density profile $<\rho_{T=0}(z)>$ and fitting $[\Delta I(\alpha, \beta = \alpha)/I_0]_{hmg}$ to the measured specular reflectivity $R(q_z)$. The best-fit R/R_F curves obtained from this fitting procedure are shown as dashed lines in Fig. 3.5(b). The corresponding intrinsic density profiles $<\rho_{T=0}(z)>$, shown in the insets of Figs. 3.12(a) and 3.13(a), are consistent with the total averages $<\rho(z)>$ obtained in Sec. 3.3.2. In both the fitting of $[\Delta I(\alpha, \beta = \alpha)/I_0]_{hmg}$ to $R(q_z)$ and the theoretical calculation of $[\Delta I(\alpha, \beta)/I_0]_{hmg}$ for β-scans, the smallest wavelength for the capillary wave modes was assumed to be of the order of the PBLG rod diameter $d \sim 12.6$ Å, and the upper cutoff wave vector value was taken to be $q_{max} \sim 2\pi/d = 0.5$ Å^{-1}.

As evident in Fig. 3.12(a), the agreement between the data $\Delta I(\alpha, \beta)/I_0$ and the theoretical curves $[\Delta I(\alpha, \beta)/I_0]_{hmg}$ is very good for the PBLG *monolayer* in Region II. The ratios between the data and the theory are close to unity, as shown in Fig. 3.12(b). Since the theory is based on the assumption that surface scattering originates only from the capillary wave fluctuations with intensity modified by the average local density profile $<\rho_{T=0}(z)>$, the good agreement implies that the monolayer is microscopically homogeneous. That is, (i) the height fluctuations of the water/monolayer and monolayer/gas interfaces are conformal with each other and consistent with the capillary wave model, and (ii) long wavelength density variations within the PBLG monolayer, if they exist, must be very small.

By contrast, Fig. 3.13(a) shows that the off-specular ($\beta - \alpha \neq 0$) parts of the data for the incomplete *bilayer* in Region IV are consistently higher than the theoretical
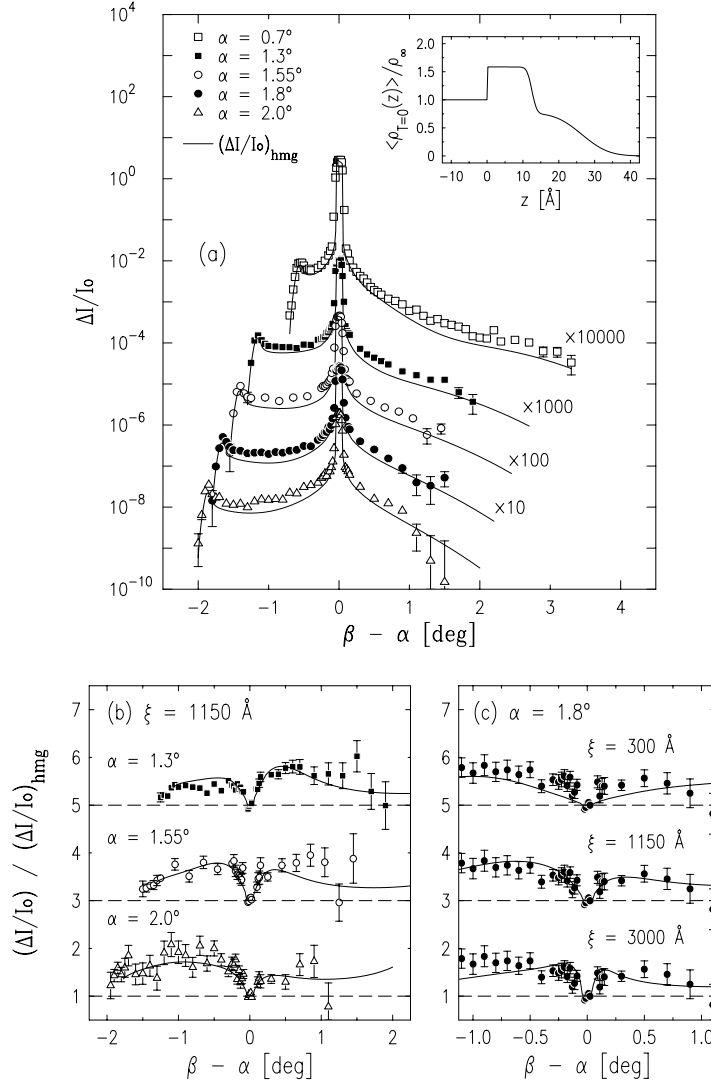
Figure 3.13: (a) β-scans at fixed α from a polydisperse PBLG bilayer at $(A, <\Pi>) = (9.7$ Å^2/monomer, 8.8 dyn/cm), shown as normalized intensity difference $\Delta I/I_0$ vs β - α. The solid curves $[\Delta I(\alpha, \beta)/I_0]_{hmg}$ (——) theoretically expected for a *homogeneous* bilayer are based on Eq. (3.6), detector resolutions, and the average *local* electron density profile $<\rho_{T=0}(z)>/\rho_\infty$ shown in the inset. The profile $<\rho_{T=0}(z)>/\rho_\infty$ for this bilayer was obtained from a double-layer box model and the fitting of $[\Delta I(\beta = \alpha)/I_0]_{hmg}$ to the observed specular reflectivity $R(q_z)$, shown by the dashed curve (---) for C' in Fig. 3.5(b). (b)-(c) The ratio of the data $\Delta I/I_0$ to the solid line (——), i.e. calculated homogeneous contributions $[\Delta I/I_0]_{hmg}$, in (a). The ratio would be unity (---) for a homogeneous PBLG bilayer. The solid lines (——) in (b) are fits based on an inhomogeneous model Eq. (3.16) with *noncapillary* fluctuations of second layer/gas interfacial heights and correspond to a roughness of $\sigma_2 = 2.2$ Å and a correlation length of $\xi = 1150$ Å along the interface. The solid lines (——) in (c) are the $\Delta I/I_0$ ratios calculated for three different values of ξ at $\alpha = 1.8°$ and $\sigma_2 = 2.2$ Å.

88

curves predicted for a homogeneous bilayer. Considering that the structure factor $\Phi_0(q_z)$ used in the homogeneous model is based on fits to the measured specular reflectivity, the agreement between data and model near the specular condition ($\beta - \alpha = 0$) is as expected. However, as clearly evident in Fig. 3.13(b) and (c), showing the same data normalized to the homogeneous model, the data exceeds the model by up to a factor of two in the off-specular regions. This additional scattering above the homogeneous prediction must originate from the term $\delta\rho_{T=0}(r_{xy}, z) \neq 0$ in Eq. (3.8). Therefore, the observation of off-specular *excess* scattering provides a measure of *non-capillary* lateral density inhomogeneities within the bilayer.

As already pointed out, the lower density in the second layer of the bilayer indicates that it is not densely packed, providing more room for (spatial) fluctuations in lateral density. The diffuseness of the second layer/gas interface evident in the average density profile for the bilayer (see the inset in Fig. 3.13(a)) is also suggestive of variations in the heights of that interface over the surface. These suggestions are supported further by the observation of relatively small differences (~ 10%) between the two inter-helix distances d_1 and d_2 in the GID despite the significant differences in average density in the two layers. Therefore, it is reasonable to assume that surface inhomogeneities with $\delta\rho_{T=0}(r_{xy}, z) \neq 0$ are mostly concentrated in the second layer of the PBLG bilayer. Given that the molecules in the second layer have been pushed out upward from the monolayer below, the origin of second layer inhomogeneities might be a distribution in the heights of molecular centers or in the orientation of the molecular axes, with some of them being not perfectly parallel to the interface. Another possibility would be molecular density variations within the second layer, with some regions of the second layer being more densely occupied than others. For example, such density variations would arise if the second layer consisted of microscopic islands on top of the first layer. It is difficult to distinguish between these possibilities from the obtained experimental data. Consequently, a quantitative analysis of the excess scattering has been carried out by

assuming a simple model in which the second layer inhomogeneities are represented as non-capillary height fluctuations of the second layer/gas interface.

The model assumes that the local electron density *within* the second layer is constant at $\rho_2 = \rho_\infty \cdot \phi_2$, but that the height $h_2(r_{xy}) + l_2 + l_1$ of the second layer/gas interface relative to the position of the monolayer/water interface fluctuates spatially about $<h_2(0)> = 0$ over the surface. Since the range of $(\beta - \alpha)$ in the measured β-scans is not large enough to probe correlations on the length scale of molecular anisotropies, it is convenient to assume that the variations in $h_2(r_{xy})$ are isotropic. Then, in the laboratory frame, the height variations of the second layer/gas interface can be described by the sum $\{h_{\mathrm{tot}}(r_{xy})\} = \{h(r_{xy})\} + \{h_2(r_{xy})\}$ of the capillary $\{h(r_{xy})\}$ and the non-capillary $\{h_2(r_{xy})\}$ height distributions. Assuming that $\{h(r_{xy})\}$ and $\{h_2(r_{xy})\}$ are statistically independent, the use of this model in Eq. (3.8) in the limit that the h_2-h_2 correlation function $c_2(r_{xy}) \equiv <h_2(r_{xy})h_2(0)> << 1/q_z^2$ leads to

$$\frac{1}{A_0}\left(\frac{d\sigma}{d\Omega}\right)_{inhmg} \approx \frac{1}{16\pi^2}\left(\frac{q_c}{2}\right)^4 \frac{\phi_2^2 e^{-\sigma_2^2 q_z^2}}{\sin(\alpha)}$$
$$\times \int d^2\mathbf{r}_{xy} e^{-i\mathbf{q}_{xy}\cdot\mathbf{r}_{xy}} e^{-\frac{1}{2}g(r_{xy})q_z^2} c_2(r_{xy})$$

(3.13)

where $\sigma_2^2 = <h_2^2(0)>$ is the mean-square roughness of the second layer/gas interface and $g(r_{xy}) = <[h(r_{xy}) - h(0)]^2>$. Using the convolution theorem and the proper normalization of the capillary wave spectrum [69, 70], Eq. (3.13) can be expressed as a convolution of the capillary (h) and non-capillary (h_2) height fluctuations in reciprocal space:

$$\frac{1}{A_0}\left(\frac{d\sigma}{d\Omega}\right)_{inhmg} \approx \frac{1}{16\pi^2}\left(\frac{q_c}{2}\right)^4 \frac{\phi_2^2 e^{-\sigma_2^2 q_z^2}}{\sin(\alpha)}$$

$$\times \frac{1}{(2\pi)^2} \int_{q'_{xy} \le q_{max}} d^2\mathbf{q}'_{xy} \frac{2\pi\eta}{q'^2_{xy}}\left(\frac{q'_{xy}}{q_{max}}\right)^\eta C_2\left(\mathbf{q}_{xy} - \mathbf{q}'_{xy}\right)$$

(3.14)

where $\eta = (k_B T/2\pi\gamma)q_z^2$ as in the homogeneous case, and $C_2(\mathbf{q}_{xy})$ is the 2D Fourier transform of $c_2(r_{xy})$. For computational simplicity, an exponentially decaying h_2-h_2 correlation function

$$c_2\left(r_{xy}\right) = \sigma_2^2 e^{-r_{xy}/\xi}$$

(3.15a)

is assumed with a correlation length ξ, such that

$$C_2\left(\mathbf{q}_{xy}\right) = \frac{2\pi\sigma_2^2\xi^2}{\left[1 + \xi^2\left|\mathbf{q}_{xy}\right|^2\right]^{3/2}}.$$

(3.15b)

With the substitution of (3.15b), Eq. (3.14) becomes

$$\frac{1}{A_0}\left(\frac{d\sigma}{d\Omega}\right)_{inhmg} \approx \frac{1}{16\pi^2}\left(\frac{q_c}{2}\right)^4 \frac{4\phi_2^2\sigma_2^2\xi^2 e^{-\sigma_2^2 q_z^2}}{q_{max}^\eta \sin(\alpha)} \int_0^{q_{max}^\eta} dt\, X\left(q'_{xy} = t^{1/\eta}\right),$$

(3.16a)

with $q_{xy} = \left|\mathbf{q}_{xy}\right|$, $q'_{xy} = \left|\mathbf{q}'_{xy}\right|$, and

$$X\left(q'_{xy}\right) = \frac{1}{\left[1 + \xi^2\left(q_{xy} - q'_{xy}\right)^2\right]\sqrt{1 + \xi^2\left(q_{xy} + q'_{xy}\right)^2}} E\left(\sqrt{\frac{4\xi^2 q_{xy}q'_{xy}}{1 + \xi^2\left(q_{xy} + q'_{xy}\right)^2}}\right),$$

(3.16b)

where $E(k)$ is the complete elliptic integral of the second kind. The q'_{xy}-integration in (3.16a) is done numerically.

In order to obtain a correlation length associated with second layer inhomogeneities, the numerical convolution of Eq. (3.16) with the experimental resolution function has been fit simultaneously to all of the measured *excess* scattering, $[\Delta I(\alpha, \beta)/I_0]_{inhmg} = \Delta I(\alpha, \beta)/I_0 - [\Delta I(\alpha, \beta)/I_0]_{hmg}$, observed from the PBLG bilayer at various sets of (α, β). Only σ_2 and ξ were allowed to vary in the fitting, while $q_{max} = 0.5$ Å^{-1} was used as in the homogeneous case, and the relative electron density in the second layer was fixed at the XR-based value of $\phi_2 = \rho_2/\rho_\infty = 0.80$. All the other parameters are known. The best fit is obtained with $\xi = 1150$ Å and $\sigma_2 = 2.2$ Å, where the range of errors determined by 67% confidence limits are 400 Å $< \xi < 3200$ Å and 1.7 Å $< \sigma_2 < 3.1$ Å. The normalized intensity ratios $[\Delta I(\alpha, \beta)/I_0]/[\Delta I(\alpha, \beta)/I_0]_{hmg}$ calculated from the best fit are plotted as solid curves in Fig. 3.13(b) at various incident angles α. The ratio is unity at $\beta = \alpha$ and increases above unity as β moves away from α. The inverse width of the "valley" centered at $\beta = \alpha$ is a measure of the correlation length ξ, as demonstrated in Fig. 3.13(c), in which the intensity ratios are plotted at $\alpha = 1.8°$ and $\sigma_2 = 2.2$ Å for three different values of ξ.

From the above analysis, one can estimate the correlation length associated with the second layer inhomogeneity to be on the order of $\xi \sim 1000$ Å, which is about 80 times the rod diameter or about 7-8 times the rod length of typical PBLG molecules. For example, if the inhomogeneity arose from second layer islands on top of the monolayer, this would imply a mean island (or hole) size of ~ 1000 Å. Since the obtained correlation length is one order of magnitude greater than the molecular size, and since there is no reason to expect a critical behavior in this system, it is unlikely that the origin of the inhomogeneity can be attributed to local or *intra*molecular density variations, such as random configurations of side chains of PBLG helices. The above analysis cannot distinguish between other plausible possibilities such as lateral variations in molecular height, orientation, or packing density over the second layer. However, it does clearly show that the observation of excess scattering from the PBLG bilayer in Region IV is

consistent with non-homogeneity of the newly formed second layer. This result is to be contrasted from the case of compressed PBLG monolayers in Region II, for which all of the long-wavelength surface fluctuations can be attributed to capillary waves.

3.4 Summary

The structures of both mono- and polydisperse PBLG Langmuir films on water have been studied using BAM and x-ray scattering techniques. The observed microscopic behavior showed no significant dependence on sample dispersity. In particular, no evidence was found for the presence of smectic layers in monodisperse films. On the basis of the results presented, the following summarizes a model for the structural changes that the PBLG LM undergoes with decreasing A:

(I) $A > \sim 21$ $\mathring{A}^2$/monomer: As soon as being spread on water surface, PBLG rods lie down flat on water surface, self-aggregate laterally, and align themselves parallel to their immediate neighbors to form solid-like 2D islands. Compression in this regime ($\Pi = 0$) only reduces areas of bare water surface coexisting with monolayer islands and results in no structural changes at the intermolecular level.

(II) $\sim 18.5 < A < \sim 21$ $\mathring{A}^2$/monomer: The PBLG monolayer homogeneously covers the entire surface. Compression in this regime results in both a steep rise in surface pressure and a reduction of the inter-helix distance between aligned PBLG rods from ~ 13.6 $\mathring{A}$ at $\Pi = 0$ to ~ 12.6 $\mathring{A}$ at $\Pi \sim 9$ dyn/cm. PBLG rods remain parallel to the interface during compression.

(III) $\sim 11.5 < A < \sim 18.5$ $\mathring{A}^2$/monomer: The PBLG monolayer can sustain surface pressures only up to a maximum of $\Pi \sim 9$ dyn/cm. Compression past this limit results in an upward transfer of PBLG molecules to a second layer. The bilayer formation is not uniform over the surface, but starts preferably near the moving barrier and grows in the compression direction. During compression through this coexistence region, the structure of the monolayer phase remains similar to that of a highly compressed monolayer in (II).

(IV) $A < \sim 11.5$ Å^2/monomer: The film is dominated by an incomplete, incommensurate, and inhomogeneous bilayer. There are sizable homogeneous fractions within the second layer, and these are less densely occupied than the close packed first layer. Within these fractions, the inter-helix distance is larger than that of the underlying monolayer but is comparable to that observed for uncompressed monolayer islands in (I). The fact that the monolayer d-spacing continues to decrease with increasing Π in this region, suggests that the presence of the second layer hinders a further upward transfer of PBLG molecules out of the first layer.

The analysis of inter-helix GID peaks shows that for both mono- and bilayers, the extent of lateral positional correlations between aligned PBLG rods is limited to a range of a few to no more than 15 inter-helix distances. This result on PBLG LM is one of the limited number of cases where a LM phase with only short-range positional order provided observable x-ray scattering. Moreover, it supports the recently made suggestion [27] that the increased scattering power provided by molecules with a large number of electrons might enable x-ray scattering studies of noncrystalline LM phases and phase transitions involving such phases.

One consequence of the use of large molecules, however, is stronger mutual attraction between them and hence their tendency to aggregate into a solid monolayer phase. Moreover, the results of this study suggest that if the solid LM phase formed is noncrystalline and involves large rod-like molecules, it tends to remain noncrystalline up to the highest surface pressure that can be sustained by the monolayer. This is probably because structural rearrangements required to transform the glassy phase into another 2D phase would include extensive molecular reorientations and are therefore more difficult to achieve with such large molecules confined in tightly packed spaces. One possibility for avoiding this type of aggregation behavior might be introduction of some repulsive forces between large molecules (e.g. through chemical modifications of side chains for helical polypeptides). If this can be achieved, x-ray scattering studies of 2D phase

transitions involving fluid LM phases may become possible. For α-helical polypeptides, the reduction of intermolecular attraction is an important next step that might facilitate monodispersity-induced smectic layering in LMs.

References for Chapter 3

[1] C. M. Knobler, *Adv. Chem. Phys.* **77,** 397 (1990).

[2] C. M. Knobler and R. C. Desai, *Annu. Rev. Phys. Chem.* **43,** 207 (1992).

[3] H. Möhwald, *Annu. Rev. Phys. Chem.* **41,** 441 (1990).

[4] J. Als-Nielsen and H. Möhwald, in *Handbook of Synchrotron Radiation*, Vol. 4, edited by S. Ebashi, E. Rubenstein and M. Koch (North Holland, Amsterdam, 1991), pp. 1.

[5] J. Als-Nielsen, D. Jacquemain, K. Kjaer, F. Leveiller, M. Lahav and L. Leiserowitz, *Phys. Rep.* **246,** 251 (1994).

[6] P. S. Pershan, *Structure of Liquid Crystal Phases* (World Scientific, Singapore, 1988).

[7] J. D. Brock, R. J. Birgeneau, J. D. Litster and A. Aharony, *Physics Today* **July,** 52 (1989).

[8] O. M. Magnussen, B. M. Ocko, M. Deutsch, M. J. Regan, P. S. Pershan, D. Abernathy, G. Grubel and J.-F. Legrand, *Nature* **384,** 250 (1996).

[9] M. Deutsch, O. M. Magnussen, B. M. Ocko, M. J. Regan and P. S. Pershan, in *Self-Assembled Monolayers of Thiols*, edited by A. Ulman (Academic Press, San Diego, 1998).

[10] B. R. Malcolm, *Nature* **195,** 901 (1962).

[11] B. R. Malcolm, *Polymer* **7,** 595 (1966).

[12] B. R. Malcolm, *Proc. Roy. Soc. A.* **305,** 363 (1968).

[13] G. I. Loeb, *J. Colloid Interface Sci.* **26,** 236 (1968).

[14] G. I. Loeb and R. E. Baier, *J. Colloid Interface Sci.* **27,** 38 (1968).

[15] B. R. Malcolm, *J. Polymer Sci.* **C 34,** 87 (1971).

[16] D. W. Goupil and F. C. Goodrich, *J. Colloid Interface Sci.* **62,** 142 (1977).

[17] D. G. Cornell, *J. Colloid Interface Sci.* **70,** 167 (1979).

[18] T. Takenaka, K. Harada and M. Matsumoto, *J. Colloid Interface Sci.* **73,** 569 (1980).

[19] G. Gabrielli, P. Baglioni and E. Ferroni, *J. Colloid Interface Sci.* **81,** 139 (1981).

[20] F. Takeda, M. Matsumoto, T. Takenaka and Y. Fujiyoshi, *J. Colloid Interface Sci.* **84,** 220 (1981).

[21] F. Takeda, M. Matsumoto, T. Takenaka, Y. Fujiyoshi and N. Uyeda, *J. Colloid Interface Sci.* **91,** 267 (1983).

[22] B. R. Malcolm, *J. Colloid Interface Sci.* **104,** 520 (1985).

[23] H. Motschmann, R. Reiter, R. Lawall, G. Duda, M. Stamm, G. Wegner and W. Knoll, *Langmuir* **7,** 2743 (1991).

[24] P. Lavigne, P. Tancrede, F. Lamarche and J.-J. Max, *Langmuir* **8,** 1988 (1992).

[25] P. Lavigne, P. Tancrede, F. Lamarche, M. Grandbois and C. Salesse, *Thin Solid Films* **242,** 229 (1994).

[26] D. Sohn, H. Yu, J. Nakamatsu, P. S. Russo and W. H. Daly, *J. Poly. Sci.* **B 34,** 3025 (1996).

[27] M. Fukuto, K. Penanen, R. K. Heilmann, P. S. Pershan and D. Vaknin, *J. Chem. Phys.* **107,** 5531 (1997).

[28] I. Uematsu, *Adv. Poly. Sci.* **59,** 37 (1984).

[29] J. Watanabe, Y. Fukuda, R. Gehani and I. Uematsu, *Macromolecules* **17,** 1004 (1984).

[30] J. Watanabe, H. Ono, I. Uematsu and A. Abe, *Macromolecules* **18,** 2141 (1985).

[31] J. Watanabe, M. Goto and T. Nagase, *Macromolecules* **20,** 298 (1987).

[32] E. Iizuka, K. Abe, K. Hanabusa and H. Shirai, in *Current Topics in Polymer Science*, Vol. I (Hanser, Munich, 1987), pp. 235.

[33] M. Ballauff, *Angew. Chem. Int. Ed. Engl.* **28,** 253 (1989).

[34]   G. Duda, A. J. Schouten, T. Arndt, G. Lieser, G. F. Schmidt, C. Bubeck and G. Wegner, *Thin Solid Films* **159,** 221 (1988).

[35]   S. Schwiegk, T. Vahlenkamp, G. Wegner and Y. Xu, *Thin Solid Films* **210/211,** 6 (1992).

[36]   S. Schwiegk, T. Vahlenkamp, Y. Xu and G. Wegner, *Macromolecules* **25,** 2513 (1992).

[37]   K. Mathauer, A. Schmidt, W. Knoll and G. Wegner, *Macromolecules* **28,** 1214 (1995).

[38]   W. Hickel, G. Duda, M. Jurich, T. Krohl, K. Rochford, G. I. Stegeman, J. D. Swalen, G. Wegner and W. Knoll, *Langmuir* **6,** 1403 (1990).

[39]   S. Lee, J. R. Dutcher, B. Hillebrands, G. I. Stegeman, W. Knoll, G. Duda, G. Wegner and F. Nizzoli, *Mat. Res. Soc. Symp. Proc.* **188,** 355 (1990).

[40]   F. Nizzoli, B. Hillebrands, S. Lee, G. I. Stegeman, G. Duda, G. Wegner and W. Knoll, *Mat. Sci. Eng. B* **5,** 173 (1990).

[41]   K. Mathauer, A. Mathy, C. Bubeck, G. Wegner, W. Hickel and U. Scheunemann, *Thin Solid Films* **210/211,** 449 (1992).

[42]   A. Mathy, K. Mathauer, G. Wegner and C. Bubeck, *Thin Solid Films* **215,** 98 (1992).

[43] H. Menzel, B. Weichart and M. L. Hallensleben, *Thin Solid Films* **223,** 181 (1993).

[44]   H. Menzel, M. L. Hallensleben, A. Schmidt, W. Knoll, T. Fischer and J. Stumpe, *Macromolecules* **26,** 3644 (1993).

[45] V. V. Tsukruk, M. D. Foster, D. H. Reneker, A. Schmidt and W. Knoll, *Langmuir* **9,** 3538 (1993).

[46] I. H. Musselman, D. L. Smith, E. P. Enriquez, V. F. Guarisco and E. T. Samulski, *J. Vac. Sci. Technol. A* **12,** 2523 (1994).

[47]   A. Schmidt, K. Mathauer, G. Reiter, M. D. Foster, M. Stamm, G. Wegner and W. Knoll, *Langmuir* **10,** 3820 (1994).

[48]   V. V. Tsukruk, M. D. Foster, D. H. Reneker, A. Schmidt, H. Wu and W. Knoll, *Macromolecules* **27,** 1274 (1994).

[49]   T. R. Vierheller, M. D. Foster, A. Schmidt, K. Mathauer, W. Knoll, G. Wegner, S. Satija and C. F. Majkrzak, *Macromolecules* **27,** 6893 (1994).

[50] G. Wegner and K. Mathauer, *Mat. Res. Soc. Symp. Proc.* **247,** 767 (1992).

[51] D. Neher, *Adv. Mater.* **7,** 691 (1995).

[52] C. Robinson, *Trans. Farad. Soc.* **52,** 571 (1956).

[53] C. Robinson and J. C. Ward, *Nature* **180,** 1183 (1957).

[54] C. Robinson, J. C. Ward and R. B. Beevers, *Disc. Faraday Soc.* **25,** 29 (1958).

[55] E. L. Wee and W. G. Miller, *J. Phys. Chem.* **75,** 1446 (1971).

[56] P. S. Russo and W. G. Miller, *Macromolecules* **16,** 1690 (1983).

[57] F. Livolant and Y. Bouligand, *J. Physique* **47,** 1813 (1986).

[58] A. Hill and A. M. Donald, *Liquid Crystals* **6,** 93 (1989).

[59] J. C. Horton, A. M. Donald and A. Hill, *Nature* **346,** 44 (1990).

[60] H. Block and C. P. Shaw, *Polymer* **33,** 2459 (1992).

[61] S. M. Yu, V. Conticello, G. Zhang, C. Kayser, M. J. Fournier, T. L. Mason and D. A. Tirrell, *Nature* **389,** 167 (1997).

[62] D. K. Schwartz, M. L. Schlossman and P. S. Pershan, *J. Chem. Phys.* **96,** 2356 (1992).

[63] W. J. Foster, M. C. Shih and P. S. Pershan, *J. Chem. Phys.* **105,** 3307 (1996).

[64] The use of small amounts of trifluoroacetic acid (TFA) in the spreading solvent was necessary to dissolve monodisperse PBLG in chloroform, while the polydisperse PBLG dissolves in pure chloroform. The use of either pure chloroform or TFA/chloroform mixture as the spreading solvent for polydisperse PBLG samples did not have any noticeable effects on any of the measurements presented here. Since TFA is volatile, we expect most of it to evaporate from the monolayer surface after the spreading of the film, together with chloroform.

[65] P. S. Pershan and J. Als-Nielsen, *Phys. Rev. Lett.* **52 ,** 759 (1984).

[66] S. K. Sinha, E. B. Sirota, S. Garoff and H. B. Stanley, *Phys. Rev. B* **38,** 2297 (1988).

[67] M. K. Sanyal, S. K. Sinha, K. G. Huang and B. M. Ocko, *Phys. Rev. Lett.* **66,** 628 (1991).

[68] J. Daillant, L. Bosio, B. Harzallah and J. J. Benattar, *J. Phys. II (France)* **1,** 149 (1991).

[69] M. Fukuto, R. K. Heilmann, P. S. Pershan, J. A. Griffiths, S. M. Yu and D. A. Tirrell, *Phys. Rev. Lett.* **81,** 3455 (1998).

[70] H. Tostmann, E. DiMasi, P. S. Pershan, B. M. Ocko, O. G. Shpyrko and M. Deutsch, *Phys. Rev. B* **59,** 783 (1999).

[71] When the singularity in $(d\sigma/d\Omega)_{hmg} \sim 1/q'^{2-\eta}_{xy}$ at $q'_{xy} = 0$ falls within the detector opening $\delta q_x \times \delta q_y$, the convolution of $1/q'^{2-\eta}_{xy}$ with the rectangular resolution function Ξ_q in Eq. (3.10b) can be done more conveniently by using the cylindrical coordinates (q'_{xy}, ϕ'), where $\tan(\phi') = q'_y/q'_x$. Since $\eta > 0$, the radial q'_{xy}-integration at fixed ϕ' analytically removes the singularity, and the azimuthal ϕ'-integrations can be done numerically.

[72] For example, Hickel et al. [Langmuir 6, 1403 (1990)] studied optical anisotropy in structurally ordered Langmuir Blodgett multilayer films formed by a different kind of α-helical polypeptide and found the refractive index parallel to molecular axes to be only about 1 to 1.5 % higher than the indices in the perpendicular directions.

[73] D. K. Schwartz, M. L. Schlossman, E. H. Kawamoto, G. J. Kellogg, P. S. Pershan and B. M. Ocko, *Phys. Rev. A* **41,** 5687 (1990).

[74] J. Daillant, L. Bosio, J. J. Benattar and J. Meunier, *Europhys. Lett.* **8,** 453 (1989).

[75] If the orientational correlation length were long and the illuminated sample area viewed by the detector were not large enough to contain many randomly oriented domains, a full powder average would not be achieved. In such a case, the diffraction condition would depend on the orientation of the sample relative to the incident beam (as in the case of single crystals) and variations in peak intensity would be observed upon rotation about the surface normal.

Chapter 4

Internal Segregation and Side Chain Ordering in Hairy-Rod Polypeptide Monolayers at the Gas/Water Interface

4.1 Introduction

α-helical polypeptides possessing long side chains are representative of polymers that are often described as "hairy rods" [1, 2]. The composite character of these molecules implies that they can display structural order at two levels, i.e., in the arrangements of their rigid rod-like cores and in the packing of side chains. This is partly responsible for the richness of phase behaviors exhibited by hairy-rod polypeptides in bulk. For example, in the case of poly(glutamate) derivatives with long alkyl side chains, temperature-dependent studies of their bulk properties revealed a variety of condensed phases, such as solid phases with different degrees of side-chain order, a cholesteric liquid crystal that can be induced thermotropically, and an isotropic liquid [3-7]. The thermotropic liquid crystalline behavior has been attributed to the melting of side chains, which act as a "solvent" for the rod-like cores [3-5].

Hairy-rod polypeptides can also be spread as a stable Langmuir monolayer (LM) at the water/vapor interface [8, 9], and furthermore many of such LMs can be deposited sequentially onto solid substrates to form Langmuir-Blodgett (LB) multilayer films. Over the last decade, LB films of hairy-rod poly(glutamate)s have attracted considerable interest because of their potential [1, 2, 10] for use in optical [11-13], optoelectronic [14-16] and sensor device applications [17, 18]. Many of the experiments done in this active field of research have been concerned with the microscopic structures of these LB films. One of the interesting findings that emerged from these studies is that as-deposited LB

multilayers often display a bilayer periodicity along the film normal [14-16, 19-23]. The common explanation for this observation is that in the LM state prior to LB deposition, hydrophobic side chains of hairy rods segregate at the film/air interface, resulting in a non-uniform density distribution normal to the monolayer. However, no direct measurements of the corresponding LM structures has been done yet to confirm this inference, albeit a very reasonable one.

This chapter describes a structural study of LMs formed by a hairy-rod polypeptide poly(γ-4-(n-hexadecyloxy)benzyl α,L-glutamate) (C16-O-PBLG; see Fig. 4.1). We first report the results of surface pressure (Π) vs. area/monomer (A) isotherm measurements at various temperatures. The microscopic structures of the C16-O-PBLG LM at room temperatures have been probed by *in-situ* x-ray specular reflectivity (XR) and grazing incidence diffraction (GID) measurements.

The C16-O-PBLG LM can be regarded as encompassing structural attributes of less complex LM systems whose microscopic structures have already been characterized by previous x-ray scattering studies. First of all, the present study is an extension of our recent work on LMs of poly(γ-benzyl L-glutamte) (PBLG) [24]. In that study, we showed that in the monolayer these rod-like PBLG molecules lie down parallel to the interface and align locally with their immediate neighbors, and also characterized the structural changes across the monolayer-bilayer transition. In the present study on C16-O-PBLG, we probe how the attachment of extra –O-C16 chains modifies the 2D arrangements of PBLG rods as well as how it affects the monolayer-bilayer transition.

Secondly, given that the packing of –O-C16 chains is a major issue concerning the LM structure of C16-O-PBLG, another type of LM systems of particular relevance are those formed by simple long-chain surfactants, such as fatty acids, alcohols, esters, and phospholipids [25-28]. The ordered phases of these latter systems have been shown to consist of two-dimensional (2D) packing of long alkyl chains that are tilted with respect to the surface normal at low surface pressure Π and become untilted at high Π. In

the case of fatty acid LMs, the structural details for each of the several 2D crystalline and liquid crystalline phases (at least eight in total) in the generalized Π-T phase diagram are now fairly well established [28]. In contrast to these LMs of "isolated" alkyl chains, the C16-O-PBLG LM provides an opportunity to study the 2D ordering of "constrained" alkyl chains at the water/gas interface. In particular, one of the principal aims of the present study is to elucidate how the lateral packing of –O-C16 chains is influenced by both the tethering to and the ordering of rod-like PBLG cores.

The rest of the chapter is organized as follows: Sec. 4.2 provides a brief description of experimental details. In Sec. 4.3, the experimental results from Π-A isotherm, XR, and GID measurements are presented and discussed. In Sec. 4.4, the main conclusions are summarized.

4.2 Experimental Details

4.2.1 Sample and Π-A isotherm measurements

Two different samples of poly(γ-4-(n-hexadecyloxy)benzyl α,L-glutamate) (C16-O-PBLG) molecules were used in this study: a polydisperse, high-MW sample [MW 149,000 (vis); DP 325 (vis), PDI 1.32] and a monodisperse, low-MW sample [MW 34,900; DP 76], which was synthesized by Yu *et al*. [7, 29] using the recombinant DNA method. Throughout this chapter, the polydisperse/high-MW and the monodisperse/low-MW samples are referred to as "PD325" and "MD76," respectively. Due to the α-helix conformation, the C16-O-PBLG molecule resembles a hairy rod structure consisting of a rigid rod-like PBLG core and the hexadecyloxy chains (abbreviated as -O-C16) emanating from it (one chain per monomer). Figs. 4.1(a) and 4.1(b) show the chemical structure of the monomer and a pictorial representation of a hairy rod, respectively. Based on the α-helix pitch of $L_1 = 1.5$ Å/monomer along the helical axis, the length of the rod is about $L = 115$ Å for the MD76 sample and on the order of $L \sim 500$ Å for the PD325 case.

(a)

(b)

(c)
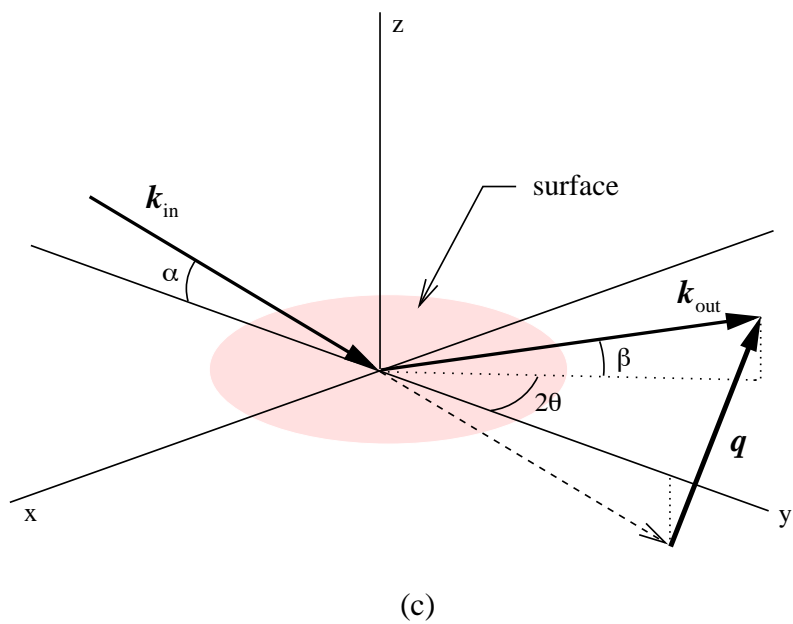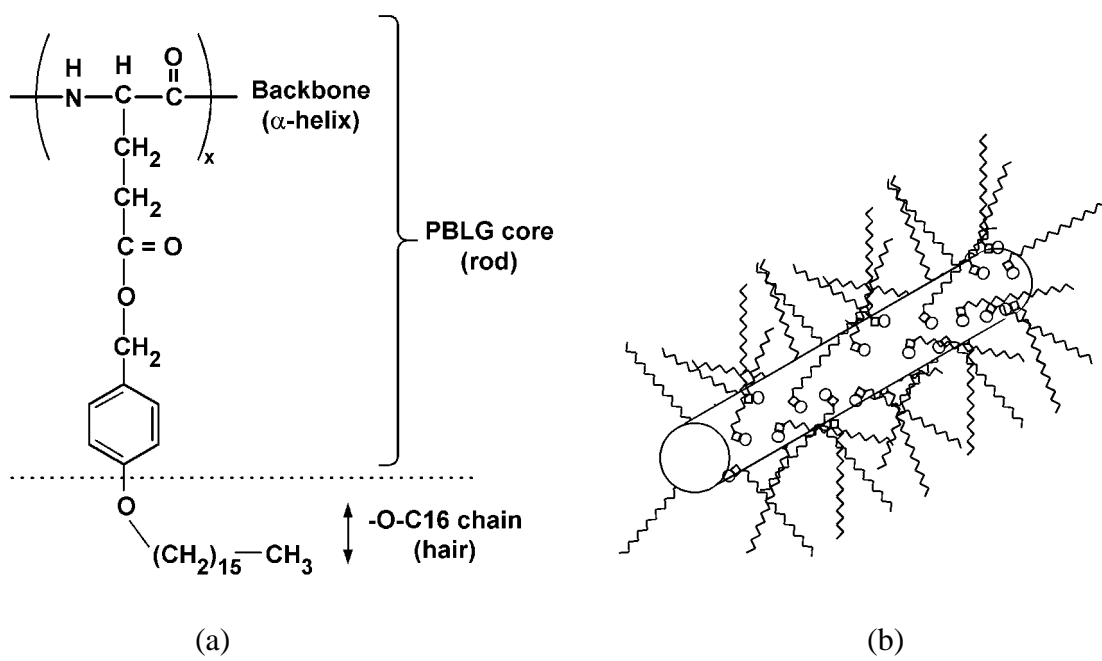
Figure 4.1: (a) Chemical structure of the C16-O-PBLG monomer. (b) A pictorial representation of a hairy rod. (c) X-ray scattering geometry.

Detailed descriptions of the Langmuir trough, the cleaning procedures, the temperature control and the film deposition method used have been given previously [30-32]. The entire trough assembly, including a Wilhelmy balance, is enclosed in a sealed aluminum box. For isotherm measurements, the box was filled with high purity N_2 gas. For x-ray measurements, it was filled with high purity He in order to minimize the background scattering. A Langmuir film of C16-O-PBLG was prepared by spreading a measured volume of chloroform solution of C16-O-PBLG on pure water surface (Milli-Q quality). Prior to spreading, the subphase was maintained at the temperature of interest for a period of 1 h or longer. The nominal concentration of the spreading solutions used ranged from 0.30 to 0.42 mg/mL, and typical volume spread ranged from 90 to 120 μL. In terms of area/monomer A, this corresponded to spreading each film at an initial area of $A > 40$ Å^2/monomer.

For all the isotherm results to be presented, the following stepwise continuous method was used for film compression. Surface pressure Π was measured 15 sec after the end of each compression step (typically, $\Delta A \sim 0.25$ Å^2/monomer per step), followed immediately by the next compression step. The barrier speed used in typical measurements corresponded to a compression rate of ~0.02 (Å^2/monomer)/sec. During x-ray experiments, the same stepwise continuous method was used for compression from one area of interest to the next, but after the target area/monomer was reached, the film was allowed to relax before measurement.

4.2.2 X-ray measurements

The x-ray experiments were carried out using the Harvard/BNL liquid surface spectrometer [30] at Beamline 22B at the National Synchrotron Light Source, with an x-ray wavelength of $\lambda = 1.55$ Å. The general scattering geometry illustrated in Fig. 4.1(c) defines scattering angles (α, β, and 2θ) and wave vectors. The surface lies in the *x-y* plane, and the plane of incidence defines the *y-z* plane ($2\theta = 0$). The wave vector transfer

q is defined to be the difference between the scattered and incident wave vectors: $\mathbf{q} = \mathbf{k}_{out} - \mathbf{k}_{in}$. The components along the surface normal (the z-axis) and parallel to the surface plane are given by $q_z = (2\pi/\lambda)[\sin(\alpha) + \sin(\beta)]$ and $q_{xy} = (2\pi/\lambda)[\cos^2(\alpha) + \cos^2(\beta) - 2\cos(\alpha)\cos(\beta)\cos(2\theta)]^{1/2}$, respectively. For all measurements, scattered signals were measured by a NaI scintillation detector. Between the sample and the detector, two sets of crossed Huber slits were placed, one set at $S_1 = 209$ mm after the sample center and the other (detector slits) at $S_2 = 677$ mm. In the following, the height and width of slit opening at S_i are indicated as (H_i, W_i).

X-ray specular reflectivity (XR). In XR, a fraction R of the incident x-ray intensity that is reflected specularly in the plane of incidence (i.e., $\beta = \alpha$ and $2\theta = 0$, or $q_{xy} = 0$) is measured as a function of the incident angle α or wave vector transfer $q_z = (4\pi/\lambda)\sin(\alpha)$. The specular reflectivity reported here is the difference between this signal at $2\theta = 0$ and the background intensities measured at 2θ offsets of $\pm 0.25°$. The detector resolutions were defined by the detector slit opening $(H_2, W_2) = (2.5$ mm, 3.0 mm$)$ at S_2 and corresponded to $\delta q_x = 0.018$ Å^{-1}, $\delta q_y = 0.00185 q_z$, and $\delta q_z = 0.015$ Å^{-1}.

Specular reflectivity originates from the variation in the average electron density profile $<\rho(z)>$ across the interface (averaged over appropriate coherence lengths in the x-y plane). For $q_z/q_c > 4 \sim 5$, with q_c denoting the critical wave vector for total reflection ($q_c = 0.0218$ Å^{-1} for pure water subphase), the reflectivity $R(q_z)$ from a macroscopically homogeneous surface is well described by the "master formula" approximation [33-35]:

$$\frac{R(q_z)}{R_F(q_z)} \cong \left| \int_{-\infty}^{+\infty} dz \frac{d}{dz} \left[\frac{\langle \rho(z) \rangle}{\rho_\infty} \right] e^{-iq_z z} \right|^2 \tag{4.1}$$

where ρ_∞ is the electron density in the bulk subphase ($\rho_\infty = 0.334$ electrons/Å^3 for water). $R_F(q_z)$ is the Fresnel reflectivity of an ideally flat and sharp subphase/gas interface, which is equal to $R_F(q_z) = 1$ for $q_z \leq q_c$ (total reflection) and decays algebraically as $R_F(q_z) \approx (q_c/2q_z)^4$ for $q_z \gg q_c$.

Grazing incidence diffraction (GID). In this geometry, the incident angle α is fixed below the critical angle α_c (at $\lambda = 1.55$ Å, $\alpha_c = 0.154°$ for water subphase), and scattered intensities are measured as a function of 2θ or q_{xy} [$\approx (4\pi/\lambda)\sin(\theta)$ for $\beta \sim 0$]. For $\alpha < \alpha_c$, the reflectivity is essentially total, with the only field below the interface being evanescent waves. As a result, diffuse scattering from the bulk subphase is largely suppressed. The existence of 2D order with a repeat distance d along the surface (e.g., a crystalline monolayer) would result in a peak at $q_{xy} = 2\pi/d$. By performing 2θ (or q_{xy}) scans near a GID peak at $q_{xy} \sim 2\pi/d$ but above the surface horizon (i.e., with finite $\beta > 0$ or $q_z > 0$), one can obtain information about how the 2D order responsible for the peak is correlated along the surface normal (i.e., the z-axis) [34].

The settings used to collect most of the GID data are as follows: The incident angle was fixed at $\alpha = 0.12°$, and the illuminated footprint on the surface extended over approximately $L_f \sim 50$ mm along the beam direction. The slit settings used are: (H_1, W_1) = (6.0 mm, 3.0 mm) at S_1 (all cases), (H_2, W_2) = (18.0 mm, 2.0 mm) at S_2 for $2\theta < \sim 10°$, and (H_2, W_2) = (18.0 mm, 3.0 mm) for $2\theta > \sim 10°$. The in-plane FWHM (full width at half maximum) resolution δq_{xy}, which depends on 2θ, L_f, and W_i, varied as $\delta q_{xy} \sim 0.070q_{xy}$ for 0.17 Å$^{-1} < q_{xy} < 0.37$ Å^{-1}. For $q_{xy} > q' = 0.37$ Å^{-1}, the resolution was limited by the fixed horizontal opening W_1 of the front slits and therefore was constant at $\delta q_{xy} \sim 0.026$ Å^{-1}, but only a fraction $\sim q'/q_{xy}$ of the illuminated path L_f contributed to the raw intensities observed by the detector. The relatively large vertical opening H_2 of the detector slits corresponded to the integration of scattered signals over $\Delta q_z \sim 0.11$ Å^{-1}.

Comments on radiation effects. At an early stage in the experiment, C16-O-PBLG films were found to be sensitive to x-rays when high incident intensities were used. With a full incident flux ($\sim 10^9$ cts/sec) striking the film-coated surface, time-dependent changes could be observed in the scattered intensities. In the case of GID, the use of high intensity beams resulted in a loss of diffraction peaks within an hour. Consequently, both the incident intensity and exposure time were reduced in the

subsequent measurements by using absorbers, small beam divergence, and reduced counting time. Moreover, during measurements at any given A, the surface was translated perpendicular to the incident beam (along the x-axis in Fig. 4.1(c)) from time to time to introduce a fresh spot into the beam for illumination. This also served to limit x-ray exposure on any given spot on the film surface. By performing frequent quick reflectivity scans, it was possible to verify that there were no significant radiation-induced changes in the reported film structure. The reduced incident intensity and counting time resulted in some loss of counting statistics in the scattering data; however, there was no other recourse.

4.3 Results and Discussion

4.3.1 Π-A isotherms

A series of Π-A isotherms measured at various temperatures are summarized in Fig. 4.2(a) for the PD325 films and in Fig. 4.2(b) for the MD76 films, respectively. Each curve corresponds to the first compression scan on an as-spread film. For $T = 22$ and 30 °C, at which many films were spread, isotherms obtained from separate films are presented together to demonstrate the reproducibility of the isotherms.

Prominent features in the C16-O-PBLG isotherms and their temperature dependence are qualitatively independent of the differences between the two samples. At large areas ($A > \sim 35$ Å^2/monomer), the surface pressure remains equal to zero. For $T \geq$ 22 °C, compression past $A \sim 35$ Å^2/monomer results in a characteristic "shoulder" or plateau-like feature at low surface pressure ($\Pi < \sim 5$ dyn/cm), in which an initial rise in Π to a few dyn/cm is followed by a kink and then a much slower increase in Π. At $T = 11$ °C, on the other hand, such a shoulder-like feature is absent. In all cases ($11 \leq T \leq 43$ °C), further compression above ~ 5 dyn/cm results in a steep rise in Π, which continues until the pressure exceeds a few tens of dyn/cm and the film collapses (indicated by the isotherms bending down at high Π). For each of the two samples, the low-Π part of the
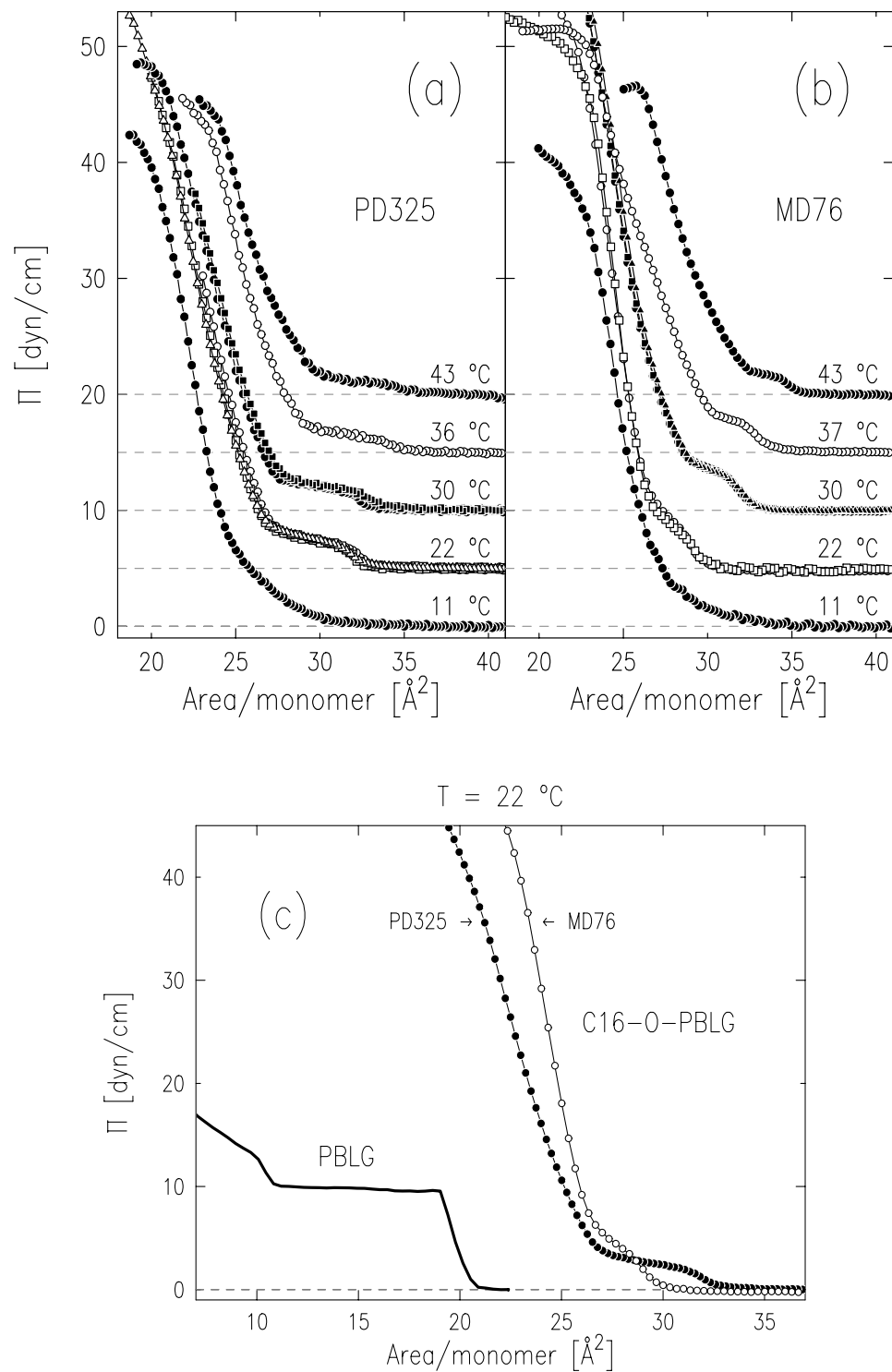
Figure 4.2: Π-*A* isotherms from C16-O-PBLG monolayers: (a) PD325 films and (b) MD76 films at various temperatures (shifted vertically for clarity). (c) Room-temperature comparison between PD325 and MD76 films of C16-PBLG and bare PBLG.

isotherms shift to larger areas as the temperature is raised, which suggests thermal expansion of C16-O-PBLG films.

In Fig. 4.2(c), the room-temperature isotherms (22 °C) of the two C16-O-PBLG samples are compared with that of bare PBLG. The PBLG isotherm exhibits a well-defined plateau at $\Pi \sim 9$ dyn/cm, which has been shown to be consistent with a first-order monolayer/bilayer transition [24]. The very different Π-A characteristics displayed by the C16-O-PBLG monolayers must be related to the presence of the additional alkyl chains (-O-C16).

Disregarding the shoulder feature at low Π for the moment, extrapolations of the low compressibility part (where Π increases sharply) of the isotherms down to the A-axis ($\Pi = 0$) yield $A_{lim} \sim 27$ Å^2/monomer for the two samples of C16-O-PBLG at 22 °C. This value of A_{lim} is clearly greater (by ~ 30 %) than $A_{lim} \sim 20.5$ Å^2/monomer for PBLG. It should be mentioned that the A_{lim} value for PBLG is quantitatively consistent with the microscopic structure of the PBLG monolayer, in which the rigid PBLG rods lie down flat on the water surface and are aligned parallel to their immediate neighbors [24]. The lateral inter-helix distance (perpendicular to the helical axis) in an uncompressed PBLG monolayer ($\Pi = 0$) has been shown to be $d = 13.6$ Å. This and the α-helix pitch of $L_1 = 1.5$ Å/monomer along the helical axis implies a microscopic area/monomer of $A = d \times L_1 = 20.4$ Å^2/monomer, which agrees with the A_{lim} estimated from the isotherm. Similarly, the x-ray results to be presented below indicate that the hairy rods C16-O-PBLG are also oriented parallel to the water surface and satisfy the relation $A = d \times L_1$ for $\Pi > \sim 5$ dyn/cm. Therefore, the greater value of A_{lim} for C16-O-PBLG can be interpreted as arising primarily from an increase in inter-helix distance between aligned rods.

More quantitatively, the ~ 30 % difference in A_{lim} between C16-O-PBLG and PBLG is equivalent to an increase in the inter-helix d-spacing by $\Delta d \sim 5$ Å. This difference which would correspond to the width of the gap between an adjacent pair of aligned PBLG cores in the C16-O-PBLG monolayer. Note that this width Δd is

considerably shorter than the length of the –O-C16 chain, which stretches out to 16 ×

1.27 Å = 20.3 Å in the all-*trans* conformation. It is however comparable to a typical

nearest-neighbor distance $a \sim 5$ Å found in the ordered monolayer phases of alkyl chains

[28, 36]. According to these considerations, the –O-C16 chains that are stuck between a

pair of aligned PBLG cores cannot be directed from one core toward the other, parallel to

the surface. Instead, it is more likely that such chains point away from the water surface,

an inference that is also consistent with their hydrophobicity.

Another important observation is that the C16-O-PBLG monolayers withstand

relatively high surface pressures, up to $\Pi > 40$ dyn/cm at 22 °C. This is to be contrasted

from the case of the PBLG monolayer, which collapses at $\Pi \sim 9$ dyn/cm to form a bilayer

(see Fig. 4.2(c)). The origin of the higher stability for C16-O-PBLG monolayers will be

illuminated by the x-ray results to be discussed in the following sections.

A unique feature of the C16-O-PBLG isotherms is the appearance of the small

shoulder-like plateau at low Π for $T \geq 22$ °C. Evidence that this is not an artifact but

originates from compression-induced changes in the internal structure of the monolayer,

is provided by the isotherm data shown in Figs. 4.3 and 4.4. The results of these two

different sets of measurements can be summarized as follows.

Figure 4.3 illustrates the reversibility of the C16-O-PBLG isotherms. The four

scans shown were obtained from a *single* film that underwent two compression/expansion

cycles at 22 °C. Compression was restricted to $\Pi \leq 25$ dyn/cm in order to avoid a

significant loss of material from the monolayer that can result from a collapse at high Π

(e.g., formation of 3D aggregates above or below the monolayer, deposition along the

trough edges and the barrier, etc.). It is clear from the overlaps between the first and

second compression/expansion scans that the isotherm is reversible as long as the

pressure remains well below the collapse point. Moreover, the expansion isotherms

consistently exhibit the same shoulder feature, although there is some hysteresis on the

large A side where $\Pi \sim 0$. The observation suggests that in the range of A over which this
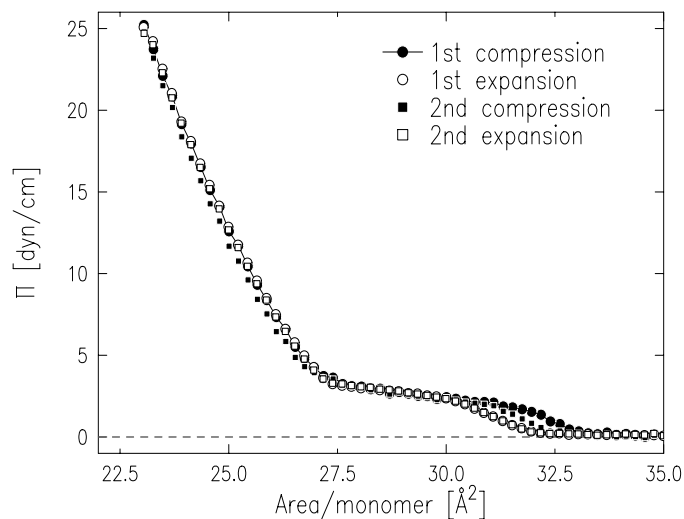
Figure 4.3: Compression/expansion isotherms taken on a C16-O-PBLG film (PD325) at 22 °C (*the same* film for all scans). The film was compressed only up to Π = 25 dyn/cm, and went through two compression/expansion cycles.
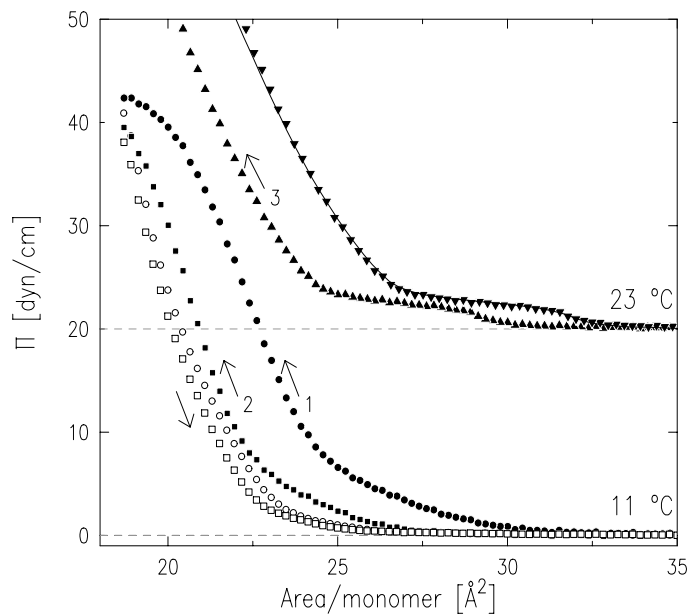
Figure 4.4: Compression (filled symbols) and expansion (open symbols) isotherms taken on a PD325 film. The first two cycles were measured at 11 °C. After the second expansion, the film was left undisturbed for 5 h at $A = 42$ Å^2/monomer while the temperature was raised to 22.7 °C. After a 9 % correction in area/monomer for material loss, the third compression scan (triangles) agrees with an isotherm on a fresh film at 22 °C. The isotherms at 22 °C have been shifted vertically for clarity.

111

plateau occurs, the surface does not contain bare water areas of macroscopic size. It is conceivable that for a very stiff film, the presence of macroscopic voids might still lead to a small but finite pressure upon compression; however, it seems unlikely that the same feature should appear in the expansion isotherm. These voids should vanish after the first compression and would not reproduce the width of the plateau between the first and second compression isotherms.

The temperature dependence of the shoulder feature, i.e., its presence for $T \geq 22$ °C and its absence at 11 °C, is demonstrated more convincingly in Fig. 4.4. The figure shows another set of isotherms obtained from *one* film. This film was first subjected to two cycles of compression/expansion at 11 °C, where the compression in each cycle was allowed to go beyond the collapse point. The isotherms shifted to smaller areas due to material loss, which is estimated to be ~ 8 % after the first compression (from the area shift between the first and second compression scans) and ~ 1 % after the second compression (from the shift between the first and second expansion scans). Apart from these shifts in A, all of these four scans show a monotonic behavior at low Π. After the second expansion, the film was left undisturbed at $A = 42$ Å^2/monomer for 5 h while the subphase temperature was raised and stabilized at 22.7 °C. The film was then compressed for the *third* time but now at 22.7 °C. The corresponding isotherm (up triangles in Fig. 4.4) now clearly exhibits the shoulder feature at low Π. Moreover, when this third scan is shifted horizontally to account for the total material loss of ~ 9 % due to the first two compressions (down triangles), it agrees very well with the scan on a fresh film at 22 °C (line).

Although the isotherms of the two C16-O-PBLG samples display qualitatively similar overall behaviors, there are quantitative differences between them. The most obvious of all is the difference in the width of the shoulder feature, which is wider for the PD325 sample by a factor of 2 to 3. The comparison shown in Fig. 4.2(c) also indicates that at 22 °C, the PD325 film is more compressible than the MD76 film at high Π ($> \sim 5$

dyn/cm). The question of how these discrepancies between the two samples are related to the differences in dispersity and the molecular size (DP or MW) cannot be answered here. Some of these issues as well as the origin of the shoulder feature are discussed further in the subsequent sections.

4.3.2 XR: Segregation within the monolayer

Representative XR data from C16-O-PBLG films are displayed in Fig. 4.5 in terms of the normalized reflectivity $R(q_z)/R_F(q_z)$. These data sets were obtained from the PD325 films at various stages of compression at $T = 22.5$ °C, and the corresponding positions along the isotherm are indicated on the right side of the figure. Very similar results have been obtained from the MD76 films at $T = 22.5$ °C and 30.9 °C (not shown). The figure clearly shows that the oscillation periods (in q_z) of the R/R_F curves shorten with increasing Π, which implies thickening of the film as a result of compression.

The extraction of the average electron density profiles across the water/C16-O-PBLG/gas interface has been carried out using a simple "n-box" model for $<\rho(z)>/\rho_\infty$ that is based on the combination of $n + 1$ error functions. A schematic representation for the most relevant case of $n = 2$ (the "2-box" model) is given in Fig. 4.6(a). In an n-box model, each of the n layers assumed between the water subphase ($\rho/\rho_\infty = 1$) and the vapor above ($\rho/\rho_\infty = 0$) is represented by a box of height $\phi_i = \rho_i/\rho_\infty$ and thickness $l_i = z_i - z_{i-1}$, and each of the $n + 1$ interfaces is then smeared out by a Gaussian roughness σ_i. In the analysis, theoretical R/R_F curves based on this model profile and Eq. (4.1) have been fit to the data in the range $q_z \geq 0.1$ Å^{-1} (i.e., $q_z/q_c \geq 4.5$).

For all the reflectivity data obtained from the C16-O-PBLG films, the use of the 2-box model with $\phi_1 > 1$ and $\phi_2 < 1$ (see Fig. 4.6(a)) is both necessary and sufficient to produce good fits. The analysis based on the 1-box model ($\phi_i = 0$ for $i \geq 2$) leads to fits whose visible discrepancies from the data are too large to be acceptable, indicating that the ability of the 2-box model to create a non-uniform density distribution across the film
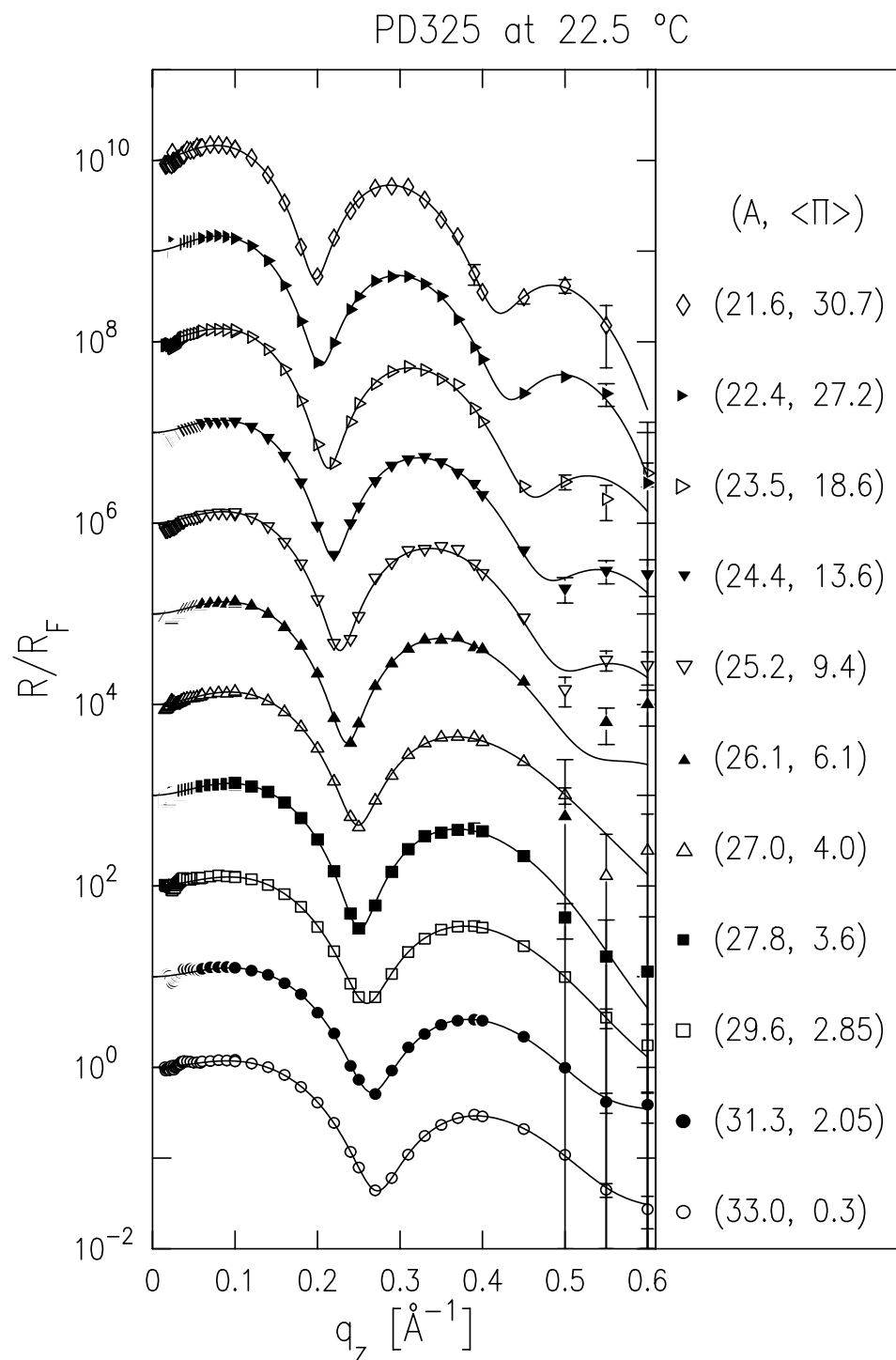
Figure 4.5: Specular reflectivity normalized to the Fresnel reflectivity, measured from C16-O-PBLG films (PD325) at 22.5 °C and at various area/monomer A or surface pressure Π (shifted vertically for clarity). The solid lines are the best-fit R/R_F curves based on a 2-box model for the average electron density profiles $<\rho(z)>$.
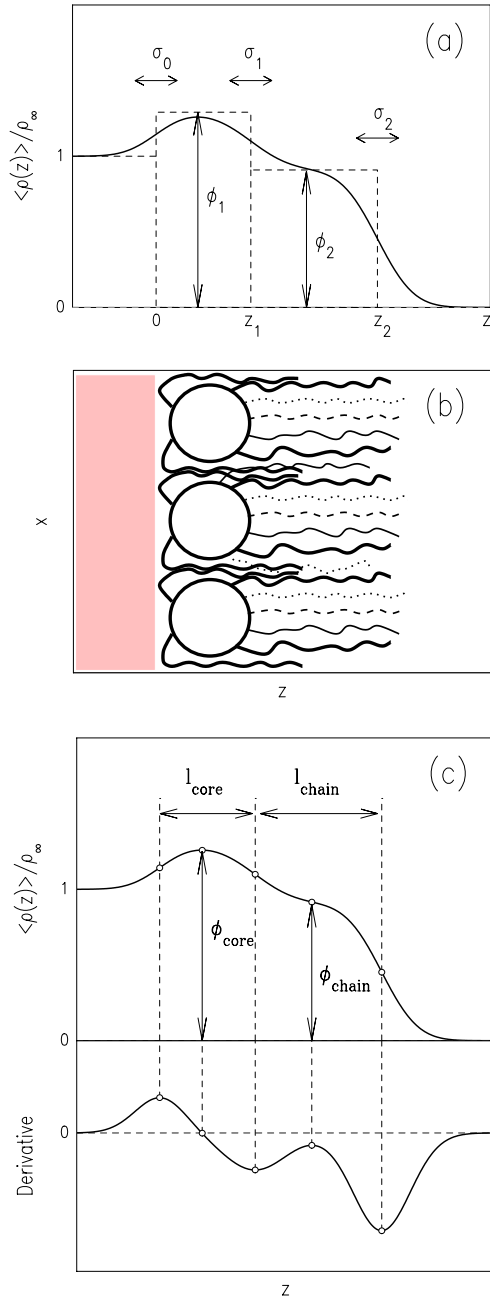
Figure 4.6: (a) 2-box model for average electron density profile $\langle\rho(z)\rangle$. The parameters shown in (a) are the fitting parameters that *define* the profile. (b) Pictorial representation (end-on view) of hairy rods sitting on the water surface. The –O-C16 chains prefer to stay away from water and PBLG cores lie parallel to and near the interface with water. (c) New parameters l_{core}, l_{chain}, ϕ_{core}, ϕ_{chain} that are derived from the density profiles. They are defined by the extremum points in the profile and the gradient, which is shown at the bottom.
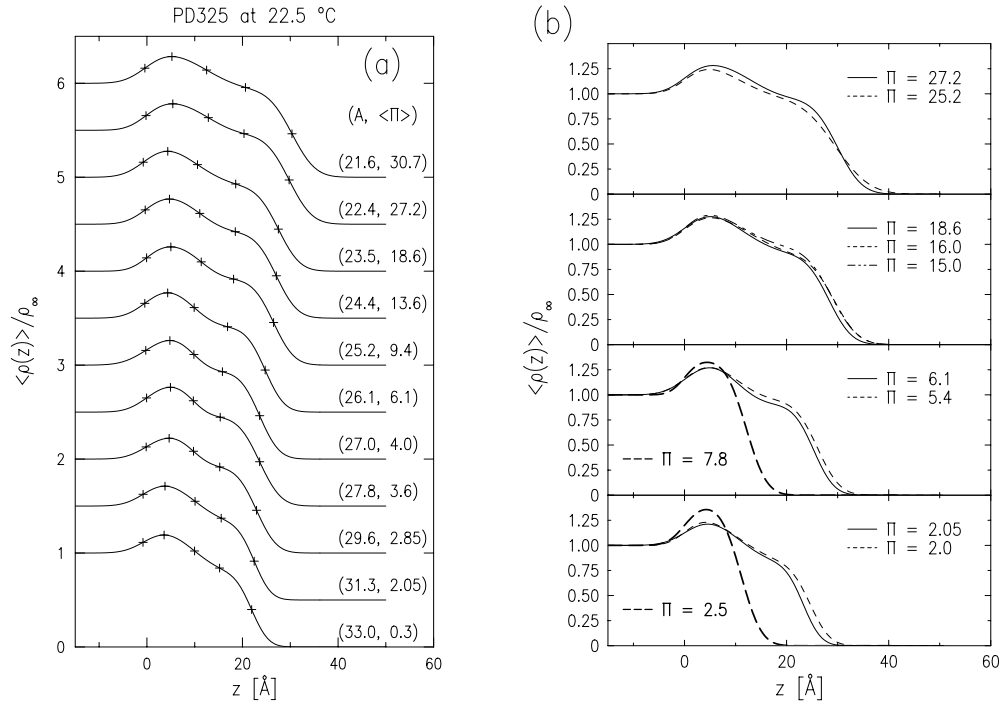
Figure 4.7: Average electron density profiles $\langle\rho(z)\rangle/\rho_\infty$ of the water/C16-O-PBLG/gas interface. They were extracted from the best fits to the R/R_F data and are based on the 2-box model. (a) PD325 films at various area/monomer and surface pressures (shifted vertically for clarity). (b) Comparisons between the profiles from PD325 films at 22.5 °C (solid lines) and MD76 films at 30.9 °C (short dashed lines) and at 22.5 °C (long-short dashed lines). The thick and long dashed lines are 1-box model profiles from bare PBLG monolayers.

is essential. On the other hand, a relatively small number of measurement points and large uncertainties in the R/R_F data at high q_z (see the comments on radiation effects in Sec. 4.2.2) prevent an independent determination of all the 2-box parameters if they are allowed to vary freely. Consequently, two kinds of constraints were used in the fitting. First, the thickness of the first layer, which will be later identified as a sub-layer dominated by PBLG cores (see Fig. 4.6(b)), was constrained as $z_1 = l_1 \geq 9.6$ Å on the basis of the smallest observed thickness of $l_1 = 10.6 \pm 1.0$ Å for PBLG monolayers [24]. Second, the lower bound on each roughness parameter (σ_1, σ_2, and σ_3) was set to be equal to the predicted capillary wave roughness σ_{cw}. The latter can be calculated from

Table 4.1: Typical range of parameters for the average electron density profile $\langle\rho(z)\rangle/\rho_\infty$ across the water/C16-O-PBLG/gas interface, determined by 67 % confidence limits (i.e., from the $\Delta\chi^2 = 1$ contour in the parameter space).

(a) 2-box fitting parameters.

	$\Pi = 2.05$ dyn/cm ($\chi^2_{min} = 0.81$)	$\Pi = 9.4$ dyn/cm ($\chi^2_{min} = 3.3$)	$\Pi = 30.7$ dyn/cm ($\chi^2_{min} = 0.75$)
z_1 [Å]	9.6* – 12.7	9.6* – 12.3	9.6* – 14.3
z_2 [Å]	22.4 – 24.1	25.6 – 27.0	29.5 – 30.4
ϕ_1	1.20 – 1.42	1.25 – 1.42	1.29 – 1.59
ϕ_2	0.72 – 0.97	0.84 – 0.96	0.85 – 0.97
σ_0 [Å]	2.54† – 3.8	2.68† – 3.9	3.30† – 4.6
σ_1 [Å]	2.54† – 7.2	2.68† – 6.2	4.0 – 9.4
σ_2 [Å]	2.54† – 3.7	3.0 – 3.8	3.5 – 4.2

* Lower bound on $z_1 = l_1$ constrained by the smallest thickness of $l_1 = 10.6 \pm 1.0$ Å observed for PBLG monolayers.

† Lower bound on σ_i constrained by the predicted capillary-wave roughness.

(b) Parameters derived from 2-box profiles.

	$\Pi = 2.05$ dyn/cm	$\Pi = 9.4$ dyn/cm	$\Pi = 30.7$ dyn/cm
l_{core} [Å]	9.7 – 12.8	10.6 – 12.3	12.0 – 14.4
l_{total} [Å]	22.8 – 24.1	26.1 – 27.0	30.4 – 31.2
l_{chain} [Å]	11.2 – 13.2	14.7 – 15.6	16.9 – 18.4
ϕ_{core}	1.195 – 1.218	1.247 – 1.263	1.273 – 1.288
ϕ_{chain}	0.834 – 0.961	0.882 – 0.953	0.937 – 0.976

(c) Comparison between the uncertainties of parameters in (a) and (b).
Note: For each parameter p, Δp = upper limit{p} – lower limit{p}.

Ratio	$\Pi = 2.05$ dyn/cm	$\Pi = 9.4$ dyn/cm	$\Pi = 30.7$ dyn/cm
$\Delta l_{core}/\Delta z_1$	1.0	0.63	0.50
$\Delta l_{total}/\Delta z_2$	0.74	0.60	0.49
$\Delta\phi_{core}/\Delta\phi_1$	0.11	0.094	0.050
$\Delta\phi_{chain}/\Delta\phi_2$	0.51	0.60	0.31

the surface tension $\gamma = \gamma_w - \Pi$ (γ_w for water), the relation $\sigma_{cw}^2 \propto T/\gamma$ [37], and $\sigma_{cw} = 2.50$ Å for a clean water surface at 22.5 °C, which was measured using the same experimental resolutions as for the films. This second constraint assumes that the density profile $<\rho(z)>/\rho_\infty$ cannot have features that are sharper than σ_{cw}.

The best-fit R/R_F curves based on the 2-box model are indicated by the solid lines in Fig. 4.5 and the corresponding profiles $<\rho(z)>/\rho_\infty$ are shown in Fig. 4.7(a) for the PD325 films. The range of the 2-box parameters determined from the $\Delta\chi^2 \sim 1$ contour in the parameter space (67% confidence limits) are listed in Table 4.1(a) for three representative films. In Fig. 4.7(b), comparisons are made between the profiles extracted for PD325 and MD76 films at comparable surface pressures. The bottom two panels in the figure also show the 1-box profiles obtained previously for the PBLG monolayer [24].

Figure 4.7 shows that for all the C16-O-PBLG films, the lower half of the film (immediately above the water/film interface) is clearly denser than the upper half. While the thickening of the film broadens the profile with increasing Π, the non-uniform and asymmetric density distribution across the film persists up to high Π. Fig. 4.7(b) shows that the width of the denser region is comparable to the thickness of PBLG monolayers. As depicted pictorially in Fig. 4.6(b), these observations suggest that the C16-O-PBLG monolayer is composed of the following two physically separate sub-layers: (i) a lower layer dominated by the rod-like PBLG cores (i.e., the helical backbone and part of the side chains closer to it) lying parallel to the interface, and (ii) an upper layer consisting primarily of the –O-C16 chains. This type of segregation at the sub-monolayer level is consistent with both the composite character of these hairy rod molecules and the hydrophobicity of the alkyl chains.

The validity of the above interpretation can be checked through quantitative examinations of sub-layer thicknesses and densities. For the representation of such sub-layer characteristics, an obvious choice would be to simply refer to the 2-box parameters used in the fitting, if it weren't for their relatively large uncertainties (especially for ϕ_1,

ϕ_2, and σ_2; see Table 4.1(a)). On the other hand, these uncertainties reflect not only the limitations of the R/R_F data but also the effects of correlations between the 2-box parameters. In fact, the density profiles obtained from different sets of parameters along the $\Delta\chi^2 \sim 1$ contour do not differ much from the best-fit profile. Therefore, as alternative (and more physically meaningful) measures of layer thicknesses and densities, it is useful to define parameters l_{core}, l_{chain}, l_{total} (= $l_{core} + l_{chain}$), ϕ_{core}, and ϕ_{chain} in terms of the extremum points in the actual profile $<\rho(z)>/\rho_\infty$ and its gradient, as shown in Fig. 4.6(c). Table 4.1(b) lists typical ranges of these parameters (derived from the profiles with $\Delta\chi^2 \sim 1$), and Table 4.1(c) demonstrates the narrower ranges of their uncertainties by comparing them with those of the corresponding 2-box parameters.

The layer thicknesses l_{core}, l_{chain}, and l_{total} and the sub-layer densities ϕ_{core} and ϕ_{chain} thus derived are plotted as a function of A in Fig. 4.8 and as a function of Π in Fig. 4.9. The quantity ρ_s in Fig. 4.8(a) represents the number of electrons per unit area belonging to the C16-O-PBLG molecules, which contain n_0 = 255 electrons/monomer. The experimentally derived estimates $\rho_s = \rho_\infty(\phi_{core} \cdot l_{core} + \phi_{chain} \cdot l_{chain})$ (triangles) and the theoretical curve $\rho_s = n_0/A$ expected for a laterally uniform, mono-molecular film (dashed curve) agree within ~10 % of each other, all the way up to $\Pi \sim 30$ dyn/cm. The good agreement indicates that the two sub-layers together account for nearly all of the C16-O-PBLG molecules on the surface. Moreover, it reinforces the validity of the underlying assumption that the C16-O-PBLG film is indeed a monolayer (as opposed to, say, a bilayer) and remains so up to high Π with little loss of material.

As already inferred from Fig. 4.7(b), the thickness l_{core} of the lower sub-layer (squares in Figs. 4.8(c) and 4.9(b)) compares well with the thickness $l_1 = 10.6 \sim 12.1$ Å observed for PBLG monolayers [24]. This is consistent with the rod-like PBLG cores of C16-O-PBLG that are oriented parallel to and concentrated near the water/film interface with a relatively narrow height distribution. The plausibility of the maximum density ϕ_{core} can be checked as follows. If the fraction A_{PBLG}/A of the area in the lower sub-layer
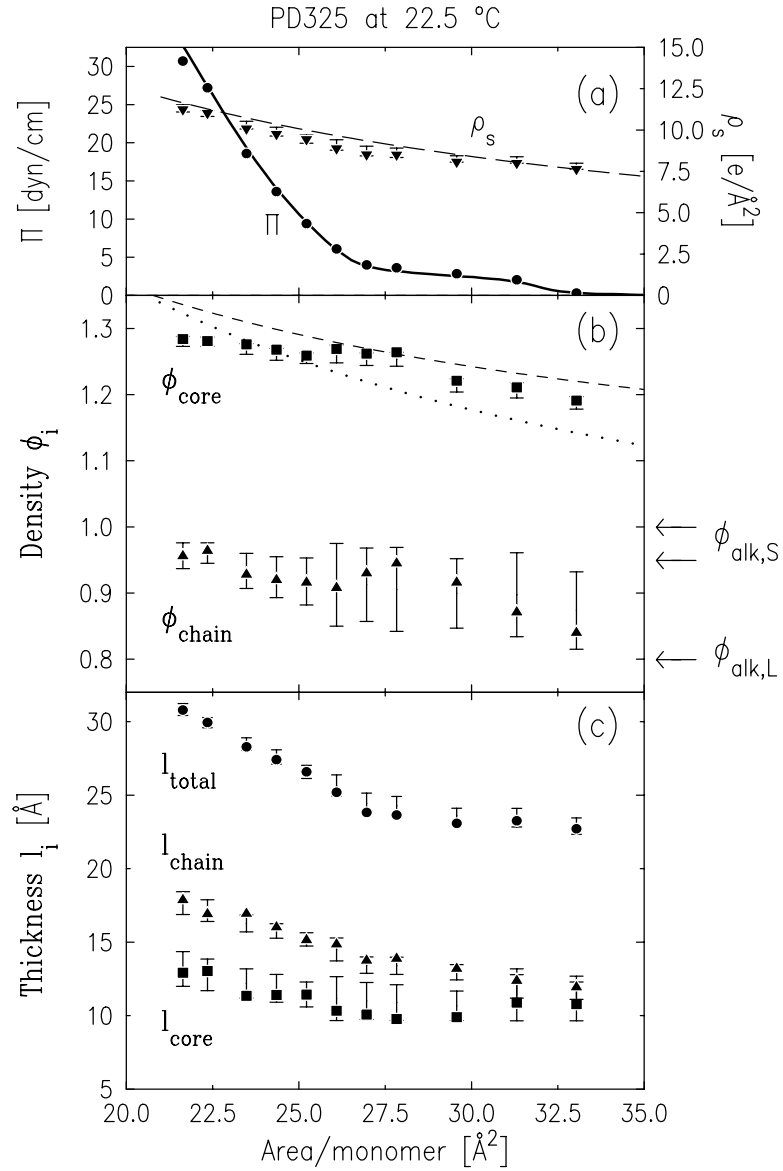
Figure 4.8: (a) The surface electron density from C16-O-PBLG molecules, (b) relative density parameters, and (c) thickness parameters derived from best-fit profiles as a function of area/monomer for PD325 film at 22.5 °C. In panel (a), the down triangles correspond to $\rho_s = \rho_\infty(\phi_{core}\cdot l_{core} + \phi_{chain}\cdot l_{chain})$ based on the extracted parameters, and the dashed line to the theoretical curve $\rho_s = n_0/A$. In panel (b), the dashed line corresponds to the upper limit $\phi_{core}{}^+$ in Eq. (4.2a) and the dotted line to the lower limit $\phi_{core}{}^-$ in Eq. (4.2b). The quantities $\phi_{alk,i} = \rho_{alk,i}/\rho_\infty$ indicated on the right stand for the electron density in a crystalline (i = S) or liquid (i = L) phase of alkyl chains normalized to that of water.
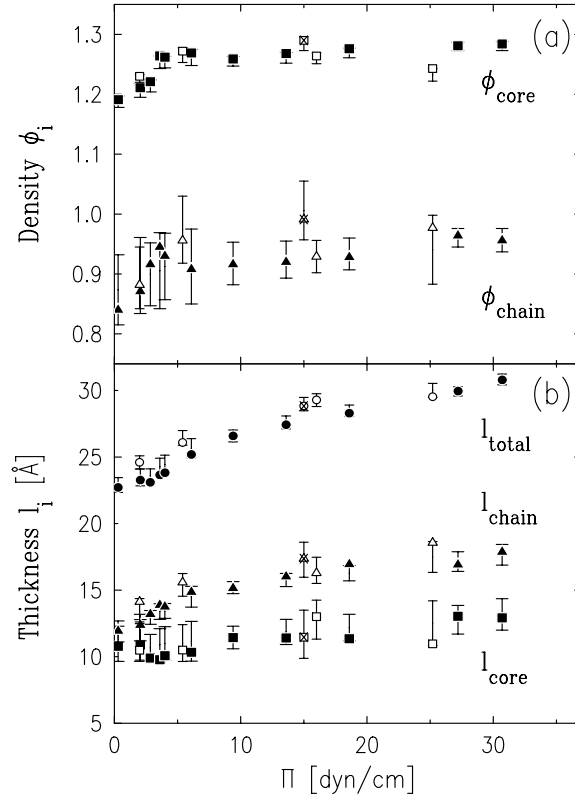
Figure 4.9: (a) The relative density parameters and (b) thickness parameters derived from best-fit profiles as a function of Π; PD325 films at 22.5 °C (filled symbols); MD76 films at 30.9 °C (open symbols) and 22.5 °C (crossed open symbol).

is attributed to the PBLG cores and the remaining fraction to alkyl chains, upper and lower bounds on ϕ_{core} can be estimated using

$$\phi_{core}^{+} = (A_{PBLG}/A)\phi_{PBLG} + (1 - A_{PBLG}/A)\phi_{alk,S}, \qquad (4.2a)$$

$$\phi_{core}^{-} = (A_{PBLG}/A)\phi_{PBLG} + (1 - A_{PBLG}/A)\phi_{alk,L}, \qquad (4.2b)$$

where A_{PBLG} and ϕ_{PBLG} represent the area/monomer and the maximum value of $<\rho(z)>/\rho_\infty$ for a close packed PBLG monolayer on water, respectively. The quantity $\phi_{alk,i} = \rho_{alk,i}/\rho_\infty$ stands for the electron density in a crystalline (i = S) or liquid (i = L) phase of alkyl chains normalized to that of water. The parameters for PBLG can be represented by

121

$A_{\text{PBLG}} = 20.2$ Å^2/monomer and $\phi_{\text{PBLG}} = 1.36$ observed at $\Pi = 2.5$ dyn/cm (see Fig. 4.7(b)).

As for $\phi_{\text{alk},i}$, the bulk liquid density of n-alkanes [36, 38] can be used to set $\phi_{\text{alk,L}} = 0.80$, while electron densities measured previously for ordered monolayer phases of simple surfactants [30, 33, 39-41] and for surface frozen and bulk rotator phases of n-alkanes [36, 38] lead to $\phi_{\text{alk,S}} = 0.95 \sim 1.0$. The bounds calculated using these values in Eq. (4.2) are indicated by the dashed curve (ϕ_{core}^+ with $\phi_{\text{alk,S}} = 1.0$) and the dotted curve ($\phi_{\text{core}}^-$) in Fig. 4.8(b). The fact that the experimentally derived values for ϕ_{core} (squares in Figs. 4.8(b) and 4.9(a)) fall between these two limiting curves at low Π provides additional evidence for the segregation of PBLG cores near the water/film interface. On the other hand, the fact that the values for the upper layer density ϕ_{chain} (triangles in Figs. 4.8(b) and 4.9(a)) fall within the range $\phi_{\text{alk,L}} = 0.80 < \phi_{\text{chain}} \leq \phi_{\text{alk,S}} \sim 1$ suggests that alkyl chains are the primary constituents of the upper sub-layer. This observation is consistent with the segregation of –O-C16 chains near the film/vapor interface.

Figures 4.8 and 4.9 show that the behaviors of the thicknesses and the densities seem to change around $A_{\text{lim}} \sim 27$ Å^2/monomer and $\Pi \sim 4$ dyn/cm. The "shoulder" region on the lower density side of this point ($A > A_{\text{lim}}$) is characterized by the little or no variations in any of the three thicknesses. In this constant thickness regime, the density ϕ_{core} of the lower sub-layer starts out (at $\Pi \sim 0$) being close to the midpoint between the two limiting curves $\phi_{\text{core}}^\pm$, increases gradually with compression, and becomes comparable to its upper bound ϕ_{core}^+ as the area reaches $A_{\text{lim}} \sim 27$ Å^2/monomer. Further compression to $A < A_{\text{lim}}$ and $\Pi > 5$ dyn/cm produces little further changes in ϕ_{core}, but it is now accompanied (together with the steep rise in Π) by film thickening characterized by a slight increase in l_{core} and more rapid increases in l_{chain} and l_{total}. These observations (together with $\phi_{\text{core}} \sim \phi_{\text{core}}^+$ at $A \sim A_{\text{lim}}$) suggest that at the limiting area A_{lim}, the lower sub-layer achieves the maximum packing configuration that is possible without deformation or vertical displacements of PBLG cores.

The behavior of the upper layer density ϕ_{chain} at low Π cannot be determined

unambiguously due to its relatively large uncertainties. Nevertheless, according to its best-fit values, ϕ_{chain} is closer to $\phi_{alk,L} = 0.80$ at $\Pi \sim 0$ and increases as the area is reduced to A_{lim}. This seems to indicate that at least on the low-density side of the "shoulder" region ($\Pi \leq \sim 2$ dyn/cm), the –O-C16 chains in the upper layer may be disordered. By contrast, the values for ϕ_{chain} on the high-density side ($A < A_{lim}$, $\Pi > 5$ dyn/cm) are comparable to $\phi_{alk,S} = 0.95 \sim 1.0$, suggesting more solid-like packing of these chains. The thickness of $l_{chain} \sim 18$ Å observed at the highest pressure probed ($\Pi \sim 30$ dyn/cm) would correspond to an average tilt angle of $\theta = \cos^{-1}(18/20.3) \sim 30°$ relative to the surface normal for fully extended –O-C16 chains if all of them were anchored on a single plane. Since this latter condition is clearly not satisfied in the present case, the above average value should only be viewed as an estimate for possible magnitudes. Given that the side chains are tethered to the helical backbones and some of the alkyl ends reside between PBLG cores in the lower layer, a relatively large distribution in local tilt angles is to be expected. The issues concerning the ordering of –O-C16 chains at high Π will be illuminated further by the GID results to be discussed in the following section.

4.3.3 GID: In-plane structures

The GID results reveal that two different types of structural order coexist within the C16-O-PBLG monolayers. One corresponds to lateral positional order arising from the alignments of rod-like PBLG cores, and the other originates from the packing of chain-like –O-C16 part of the side chains. These two types of in-plane order involve dissimilar intermolecular repeat distances and therefore manifest themselves in different regions of wavevector space. The principal results elucidating the inter-rod and inter-chain structures are presented separately below.

Inter-helix order.

GID intensities measured at relatively small lateral wavevectors q_{xy} and near the

surface horizon ($0 < q_z < 0.11$ Å^{-1}) exhibit a peak centered in the range $0.33 < q_{xy} < 0.45$ Å^{-1}. This is illustrated in Fig. 4.10, which shows a series of representative data collected from PD325 films under different degrees of compression at 22.5 °C. The presence of a peak is evident in each data set and indicates the existence of a laterally periodic structure within the C16-O-PBLG monolayers. As the film is compressed and the surface pressure rises, the center q_0 of the peak shifts to larger q_{xy}, implying a compression-induced decrease in the corresponding in-plane repeat distance $d = 2\pi/q_0$. The position q_0 has been determined by fitting a Lorentzian with constant and linear background terms to each GID pattern. The best fits are shown as the solid curves in Fig. 4.10. The d-spacing
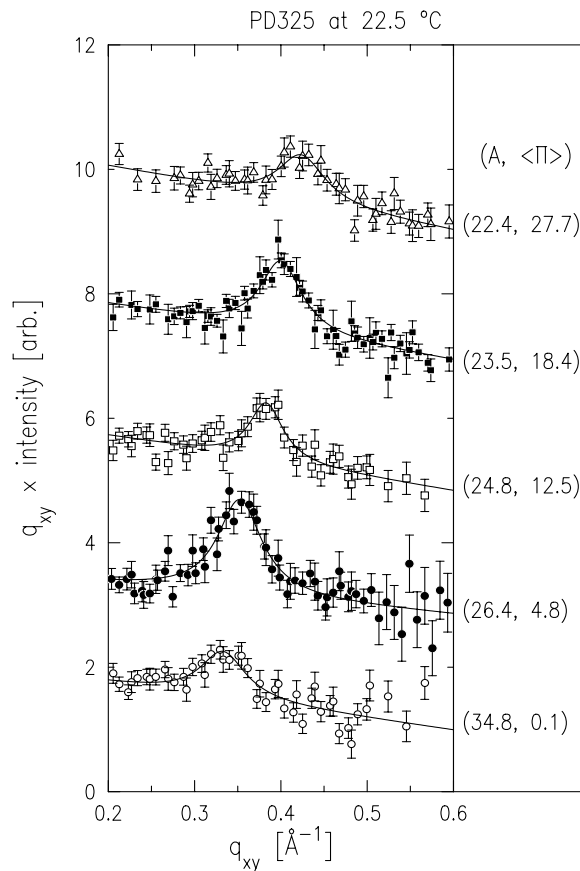
Figure 4.10: Inter-helix GID peaks from C16-O-PBLG monolayers (PD325) at 22.5 °C and various Π. The curves have been shifted vertically for clarity. The lines are Lorentzian fits.
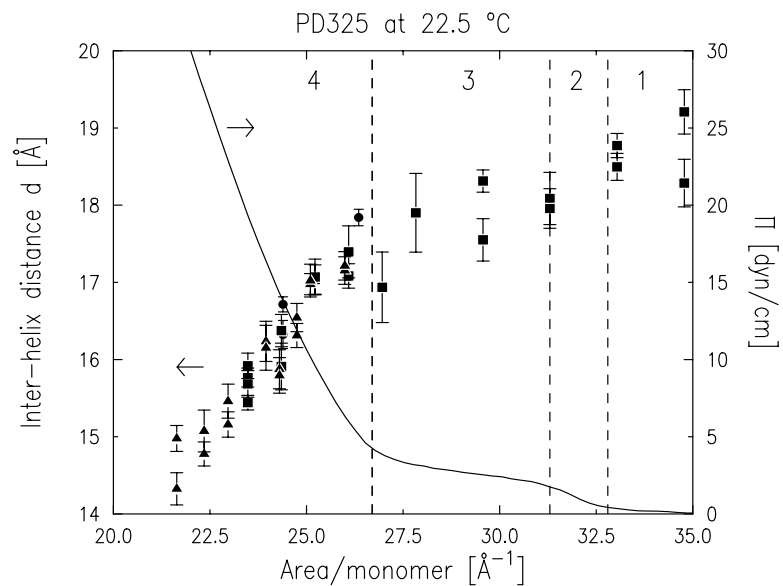
Figure 4.11: Inter-helix distance (symbols) and surface pressure Π (line) as a function of area/monomer A for C16-O-PBLG monolayers (PD325 films) at 22.5 °C. Vertical dashed lines divide the separate regions.
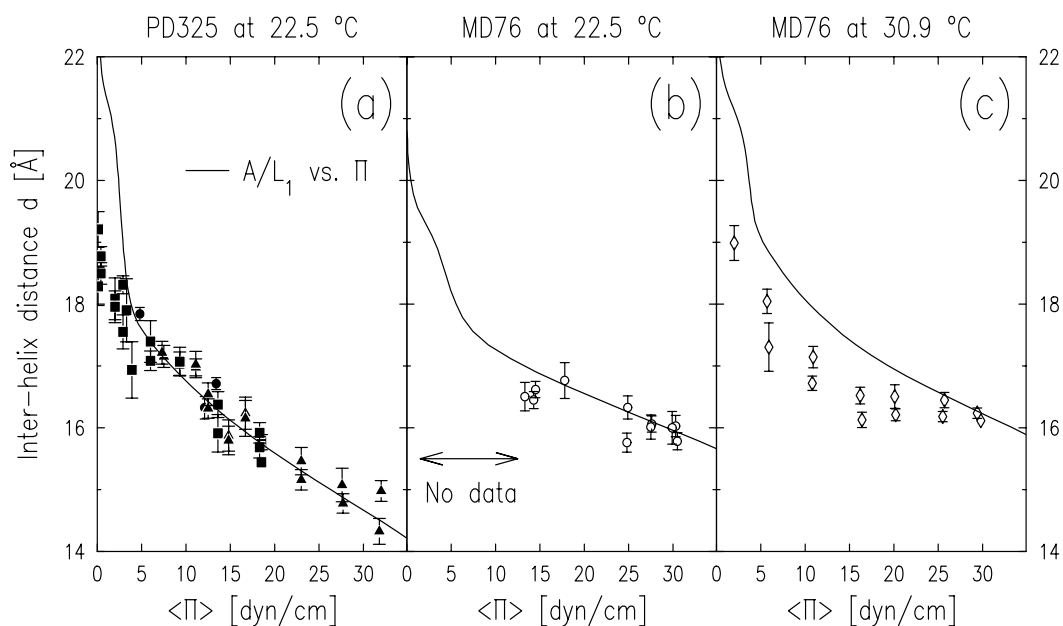
Figure 4.12: Inter-helix d-spacing vs. Π for C16-O-PBLG monolayers: (a) PD325 films at 22.5 °C, (b) MD76 films at 22.5 °C and (c) MD76 films at 30.9 °C. Each solid line is given by dividing the area from isotherm by the helical pitch $L_1 = 1.5$ Å/monomer along the helical axis.

$d = 2\pi/q_0$ is plotted as a function of A in Fig. 4.11 (PD325 films only) and as a function of Π in Fig. 4.12 (both PD325 and MD76 films), respectively.   The figures show that the d-spacing starts out around $d = 19$ Å at low Π and compression to $\Pi \sim 30$ dyn/cm reduces it to $d = 14.5$ Å for PD325 films and to $d = 16$ Å for MD76 films.

In the previous GID measurements on PBLG monolayers, a peak that resembles those shown in Fig. 4.10 was observed but at slightly larger q_{xy} [24]. The similarities with the results on PBLG suggest that the rod-like PBLG cores of C16-O-PBLG molecules are aligned parallel to their near neighbors within the lower sub-layer of the monolayer. According to this interpretation, the observed GID peak is associated with the lateral positional periodicity in the direction perpendicular to the aligned rod axes, and the d-spacing d can be identified with a nearest-neighbor inter-helix distance along the same direction. The main difference between bare PBLG and C16-O-PBLG is in the exact magnitude of the inter-helix distance. Over the range of Π in which the monolayer is stable, the d-spacing between PBLG rods has been found to vary from $d = 13.6$ Å at $\Pi = 0$ to $d = 12.6$ Å at $\Pi = 9$ dyn/cm [24]. Fig. 4.12 shows that over the same range of Π, the inter-helix distance between hairy rods C16-O-PBLG also decreases but remains greater than the values for PBLG by $\Delta d \sim 5$ Å. This extra d-spacing for C16-O-PBLG suggests that –O-C16 chains are present in the core-dominated lower sub-layer and are confined between pairs of aligned PBLG cores.

The widths of the GID peaks observed from C16-O-PBLG monolayers do not show any compression-dependent behavior. However, in all cases, the peak widths are broader than the resolution δq_{xy} (~ 0.026 Å^{-1}), and the FWHM values Δq_{xy} determined from the Lorentzian fits scatter in the range $\Delta q_{xy} = 0.04$ to 0.1 Å^{-1}. By identifying the inverse of the resolution-corrected half-width with a lateral correlation length [28, 33], i.e., $\xi_\perp = 2/[\Delta q_{xy} - \delta q_{xy}]$, the extent of the lateral positional correlations is estimated to be on the order of only $\xi_\perp/d = 2 \sim 10$ inter-helix distances, which implies short-range order. This estimate for $\xi_\perp/d$ is comparable to the values found for the PBLG monolayer [24].

The limited extent of $\xi_\perp$ and its apparent insensitivity to changes in Π suggest that C16-O-PBLG molecules form a 2D glassy phase consisting of many small, locally ordered domains, which remain "frozen in" up to high Π. Moreover, a sample rotation scan with the detector position fixed at the peak center shows no intensity variations; therefore, it is likely that such small domains are oriented randomly within the monolayer plane (i.e., a powder average).

Some insights on how the microscopic structure of the monolayer responds to macroscopic compression can be gained by examining the compression-dependent variations of the inter-helix distance. For that purpose, Fig. 4.11 makes a comparison between the Π-A and "d-A" isotherms for PD325 films at 22.5 °C. The figure is divided into four area/monomer regions (Region 1 through 4) to emphasize the different surface pressure behavior that can be seen in each region. The behavior of d can be summarized as follows:

In Region 1, in which $\Pi \sim 0$ throughout, the d-spacing can be considered, on average, to be roughly constant at $d = 18.5 \sim 19$ Å. This is consistent with a macroscopic coexistence of monolayer islands and bare water regions, just as in the case of the PBLG monolayer for $A > A_\text{lim}$ and $\Pi = 0$ [24]. The fact that an inter-helix GID peak is already observed in this region indicates a tendency of C16-O-PBLG rods to aggregate laterally and align themselves with neighboring rods immediately upon spreading, without external pressure.

For Region 2, the number of data points is too small to make any definite conclusions about a possible change in d. Nevertheless, the small initial rise in Π in this region appears to be accompanied by a slight decrease in the d-spacing to $d \sim 18$ Å. If this is a real effect of compression, it implies an actual microscopic compression of the C16-O-PBLG monolayer. This suggests that bare water areas of macroscopic sizes are probably absent at the onset of Region 2, as already inferred from the reversibility of the isotherm.

In Region 3, which is defined by the plateau in the Π-A isotherm, the d-spacing also exhibits a plateau-like behavior. It is interesting to note that the non-negligible change in surface area over this region ($A = 31.5 \rightarrow A_{\lim} \sim 27.0$ $\mathring{A}^2$/monomer, or $\Delta A/A \sim$ 15 %) leaves the inter-helix distance almost unaffected (constant at $d \sim 18$ $\mathring{A}$, within a scatter of $\delta d/d \sim 5$ %). Any physical model that attempts to explain the shoulder feature in the isotherm must be able to account for this apparent discrepancy as well.

In Region 4, decreasing area results in both a steep rise in Π and a significant decrease in the inter-helix distance. Therefore, unlike the behavior seen in Region 3, macroscopic film compression in Region 4 seems to lead directly to microscopic compression of aligned C16-O-PBLG rods within the locally ordered domains.

The relationship between macro- and microscopic compression is illuminated further by the d vs. Π plot shown in Fig. 4.12. Each of the "A/L_1 vs. Π" curves shown (solid lines) has been obtained by dividing the nominal area/monomer A in the isotherm by the α-helix pitch of $L_1 = 1.5$ $\mathring{A}$/monomer. These curves are based on the assumption that the total length L of a C16-O-PBLG rod consisting of n monomers is fixed at $L = n \times L_1$ at all times. Fig. 4.12(a) shows that for PD325 films at 22.5 °C, the observed d-spacing is described very well by the linear relation $d = A/L_1$ for $\Pi > \sim 5$ dyn/cm (i.e., in Region 4). Although the data is less complete for MD76 films, Fig. 4.12(b) and (c) show that the behavior $d = A/L_1$ also seems to hold for the MD76 films at high Π (≥ 15 dyn/cm at 22.5 °C and ≥ 25 dyn/cm at 30.9 °C). These observations imply that at high Π, close packing of ordered domains almost completely accounts for the entire surface coverage, and there is a direct correspondence between intermolecular and macroscopic compressions.

By contrast, Fig. 4.12(a) shows that for PD325 films at low Π ($< \sim 5$ dyn/cm), the observed d-spacing clearly deviates from the A/L_1 curve but simply extrapolates the high-Π behavior down to $\Pi = 0$. This deviation is equivalent to the discrepancy noted earlier between the magnitudes of variations in d and A across Region 3 (see Fig. 4.11). For the

MD76 film at 30.9 °C, a slight difference between d and A/L_1 ($> d$) seems to persist up to a pressure of $\Pi \sim 20$ dyn/cm, which is well above the values along the shoulder feature. These results indicate that a compression mode other than the reduction of inter-helix distance is operating at low Π.

One possible explanation for the observation $A/L_1 > d$ at low Π is that over the "shoulder" feature in the isotherm, the film-coated surface is still not homogeneous at the microscopic level. The behavior $d = A/L_1$ in Region 4 and the relatively narrow width of the shoulder feature ($\Delta A/A \sim 15$ % for PD325) suggest that even in Region 3, a substantial fraction of the surface is occupied by the locally ordered domains. The remaining fraction of the surface area may be due to microscopic holes within such a domain and/or small gaps where neighboring domains meet. Another plausible possibility is the presence of lower-density domains on the surface in which the rods are not perfectly aligned and therefore occupy, on average, a larger area/monomer than $A_{\lim} \sim$ 27 Å/monomer. This type of disorder might occur near the boundaries of ordered domains. According to these hypotheses, the compression across Region 3 would be accomplished by reducing microscopic areas that are either empty or disordered, while keeping the intermolecular spacing in ordered domains more or less intact. The GID results presented here cannot distinguish between these possibilities.

Finally, as far as the inter-helix order is concerned, the most prominent difference between the two samples of C16-O-PBLG monolayers appears to be in the inter-helix compressibility. The discrepancy between the slopes of their Π-A isotherms has already been emphasized in Fig. 4.2(c). Similarly, comparison between Fig. 4.12(a) and (b) shows that locally ordered domains formed within the MD76 film at 22.5 °C are less compressible than those in the PD325 film. Since both of these films display the behavior $d = A/L_1$ at high Π, it is clear that the apparent discrepancy between their macroscopic compressibilities arises directly from the difference in inter-helix compressibility. It is unclear how this effect depends on the differences in sample

dispersity and/or molecular size between the two samples. However, there is further evidence that the effect is also related to the extent to which the –O-C16 chains are ordered, which is part of the next subject to be discussed.

Side chain order.

The results of GID measurements at large q_{xy} (> 1 Å^{-1}) show evidence for lateral ordering of –O-C16 chains in the C16-O-PBLG monolayer. Fig. 4.13 illustrates typical GID scans near the surface plane ($0 < q_z < 0.11$ Å^{-1}) over the range of q_{xy} where the lowest-order peaks due to packing of alkyl chains are observed. In the figure, data collected at various stages of compression are shown separately for PD325 films at 22.5 °C and a MD76 film at 30.9 °C. Salient features in the GID patterns are independent of
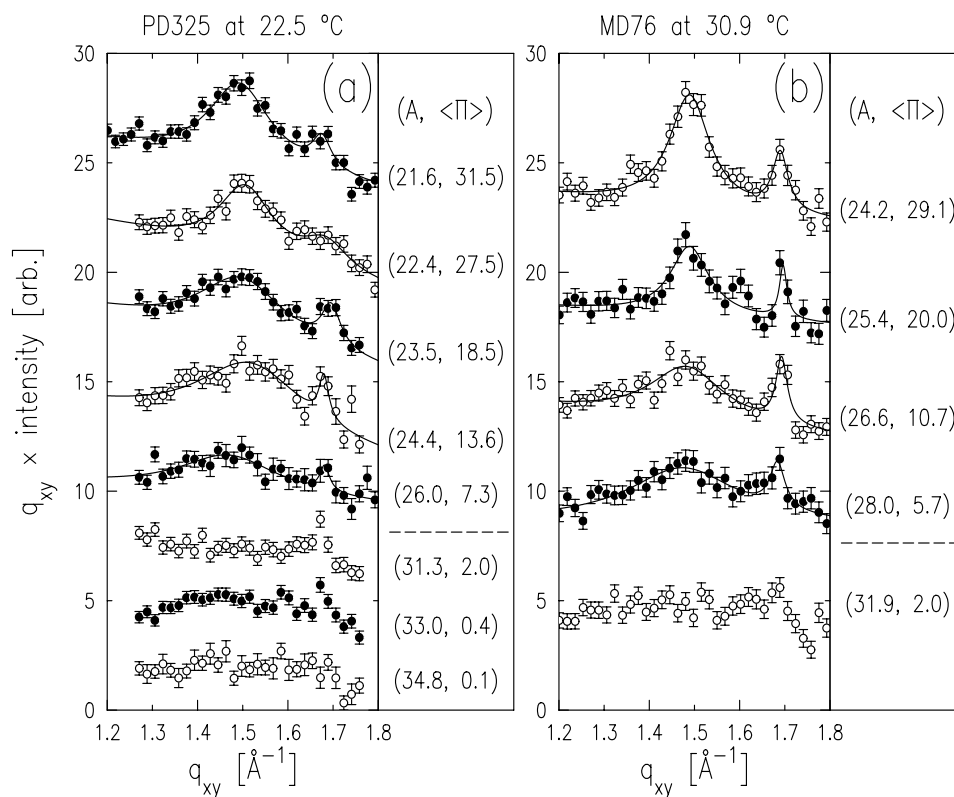
Figure 4.13: High-q_{xy} GID scans on C16-O-PBLG monolayers at various surface pressures Π: (a) PD325 films at 22.5 °C and (b) MD76 films at 30.9 °C. The curves have been shifted vertically for clarity.
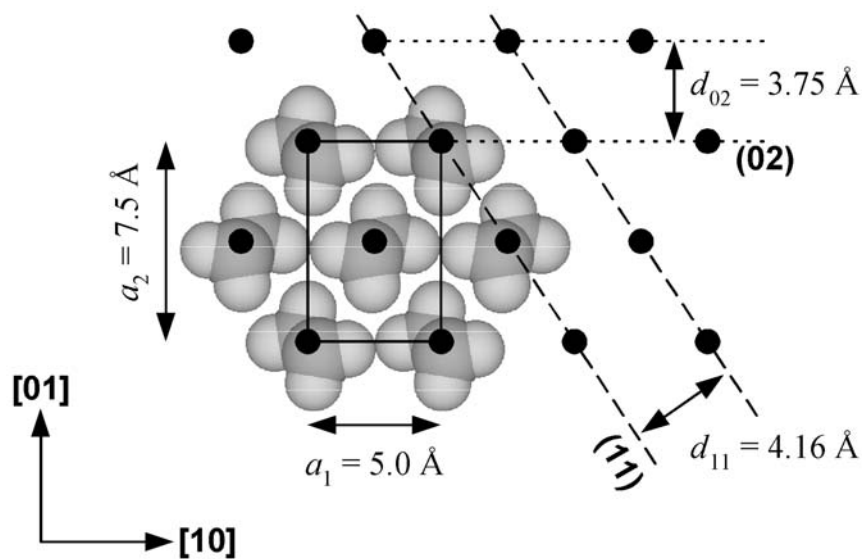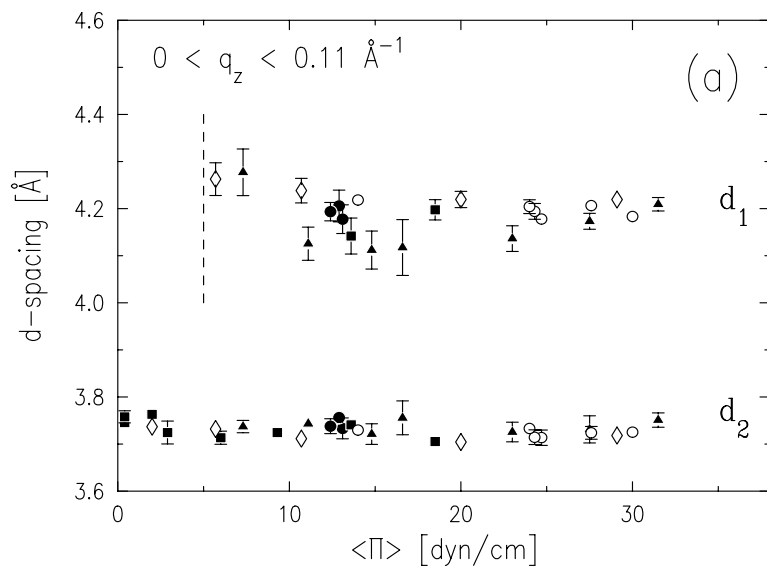
Figure 4.14: (a) The d-spacing $d_1 = 2\pi/q_1$ and $d_2 = 2\pi/q_2$ extracted from the GID measurements on C16-O-PBLG monolayers: PD325 films at 22.5 °C (filled symbols) and MD76 films at 22.5 °C (open circles) and at 30.9 °C (open diamonds). (b) End-on view of the herringbone (HB) packing arrangement of alkyl chains and the rectangular HB unit cell.

the differences between the two samples and can be summarized as follows. First, a relatively broad peak centered at $q_{xy} = q_1 \sim 1.5$ Å^{-1} appears at high Π ($> \sim 5$ dyn/cm). This "first peak" is present only on the high-density side of the shoulder feature in the isotherm and seems to grow with increasing Π. Second, another peak that is weak but often sharper than the other peak is observed at $q_{xy} = q_2 \sim 1.68$ Å^{-1}. This "second peak" seems to be always present, even at low Π where the isotherms exhibit the plateau-like behavior. In contrast to the inter-helix peak observed at smaller q_{xy}, these two peaks shift very little with varying Π. Qualitatively, these observations imply that compression increases the number of –O-C16 chains belonging to an *ordered* packing structure (yet to be determined) while leaving the inter-chain spacings in such a structure almost unaffected.

The observed GID patterns can be fitted fairly well by one or two Lorentzians with constant and linear background terms. The best fits to high-Π data containing the two peaks are indicated by the solid curves in Fig. 4.13. The extracted d-spacings $d_i = 2\pi/q_i$ are plotted as a function of Π in Fig. 4.14(a). The two d-spacings are nearly independent of Π and can be considered constant at $d_1 \sim 4.2$ Å and $d_2 \sim 3.75$ Å. The lack of data for d_1 below ~ 5 dyn/cm signifies the absence of the first peak at low Π.

The q_z dependence of the GID peaks has been probed by means of a series of q_{xy} scans at various detector heights $\langle q_z \rangle$ above the surface plane. The measurements of this type were restricted to films at high Π, for which the first peak at $q_{xy} = q_1$ is well pronounced. Representative data are shown in Fig. 4.15(a) for a MD76 film at $\Pi = 13.9$ dyn/cm and $T = 22.5$ °C. All available data for the positions ($q_{xy} = q_1$, $\langle q_z \rangle$) of the first peak are presented together as a reciprocal space plot in Fig. 4.15(b), where the vertical error bars for q_z represent the fixed vertical detector acceptance $\Delta q_z = 0.11$ Å^{-1}. The results show that with increasing q_z, the first peak at $q_{xy} = q_1$ (~ 1.5 Å^{-1} at $q_z \sim 0$) continually shifts to smaller q_{xy} while its magnitude changes little. Up to the largest q_z value of $\langle q_z \rangle_{max} \sim 0.64$ Å^{-1} (close to the experimentally accessible limit), the shift in the
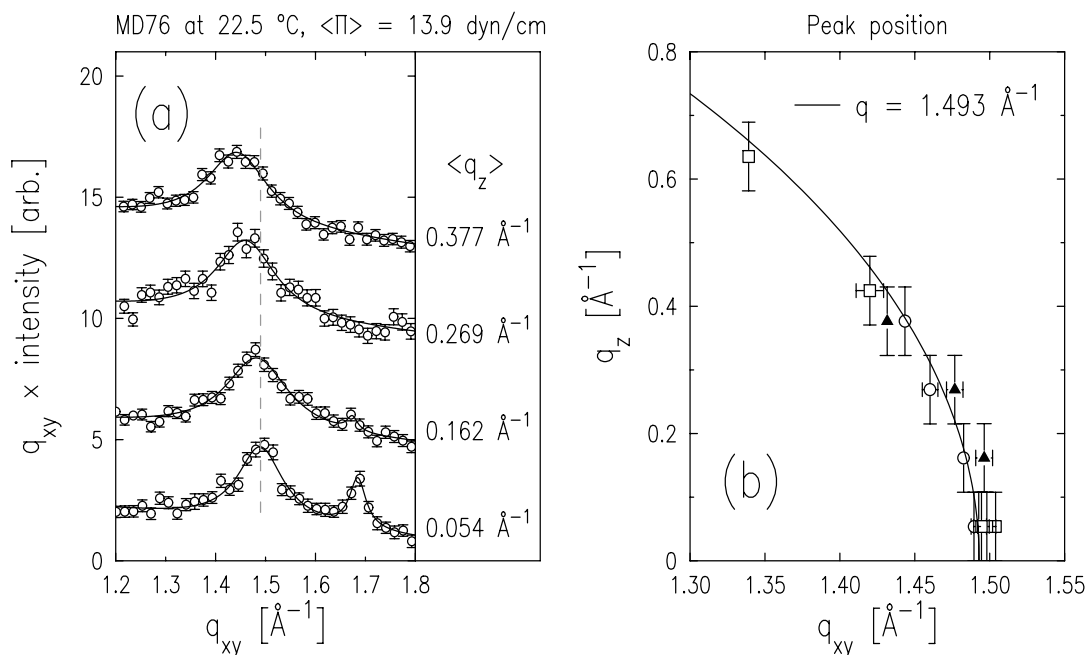
Figure 4.15: (a) q_{xy} scans at various height $<q_z>$ above the surface (vertically shifted for clarity) measured on a MD76 film at 22.5 °C and Π = 13.9 dyn/cm. (b) Peak positions in reciprocal space: MD76 films at 13.9 dyn/cm (open circles) and at 24.0 dyn/cm (open squares), and a PD325 film at 31.3 dyn/cm (filled triangles), all at 22.5 °C.

peak center roughly follows a circle of constant $q \sim 1.5$ Å^{-1} (solid curve in Fig. 4.15(b)), where $q^2 = q_{xy}^2 + q_z^2$. This behavior of the first peak is indicative of a range of tilts for the orientations of –O-C16 chain axes relative to the surface normal, as discussed further below.

By contrast, the second peak at $q_{xy} = q_2 \sim 1.68$ Å^{-1} is centered at $q_z = 0$, diminishes rapidly with increasing q_z and disappears almost completely for $<q_z> \geq 0.2$ Å^{-1}. A quantitative characterization of the intensity falloff along q_z is hindered by a combination of the use of relatively wide acceptance Δq_z, the nevertheless small magnitude of this peak, and a background due to the tail of the first peak. However, some estimates can be made on possible forms of this falloff. For example, suppose that vertical (or "untilted") straight chains of length l were to form a monolayer with no

distribution in their heights h (i.e., $<h^2> = 0$). Then the intensity distribution along a Bragg rod would be described by the form $S_{rod}(q_z) = T_F(\beta) \, [\sin(q_z l/2)/(q_z l/2)]^2$, where $T_F(\beta)$ is the Fresnel transmission factor of an ideally flat and sharp water/vapor interface as a function of the output angle β [30]. The intensity $I_{rod}(<q_z>)$ actually observed is equal to the integration of $S_{rod}(q_z)$ over $|q_z - <q_z>| \leq \Delta q_z/2$. Using $l = 20.3$ Å for the all-*trans* length of –O-C16, one would expect the ratio $I(<q_z>)/I(0.054 \text{ Å}^{-1})$ to be only 20 % at $<q_z> = 0.2$ Å^{-1} and much less for higher $<q_z>$. If $<h^2> \neq 0$, as is most likely to be the case for –O-C16 chains, the falloff along q_z would be even faster since $S_{rod}(q_z)$ would acquire a multiplicative Debye-Waller-like factor $\exp(-<h^2>q_z^2)$ in that case. These estimates show that the absence of a measurable peak intensity above $<q_z> \sim 0.2$ Å^{-1} is roughly consistent with the length of the –O-C16 chain.

Having established the peak positions in the reciprocal space, possible packing structures of –O-C16 chains can now be considered. The observation of the second peak centered at $q_{xy} = q_2 \sim 1.68$ Å^{-1} and $q_z = 0$ is significant in that the CS and L$_2$" phases of fatty acid [42-45], alcohol [42, 46], and ester [31] monolayers display a peak at exactly the same location. Of these two low-temperature 2D crystalline phases of single-chain amphiphiles, the CS phase occurs at higher Π and consists of long alkyl tails oriented normal to the surface, while the L$_2$" phase is a low-Π analog in which tails are tilted towards the nearest neighbors (NN) [28]. Durbin *et al*. recently confirmed experimentally that the CS and L$_2$" phases, which are related by a continuous transition, arise from a common local packing structure that is based on the "herringbone (HB)" arrangement of tails [45].

The HB packing of alkyl chains, which occur also in bulk organic crystals, has been described previously [28, 47, 48]. It is characterized by an orthorhombic (or "distorted hexagon") unit cell of fixed dimensions $a_1 \times a_2 = 5.0$ Å $\times$ 7.5 Å *in the plane perpendicular to chain axes* [28, 47]. An end-on view of HB-packed alkyl chains and the rectangular HB unit cell (non-primitive, two chains per cell) are depicted in Fig. 4.14(b).

Defining 2D reciprocal vectors $G_{hk} \equiv 2\pi/d_{hk}$ in the plane of the HB unit cell, it can be shown that the two lowest-order sets of reciprocal points correspond to: (i) $G_{11} = 1.51$ Å^{-1} from the (11) [and (1$\bar{1}$)] planes with d-spacing $d_{11} = 4.16$ Å, and (ii) $G_{02} = 1.68$ Å^{-1} from the (02) planes with $d_{02} = 3.75$ Å. That is, if HB-packed alkyl chains are oriented normal to the water surface (as in the CS phase), the (11) and (02) peaks would be centered at $q_{xy} = G_{11}$ and $q_{xy} = G_{02}$ in the surface plane ($q_z = 0$). If the chains that are tilted towards NN in the [10] direction (as in the L_2" phase) by angle θ relative to the surface normal, the (02) peak would still be centered at $q_z = 0$ since the tilt is perpendicular to the [01] direction; however, the (11) peak would be both shifted inward ($q_{xy} < G_{11}$) and lifted above the surface plane ($q_z > 0$) such that it falls on the arc $q = [q_{xy}^2 + q_z^2]^{1/2} = G_{11}$ at $q_z = G_{10}\sin(\theta)$, where $G_{10} = 1.26$ Å^{-1} [28].

It is clear from these expectations that the two peaks observed at high Π can be identified as the (11) and (02) peaks that originate from the local HB packing of –O-C16 chains. One important observation here is that the HB order of –O-C16 chains appears to be a local effect in that the magnitude of the NN tilt is not uniform over the entire area of the C16-O-PBLG monolayer. The appearance of the (11) peak near the surface horizon ($q_z < 0.11$ Å^{-1}; Fig. 4.13) indicates that some HB-packed chains must be untilted at high Π. On the other hand, its shifting behavior ($q = G_{11}$) above the surface plane ($q_z > 0.11$ Å^{-1}; Fig. 4.15) signifies not only a finite NN tilt of other HB-packed chains but also a continuous distribution in the values of the NN tilt angle θ that occur simultaneously over the surface. For example, at $\Pi = 24.0$ dyn/cm, where the (11) peak is still visible at $\langle q_z \rangle_{max} = 0.64$ Å^{-1}, the tilt angle can be estimated to range from $\theta = 0$ (untilted) to more than $\theta = \sin^{-1}(\langle q_z \rangle_{max}/G_{10}) \sim 30°$.

The observation of a relatively wide range of tilt angles within a single monolayer is not too surprising for –O-C16 chains since they are not isolated molecules sitting on a flat surface but are attached indirectly to the helical backbone. The occurrence of somewhat large tilt angles ($\theta \sim 30°$) even at high Π has already been suggested in the XR

section and is roughly consistent with the estimate based on the magnitude of the upper sub-layer thickness l_{chain} (see Sec. 4.3.2). Another check on the possibility of large θ at high Π is provided by a comparison between the cross-sectional area $A_{\text{HB}} = a_1 a_2 / 2 = 18.8$ Å^2/chain taken up by one –O-C16 chain in the HB unit cell (Fig. 4.14(b)) and the area/monomer A, which corresponds to the average surface area available per chain. For example, an NN tilt by $\theta = 30°$ would require an area of $A \geq A_{\text{HB}} / \cos(30°) = 21.7$ Å^2/monomer, a condition well satisfied up to $\Pi \sim 30$ dyn/cm (Fig. 4.2(c)).

The extent of lateral correlations associated with the HB order of –O-C16 chains can be inferred from the observed peak widths. The lack of a *fixed* NN tilt at given Π suggests that the correlations along any direction [uv] with a nonzero component $u \neq 0$ along the NN tilt are likely to be short-range. An indication of that is provided by the broadness of the (11) peak in Fig. 4.13. For highly compressed films, the (11) peak is well defined and its FWHM $\Delta q_{\text{xy}} = \Delta q_1$ based on the Lorentzian fits can be used to estimate a characteristic correlation length $\xi_{11} = 2/[\Delta q_1 - \delta q_{\text{xy}}]$ along the direction of d_{11}. The correlation length ξ_{11} thus determined is only of the order of $\xi_{11} = 13 \sim 17$ Å ($\xi_{11}/d_{11} = 3 \sim 4$) for the PD325 films at $\Pi > 25$ dyn/cm and $\xi_{11} = 21 \sim 25$ Å ($\xi_{11}/d_{11} = 5 \sim 6$) for the MD76 films at $\Pi > 15$ dyn/cm; it should be even shorter at lower Π, where the (11) peak is both broader and weaker.

As for the (02) peak at $q_{\text{xy}} = q_2$, its relatively small magnitude and the limited number of data points over it prevent a quantitatively reliable determination of its FWHM Δq_2. Nevertheless, the width Δq_2 is usually much narrower than Δq_1, and therefore the correlation length ξ_{02} along the [01] axis should be significantly larger than ξ_{11}. For example, the fit to the bottommost data curve shown in Fig. 4.15(a) gives $\Delta q_2 = 0.04 \pm 0.01$ Å^{-1}, which translates into $\xi_{02} = 140 \pm 100$ Å. Taking this as a rough estimate, we expect the correlation length ξ_{02} to be of the order of $\xi_{02} \sim 100$ Å or possibly longer. The directional dependence displayed by the relative magnitudes of ξ_{hk} as evidenced by $\xi_{02} \gg \xi_{11}$ is consistent with the case of tilted monolayer phases of alkyl chains, for which the

longest positional correlations usually occur along the direction perpendicular to the tilt [28].

The magnitudes of the correlation lengths ξ_{hk} estimated above suggest that the extent of the HB order of –O-C16 chains is actually limited by the physical dimensions of C16-O-PBLG molecules. First of all, $\xi_{02} \sim 100$ Å is roughly of the same order of magnitude as the lengths L of typical C16-O-PBLG rods. Second, if the projection ζ_{10} of ξ_{11} onto the [10] axis (i.e., $\zeta_{10} \equiv a_2/[a_1^2 + a_2^2]^{1/2} \times \xi_{11} = 0.83\xi_{11}$) is taken to be a measure of the HB correlations along the NN tilt direction, then, the maximum value that it reaches upon compression to high Π is given by $\zeta_{10,max} = 11 \sim 14$ Å for the PD325 films and $\zeta_{10,max} = 17 \sim 21$ Å for the MD76 films. These estimates for $\zeta_{10,max}$ are comparable to the inter-helix distance d observed at high Π (see Fig. 4.12). These observations strongly suggest that the [01] axis of the HB unit cell runs parallel to the helical axes of aligned PBLG cores while the [10] axis and hence the NN tilt of –O-C16 chains are in the direction normal to the helical axis.

The well-defined orientation of the HB unit cell with respect to the molecular axis of C16-O-PBLG implies that the HB order must develop with compression in such a way that it is structurally consistent not only with the segregation behavior along the surface normal but also with the in-plane structure of PBLG cores. Fig. 16 illustrates one possible model for the spatial development of the HB order that takes into account these various structural aspects of the C16-O-PBLG monolayer. The in-plane view in Fig. 16(a) depicts a model structure at high Π, showing a HB-packed domain of –O-C16 chains with its [01] axis oriented parallel to the lengths of aligned C16-O-PBLG rods. The following considers how such a structure can result from lateral compression of a less two-dimensionally ordered structure that is first formed at low Π.

The presence of a weak (02) peak and the near absence of the (11) peak at low Π ($< \sim 5$ dyn/cm) indicate that a small fraction of the –O-C16 chains first form a locally HB-packed structure with a relatively large correlation length parallel to the aligned
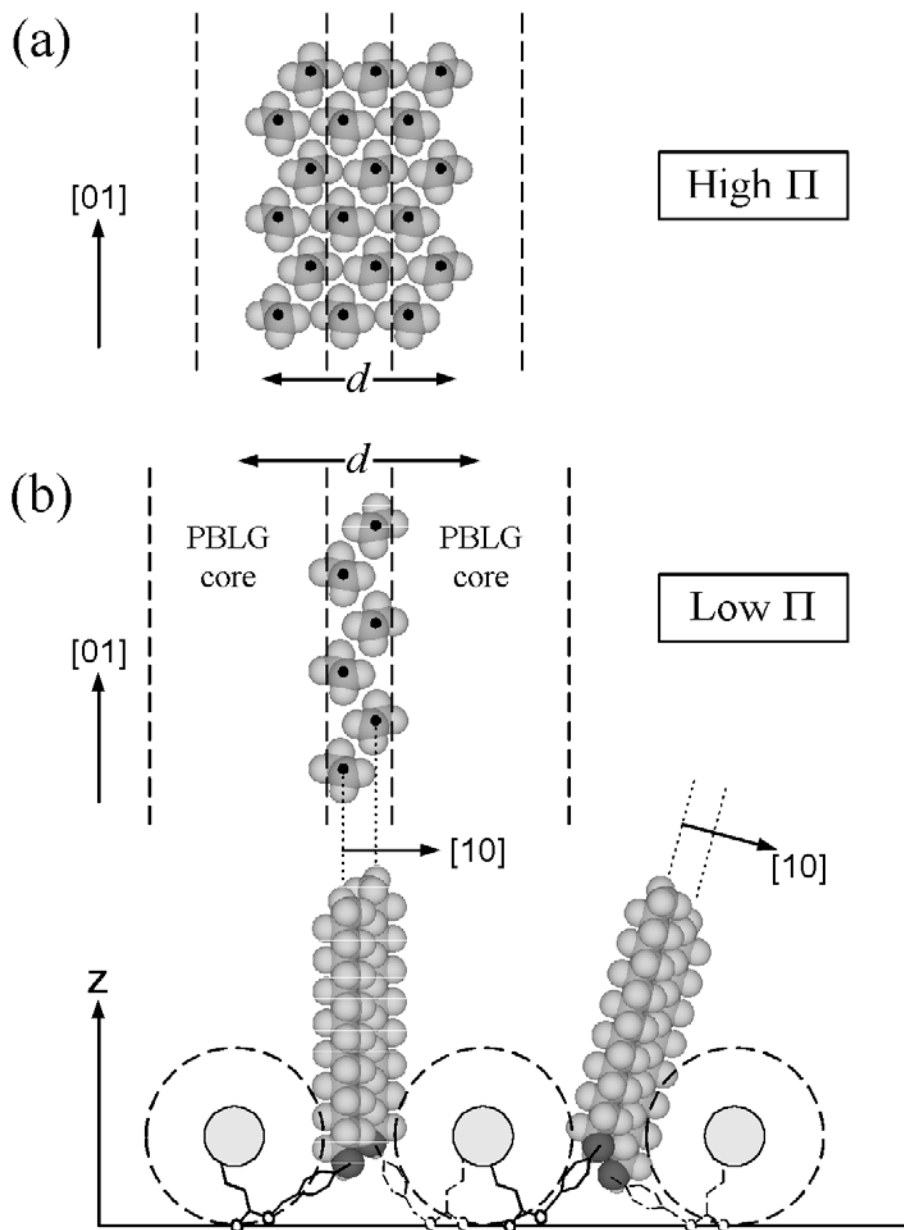
Figure 4.16: A model for ordering of side chains. (a) Top view of herringbone (HB) packing at high surface pressure Π. The [01] axis of the HB unit cell is oriented parallel to the α-helical axes of aligned PBLG cores. (b) Top view and side view of zigzag packing at low Π, with 1D HB order for –O-C16 chains that are confined between aligned PBLG cores. The –O-C16 chains can be untilted or tilted perpendicular to the α-helix axes of PBLG cores.

PBLG-core axes (i.e., along [01]) but with only very limited extent perpendicular to them. The two important characteristics of this initial structure are its pseudo-1D nature and highly dense packing implied by the HB order. If it weren't for the presence of PBLG cores, the latter would be somewhat surprising given the fact that for $\Pi < \sim 5$ dyn/cm, the average surface area available per chain $A \geq A_{\lim} \sim 27$ Å^2/monomer is still significantly larger than $A_{HB} = 18.8$ Å^2/chain. On the other hand, it has been shown that PBLG cores align locally on the surface without external pressure. Presumably, this reflects a strong mutual attraction and tendency to self-aggregate into 2D solid (see the preceding subsection on inter-helix order and [24]). There are a fixed number of -O-C16 chains per unit length of a PBLG core (i.e. $1/L_1$ = one monomer per 1.5 Å), and approximately one quarter of them are tethered to the water side of the core. Since these chains are hydrophobic, they will have to fold around the subsurface of the core to get away from water. These chains that are confined semi-one-dimensionally between pairs of aligned PBLG cores must then pack more densely than unconfined chains sitting directly above the cores. These confined chains would be subjected to a rather high internal local pressure even at $\Pi = 0$. On the basis of these considerations, we suggest that the initial ordering of –O-C16 chains at low Π is a consequence of the 1D confinement imposed by the local alignments of PBLG cores and can be attributed mostly to chains in the confined regions.

Figure 4.16(b) illustrates an idealized model (a "zigzag" model) of a possible initial structure ($\Pi < \sim 5$ dyn/cm) that is based on the HB packing of confined –O-C16 chains. The figure omits unconfined chains, which are expected to be disordered at low Π. The model consists of two rows of chains forming a zigzag pattern in the confined region, where each row is contributed by one of the two neighboring C16-O-PBLG rods on either side. The HB packing implies that the positions of chains along each row are periodic with repeat distance of a_2 and are related to those of the other row by a vector ($a_1/2$, $a_2/2 = d_{02}$) that is normal to the axes of the –O-C16 chains. Due to the physical

size of alkyl chains, it is not possible to fit more than two rows within the measured gap between the PBLG cores, whose estimated width $\Delta d \sim 5$ Å is comparable to a_1. Given that the side chain as a whole is tethered to the helical backbone, there may be a distribution in the heights of –O-C16 chains within a given ordered domain, and any given domain may be tilted in the direction normal to the helical axis (see Fig. 4.16(b)).

The case for the above interpretation is strongly supported by the following. First, the HB unit cell dimension of $a_2 = 7.5$ Å along the [01] axis happens to be an integer multiple of the α-helix pitch $L_1 = 1.5$ Å/monomer along the helical axis, i.e., $a_2 = 5L_1$. According to the model, *on average*, *every segment of five monomers* in a C16-O-PBLG rod would contribute one chain to the zigzag structure on one side of the core and another to the other side. The surface area A_5 predicted to be taken up by a five-monomer segment of a C16-O-PBLG rod should roughly be equal to $A_5 \sim 5A_{PBLG} + 2A_{HB}$. Taking the low-$\Pi$ value of $A_{PBLG} \sim 20$ Å^2/monomer for the core (Fig. 4.2(c)), the area/monomer for C16-O-PBLG based on the zigzag model is estimated to be $A_5/5 \sim 27.5$ Å^2/monomer. The fact that this estimate agrees well with $A_{lim} \sim 27$ Å^2/monomer from the isotherms is further evidence for the plausibility of the model. As for the unconfined chains left above the core (roughly three per five-monomer segment), an average area of $(5/3)A_{PBLG} \sim 33$ Å^2/chain available to each at low Π is more than enough room for these chains to be disordered.

It should be emphasized that the interpretation given above does *not* imply that *every fifth monomer* in a C16-O-PBLG rod contributes its chain to formation of one row in a zigzag structure. In a given α-helix, the position at which the side chain of the mth monomer is tethered to the helical backbone can be described by the cylindrical coordinates $(r, m\varphi_1, mL_1)$, where $r = 2.3$ Å is the backbone radius of the α-helix and $\varphi_1 = 100°$ [49]. The notion that every fifth monomer has its side chain protruding always on the same side of the rod is inconsistent with the azimuthal angle change of $\Delta\varphi = 140°$ over five monomers. Given the hydrophobicity of alkyl chains, it is more likely that the

monomers contributing to the HB packing in the confined region are those whose side chains are tethered near the bottom (i.e., towards water) of the helical backbone. The ordering of their –O-C16 part is probably accomplished by means of some appropriate conformational and orientational rearrangements of the "spacer" part (i.e., -(CH$_2$)$_2$-COO-CH$_2$-C$_6$H$_4$-; see Fig. 4.1(a)), whose end-to-end length can stretch out to ~ 10 Å.

Regardless of the specific molecular-level details of how the surface area is reduced with increasing Π, it is clear that the free area available to –O-C16 chains must become reduced. At high Π (> ~ 5 dyn/cm), the area constraint will enhance the packing order of chains, thereby increasing the number of unconfined chains participating in the HB order (see Fig. 16(a)). The area reduction might occur through deformation of PBLG cores, as suggested by the slight increase in l_{core} with compression (Figs. 4.8 and 4.9), or alternatively, by either reducing the tilt within the zigzag structures or vertically displacing one row of chains relative to the other row. While the exact nature of the mechanism is not clear, both the behavior $d = A/L_1$ (Fig. 4.12) and the increase in l_{chain} at high Π indicate that the unconfined –O-C16 chains in the upper sub-layer do experience effects of reduced area as the film is compressed. Therefore, it is reasonable to suppose that compression causes these chains to be brought into alignment with nearby chains and conform to the HB structures initially formed in the confined regions. This interpretation is consistent with the observed behavior of the (11) peak that implies a lateral growth of the HB order with increasing Π in the direction perpendicular to the core axes.

As noted earlier, the C16-O-PBLG monolayer is characterized by the fact that it sustains high surface pressures. This stability can now be understood as a consequence of the lateral ordering of –O-C16 chains. According to the estimated values of $\xi_{10,max}$ that is reached at high Π, –O-C16 chains in the MD76 films achieve a slightly higher degree of the HB order perpendicular to PBLG core axes than those in the PD325 films. This is likely to be the origin of the lower compressibility of the MD76 films, which is evidenced by the high-Π behaviors of both their isotherms (Fig. 4.2(c)) and inter-helix d-spacing

(Fig. 4.12). It is yet unclear how this discrepancy between the two samples depends on the differences in dispersity and molecular weight.

From the structural point of view, the ordering of –O-C16 chains evidenced by the results presented above is quite consistent with a highly dense structure based on the HB packing. However, at first glance, the observation of the HB order at room temperature appears to be in conflict with known thermodynamics of various monolayers formed by simple isolated alkyl chains of comparable length. For example, according to the generalized phase diagram of fatty acid monolayers, the ordered phase formed by C16 acid at room temperature (and high Π) should have a less dense structure with a hexagonal symmetry, and the L_2" and CS phases would not occur at all unless the subphase temperature could be reduced to $T < -20$ °C [28]. However, this discrepancy is not so unreasonable if one takes into account the fact that the –O-C16 chain is not a isolated chain but one end of it is attached to a rod-like PBLG core. The constraint of a fixed number of side chains per unit length of α-helix together with confinement imposed by the parallel alignments of PBLG cores significantly reduces the number of various degrees of freedom (conformational, rotational, orientational, translational, etc.) that is available to the confined chains. This reduction in chain entropy is probably the reason why -O-C16 chains favor the HB structure, which is a well-known low-energy packing mode of alkyl chains [28, 47].

4.4 Summary

Langmuir monolayers of hairy-rod polypeptide C16-O-PBLG have been studied. The Π-A isotherms show that the C16-O-PBLG monolayers sustain much higher surface pressure (up to $\Pi > 40$ dyn/cm at 22 °C) than the PBLG monolayer, which collapses at ~ 9 dyn/cm to form a bilayer. For $T \geq 22$ °C, the isotherms of C16-O-PBLG display a relatively narrow plateau-like feature at low Π ($\Delta A/A \sim 15$ % or less), while such a feature is absent at $T = 11$ °C. The exact origin of this low-Π behavior is still unknown.

However, the reversibility of the plateau feature upon compression and expansion suggests that it is an intrinsic property of the C16-O-PBLG monolayer.

The microscopic structures of the monolayers at room temperature have been probed using x-ray reflectivity and grazing incidence diffraction techniques. The main results can be summarized as follows:

The electron density profiles extracted from XR data are consistent with the formation of a monolayer in which C16-O-PBLG rods are oriented parallel to the water. However, the non-uniformity of the profiles across the film indicates that the hydrophobicity of –O-C16 chains results in internal segregation of the monolayer into an upper sub-layer occupied by -O-C16 chains and a PBLG core-dominated lower sub-layer. The monolayer thickens with increasing Π, but this segregated structure is maintained up to high Π (~ 30 dyn/cm).

The observation of a low-q_{xy} GID peak at $\Pi \sim 0$ indicates that C16-O-PBLG rods aggregate laterally and form locally aligned domains in the monolayer. The inter-helix distance d between aligned rods decreases continuously with increasing Π and scales linearly with A at high Π. This linear behavior shows that macroscopic compressibility of the monolayer at high Π is directly related to the microscopic inter-helix compressibility. Due to the presence of –O-C16 chains that are confined between aligned PBLG cores, the inter-helix d-spacing for C16-O-PBLG is larger than that found in the PBLG monolayer. The width $\Delta d \sim 5$ Å of this extra spacing for C16-O-PBLG is consistent with the "confined" chains pointing away from water.

For $\Pi > \sim 5$ dyn/cm, GID patterns exhibit two additional peaks at higher q_{xy} that are consistent with ordered packing of –O-C16 chains. This suggests that the stability of the C16-O-PBLG monolayers at high Π is a result of the lateral ordering of -O-C16 chains in the upper sub-layer. The peak positions are consistent with the herringbone (HB) packing of alkyl chains that are commonly found in two low-T phases CS (untilted) and L$_2$" (tilted toward NN) of fatty acid monolayers. The results also show that there is a

wide distribution in the NN tilt of –O-C16 chains, such that the tilt angle for a given HB-packed domain can be anywhere from $0°$ (untilted) to $> 30°$ relative to the surface normal. Various features of these peaks suggest that the HB structure of -O-C16 chains has a specific in-plane orientation with respect to the helical axes of aligned PBLG cores. The orientation is such that the NN tilt direction is always perpendicular to the helix axes.

For $\Pi < \sim 5$ dyn/cm, one of the two peaks is absent. This observation together with the results at high Π suggests that the initial structure formed at low Π has an one-dimensional character, such that the extent of HB order is relatively large only in the direction parallel to the axes of aligned PBLG cores. We have proposed a model in which the initial one-dimensionally ordered structure consists of HB packing of "confined" –O-C16 chains. The model is consistent with the various structural characteristics of the monolayers that have been elucidated in this study. In the C16-O-PBLG monolayers, the HB order of –O-C16 chains appears to be a consequence of the 1D confinement imposed by the local alignments of PBLG cores and the tethering constraints and hydrophobicity of these chains.

References for Chapter 4

[1] G. Wegner, *Thin Solid Films* **216,** 105 (1992).

[2] G. Wegner and K. Mathauer, *Mat. Res. Soc. Symp. Proc.* **247,** 767 (1992).

[3] J. Watanabe, Y. Fukuda, R. Gehani and I. Uematsu, *Macromolecules* **17,** 1004 (1984).

[4] J. Watanabe, H. Ono, I. Uematsu and A. Abe, *Macromolecules* **18,** 2141 (1985).

[5] E. Iizuka, K. Abe, K. Hanabusa and H. Shirai, in *Current Topics in Polymer Science*, Vol. I (Hanser, Munich, 1987), pp. 235.

[6] K. Hanabusa, M. Sato, H. Shirai, K. Takemoto and E. Iizuka, *J. Polym. Sci.: Polym. Lett. Ed.* **22,** 559 (1984).

[7] S. M. Yu and D. A. Tirrell, *Biomacromolecules* **1,** 310 (2000).

[8] H. Motschmann, R. Reiter, R. Lawall, G. Duda, M. Stamm, G. Wegner and W. Knoll, *Langmuir* **7,** 2743 (1991).

[9] D. Sohn, H. Yu, J. Nakamatsu, P. S. Russo and W. H. Daly, *J. Poly. Sci.* **B 34,** 3025 (1996).

[10] D. Neher, *Adv. Mater.* **7,** 691 (1995).

[11] W. Hickel, G. Duda, M. Jurich, T. Krohl, K. Rochford, G. I. Stegeman, J. D. Swalen, G. Wegner and W. Knoll, *Langmuir* **6,** 1403 (1990).

[12] K. Mathauer, A. Mathy, C. Bubeck, G. Wegner, W. Hickel and U. Scheunemann, *Thin Solid Films* **210/211,** 449 (1992).

[13] A. Mathy, K. Mathauer, G. Wegner and C. Bubeck, *Thin Solid Films* **215,** 98 (1992).

[14] H. Menzel, B. Weichart and M. L. Hallensleben, *Thin Solid Films* **223,** 181 (1993).

[15] H. Menzel, M. L. Hallensleben, A. Schmidt, W. Knoll, T. Fischer and J. Stumpe, *Macromolecules* **26,** 3644 (1993).

[16] M. Mabuchi, S. Ito, M. Yanamoto, T. Miyamoto, A. Schmidt and W. Knoll, *Macromolecules* **31,** 8802 (1998).

[17] A. Vogel and B. Hoffmann, *Sensors and Actuators B* **4,** 65 (1991).

[18] G. Wiegand, T. Jaworek, G. Wegner and E. Sackmann, *Langmuir* **13,** 3563 (1997).

[19] H. Menzel, B. Weichart and M. L. Hallensleben, *Thin Solid Films* **242,** 56 (1994).

[20] A. Schmidt, K. Mathauer, G. Reiter, M. D. Foster, M. Stamm, G. Wegner and W. Knoll, *Langmuir* **10,** 3820 (1994).

[21] T. R. Vierheller, M. D. Foster, A. Schmidt, K. Mathauer, W. Knoll, G. Wegner, S. Satija and C. F. Majkrzak, *Macromolecules* **27,** 6893 (1994).

[22] K. Mathauer, A. Schmidt, W. Knoll and G. Wegner, *Macromolecules* **28,** 1214 (1995).

[23] M. Buchel, Z. Sekkat, S. Paul, B. T. Weichart, H. Menzel and W. Knoll, *Langmuir* **11,** 4460 (1995).

[24] M. Fukuto, R. K. Heilmann, P. S. Pershan, S. M. Yu, J. A. Griffiths and D. A. Tirrell, *J. Chem. Phys.* **111,** 9761 (1999).

[25] C. M. Knobler, *Adv. Chem. Phys.* **77,** 397 (1990).

[26] C. M. Knobler and R. C. Desai, *Annu. Rev. Phys. Chem.* **43,** 207 (1992).

[27] H. Möhwald, *Annu. Rev. Phys. Chem.* **41,** 441 (1990).

[28] V. M. Kaganer, H. Möwald and P. Dutta, *Rev. Mod. Phys.* **71,** 779 (1999).

[29] S. M. Yu, V. Conticello, G. Zhang, C. Kayser, M. J. Fournier, T. L. Mason and D. A. Tirrell, *Nature* **389,** 167 (1997).

[30] D. K. Schwartz, M. L. Schlossman and P. S. Pershan, *J. Chem. Phys.* **96,** 2356 (1992).

[31] W. J. Foster, M. C. Shih and P. S. Pershan, *J. Chem. Phys.* **105,** 3307 (1996).

[32] G. M. Bommarito, W. J. Foster, P. S. Pershan and M. L. Schlossman, *J. Chem. Phys.* **105,** 5265 (1996).

[33] J. Als-Nielsen and H. Möhwald, in *Handbook of Synchrotron Radiation*, Vol. 4, edited by S. Ebashi, E. Rubenstein and M. Koch (North Holland, Amsterdam, 1991), pp. 1.

[34] J. Als-Nielsen, D. Jacquemain, K. Kjaer, F. Leveiller, M. Lahav and L. Leiserowitz, *Phys. Rep.* **246,** 251 (1994).

[35] P. S. Pershan and J. Als-Nielsen, *Phys. Rev. Lett.* **52 ,** 759 (1984).

[36] B. M. Ocko, X. Z. Wu, E. B. Sirota, S. K. Sinha, O. Gang and M. Deutsch, *Phys. Rev. E* **55,** 3164 (1997).

[37] A. Braslau, P. S. Pershan, G. Swislow, B. M. Ocko and J. Als-Nielsen, *Phys. Rev. A* **38,** 2457 (1988).

[38] X. Z. Wu, E. B. Sirota, S. K. Sinha, B. M. Ocko and M. Deutsch, *Phys. Rev. Lett.* **70,** 958 (1993).

[39] J. Daillant, L. Bosio, J. J. Benattar and J. Meunier, *Europhys. Lett.* **8,** 453 (1989).

[40] J. Daillant, L. Bosio and J. J. Benattar, *Europhys. Lett.* **12,** 715 (1990).

[41] J. P. Rieu, J. F. Legrand, A. Renault, B. Berge, B. M. Ocko, X. Z. Wu and M. Deutsch, *J. Phys. II (France)* **5,** 607 (1995).

[42] T. M. Bohanon, B. Lin, M. C. Shih, G. E. Ice and P. Dutta, *Phys. Rev. B* **41,** 4846 (1990).

[43] B. Lin, M. C. Shih, T. M. Bohanon, G. E. Ice and P. Dutta, *Phys. Rev. Lett.* **65,** 191 (1990).

[44] R. M. Kenn, C. Böhm, A. M. Bibo, I. R. Peterson, H. Möhwald, K. Kjær and J. Als-Nielsen, *J. Phys. Chem.* **95,** 2092 (1991).

[45]   M. K. Durbin, A. G. Richter, C.-J. Yu, J. Kmetko, J. M. Bai and P. Dutta, *Phys. Rev. E* **58,** 7686 (1998).

[46]   M. C. Shih, T. M. Bohanon, J. M. Mikrut, P. Zschack and P. Dutta, *J. Chem. Phys.* **97,** 4485 (1992).

[47]   I. Kuzmenko, V. M. Kaganer and L. Leiserowitz, *Langmuir* **14,** 3882 (1998).

[48]   D. M. Small, *The Physical Chemistry of Lipids: From Alkanes to Phospholipids* (Plenum Press, New York and London, 1986).

[49]   G. E. Schulz and R. H. Schirmer, *Principles of Protein Structure* (Springer-Verlag, New York, 1979).

Chapter 5

Monolayer/Bilayer Transition in Langmuir Films of Derivatized Gold Nanoparticles at the Gas/Water Interface

5.1 Introduction

Chemically synthesized metallic and semiconductor nanoparticles—also referred to as nanoclusters, nanocrystals, nanocolloids or quantum dots—have been receiving a great deal of attention in recent years. Interests in such particles originate from the fact that due to their small sizes, which typically range from ~ 10 to ~ 100 Å, the effects of finite size or "confinement" play an essential role in determining their electronic, optical and other physical behaviors [1-4]. The nanoparticles also serve as building blocks for new materials and devices, and many studies have been directed toward exploiting their unique size-dependent properties in practical applications, e.g., in optoelectronics, micro- or nanoelectronics, chemical and biosensors, and catalysis [2, 5-7]. One of the challenges in this field of research is to find ways to organize these particles into microscopically well-defined three-dimensional (3D) or 2D structures such that they are useful for some of these applications [3, 6, 8, 9].

In the case of 2D structures, several different methods have been used to form a monolayer of nanoparticles on a substrate, where all of them utilize, in one way or another, solubility of these particles in organic solvents or even in water in some cases [10]. One approach is to deposit nanoparticles directly from a solution onto a solid substrate, either by letting drops to wet and evaporate on the substrate or by dipping the substrate in the solution to allow nanoparticles to self-assemble at the interface [6, 9, 11]. Another approach is to spread the solution on the water surface to form a Langmuir

monolayer, which then can be transferred onto a solid substrate by using either Langmuir-Blodget (LB) or Langmuir-Schaeffer (i.e., "stamping") techniques [10, 12-14]. One advantage of this Langmuir method is the ability to control the surface coverage and possibly also the inter-particle spacing if the initial microscopic packing density can be increased further by laterally compressing the film. Finally, one of the more complex methods that have been used is based on attractive interactions between colloidal nanoparticles in an aqueous solution and a charged surfactant monolayer at the solution/air interface [10, 15]. In this approach, nanoparticles form a monolayer of their own just below the surfactant monolayer, and the composite film thus formed is transferred onto a solid support by the LB method.

One of the most commonly studied classes of metallic nanoparticles consists of colloidal gold or silver crystallites that are nucleated and grown from metallic ions in solution and are stabilized by simultaneous attachments of alkanethiols $HS\text{-}(CH_2)_{n-1}\text{-}CH_3$ (or thiol derivatives) onto their surface (denoted as "AuSCn" or "AuSCn") [11, 14, 16-26]. Heath and coworkers recently studied Langmuir films of this class of nanoparticles and obtained some interesting results [14, 25]. Their samples consisted of AuSCn (n = 9, 12, 18) and AgSCn (n = 3, 6, 10, 12) particles with mean metal-core diameters D ranging from 18 to 40 Å and standard deviation ΔD of the size distributions ranging from $\Delta D/D =$ 10 to 20 %. Their TEM images of transferred Langmuir-Schaeffer films indicate that in compressed monolayers AuSCn and AgSCn particles form close packed structures with local 2D hexagonal order. They also measured the linear and non-linear optical response of AgSCn monolayers at the air/water interface. Their results show that for particles coated with short-chain thiols (AgSC3, AgSC6), compression of a monolayer leads to a sharp and discontinuous drop in the second-harmonic signal when the edge-to-edge separation δ between adjacent Ag cores is reduced to a critical value $\delta \sim 5$ Å. They interpreted it as evidence for a 2D metal/insulator transition, attributing the observed effect to delocalization of electrons caused by sufficient overlaps between electronic

149

wave functions of adjacent particles [25].

In this chapter, we present surface pressure (Π) vs. area/particle (A) isotherm and synchrotron x-ray studies of Langmuir films formed by gold nanoparticles derivatized with carboxylic acid-terminated alkylthiol chains HS-$(CH_2)_{15}$-COOH ("AuSC16"). The Π-A isotherms at room temperature (25 °C) display clear signatures that are consistent with a first-order monolayer/bilayer transition. The microscopic structures of both monolayer and bilayer AuSC16 films have been probed using x-ray specular reflectivity (XR), grazing incidence diffraction (GID), and off-specular diffuse scattering (XOSDS) techniques. The XR and XOSDS results are consistent with the formation of a laterally homogeneous monolayer immediately prior to the onset of the transition, while the GID peaks observed from the monolayer provide evidence for local 2D hexagonal packing of AuSC16 particles with only short-range positional order. The limited extent of lateral order appears to be a result of the polydispersity in the size of Au cores. The results from the high-density side of the coexistence plateau are consistent with the presence of a laterally inhomogeneous bilayer. The average number of particles in the newly created second layer is slightly less than that in the first layer. The GID results from the bilayer suggest that a certain degree of inter-layer correlations exist between the local hexagonal order in the two layers; however, each layer of the bilayer is more disordered than in the case of the monolayers.

The rest of the chapter is organized as follows. Sec. 5.2 describes relevant experimental details. In Sec. 5.3.1 through 5.3.4, the results of Π-A isotherm, XR, XOSDS, and GID measurements are presented and discussed in turn. In Sec. 5.3.5, we address some of the issues concerning the uncertainties in average particle size and area/particle. Main conclusions from this study are summarized in Sec. 5.4.

5.2 Experimental Details

5.2.1 Sample and Π-*A* isotherm measurements

The AuSC16 sample used consists of polydisperse gold nanoparticles derivatized with carboxylic acid-terminated alkylthiol chains HS-$(CH_2)_{15}$-COOH. The sulfur end of each thiol chain is chemically bonded to the surface of Au nanoparticles. The synthesis and characterization of the particle size distribution in the sample were conducted by Prof. R. B. Lennox's group at McGill University (Department of Chemistry, McGill University, 801 Sherbrroke St. W., Montreal H3A 2K6, Canada). The synthetic procedures used have been described previously [16, 17, 19, 22]. Based on TEM images of a few hundreds of these particles, the mean diameter of Au cores has been determined to be $D_{TEM} = 27$ Å with a standard deviation of $\Delta D_{TEM} = \pm 6$ Å.

The average MW of particles in the sample is a difficult quantity to determine with certainty. The difficulty arises from the size and shape polydispersity of Au cores, distributions and uncertainties in the number of Au atoms on the core surfaces, that of thiol chains and their ratio, the limited resolution and sampling size in the TEM measurements, etc. In this study, the average MW was estimated in two ways. One of them relies on the analysis of various x-ray results yet to be presented, and therefore it will be neither referred to nor described until Section 5.3.5. The following summarizes the other approach used for estimating area/particle in the isotherm measurements.

Whetten and coworkers previously used similar synthetic procedures to produce thiol-capped Au nanoparticles with Au core diameters comparable to those in our sample [11]. They also conducted mass spectroscopy, high-resolution TEM and x-ray diffraction measurements on their samples and compared the results with their theoretical calculations on various forms of energy-minimizing Au crystallite morphologies. Their analysis showed that the most abundant configuration in this range of Au core sizes is consistent with a truncated octahedron TO Au_{459}, which is based on fcc packing and comprised of 459 Au atoms. In TO Au_{459}, 234 Au atoms are exposed as "surface atoms,"

151

and opposing (111) facets are separated by $D_{111} = 21$ Å and opposing (100) facets by $D_{100} = 27$ Å. Badia and coworkers, who also synthesized similarly sized thiol-coated Au nanoparticles, showed that the total Au to S ratio obtained from the elementary analysis of their samples would lead to a surface Au to thiol ratio of about 1.8 if the TO Au_{459} motif were assumed [19, 21]. If AuSC16 particles consisted of TO Au_{459} cores with this surface Au to thiol ratio, such "ideal" particles would have MW = 128,000 g/mole. This value of MW was used to estimate the number of particles spread on the suphase surface in the Langmuir trough. The area per particle deposited on the tough A_t is an estimate given by the ratio of the available trough surface area to this number.

Details on the Langmuir trough used in the present study have been described previously [27-29]. A teflon trough and a Wilhelmy-type surface pressure balance are enclosed in a sealed aluminum box. For isotherm measurements, the box was filled with high-purity N_2 gas. For x-ray measurements, high-purity He gas was used instead in order to reduce background scattering from gas in the beam path. All the measurements to be reported here were carried out at $T = 25.0$ °C. An aqueous subphase solution which was preadjusted to pH = 3 by adding an appropriate amount of HCl (J. T. Baker, ULTREX II ultra pure regent) to pure water (Milli-Q quality) was used both for flushing of the trough prior to spreading of a film and as the subphase. The acidic subphase was chosen to prevent ionization of the carboxylic groups around the particles. The spreading solution was prepared by dissolving a dry sample of AuSC16 particles in benzene (Sigma, HPLC grade); the nominal concentration of the solutions used ranged from 1.45 to 1.66 mg/mL. A film was deposited on the surface by spreading a measured volume of the solution, which ranged from 90 to 130 μL and corresponded to an initial, as-spread area of $A_t > 2000$ Å^2/particle.

Π-A isotherms were measured by using two different methods. In a step-wise continuous scan, surface pressure Π was measured 15 sec after the end of each compression step (typically, $\Delta A_t = 10$ Å^2/particle per step), followed immediately by the

next compression step. In a relaxation scan [27-29], the film was allowed to relax after each compression step ($\Delta A_t = 40$ Å^2/particle per step); at each A_t, the surface pressure was monitored every minute during relaxation until the pressure change over 5 min was less than 0.05 dyn/cm, at which point a final pressure was recorded and the film was compressed to the next area. For both methods, the barrier speed used for film compression corresponded to a compression rate of $dA_t/dt = 1.0$ (Å^2/particle)/s. For x-ray experiments, the film was compressed using the step-wise continuous method, but it was allowed to relax once a target area was reached. X-ray measurements were started only after the surface pressure had relaxed to the value given by the relaxation isotherm.

5.2.2 X-ray measurements

X-ray experiments were carried out at the Beamline X22B of the National Synchrotron Light Source, using the Harvard/BNL liquid surface spectrometer [27] operated at an x-ray wavelength of $\lambda = 1.55$ Å. The relationships between the surface (the x-y plane) and the scattering angles ($\alpha, \beta, 2\theta$) are illustrated in Fig. 5.1. The
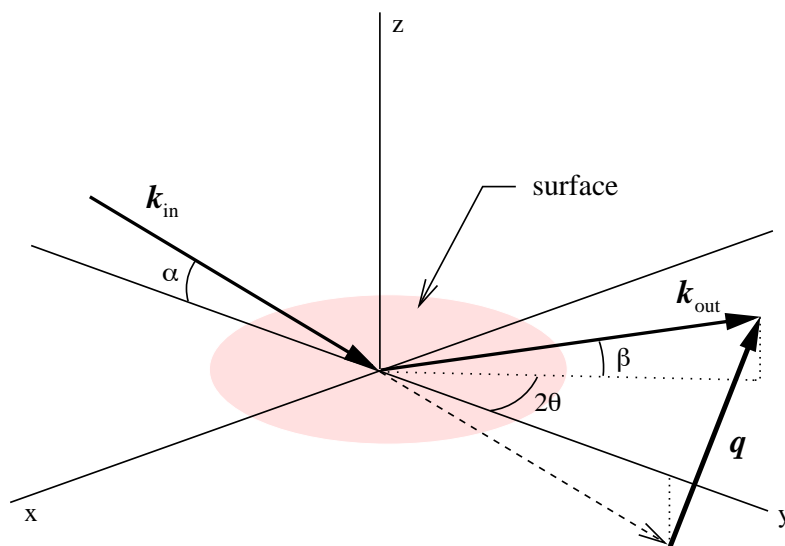
Figure 5.1: X-ray scattering geometry.

difference between the scattered and incident wave vectors defines the wave vector transfer $\mathbf{q} = \mathbf{k}_{out} - \mathbf{k}_{in}$. Its three Cartesian components are given by $q_x = k\cos(\beta)\sin(2\theta)$, $q_y = k[\cos(\beta)\cos(2\theta) - \cos(\alpha)]$, and $q_z = k[\sin(\alpha) + \sin(\beta)]$, where $k = 2\pi/\lambda$. For all the x-ray data reported here, scattered intensities were measured using a NaI scintillation detector. Two sets of crossed Huber slits were placed between the sample and the detector, one set located at $S_1 = 183$ mm and the other (detector slits) at $S_2 = 657$ mm from the sample center. In what follows, the height and width of slit opening at S_i are denoted as (H_i, W_i).

Specular reflectivity (XR) and off-specular diffuse scattering (XOSDS). In XR, intensity I reflected from the surface at the specular condition ($\beta = \alpha$, $2\theta = 0$; $q_{xy} = 0$) is measured as a function of the incident angle α or wave vector transfer $q_z = 2k\sin(\alpha)$ along the surface normal. The background intensities were measured at 2θ offsets of $2\theta_b = \pm 0.25°$ and subtracted from the specular signal at $2\theta = 0$. The opening of the detector slits at S_2 was set to $(H_2, W_2) = (2.5$ mm, 3.0 mm) and corresponded to angular detector resolutions of $\delta\beta = 0.22°$ and $\delta(2\theta) = 0.26°$, or equivalently, reciprocal-space resolutions of $\delta q_x = 0.0185$ Å^{-1}, $\delta q_y = 0.0019q_z$, and $\delta q_z = 0.0155$ Å^{-1}.

XOSDS was measured using a β-scan method, in which the incident angle α is fixed and intensities scattered in the incidence plane ($2\theta = 0$) are measured as a function of the output angle β. The background intensities were measured at 2θ offsets of $2\theta_b = \pm 0.3°$ and subtracted from the signal at $2\theta = 0$. The detector slit setting of $(H_2, W_2) = (1.0$ mm, 3.0 mm) used for the β-scans corresponded to angular resolutions of $\delta\beta = 0.087°$ and $\delta(2\theta) = 0.26°$. The equivalent q-space resolutions are given by $\delta q_x = 0.0185$ Å^{-1} and $\delta q_z = 0.0062$ Å^{-1}, while the q_y resolution varied with β as $\delta q_y = k\sin(\beta)\delta\beta = (0.0062$ Å$^{-1})$ $\times \sin(\beta)$.

The measured quantity for XOSDS is the normalized intensity difference $\Delta I(\alpha, \beta)/I_0$, where I_0 is the incident intensity and

$$\Delta I(\alpha, \beta) = I(\alpha, \beta, 2\theta = 0) - (1/2)[I(\alpha, \beta, +2\theta_b) + I(\alpha, \beta, -2\theta_b)]. \tag{5.1}$$

The specular reflectivity $R(q_z)$ measured in XR is a special case of the above, i.e., $R(\alpha) = \Delta I(\alpha, \beta = \alpha)/I_0$. In general, the observed intensity is equal to the convolution of the differential cross section $d\sigma/d\Omega$ with an instrumental resolution function Ξ. For the experimental setups described above, the size of the detector slit opening is much larger than the cross sectional area A_0 of the incident beam (0.1 mm × 0.5 mm). Therefore, it is appropriate to take $\Xi = 1$ inside the resolution volume and $\Xi = 0$ outside, such that

$$\frac{I(\alpha, \beta, 2\theta)}{I_0} = \int_{\left(\beta - \frac{1}{2}\delta\beta\right)}^{\left(\beta + \frac{1}{2}\delta\beta\right)} d\beta' \int_{\left[2\theta - \frac{1}{2}\delta(2\theta)\right]}^{\left[2\theta + \frac{1}{2}\delta(2\theta)\right]} d(2\theta') \frac{1}{A_0} \frac{d\sigma}{d\Omega}(\alpha, \beta', 2\theta'). \tag{5.2}$$

An equivalent expression based on the integration in the reciprocal space can be obtained by using the approximation $d\Omega \approx d\beta d(2\theta) \approx d^2\mathbf{q}_{xy}/[k^2\sin(\beta)]$.

In the case of liquid surfaces, the scattering cross section is characterized by a power-law behavior of form $d\sigma/d\Omega \sim 1/q_{xy}^{2-\eta}$, where $0 < \eta = (k_BT/2\pi\gamma)q_z^2 < 2$ [30, 31]. This behavior originates from the two-dimensional nature of the interface and the presence of capillary waves, which are thermally excited fluctuations of liquid/gas interfacial heights $h(r_{xy})$ against surface tension γ. If the liquid surface is laterally homogeneous and height fluctuations of all interfaces are conformal with each other, $d\sigma/d\Omega$ is described well by the following normalized form [32-34]:

$$\frac{1}{A_0}\left(\frac{d\sigma}{d\Omega}\right)_{hmg} \approx \frac{1}{16\pi^2}\left(\frac{q_c}{2}\right)^4 \frac{|\Phi_0(q_z)|^2}{q_z^2 \sin(\alpha)} \frac{2\pi\eta}{q_{xy}^2}\left(\frac{q_{xy}}{q_{max}}\right)^\eta, \tag{5.3}$$

where $q_c = 2k\sin(\alpha_c)$ is the critical wave vector for total reflection (for water subphase, $q_c = 0.0218$ Å^{-1} or $\alpha_c = 0.154°$ at $\lambda = 1.55$ Å). The inverse $2\pi/q_{max}$ of the upper cutoff wave vector corresponds to the smallest capillary wavelength, which is on the order of the nearest neighbor distance between molecules on the surface. The structure factor $|\Phi_0(q_z)|^2$ arises from an average local or "intrinsic" electron density profile $<\rho_{T=0}(z)>$

155

across the interface and can be expressed as (see Appendix B)

$$|\Phi_0(q_z)|^2 = \frac{R_{T=0}(q_z)}{R_F(q_z)}, \tag{5.4}$$

where $R_F(q_z)$ is the Fresnel reflectivity of an ideally flat and sharp subphase/gas interface. $R_{T=0}(q_z)$ refers to the reflectivity due to the intrinsic profile $\langle\rho_{T=0}(z)\rangle$ that would be obtained if the capillary waves were absent, i.e., if $\langle h^2(0)\rangle = 0$. In the limit $q_z \gg q_c$, Eq. (5.4) approaches the well known expression based on the Born approximation [32-34]

$$|\Phi_0(q_z)|^2 \approx \left| \int_{-\infty}^{+\infty} dz \frac{d}{dz} \left[\frac{\langle\rho_{T=0}(z)\rangle}{\rho_\infty} \right] e^{-iq_z z} \right|^2, \tag{5.5}$$

where ρ_∞ is the electron density in the bulk subphase ($\rho_\infty = 0.334$ e/Å^3 for water). For small values of q_z that are comparable to q_c, Eq. (5.4) can be evaluated by using the matrix method of the Parratt formalism, which is based on a division of $\langle\rho_{T=0}(z)\rangle$ into many constant-density slabs and the application of the exact boundary conditions at each slab/slab interface [35, 36].

In the analysis, the intrinsic profile $\langle\rho_{T=0}(z)\rangle$ is extracted by constructing a model profile and fitting the corresponding $R(q_z)$ based on Eqs. (5.1)-(5.5) to the measured XR data. This procedure also allows the extraction of the structure factor $|\Phi_0(q_z)|^2$. Assuming that this factor is known, the theoretical XOSDS curve $[\Delta I(\alpha, \beta)/I_0]_{hmg}$ that would be expected for a homogeneous film can be calculated with no adjustable parameters and can be compared with the observed intensity $\Delta I(\alpha, \beta)/I_0$. If there exist some thermal or static surface inhomogenities (i.e., lateral density fluctuations other than those due to capillary waves) at lateral length scales that are accessible by β-scans (100 Å to 1 μm), then, excess scattering $\Delta I/I_0 - [\Delta I/I_0]_{hmg} > 0$ will be observed in off-specular regions [32, 37].

Grazing incidence diffraction (GID). All the GID measurements to be reported, including the characterization of Bragg rods [38], were made by scanning the intensities

scattered away from the incidence plane ($2\theta \neq 0$) and near the surface plane ($0 < \beta < 5°$), as a function of 2θ or the lateral wave vector q_{xy}. The incident angle was fixed at $\alpha = 0.12°$ ($< \alpha_c = 0.154°$), corresponding to an illuminated footprint of extension ~ 50 mm along the incident beam direction. The slit settings used in typical scans were: (H_1, W_1) = (8.0 mm, 2.0 mm) at S_1 and (H_2, W_2) = (11.5 mm, 2.0 mm) at S_2. The in-plane resolution was limited by the horizontal slit width W_1 at S_1 and corresponded to a FWHM (full width at half maximum) resolution of $\delta(2\theta) = W_1/(S_2 - S_1) = 0.24°$ or $\delta q_{xy} \approx 2k\delta(2\theta) = 0.017$ Å^{-1}. Due to the relatively large vertical opening H_2 of the detector slits, signals scattered over $\Delta\beta = 1.0°$ or $\Delta q_z = 0.071$ Å^{-1} were accepted by the detector.

5.3 Results and Discussion

5.3.1 Π-*A* Isotherms

Representative isotherms obtained from AuSC16 films at 25.0 °C are shown in Fig. 5.2. Three separate step-wise continuous scans (lines; each from a fresh film) are plotted together to demonstrate the reproducibility of the isotherm. A relaxation isotherm is indicated by the filled circles. The only significant difference between the two types of isotherms is that at a given area/particle *A*, the surface pressure in the relaxation isotherm is consistently lower than that in the continuous isotherm. Apart from this difference due to relaxation effects, the qualitative shape of the isotherms is nearly independent of the two different compression methods used, and the main features in the isotherms occur at almost the same values of *A*.

The isotherms are characterized by the appearance of a broad plateau-like region of finite surface pressure ($\Pi \sim 5$ dyn/cm in the continuous scans) whose width is consistent with a first-order monolayer/bilayer transition. Around $A_t \sim 1700$ Å^2/particle, just to the right of this plateau where an initial steep rise in Π is observed, the entire surface should to be coated uniformly by a close packed AuSC16 monolayer. At $A_t \sim 1650$ Å^2/particle, the increase in Π is halted and replaced by the plateau, indicating a
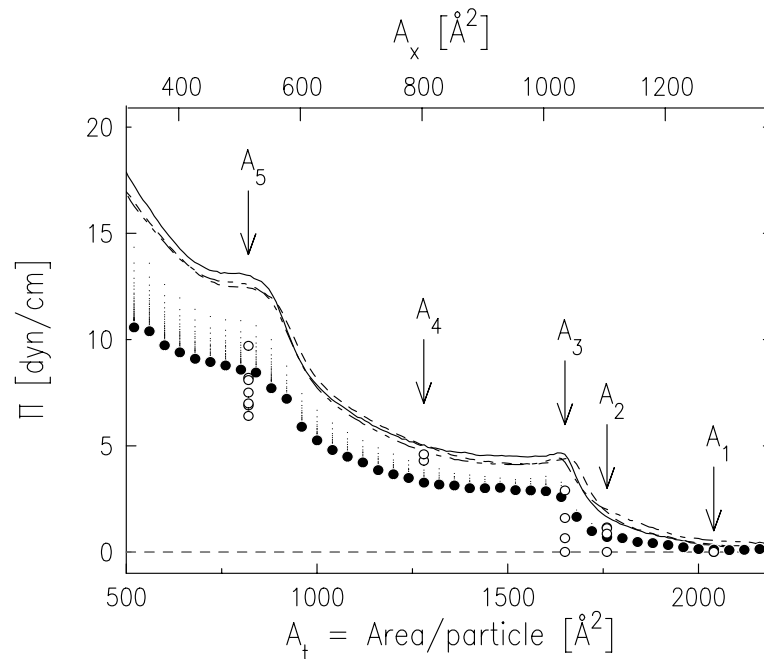
Figure 5.2: Step-wise continuous (lines) and relaxation (filled circles) isotherms on AuSC16 films on HCl/water subphase (pH = 3) at 25 °C. Points where x-ray measurements were made are indicated by open circles and A_i. The two area/particle scales on the bottom and top are related by $A_t = 1.6\,A_x$. See sec. 5.3.5.

collapse of the monolayer and the beginning of a transfer of particles into the third dimension in some way. Compression across the plateau region leads to only a very slow increase in Π until a second well-defined rise is observed around $A_t \sim 900$ Å^2/particle. The fact that the area/particle values over this second rise are close to half of the values observed for the initial rise on the low-density side of the plateau, suggests that the AuSC16 film consists primarily of a bilayer at $A_t \sim 900$ Å^2/particle. According to this interpretation, the plateau region corresponds to coexistence between monolayer and bilayer domains, with the bilayer fraction increasing with compression. Other Langmuir films that undergo a monolayer/bilayer transition, such as those of rod-like polypeptide PBLG [37], are characterized by very similarly shaped isotherms.

Figure 5.2 shows some quantitative differences between the two types of isotherms. At large area ($A_t > 1750$ Å^2/particle), the continuous scans show a gradual

increase in Π (from $\Pi \sim 0$), but the surface pressure drops nearly to zero if the film is allowed to relax sufficiently. This is probably due to an incomplete surface coverage at large area and solid-like stiffness of AuSC16 monolayer islands, between which bare or uncoated surface areas still remain. As expected, the difference in Π between the two isotherms grows with compression across and past the first plateau, indicating close-packing of particles over these high-density regimes. Although the continuous scans display another rise in Π below $A_t \sim 700$ Å^2/particle, such a feature is absent in the relaxation isotherm, which only shows a gradual Π increase over the same region. This seems to indicate that the layer-by-layer growth of the film with compression does not continue beyond the bilayer, but either multilayer domains or bulk aggregates are being formed at the highest densities shown in Fig. 5.2.

As indicated by open circles in Fig. 5.2, x-ray measurements were made on films at $A = A_1$ through A_5. In terms of the "trough" area/particle A_t, these points are located at $A_{t,1} = 2040$, $A_{t,2} = 1760$, $A_{t,3} = 1650$, $A_{t,4} = 1280$, and $A_{t,5} = 820$ Å^2/particle. The XR results to be discussed below provide strong evidence that the AuSC16 film indeed undergoes a compression-induced monolayer/bilayer transition.

5.3.2 XR: Structures along surface normal

Representative reflectivity data obtained from AuSC16 films are plotted in terms of the normalized reflectivity R/R_F in Fig. 5.3. The top three curves showing a nearly identical oscillation behavior correspond to monolayers at $A = A_1$, A_2, and A_3. The q_z positions of two maxima and a minimum evident in each R/R_F curve shift very little between these data sets, indicating that the films at these surface densities have roughly the same thickness. The amplitude of the oscillation is very large; for example, $R/R_F \sim 60$ at $q_z = 0.16$ Å^{-1} for the first maximum in the data for the film at A_3. This indicates the presence of a surface layer with much higher density than that in the bulk subphase, as expected for AuSC16 films. The smaller peak value $R/R_F \sim 48$ for A_1 ($q_z = 0.17$ Å^{-1})
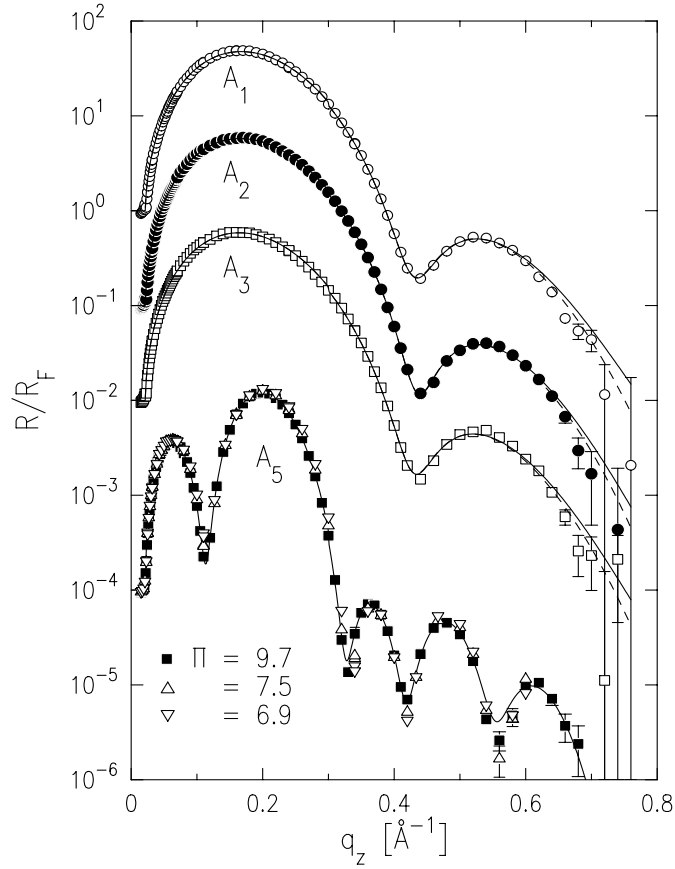
Figure 5.3: Specular reflectivity data (symbols) normalized to the Fresnel reflectivity, measured from AuSC16 films at points A_1, A_2, A_3 and A_5 in the isotherm. The three sets of data taken at A_5 are plotted together. The data taken at different A are shifted vertically for clarity. The lines are the best-fit R/R_F curves based on box-model average intrinsic profiles $<\rho_{T=0}(z)>/\rho_\infty$.

indicates that the average layer density at A_1 is lower than at A_3 and probably originates from incomplete surface coverage at large area. The data obtained from the other side of the coexistence plateau at A_5, where the film is supposedly a bilayer, are shown on the bottom of Fig. 5.3. For this area, three separate data sets obtained at $\Pi = 9.7$, 7.5, and 6.9 dyn/cm are plotted on top of each other. The reproducibility of the data evidenced by a good overlap between them demonstrates that the average film structure along the surface normal is stable over this range of Π. It is clear from the much faster oscillation of these

R/R_F curves that the film at A_5 must be significantly thicker than the monolayers at A_1, A_2, and A_3.

The quantitative analysis of the R/R_F data has been carried out by using "box models" for the average intrinsic profile $<\rho_{T=0}(z)>$, in which each layer is represented by a box of thickness l_i and relative density $\phi_i = \rho_i/\rho_\infty$. The interfacial diffuseness of the profile (or short-range intrinsic roughness of non-capillary origin) between adjacent boxes i and j = i + 1 is described by an error function, whose gradient is a gaussian with standard deviation $\sigma_{P,ij}$. Theoretical R/R_F curves based on Eqs. (5.1)–(5.5), with the intrinsic structure factor $|\Phi_0(q_z)|^2$ given by box-model profiles $<\rho_{T=0}(z)>$, were fitted to the observed data by using the known values of T, $\gamma = \gamma_w - \Pi$ ($\gamma_w = 72$ dyn/cm for water at 25 °C), and the detector resolutions. The upper cutoff wave vector in Eq. (5.3) was fixed at $q_{max} = 0.2$ Å^{-1}, which corresponds to the position of the lowest-order GID peak observed from AuSC16 films (to be discussed later). This assignment of q_{max} is equivalent to setting the shortest capillary wavelength to the size of AuSC16 particles. Any capillary modes with even shorter wavelengths, if they are not completely quenched, are assumed to contribute to the profile roughness $\sigma_{P,ij}$ in $<\rho_{T=0}(z)>$. The separation of their contribution from the true intrinsic roughness would require temperature-dependent measurements [33, 39, 40].

As will be shown below, the average electron density within the AuSC16 film relative to that of water can be as high as $\phi \sim 5.6$. This implies that in the range $q_c = 0.0218$ Å$^{-1} < q_z < \sqrt{\phi}\, q_c \sim 0.05$ Å^{-1}, the electric fields within the layer are evanescent waves and the penetration of x rays into the bulk subphase occurs only through tunneling across this layer. In such cases, the applicability of the Born approximation (BA) requires that $q_z \gg \sqrt{\phi}\, q_c$ (see Appendix B). Therefore, for the fitting over the low q_z range $0.06 < q_z < 0.3$ Å^{-1}, the factor $|\Phi_0(q_z)|^2$ was evaluated by employing the Parratt formalism, where the box-model intrinsic profile $<\rho_{T=0}(z)>$ was divided into many slabs of thickness 0.1 Å. For $q_z > 0.3$ Å^{-1}, the calculation of the fitting curve was switched to

the one based on the BA expression Eq. (5.5) for $|\Phi_0(q_z)|^2$. The fitting over these two q_z ranges were done simultaneously, using exactly the same density profile $\langle\rho_{T=0}(z)\rangle$.

The best-fits to the R/R_F data are indicated by the lines (both solid and dashed ones) in Fig. 5.3, and the corresponding intrinsic profiles $\langle\rho_{T=0}(z)\rangle$ are illustrated in Fig. 5.4. The best-fit values for the box-model parameters are summarized in Table 5.1.
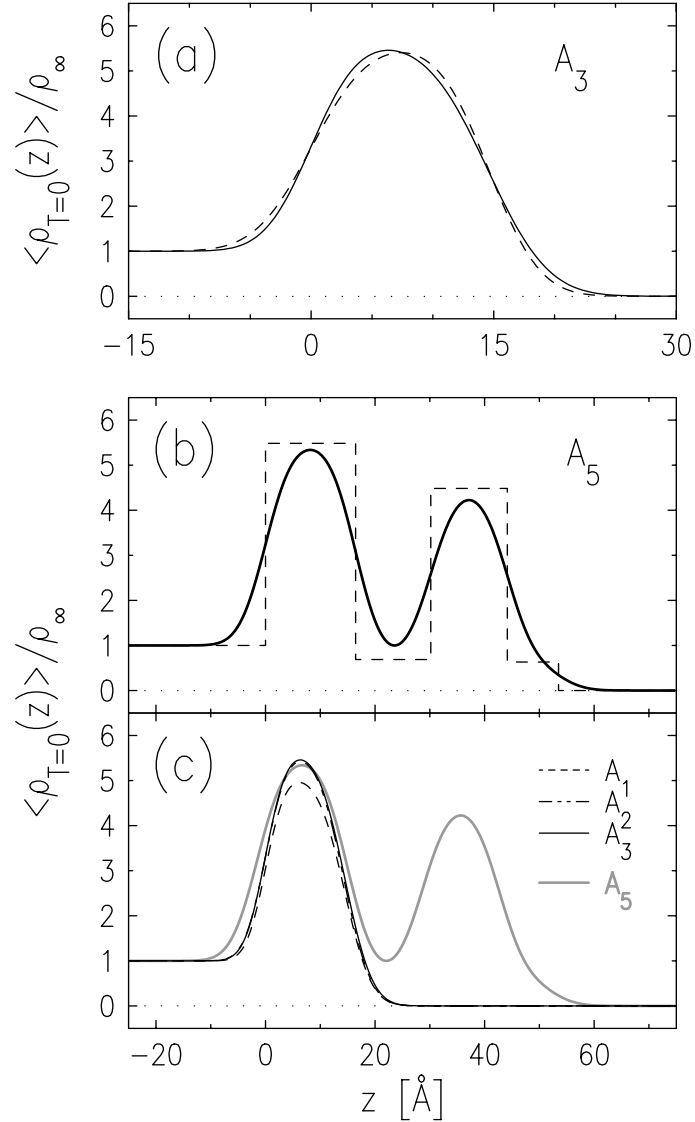

Figure 5.4: Average intrinsic electron density profiles $\langle\rho_{T=0}(z)\rangle/\rho_\infty$ extracted from the best fits to the R/R_F data. (a) AuSC16 monolayer at A_3, where the solid line is for Type I and the dashed one is for Type II profile. (b) AuSC16 bilayer at A_5, where the dashed lines are from the 4-box. Panel (c) compares the profiles obtained at different A.

Table 5.1: Best-fit parameters for the average local electron density profile $<\rho_{T=0}(z)>/\rho_\infty$ across the water/AuSC16/gas interface.

(a) 1-box model for AuSC16 monolayers.

A_t [Å²/part.]	Π [dyn/cm]	Type*	$\phi_1 = \rho_1/\rho_\infty$	l_1 [Å]	$\sigma_{P,w1}$ [Å]	$\sigma_{P,1g}$ [Å]
2040	0	I	5.09 ± 0.12	14.44 ± 0.15	2.79 ± 0.14	3.85 ± 0.18
		II	5.02 ± 0.12	14.59 ± 0.16	3.47 ± 0.19	3.13 ± 0.12
1760	0.3	I	5.63 ± 0.13	14.31 ± 0.15	3.08 ± 0.14	3.90 ± 0.18
		II	5.57 ± 0.13	14.41 ± 0.15	3.59 ± 0.19	3.37 ± 0.12
1650	2.9	I	5.65 ± 0.15	14.49 ± 0.17	3.02 ± 0.16	3.95 ± 0.19
		II	5.58 ± 0.15	14.61 ± 0.19	3.63 ± 0.22	3.31 ± 0.14

* Type I: $\sigma_{P,w1} < \sigma_{P,1g}$; Type II; $\sigma_{P,w1} > \sigma_{P,1g}$.

(b) 4-box model for a AuSC16 bilayer.†

A_t [Å²/pt.]	Π [dy/cm]	ϕ_1	ϕ_2	ϕ_3	ϕ_4	l_1 [Å]	l_2 [Å]	l_3 [Å]	l_4 [Å]	σ_P [Å]
820	9.7	5.49	0.69	4.49	0.63	16.44	13.73	13.97	9.37	3.83
		± 0.11	± 0.12	± 0.13	± 0.13	± 0.27	± 0.28	± 0.31	±0.82	± 0.15

†Single parameter σ_P was used for profile diffuseness at each box interface.

For the monolayers at $A = A_1$, A_2, and A_3, the use of a single box in the model profile is sufficient to obtain good fits. However, for each set of R/R_F data, the analysis produced two sets of parameters that fit the data equally well. For one set of parameters (Type I), the intrinsic diffuseness parameter $\sigma_{P,1g}$ for the layer/gas interface is larger than $\sigma_{P,w1}$ for the water/layer interface ($\sigma_{P,1g} > \sigma_{P,w1}$); for the other set (Type II), $\sigma_{P,1g} < \sigma_{P,w1}$. In Fig. 5.3, the fits based on Type I and II are indicated by the solid and dashed curves, respectively. Fig. 5.4(a) compares the Type-I and Type-II intrinsic profiles for the AuSC16 monolayer at $A = A_3$. From the obtained data, it is not possible to determine which of the two best-fit profiles represents the actual profile. This ambiguity probably arises from a combination of the limited q_z range of the data and the difficulty with extracting complete phase information in the complex number $\Phi_0(q_z)$, as discussed previously by Pershan [41]. This question about the uniqueness of extracted density

profiles cannot be resolved here. However, Fig. 5.4(a) shows that apart from slight differences in shape, both the Type-I and Type-II profiles are characterized by a single layer of similar density and thickness (also see Table 5.1(a)).

The intrinsic profiles $\langle\rho_{T=0}(z)\rangle$ obtained at A_1, A_2, and A_3 are consistent with the interpretation that the AuSC16 film is indeed a monolayer at these surface densities. At $A = A_3$, the thickness and density parameters of the single box layer are given by $l_1 \sim 14.5$ Å and $\phi_1 \sim 5.6$. The value for l_1 is roughly of the same magnitude as (but slightly smaller than) the FWHM Δz of the density distribution given by the projection of an Au core onto the z-axis, which can be estimated to be $\Delta z \sim D/\sqrt{2} = 19$ Å for a core approximated as a uniform sphere of diameter $D = D_{TEM} = 27$ Å ($\Delta z = l_1$ for $D = 20.5$ Å). The plausibility of the value for ϕ_1 can be seen in the following way. The electron density within the Au core is $\phi_{Au} = \rho_{Au}/\rho_\infty = 14.0$ (bulk values: $\rho_{Au} = 4.67\ e/\text{Å}^3$ for fcc gold crystal; $\rho_\infty = 0.334$ $e/\text{Å}^3$ for water), whereas the density for the alkyl chains around each core is roughly on the order of $\phi_{alk} = 1$ (assuming cross packing). According to these numbers and the assumption $\phi_1 = F \cdot \phi_{Au} + (1 - F) \cdot \phi_{alk}$, a fraction $F \sim 0.35$ of the surface area can be attributed to the Au cores in the plane through their centers. If the value $A_{t,3} = 1650$ Å^2/particle at A_3 were to be taken as a measure of the average area/particle, the average Au core diameter would be roughly equal to $D \sim 2(F \cdot A_{t,3}/\pi)^{1/2} \sim 27$ Å. The fact that this value agrees with the size distribution $D_{TEM} = 27 \pm 6$ Å obtained from the TEM measurements, indicates that the density ϕ_1 extracted from the XR measurements is reasonable for a monolayer of AuSC16 particles.

The formation of a bilayer on the high-density side of the coexistence plateau is clearly demonstrated by the intrinsic profile $\langle\rho_{T=0}(z)\rangle$ obtained at A_5, shown in Fig. 5.4(b). The fitting of the R/R_F data at A_5 required the use of a 4-box model to construct the non-uniform bilayer profile, but in order to minimize the number of fitting parameters, a single parameter σ_P was used to describe the profile diffuseness of all the box/box interfaces. The 4-box parameters for this bilayer are listed in Table 5.1(b), and

the corresponding boxes in the model are indicated by the dashed line in Fig. 5.4(b). The same bilayer profile is compared with the Type-I profiles of the monolayers at A_1, A_2, and A_3 in Fig. 5.4(c).

The presence of two distinguishable layers in the bilayer is evident from the two well-separated maxima in the profile in Fig. 5.4(b), indicating that the AuSC16 particles belong to only one or the other of the layers. Based on the positions of the two peaks, the central planes of the two layers are separated by a distance of $l_{12} = 29.0$ Å along the surface normal. The fact that the relative density is close to unity ($<\rho_{T=0}>/\rho_\infty \sim 1$) at the minimum between the layers is consistent with the presence of alkyl chains in this inter-layer region and the exclusion of Au cores. Fig. 5.4(c) shows that the first layer of the bilayer, right above the subphase, is slightly thicker than the monolayers are but its peak density is comparable to that of the monolayer at A_3. The second layer closer to the gas above is, on average, less dense (by ~ 18 %) than the first layer, indicating that this layer on top is the one newly created by lateral compression.

All these observations can be interpreted as follows: The AuSC16 monolayer achieves a maximum lateral density sustainable at the low-density end of the coexistence plateau (at A_3). Subsequent compression across the plateau displaces more and more AuSC16 particles out of the monolayer up onto the second layer to form a bilayer. It appears that during this process, a point is reached where the occupied fraction of the second layer becomes large enough to hinder a further upward transfer of AuSC16 particles and the first layer begins to experience the effect of lateral compression. This can be seen from the fact that the first layer of the bilayer is thicker than the monolayer and also from the gradual increase in Π for $A_t < \sim 1250$ Å^2/particle (see Fig. 5.2). These observations suggest that compression across the plateau increases the width of the distribution in the vertical positions of AuSC16 particles in the first layer. On the basis of this and the less than full coverage of the second layer in the bilayer, it seems reasonable to suppose that the bilayer is less likely to be laterally homogeneous than the

monolayer. The surface homogeneity of AuSC16 films is considered in the following section.

5.3.3 XOSDS: Surface homogeneity

The results of β-scans measured with the incident angle fixed at $\alpha = 1.0°$ and $2.0°$ are summarized in Fig. 5.5 for an AuSC16 monolayer at A_3 and in Fig. 5.6 for a bilayer at A_5. For each scan, a large peak at $\beta = \alpha$ corresponds to the specular reflection. The surface enhancement peak ("Yoneda" peak), which is expected to occur at $\beta = \alpha_c$ (~ $0.154°$), is not very visible in these scans. This is a consequence of the fact that the presence of a high-density layer on the surface tends to suppress the surface enhancement peak, as described in Appendix B. The characterization of off-specular spectra has been limited by the resolution $\delta\beta$ near the specular peak and by low counting rates at large β (~ $5°$). In terms of the lateral wave vector transfer q_y, these limits correspond to a range given by: $k\sin(\alpha)\delta\beta = 1.1 \times 10^{-4} \text{ Å}^{-1} < |q_y| < 1.5 \times 10^{-2} \text{ Å}^{-1}$ for $\alpha = 1.0°$ and 2.2×10^{-4} $\text{Å}^{-1} < |q_y| < 1.3 \times 10^{-2} \text{ Å}^{-1}$ for $\alpha = 2.0°$. Therefore, lateral density fluctuations over length scales of ~100 Å to 1 μm are being probed by these measurements.

In Figs. 5.5 and 5.6, the solid curves represent the theoretical normalized intensity difference $[\Delta I(\alpha, \beta)/I_0]_{\text{hmg}}$ expected from the presence of capillary waves and the assumption that the given film is otherwise laterally homogeneous. For each film, the intrinsic structure factor $|\Phi_0(q_z)|^2$ used in the calculation is based on the fitting of the specular reflectivity data which was obtained from the same film immediately before the β-scans. All the other parameters needed for the calculation are known, except that q_{max} $= 0.2 \text{ Å}^{-1}$ has been assumed as in the case of XR.

Figure 5.5 shows that in the case of a monolayer at A_3, the observed off-specular intensities $\Delta I(\alpha, \beta)/I_0$ agree fairly well with the expected curve $[\Delta I(\alpha, \beta)/I_0]_{\text{hmg}}$. This implies that the off-specular scattering can be attributed almost entirely to the interfacial height fluctuations due to capillary waves and that the close-packed AuSC16 monolayer
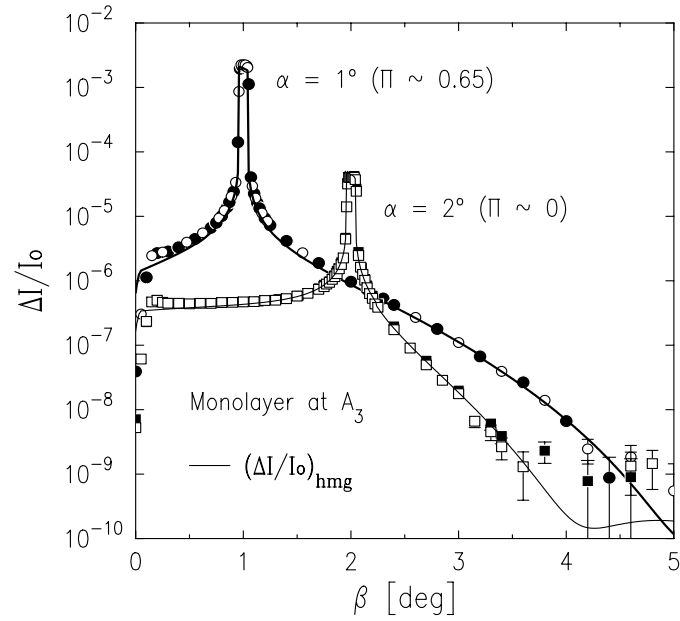
Figure 5.5: β-scans at $\alpha = 1°$ (circles) and $\alpha = 2°$ (squares) from the AuSC16 *monolayer* at A_3. The solid lines are the theoretical curves expected for a homogeneous film.

Figure 5.6: β-scans at $\alpha = 1°$ (circles) and $\alpha = 2°$ (squares) from the AuSC16 *bilayer* at A_5. The solid lines are the theoretical curves expected for a homogeneous film.
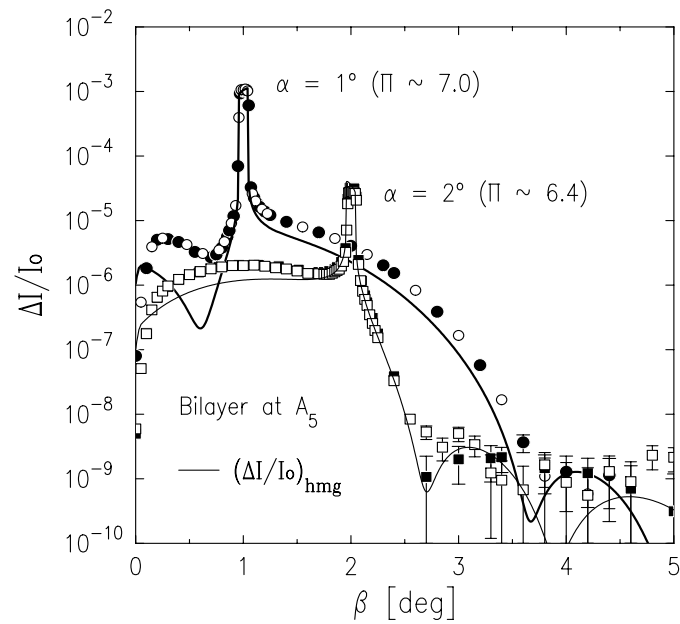
167

at A_3 is laterally homogeneous. This result is analogous to the case of a homogeneous PBLG monolayer under a finite surface pressure [32, 37].

By contrast, β-scan data shown in Fig. 5.6 for a bilayer at A_5 are consistently higher than the homogeneous curve $[\Delta I(\alpha, \beta)/I_0]_{\text{hmg}}$ in the off-specular regions, except for the range $\beta > \alpha = 2.0°$ where both the data and the theory show low intensities. It can be shown that if the local density $\rho_{T=0}(\mathbf{r})$ deviates from its lateral average $<\rho_{T=0}(z)>$, i.e., $\delta\rho_{T=0}(\mathbf{r}) = \rho_{T=0}(\mathbf{r}) - <\rho_{T=0}(z)> \neq 0$, the scattering cross section acquires a *second term* beyond Eq. (5.3), which can be expressed as [37]

$$\frac{1}{A_0}\left(\frac{d\sigma}{d\Omega}\right)_{inhmg} = \frac{1}{16\pi^2}\left(\frac{q_c}{2}\right)^4\frac{1}{A_0}\left|\int d^3 r e^{-i\vec{q}\cdot\vec{r}} e^{-iq_z h(r_{xy})}\frac{\delta\rho_{T=0}(\vec{r})}{\rho_\infty}\right|^2, \quad (5.6)$$

where the local interfacial height $h(r_{xy})$ fluctuates with capillary waves. Therefore, the observation of *excess* off-specular scattering suggests that some form of lateral density inhomogeneities $\delta\rho_{T=0}(\mathbf{r}) \neq 0$ exist within the bilayer at A_5. This result is similar to the case of a PBLG bilayer, for which the observation of excess off-specular scattering has been attributed to inhomogeneities in the newly formed second layer [32, 37]. The observation that the AuSC16 bilayer is less homogeneous than the monolayer is not too surprising given the high degree of compression that the film underwent prior to its formation and the incomplete coverage of the second layer, as pointed out at the end of the XR section.

Qualitatively, a close inspection of all curves in Fig. 5.6 shows that the magnitude $\Delta I(\alpha, \beta)/I_0 - [\Delta I(\alpha, \beta)/I_0]_{\text{hmg}} > 0$ of the excess scattering seems to decrease with increasing $q_z \sim k(\alpha + \beta)$. This behavior may be an indication that the laterally inhomogeneous regions are restricted to a certain thickness within the bilayer. Another possibility is the presence of long-wavelength height fluctuations (probably static) of AuSC16 particles that are not conformal with capillary fluctuations. Quantitative analysis of the excess off-specular scattering based on Eq. (5.6) is currently in progress.

Another important observation from Fig. 5.6 is that although the theoretical curve $[\Delta I(\alpha, \beta)/I_0]_{hmg}$ for $\alpha = 1.0°$ oscillates with β and has a well-defined minimum at $\beta \sim 0.6°$ (or equivalently, at $q_y = 4.0 \times 10^{-4}$ Å^{-1} and $q_z = 0.11$ Å^{-1}), such a dip in intensity is much less apparent in the actual data. The minimum at $q_z = 0.11$ Å^{-1} arises from the factor $|\Phi_0(q_z)|^2$ and corresponds to the first minimum in the R/R_F data shown for the bilayer in Fig. 5.3. Note that the value $\pi/q_z = 28$ Å compares well with $l_1 + l_2 = 30.2$ Å and $l_2 + l_3 = 27.7$ Å, while all the density differences across the box/box interfaces are roughly of the same order of magnitude (except for the box-4/gas interface; see Table 5.1(b) and Fig. 5.4(b)). Therefore, the minimum at $q_z = 0.11$ Å^{-1} arises from the condition that x-ray waves scattered off from the subphase/box-1 and box-1/box-2 interfaces interfere destructively with those from the box-2/box-3 and box-3/box-4 interfaces, respectively. In other words, this dip in intensity would appear in the off-specular data only if the height fluctuations of first-layer and second-layer AuSC16 particles were well correlated over a lateral distance that is comparable to or larger than $q_y^{-1} \sim 2500$ Å. The strong suppression of the minimum in the data, therefore, suggests a lack of such conformality between the two layers of the bilayer [42]. This inference is also consistent with a low degree of lateral homogeneity for the bilayer.

5.3.4 GID: In-plane structures

Representative GID patterns measured from AuSC16 films at various points in the isotherm are compared over a small range of q_{xy} in Fig. 5.7 (a linear plot) and over a larger range of q_{xy} in Fig. 5.8(a) (a semi-log plot). All the data shown correspond to scans near the surface horizon ($0 < q_z < 0.074$ Å^{-1}). In Fig. 5.7, all the dashed lines are identical and correspond to the bottommost data from a monolayer at A_1. Whether the film is a monolayer or a bilayer, the observed GID pattern is characterized by a strong peak at $q_{xy} = 0.215$ Å^{-1}. Since the peak is already present at A_1, the in-plane structure corresponding to it must be spontaneously formed upon spreading of the film. The
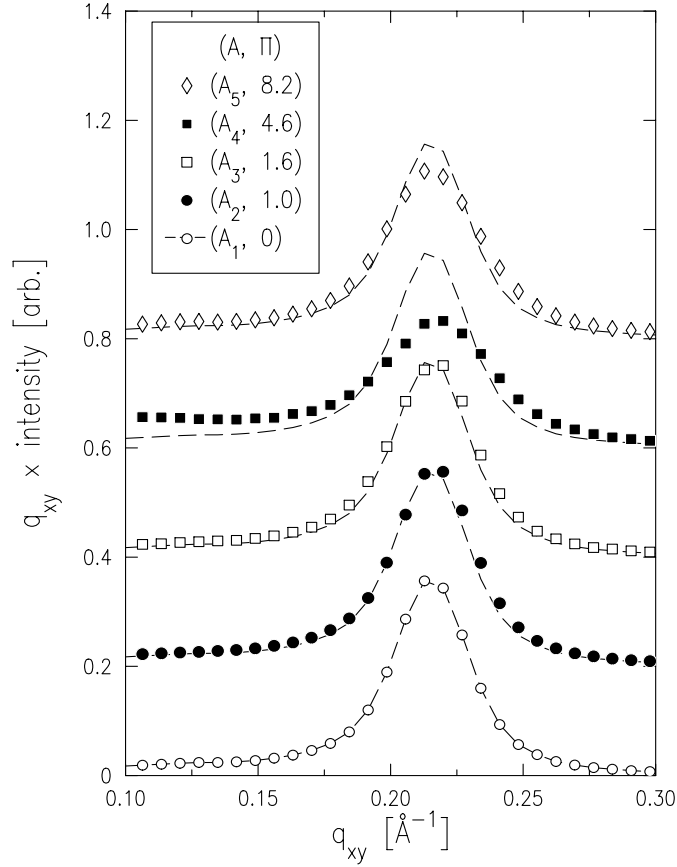
Figure 5.7: A linear plot of the lowest-order GID peaks from AuSC16 films, shifted vertically for clarity. The dashed lines are identical and correspond to the bottommost data at A_1.

position of this peak is nearly independent of A or Π, and hence lateral compression appears to have very little effect upon the average inter-particle distance in the laterally ordered domains.

Figure 5.8(a) shows some evidence for the presence of additional higher-order peaks. The patterns contain a weak peak at $q_{xy} \sim 0.56$ $\mathrm{\mathring{A}}^{-1}$ and possibly another feature around $q_{xy} \sim 0.37$ $\mathrm{\mathring{A}}^{-1}$ that is even weaker. The positions of these weak higher-order peaks and the much more intense lowest-order peak at $q_{xy} = 0.215$ $\mathrm{\mathring{A}}^{-1}$ are all consistent with 2D hexagonal packing with a nearest-neighbor distance of $a = 34$ $\mathrm{\mathring{A}}$. The number of equivalent points in the corresponding 2D reciprocal lattice (also hexagonal) is plotted as
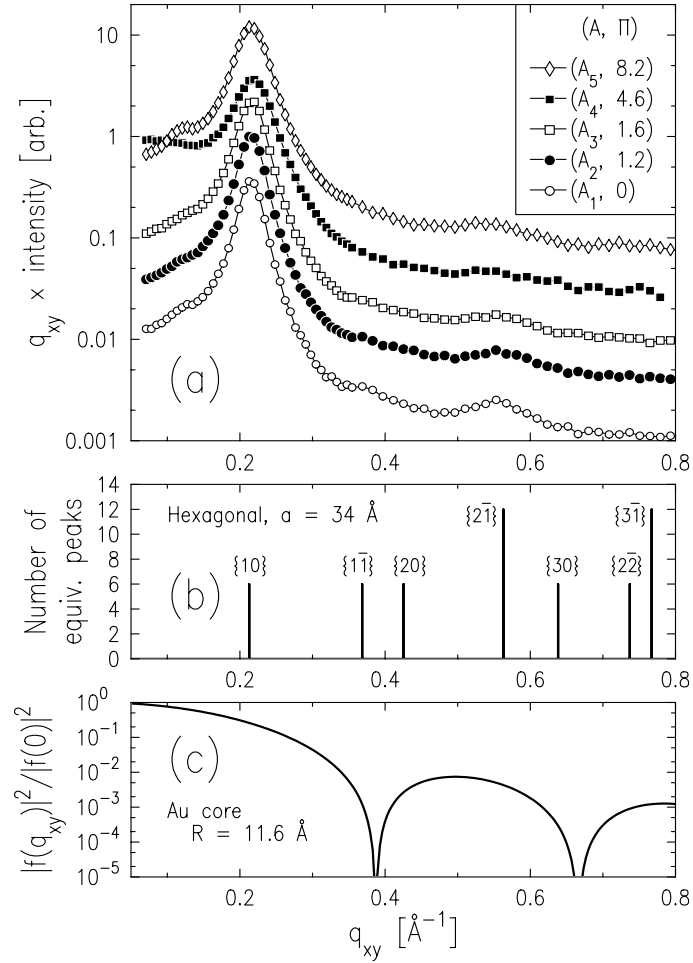
Figure 5.8: (a) A semi-log plot of GID data from AuSC16 films over larger q_{xy} range (shifted vertically for clarity), (b) the number of equivalent points in reciprocal space for a 2D hexagonal lattice with a nearest-neighbor distance $a = 34$ Å, and (c) calculated molecular form factor for a uniform sphere of diameter $D = 23.2$ Å.

a function of q_{xy} in Fig. 5.8(b). The indices $\{hk\}$ labeling each set of equivalent peaks (or lattice planes in the real space) are based on the primitive unit cell. Comparison between Figs. 5.8(a) and 5.8(b) shows that the three peaks in the data are located fairly close to the expected positions of the $\{10\}$, $\{1\bar{1}\}$ and $\{2\bar{1}\}$ peaks from the 2D hexagonal lattice.

In general, GID peaks are weaker and more difficult to observe at higher q_{xy} because the magnitudes of the molecular form factor and the Debye-Waller factor decrease with increasing q_{xy}. This is likely to be the reason for the absence of further

171

higher-order peaks for $q_{xy} > 0.6$ Å^{-1} in the observed GID patterns. The fact that the $\{2\bar{1}\}$ peak is discernable in the data probably arises from the relatively large number of reciprocal lattice points at this value of q_{xy} (see Fig. 5.8(b)). On the other hand, the $\{1\bar{1}\}$ and $\{20\}$ peaks are much less clearly visible in the data, even though they occur at lower q_{xy} than the $\{2\bar{1}\}$ peak. This can be explained in terms of the molecular form factor $|f(q)|^2$ of AuSC16 particles, as follows. Most of the contribution to $|f(q)|^2$ comes from the Au cores because of their much higher electron density compared with that of alkyl thiol chains around them. It can be shown that if the size polydispersity of Au cores is neglected and the core is approximated as a uniform sphere of radius $R = D/2$, the form factor is given by

$$|f(q)|^2 = |f(0)|^2 \left| \frac{3}{q^3 R^3} \left[\sin(qR) - qR\cos(qR) \right] \right|^2 , \tag{5.7}$$

where $q^2 = q_{xy}^2 + q_z^2$ and $f(0)$ is equal to the total number of electrons contained in an Au core of radius R. Fig. 5.8(c) plots the ratio $|f(q = q_{xy}, q_z = 0)|^2/|f(0)|^2$ for the case of $R =$ 11.6 Å (or $D = 23.2$ Å), which has a minimum around $q_{xy} \sim 0.4$ Å^{-1}. The polydispersity of Au cores should smear out this minimum. It is nevertheless clear from this plot that the form factor arising from typical sizes of AuSC16 particles should lead to a very low intensity over the range of q_{xy} where the $\{1\bar{1}\}$ and $\{20\}$ peaks are located.

The extent of lateral positional correlations associated with the in-plane order can be estimated from the observed width of the GID peaks. For this purpose, the FWHM width Δq_{xy} of the $\{10\}$ peak at $q_{xy} = G_{10}$ has been extracted by fitting it to a Lorentzian raised to a power of ν with constant and linear background terms, such that the intensity above the background is proportional to $\propto [1 + (q_{xy} - G_{10})^2/\sigma^2]^{-\nu}$. The FWHM width $\Delta q_{xy} = 2\sigma(2^{1/\nu} - 1)^{1/2}$ based on this fitting procedure is listed in Table 5.2. The table also lists a lateral correlation length ξ defined as $\xi = 2/[\Delta q_{xy} - \delta q_{xy}]$ (experimental resolution: $\delta q_{xy} = 0.017$ Å^{-1}). This definition of ξ is strictly valid only when both the resolution

Table 5.2: Observed position G_{10} and FWHM Δq_{xy} of the lowest-order GID peak based on fits to the form $q_{xy}I(q_{xy}) \propto [1 + (q_{xy} - G_{10})^2/\sigma^2]^{-\nu}$ (plus a linear and a constant background terms), where $\Delta q_{xy} = 2\sigma(2^{1/\nu} - 1)^{1/2}$. An associated lateral correlation length ξ is defined as $\xi \equiv 2/[\Delta q_{xy} - \delta q_{xy}]$, where the FWHM of the q_{xy} resolution is given by $\delta q_{xy} = 0.017$ Å^{-1}.

A_t [Å^2/part.]	Π [dyn/cm]	ν	G_{10} [± 0.001 Å^{-1}]	Δq_{xy} [± 0.002 Å^{-1}]	ξ [Å]
2040	0	1.4 ± 0.2	0.214	0.032	130 ± 14
1760	1.0	1.7 ± 0.2	0.215	0.036	104 ± 10
1650	1.6	1.9 ± 0.3	0.215	0.038	94 ± 8
1280	4.6	11 ± 13	0.217	0.050	61 ± 4
820	8.2	1.7 ± 0.2	0.215	0.042	80 ± 6

function and the line shape of a peak in the GID cross section are described by Lorentzians ($\nu = 1$), in which case the observed peak given by the convolution of the two also has a Lorentzian shape. Since this condition does not hold in the present case, the listed values of ξ should only be viewed as estimates.

For the monolayers at A_1, A_2, and A_3, the correlation length is roughly in the range $\xi \sim 90$ to 130 Å, which is only a few times larger than the nearest-neighbor distance $a = 34$ Å. Therefore, the 2D hexagonal packing of AuSC16 particles is only short-range order in the monolayer. It is interesting to note that the ratio $\xi/a \sim 3 - 4$ is comparable to the ratio $D_{TEM}/\Delta D_{TEM} = (27 \text{ Å})/(6 \text{ Å}) = 4.5$ between the mean and the standard deviation in the distribution of Au core diameters. This observation seems to suggest that the limited extent of positional correlations between AuSC16 particles originates from the polydispersity in their sizes. The A-dependent behaviors of the widths of the {10} peaks shown in Fig. 5.7 and ξ in Table 5.2 seem to indicate that compression of the monolayer from A_1 to A_3 leads to a slight reduction in the degree of lateral order. Another indication of this is provided by a slight drop in the {2$\bar{1}$} peak intensity with compression from A_1 to A_3.

Such a disordering effect of lateral compression is more clearly evident for the film at A_4 (a mid point along the coexistence plateau), for which the {10} peak is both broader and less intense than it is for the monoalyers (see Fig. 5.7 and Table 5.2). Another important observation about the data at A_4 is that the intensity scattered at low $q_{xy} < 0.2$ Å^{-1} is higher than that of the monolayers (see Fig. 5.8(a)). This suggests that some nearest-neighbor pairs of AuSC16 particles are separated by lateral distances that are larger than $a = 34$ Å. Given that the occupied fraction of the second layer should only be about a half or less on average at A_4, the observation of enhanced diffuse scattering at low q_{xy} is consistent with the presence of AuSC16 particles in the second layer.

After the film is compressed further to form a bilayer at A_5, the diffuse intensities at low q_{xy} drop back to the level close to that of the monolayers, which is consistent with a more complete coverage of the second layer. The fact that the {10} peak becomes also more intense and sharper than it is at A_4, suggests that due to their increased number some of the second-layer particles now display the same hexagonal packing order that exists in the monolayer. However, Fig. 5.7 shows that the peak intensity for the bilayer is still not as high as that of the monolayers. This seems to indicate that in spite of a nearly two-fold increase in the number of particles per unit area in going from a monolayer to a bilayer, the number of those belonging to *ordered* domains does not increase by the same amount. This issue is considered further below.

The q_z-dependence of the intense {10} peak has been characterized by taking a series of q_{xy} scans at different heights $<q_z>$ above the surface. The results for the monolayer at A_3 are summarized in Fig. 5.9. The plot against q_{xy} in Fig. 5.9(b) shows that the center of the peak shifts very little with increasing $<q_z>$, which is consistent with the behavior of a Bragg rod. The observed peak values (open circles) are plotted as a function of q_z in Fig. 5.9(c), where the horizontal bars represent the fixed width $\Delta q_z = 0.071$ Å^{-1} of the detector opening. It is clear that the Bragg rod from the monolayer is centered at $q_z = 0$ and falls off monotonically with q_z. For a GID peak arising from a

174
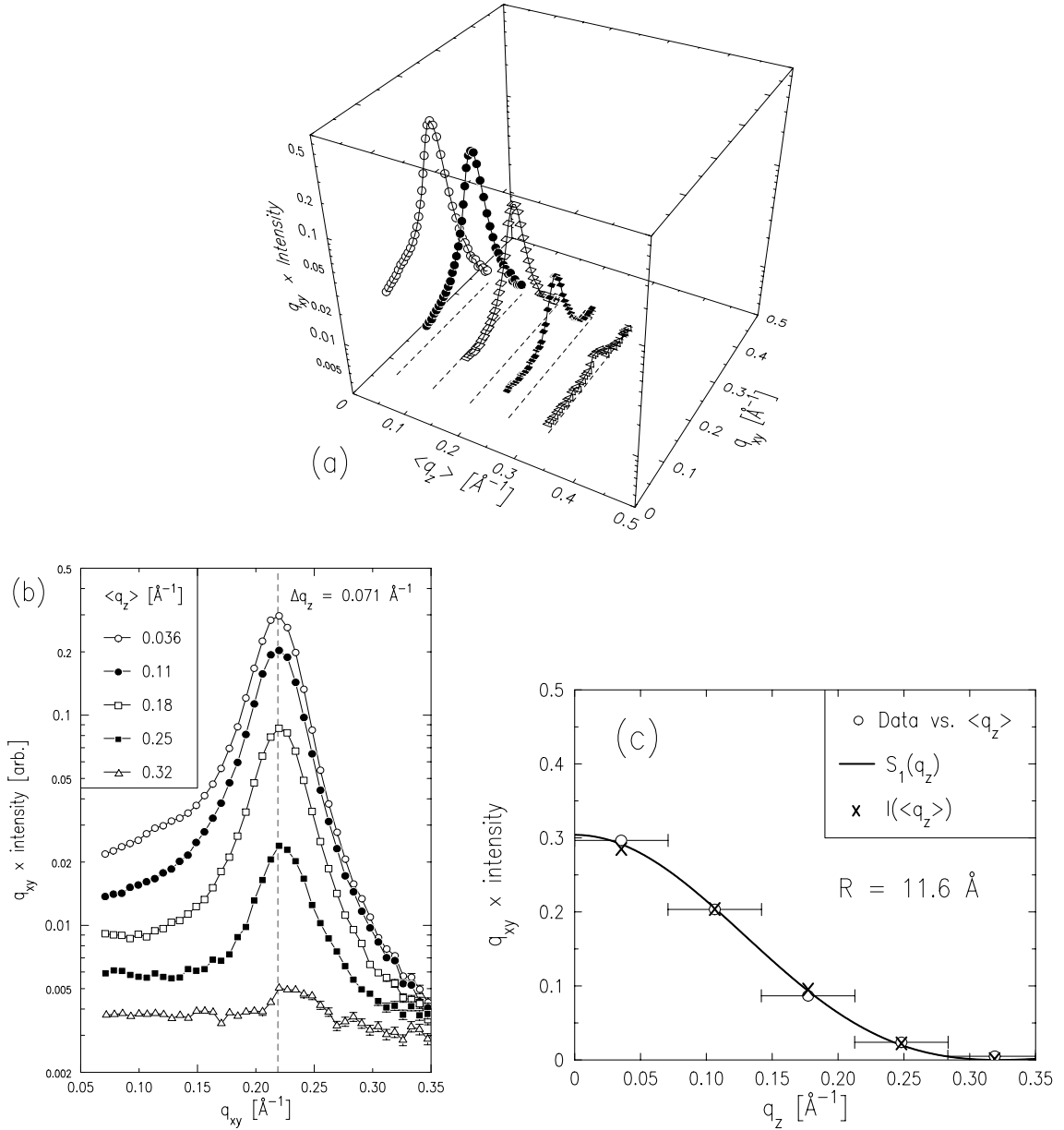
Figure 5.9: Bragg-rod data from the AuSC16 *monolayer* at A_3. The 3D representation in (a) and the q_{xy} projection in (b) are semi-log plots. The q_z projection in (c) is a linear plot. In (c), the data points (circles) correspond to the peak values in (b) and the horizontal bars represent the detector acceptance $\Delta q_z = 0.071$ Å^{-1}. The scattering amplitude $S_1(q_z)$ (solid curve) and the integrated intensity $I(<q_z>)$ (crosses) correspond to the best fit obtained by approximating the Au core with a uniform sphere of diameter $D_{BR} = 23.2$ Å.
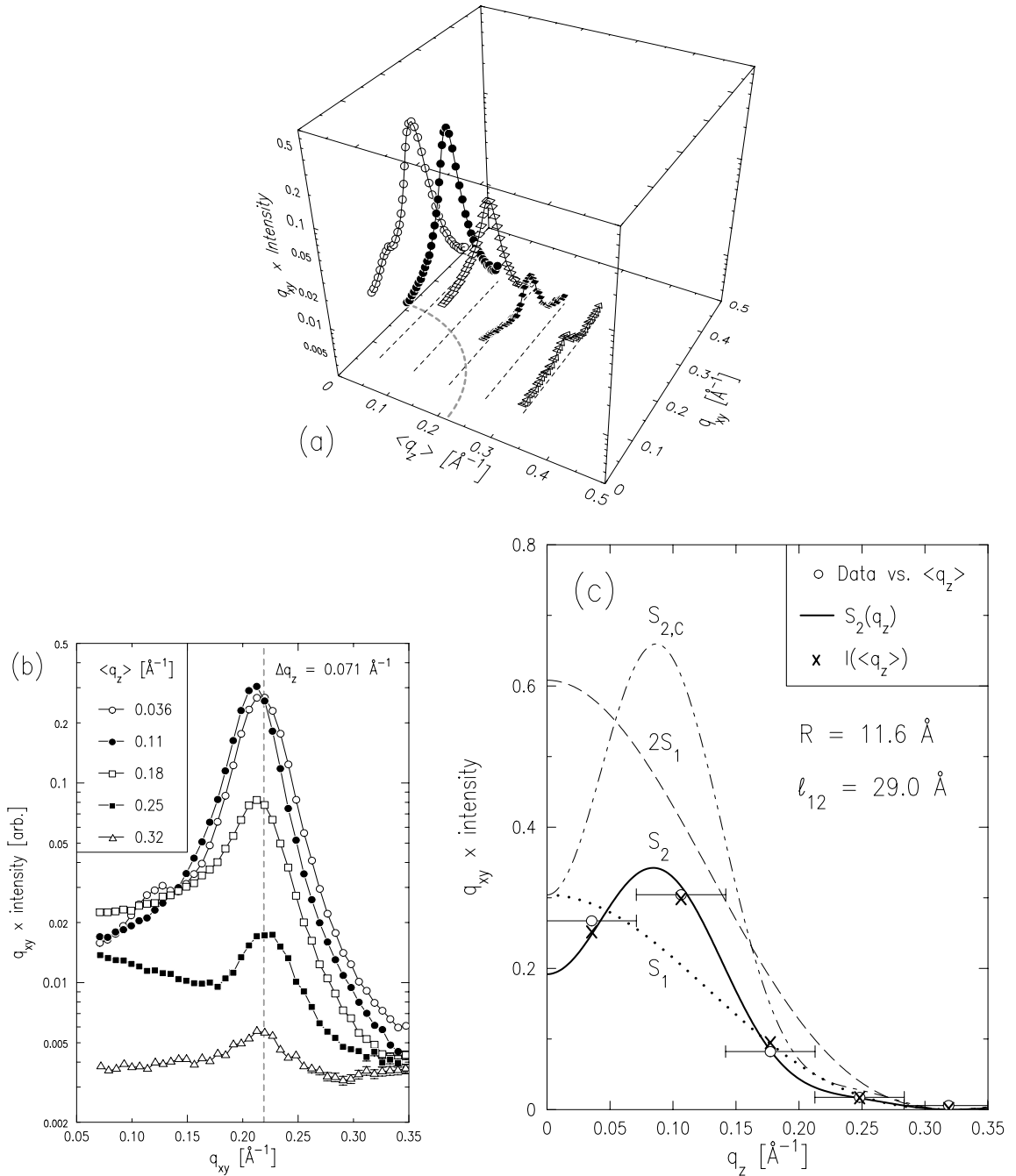
Figure 5.10: Bragg-rod data from a AuSC16 *bilayer* at A_5. The 3D representation in (a) and the q_{xy} projection in (b) are semi-log plots. The q_z projection in (c) is a linear plot. In (a), the dashed circle on the bottom describes $q = [q_{xy}^2 + q_z^2]^{1/2} = 0.216$ Å^{-1}. In (c), the data points (circles) correspond to the peak values in (b) and the horizontal bars represent the detector acceptance $\Delta q_z = 0.071$ Å^{-1}. See text for the details on the calculated scattering amplitudes S_i (curves) and the integrated intensity $I(<q_z>)$ (crosses).

purely 2D structure, the scattering cross section depends on q_z only through the form factor (aside from the surface enhancement peak at $\beta = \alpha_c$, which is negligible in the present case). Therefore, for the *monolayer*, the scattering amplitude $S(q_z)$ along q_z should be described by the following form:

$$S_1(q_z) = S_0 \cdot |f(q_{xy} = G_{10}, q_z)|^2. \tag{5.8}$$

The intensity $I(\langle q_z \rangle)$ expected at $\langle q_z \rangle$ is given by the integration of $S(q_z)$ over $|q_z - \langle q_z \rangle| < \Delta q_z/2$. The theoretical intensity $I(\langle q_z \rangle)$ based on Eq. (5.8) and the form factor in Eq. (5.7) has been fitted to the observed Bragg-rod data by varying the proportionality factor S_0 and the Au core radius R. The best fit is obtained at $R = 11.6 \pm 0.3$ Å or $D_{BR} = 23.2 \pm 0.6$ Å, which is slightly smaller than the mean value ($D_{TEM} = 27$ Å) based on the TEM measurements. Fig. 5.9(c) shows that the data agrees fairly well with the best-fit $I(\langle q_z \rangle)$ (crosses) and the corresponding $S_1(q_z)$ (solid curve). This agreement demonstrates that the observed peak indeed originates from a 2D structure of AuSC16 particles, i.e., from a monolayer.

The Bragg-rod data obtained from the bilayer at A_5 are shown in Fig. 5.10. Just as in the case of the monolayer, the {10} peak remains well centered at $q_{xy} = G_{10}$ in the region above the surface plane ($\langle q_z \rangle > 0$). However, diffuse scattering at low $q_{xy} < 0.2$ Å^{-1} shows a complicated behavior and is no longer characterized by a smooth decay with increasing q_z. In fact, a close inspection of both Fig. 5.10(a) and (b) shows that in addition to the strong {10} peak, there appears to be enhanced diffuse scattering around a "ring" of radius $q = (q_{xy}^2 + q_z^2)^{1/2} \sim 0.2$ Å^{-1}. This feature is suggestive of isotropic scattering and could be an indication for the presence of small 3D aggregates that are embedded in or sitting on top of the bilayer. It may also be due to a certain degree of inter-particle correlations across the two layers of the bilayer.

Figure 5.10(c) shows the q_z dependence of the Bragg rod that is based on the peak intensities of the q_{xy} scans. In contrast to the case of the monolayer, the Bragg rod from

the bilayer appears to display a maximum around $q_z \sim 0.1$ Å^{-1}. Also shown in the figure are several possible curves for the scattering amplitude $S(q_z)$. The dotted curve $S(q_z) = S_1(q_z)$ is identical to the best-fit curve for the monolayer shown in Fig. 5.9(c). The bilayer would also exhibit this behavior, for example, if the in-plane order in the first layer remains the same as in the monolayer but the newly created second layer is completely disordered. The dashed curve $S(q_z) = 2S_1(q_z)$ in Fig. 5.10(c) describes the case in which each of the two layers exhibits the same degree of in-plane order as the monolayer but the layers are completely uncorrelated with each other. Finally, the curve $S(q_z) = S_{2,C}(q_z)$ describes a case of a perfectly correlated bilayer in which each of the two layers are laterally ordered just like in the monolayer and the particles in the second layer reside right above the interstitial sites of the hexagonally packed first-layer particles. It can be shown that when powder-averaged in 2D, $S_{2,C}(q_z)$ is given by

$$S_{2,C}(q_z) = [1 + 2\sin^2(q_z l_{12}/2)]S_1(q_z), \tag{5.9}$$

where l_{12} is the vertical separation between the two layers. The factor multiplying S_1 in Eq. (5.9) arises from the two-particle basis across the two layers. The shown curve $S_{2,C}(q_z)$ has been calculated using the value $l_{12} = 29.0$ Å determined by the fitting of the XR data (see Sec. 5.3.2).

It is clear from Fig. 5.10(c) that none of these extreme cases agree very well with the observed data. However, just as in the data, the curve $S_{2,C}$ based on inter-layer correlations displays a maximum around $q_z \sim 0.1$ Å^{-1}. It should also be noted that if the nearest-neighbor distance *across* the two layers of the correlated bilayer were equal to the in-plane separation $a = 34$ Å, l_{12} would be equal to $l_{12} = (2/3)^{1/2}a = 28$ Å, which is close to the XR-based value $l_{12} = 29.0$ Å. These observations suggest a certain degree of *cross* correlations between the short-range 2D hexagonal order in the two layers.

On the basis of these considerations, a better description of the actual state of the bilayer may be a mixture of both uncorrelated and correlated regions, such that $S(q_z)$ is

178

described by a superposition between S_1 and $S_{2,C}$:

$$S_2(q_z) = c_1 S_1(q_z) + c_2 S_{2,C}(q_z),$$ (5.10)

where c_1 and c_2 are constants. As an example, the solid curve $S(q_z) = S_2(q_z)$ in Fig. 5.10(c) shows the case of $c_1 = 0.26$ and $c_2 = 0.41$. The intensity $I(<q_z>)$ (crosses in Fig. 5.10(c)) calculated from this particular form of $S_2(q_z)$ roughly approximates the behavior of the observed Bragg-rod data. The fact that $c_1 + 2c_2 = 1.1$ is close to unity suggests that the number of AuSC16 particles *per unit surface area* that belong to hexagonally ordered domains is similar between the bilayer and the monolayer. Since this number for the bilayer is twice the number *per monolayer*, it is clear that the bilayer consists of two monolayers each of which is less ordered than the monolayer. To summarize, the Bragg rod data from the bilayer is consistent with the presence of local 2D hexagonal order within each of the two layers and also provides evidence for inter-layer correlations of such order.

5.3.5 Comments on area/particle and particle sizes

According to the results presented in the preceding section, the area occupied by each AuSC16 particle in the hexagonally packed domains ($a = 34$ Å) is equal to $A_{hex} = (\sqrt{3}/2)a^2 = 1000$ Å^2/particle. It should be noted that this GID-based value of area/particle is noticeably smaller than the average close-packing area $A_{t,3} \sim 1650$ Å^2/particle that would be expected from the isotherms. The difference between the two area/particle values translates into a difference of about 28 % or $\Delta a \sim 10$ Å between their corresponding inter-particle distances. As explained in Sec. 5.2.1., A_t in the isotherm is an estimate based on the assumption of MW = 128,000 g/mole, a value calculated for "ideal" AuSC16 particles with TO Au$_{459}$ cores. Therefore, the discrepancy between A_{hex} and $A_{t,3}$ clearly indicates that the hexagonally packed AuSC16 particles must be smaller in size than the ideal particle. However, this does not necessarily imply that the

difference between A_{hex} and the actual average area/particle is indeed as large as indicated above. Due to the uncertainty in the average MW, it is not clear how the area discrepancy should be interpreted; nevertheless, some possible explanations for its origin are considered below.

First of all, it should be recalled that *if* the A_t value at A_3 were taken as the close-packing area/particle in the monolayer, the peak density ϕ_l extracted from the XR data would be consistent with the TEM-based mean Au core diameter $D_{TEM} = 27$ Å. This suggests that if the size distribution indicated by the TEM measurements is accurate, the MW of the ideal AuSC16 particle should be a good measure of the actual average MW. Assuming that this is the case, it would be natural to suppose that the inequality $A_{hex} < A_{t,3}$ arises from size-dependent particle segregation within the monolayer. The implication of this is that the hexagonally ordered domains consist of particles with only small Au cores and domains with larger particles are disordered. In fact, the core diameter $D_{BR} = 23$ Å extracted from the Bragg rod data is smaller than $D_{TEM} = 27$ Å. However, there are difficulties with this hypothesis. First, the difference of ~ 4 Å between the two diameter values is still too small to account for the expected difference of $\Delta a \sim 10$ Å between the "average" inter-particle distance of all particles and the nearest-neighbor distance in the hexagonal domains. Secondly, it is not clear why only the smaller particles would form ordered domains when larger particles with $D \sim D_{TEM}$ should be more numerous. Third, the above hypothesis conflicts with the expected segregation behavior based on the size dependence of van der Waals attractions. Ohara *et al*. studied size-selective segregation of polydisperse Au nanoparticles in solution-cast films [23]. Their TEM images and Monte Carlo simulations show that stronger dispersion interactions between larger particles cause the largest particles to form hexagonally packed domains in the middle of islands and they are surrounded by successively smaller particles with less order. Given these difficulties, the size-dependent segregation is highly unlikely to be the reason for $A_{hex} < A_{t,3}$.

Another possible explanation is that the size distribution of Au cores determined from the TEM images may not be a good representation of the actual distribution in the sample, probably due to some systematic error in the procedure used, such as an error in calibration, small sampling size, etc. That is, the actual average core diameter and MW may be smaller than the values based on the TEM measurements and the assumption of the ideal particle. The two inequalities already mentioned, $D_{BR} < D_{TEM}$ and $A_{hex} < A_{t,3}$, point toward this possibility. In addition, it has been pointed out in the XR section that the monolayer thickness l_1 is slightly smaller than the FWHM Δz of the projected Au-core density distribution that would be expected from D_{TEM}. The equality $l_1 = \Delta z$ would be obtained at $D_l = 20.5$ Å. On the other hand, if the close-packing area/particle is represented by A_{hex} instead of $A_{t,3}$, the core diameter based on the maximum density ϕ_1 would be equal to $D_\phi = 2(F \cdot A_{hex}/\pi)^{1/2} = 21$ Å. The fact that the three independently determined values of core diameters D_l, D_ϕ, and D_{BR} agree well with each other, supports the plausibility of the above hypothesis.

Assuming that the average $D_x = 21.5$ Å of the three x-ray-based values is representative of the mean Au core diameter of the actual sample, the average MW of AuSC16 can be re-estimated as follows. For simplicity, we assume a spherical core of diameter D_x and that each thiol chain occupies an area of $A_{thiol} = 21.4$ Å^2 on the core surface, which is equal to the value found in self-assembled monolayers of thiols on planar Au(111) surface [14, 24]. Such a AuSC16 particle consists of 308 Au atoms and 68 thiol chains, and the corresponding MW is equal to 80,300 g/mole. The x-ray-based area/particle A_x estimated from this value of MW is indicated by the top horizontal axis in the isotherm plot in Fig. 5.2. The ratio 1.6 between the two estimates of MW implies that the two scales of A are related by $A_t = 1.6 A_x$. In terms of A_x, the points $A = A_1$ through A_5 are located at $A_{x,1} = 1280$, $A_{x,2} = 1100$, $A_{x,3} = 1040$, $A_{x,4} = 800$, and $A_{x,5} = 520$ Å^2/particle. The agreement $A_{x,3} \sim A_{hex}$ arises from the consistency between the various x-ray measurements and suggests that the hexagonally packed domains may in fact consist of

AuSC16 particles of typical sizes.

From the nearest-neighbor distance a and the effective core diameter D_x, the edge-to-edge separation between adjacent Au cores can be estimated to be about $\delta \sim 12$ Å in the close packed domains. This spacing is clearly smaller than the length (~ 20 Å) of stretched-out alkylthiol chains (HS-$(CH_2)_{15}$-COOH) in the all-*trans* conformation. This suggests that the close packing of AuSC16 particles in the monolayer results in a high degree of interpenetration between thiol chains from adjacent Au cores and/or a highly deformed and compressed shape of thiol "shells" around the cores as compared to their colloidal states in solutions.

5.4 Summary

Langmuir films formed by gold nanoparticles derivatized with acid-terminated alkylthiol chains (HS$(CH_2)_{15}$COOH) on acidic aqueous subphase (pH = 3) have been studied at room temperature. The Π-A isotherm of the AuSC16 Langmuir film exhibits a coexistence plateau that is consistent with a monolayer/bilayer transition. The microscopic structures of AuSC16 films have been probed as a function of area/particle by using various surface-sensitive x-ray techniques. The results can be summarized as follows.

The electron density profiles extracted from the XR measurements are consistent with the presence of an AuSC16 monolayer on the low-density side of the coexistence plateau and a bilayer on the high-density side. The results of off-specular diffuse scattering measurements indicate that a close-packed monolayer near the onset of the transition is laterally homogeneous. Unlike the case of the monolayer, off-specular intensities scattered from a bilayer are higher than the values predicted from the presence of thermal capillary fluctuations and the assumption of homogeneity, providing evidence for lateral density inhomogeneities within the bilayer. The GID results show that upon being spread on the surface AuSC16 particles spontaneously aggregate into a 2D

hexagonal structure with only short-range order. This structure is characterized by a nearest-neighbor distance of $a = 34$ Å that is independent of the degree of lateral compression. The limited range of lateral order appears to be a consequence of the polydispersity in particle size. The Bragg rod of the lowest-order peak observed from a monolayer is consistent with a 2D array of Au cores. Subsequent compression across the coexistence plateau reduces the lateral order within the monolayer. The Bragg rod data from the bilayer suggests that some inter-layer correlations exist between the lateral order of the two layers.

This study on Au nanoparticles had been motivated partly by the fact that they are very strong scatters of x rays due to their very high electron density. The results presented show that even though these particles only display short-range lateral order in the monolayer, the resulting lowest-order GID peak is intense enough to be easily observed. If some macromolecules can be synthesized such that they bear Au nanoparticles inside and their monolayers exhibit interesting compression- and/or temperature-dependent 2D phase behaviors, then, the Au particles should act as "markers" that would enable x-ray scattering studies of structural changes across order-disorder phase boundaries.

References for Chapter 5

[1] M. G. Bawendi, M. L. Steigerwald and L. E. Brus, *Annu. Rev. Phys. Chem.* **41,** 477 (1990).

[2] G. Schmid, *Chem. Rev.* **92,** 1709 (1992).

[3] J. R. Heath, *Science* **270,** 1315 (1995).

[4] A. P. Alivisatos, *Science* **271,** 933 (1996).

[5] V. L. Colvin, M. C. Schiamp and A. P. Alivisatos, *Nature* **370,** 354 (1994).

[6] R. G. Freeman, K. C. Grabar, K. J. Allison, R. M. Bright, J. A. Davis, A. P. Guthrie,

M. B. Hommer, M. A. Jackson, P. C. Smith, D. G. Walter and M. J. Natan, *Science* **267,** 1629 (1995).

[7] R. W. Siegel, *Scientific American* **December,** 74 (1996).

[8] C. B. Murray, C. R. Kagan and M. G. Bawendi, *Science* **270,** 1335 (1995).

[9] L. Motte, F. Billoudet, E. Lacaze, J. Douin and M. P. Pileni, *J. Phys. Chem. B.* **101,** 138 (1997).

[10] J. H. Fendler and F. C. Meldrum, *Adv. Mater.* **7,** 607 (1995).

[11] R. L. Whetten, J. T. Khoury, M. M. Alvarez, S. Murphy, I. Vezmar, Z. L. Wang, P. W. Stephens, C. L. Cleveland, W. D. Luedtke and U. Landman, *Adv. Mater.* **8,** 428 (1996).

[12] B. O. Dabbousi, C. B. Murray, M. F. Rubner and M. G. Bawendi, *Chem. Mater.* **6,** 216 (1994).

[13] F. C. Meldrum, N. A. Kotov and J. H. Fendler, *Langmuir* **10,** 2035 (1994).

[14] J. R. Heath, C. M. Knobler and D. V. Leff, *J. Phys. Chem. B.* **101,** 189 (1997).

[15] M. Sastry, K. S. Mayya, V. Patil, D. V. Paranjape and S. G. Hegde, *J. Phys. Chem. B.* **101,** 4954 (1997).

[16] M. Brust, M. Walker, D. Bethell, D. J. Schiffrin and R. Whyman, *J. Chem. Soc. Chem. Commun.***,** 801 (1994).

[17] M. Brust, J. Fink, D. Bethell, D. J. Schiffrin and C. Kiely, *J. Chem. Soc. Chem. Commun.***,** 1655 (1995).

[18] D. Bethell, M. Brust, D. J. Schiffrin and C. Kiely, *J. Electroanal. Chem.* **409,** 137 (1996).

[19] A. Badia, S. Singh, L. Demers, L. Cuccia, G. R. Brown and R. B. Lennox, *Chem. Eur. J.* **2,** 359 (1996).

[20] A. Badia, W. Gao, S. Singh, L. Demers, L. Cuccia and L. Reven, *Langmuir* **12,** 1262 (1996).

[21] A. Badia, L. Cuccia, L. Demers, F. Morin and R. B. Lennox, *J. Am. Chem. Soc.* **119,** 2682 (1997).

[22] H. Schmitt, A. Badia, L. Dickinson, L. Reven and R. B. Lennox, *Adv. Mater.* **10,** 475 (1998).

[23] P. C. Ohara, D. V. Leff, J. R. Heath and W. M. Gelbart, *Phys. Rev. Lett.* **75,** 3466 (1995).

[24] D. V. Leff, P. C. Ohara, J. R. Heath and W. M. Gelbart, *J. Phys. Chem.* **99,** 7036 (1995).

[25] C. P. Collier, R. J. Saykally, J. J. Shiang, S. E. Henrichs and J. R. Heath, *Science* **277,** 1978 (1997).

[26] M. M. Alvarez, J. T. Khoury, T. G. Schaaff, M. N. Shafigullin, I. Vezmar and R. L. Whetten, *J. Phys. Chem. B.* **101,** 3706 (1997).

[27] D. K. Schwartz, M. L. Schlossman and P. S. Pershan, *J. Chem. Phys.* **96,** 2356 (1992).

[28] W. J. Foster, M. C. Shih and P. S. Pershan, *J. Chem. Phys.* **105,** 3307 (1996).

[29] G. M. Bommarito, W. J. Foster, P. S. Pershan and M. L. Schlossman, *J. Chem. Phys.* **105,** 5265 (1996).

[30] S. K. Sinha, E. B. Sirota, S. Garoff and H. B. Stanley, *Phys. Rev. B* **38,** 2297 (1988).

[31] M. K. Sanyal, S. K. Sinha, K. G. Huang and B. M. Ocko, *Phys. Rev. Lett.* **66,** 628 (1991).

[32] M. Fukuto, R. K. Heilmann, P. S. Pershan, J. A. Griffiths, S. M. Yu and D. A. Tirrell, *Phys. Rev. Lett.* **81,** 3455 (1998).

[33] H. Tostmann, E. DiMasi, P. S. Pershan, B. M. Ocko, O. G. Shpyrko and M. Deutsch, *Phys. Rev. B* **59,** 783 (1999).

[34] P. S. Pershan, *Colloids and Surfaces* **A171,** 149 (2000).

[35] L. G. Parratt, *Phys. Rev.* **95,** 359 (1954).

[36] J. Lekner, *Theory of Reflection* (Martin Nijhoff, Dordrecht, 1987).

[37] M. Fukuto, R. K. Heilmann, P. S. Pershan, S. M. Yu, J. A. Griffiths and D. A. Tirrell, *J. Chem. Phys.* **111,** 9761 (1999).

[38] J. Als-Nielsen, D. Jacquemain, K. Kjaer, F. Leveiller, M. Lahav and L. Leiserowitz, *Phys. Rep.* **246,** 251 (1994).

[39] S. Dietrich and A. Haase, *Phys. Rep.* **260,** 1 (1995).

[40] M. P. Gelfand and M. E. Fisher, *Physica A* **166,** 1 (1990).

[41] P. S. Pershan, *Phys. Rev. E* **50,** 2369 (1994).

[42] I. M. Tidswell, T. A. Rabedeau, P. S. Pershan and S. D. Kosowsky, *Phys. Rev. Lett.* **66,** 2108 (1991).

Appendix A

X-ray Measurements of Non-Capillary Spatial Fluctuations from a Liquid Surface

Abstract

Off-specular diffuse x-ray scattering measurements on both pure water and a homogeneous Langmuir monolayer of poly-γ-benzyl-L-glutamate (PBLG) on water establish the validity of a proposed sum rule for scattering from capillary fluctuations on liquid surfaces. Excess scattering above the predicted capillary contribution is observed when the PBLG monolayer is compressed beyond its elastic limit. This is interpreted in terms of a second-layer inhomogeneity with a surface correlation length of ~ 1000 Å. Excess off-specular scattering can be used to probe interface correlation lengths from 100 Å to 1 μm.

A.1 Introduction

The availability of lasers in the 1960s facilitated the first concerted application of low-angle diffuse scattering to study of critical fluctuations in bulk condensed matter [1, 2]. Later development of high brilliance x-ray sources extended these studies to both shorter lengths and other materials, such as metals and alloys, that cannot be probed with visible light [3, 4]. With increasing appreciation for the effects of reduced dimensions in statistical physics, and with refined instrumentation, x-ray and neutron scattering were widely applied to study two-dimensional (2D) critical properties of solid surfaces [5-7]. However, it is known that the periodic potential of the solid substrate suppresses certain

classes of continuous 2D phase transitions [8, 9]. Consequently attention was directed towards the study of similar phenomena on liquid surfaces.

Two x-ray scattering techniques have served as useful probes for fluctuations on a wide variety of liquid surfaces. The first, grazing incidence diffraction (GID), has been used to characterize surface structures on intermolecular length scales. The second technique, analogous to the static critical light scattering methods, is diffuse scattering at small angles away from specular reflection [10-12]. Until recently, quantitative application of this technique to liquid surfaces [13-20] has been mostly limited to characterization of thermal diffuse scattering (TDS) [11], which arises from 2D surface height fluctuations due to thermally excited capillary waves [21-23]. As Sinha et al. have shown [10, 14], the TDS from liquid surfaces diverges algebraically at the angle for specular reflection, with strong tails extending out into the surrounding off-specular regions. We show here that calculation of the angular dependence of TDS for homogeneous liquid surfaces allows one to quantitatively separate TDS from subtle diffuse scattering effects arising from other surface inhomogeneities. This ability is essential to the utility of small-angle off-specular diffuse x-ray scattering (XOSDS) for quantitative characterization of non-capillary surface inhomogeneities on submicron length scales [24].

We first demonstrate the application of a sum rule that leads to a *simple* normalized form of the capillary-wave TDS cross section predicted by Sinha et al [10, 14]. With this sum rule, the intensity of the XOSDS can be calculated *with no additional adjustable parameters beyond those required for x-ray specular reflectivity (XR)*. We apply the result to both pure H_2O and a close-packed homogeneous Langmuir monolayer (LM) formed by PBLG molecules on water. When the PBLG film is compressed beyond the elastic limit for the monolayer, we find excess scattering above the capillary contribution that can be quantitatively interpreted in terms of surface inhomogeneities with a correlation length of ~ 1000 Å.
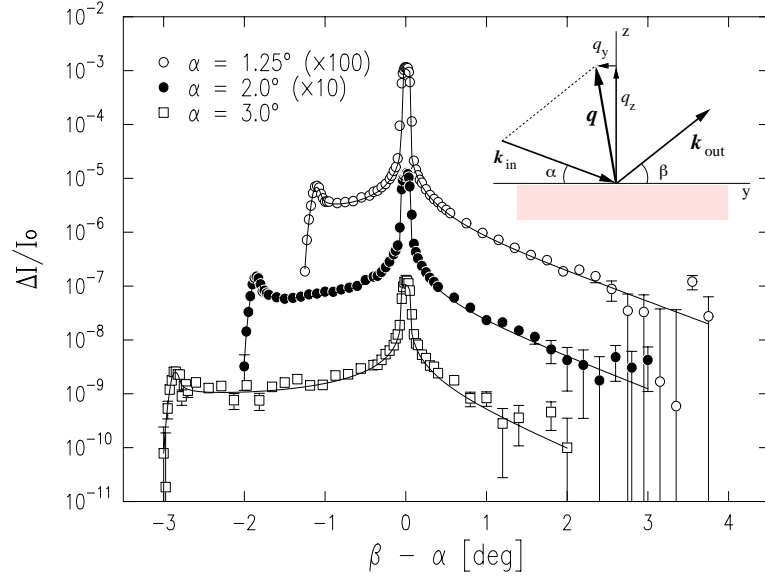
187

Figure A.1: Measured normalized intensity $\Delta I/I_0$ as a function of $(\beta - \alpha)$ at fixed α for a bare water surface, where $\Delta I \equiv I(2\theta = 0°) - (1/2)[I(+0.3°) + I(-0.3°)]$. The solid lines are theoretically expected curves. The inset is a schematic for the incident-plane $(2\theta = 0)$ scattering geometry used in the XR and XOSDS.

The scattering kinematics are illustrated in Fig. A.1. For x rays incident at angle α and scattered at angles β to the surface and 2θ to the incident plane, the wave vector transfer has components $q_z = (2\pi/\lambda)[\sin(\alpha) + \sin(\beta)]$ and $q_{xy} = (2\pi/\lambda)[\cos^2(\alpha) + \cos^2(\beta) - 2\cos(2\theta)\cos(\alpha)\cos(\beta)]^{1/2}$, normal and parallel to the surface. Capillary waves give rise to interfacial height-height correlations of the liquid surface $g(r_{xy}) = <[h(r_{xy})-h(0)]^2>$ which vary logarithmically [10, 14, 23] when the distance r_{xy} is smaller than a gravitationally imposed cutoff (~mm) and large compared to the molecular size ~d. Therefore, as Sinha et al. [10, 14] have shown, scattering from liquid surfaces does not possess a true specular reflection ($\sim\delta^{(2)}(q_{xy})$), and the surface scattering may be considered entirely as "diffuse." Neglecting the effect of the gravitational low-q cutoff (which is too small to measure with realistic resolutions), the differential cross section $d\sigma/d\Omega$ is described by a power-law singularity of the form $1/q_{xy}^{2-\eta}$ for $\eta = (k_BT/2\pi\gamma)q_z^2 < 2$ [10, 14, 20], where γ is the surface tension. Normalization of $d\sigma/d\Omega$ can be accomplished by taking into account the small

r_{xy} behavior which requires that $g(0) = 0$. Since the derivation of $S(q_{xy}) \sim 1/q_{xy}^{2-\eta}$ by Sinha et al. [10] is based on $F(q_{xy}) = $ [2D Fourier transform (F.T.) of $\exp\left(-\frac{1}{2}g\left(r_{xy}\right)q_z^2\right)$], it follows that the inverse F.T. evaluated at $r_{xy} = 0$, obtained by summing $F(q_{xy})$ over all capillary modes with $q_{xy} \leq q_{max} \sim 2\pi/d$, must be unity. The application of this sum rule leads to a simple and physically meaningful normalization of $S(q_{xy})$ from Eq. (2.32) in Sinha et al. [10], without the need for a specific resolution function [14, 25]. For the scattering from a *homogeneous* liquid surface (i.e. conformal roughness of all interfaces) with capillary fluctuations, one obtains [20]

$$\frac{1}{A_0}\left(\frac{d\sigma}{d\Omega}\right)_0 = \frac{N}{q_z^2}\left|\Phi_0\left(q_z\right)\right|^2 \frac{2\pi\eta}{q_{xy}^2}\left(\frac{q_{xy}}{q_{\max}}\right)^\eta \qquad (A.1)$$

where A_0 is the cross sectional area of the incident beam and $N = (q_c/2)^4 T_F(\alpha)T_F(\beta)/[16\pi^2\sin(\alpha)]$. $q_c = (4\pi/\lambda)\sin(\alpha_c)$ is the critical wave vector for total reflection ($q_c = 0.0218$ Å^{-1} for water) and the Fresnel transmission factor $T_F(\alpha)$ [10] is related to the Fresnel reflectivity $R_F(\alpha)$ of an ideally flat interface through $T_F(\alpha) = \left(2\alpha/\alpha_c\right)^2\sqrt{R_F(\alpha)}$ [26]. A surface structure factor $\Phi_0(q_z)$ can be defined as the 1D F.T. of $d(<\rho_{T=0}(z)>/\rho_\infty)/dz$, where ρ_∞ is the bulk electron density and $<\rho_{T=0}(z)>$ is the average local electron density profile *in the absence of thermal capillary waves*. This "intrinsic" profile $<\rho_{T=0}(z)>$ [11, 20, 21] is to be distinguished from the total average density $<\rho(z)>$, which is obtained by convoluting $<\rho_{T=0}(z)>$ with the distribution of interfacial heights induced by capillary-wave roughness. In order to obtain the number of photons scattered into the detector normalized to the number incident on the surface (i.e. I/I_0.), we carry out *a precise numerical convolution of Eq. (A.1) with the slit-defined resolution function* [20].

A.2 Experimental Details

Details of our Langmuir trough, film preparation and compression methods have been given previously [27, 28]. The temperature of the pure water subphase was maintained at 23°C. The surface tension of a film-coated surface is given by $\gamma = \gamma_w - \Pi$ where γ_w is for the bare water surface (72.3 dyn/cm) and Π is the surface pressure, monitored by the Wilhelmy balance method. Polydisperse PBLG [29] monolayers were spread at a specific area $A > 23$ Å^2/monomer from a trifluoroacetic acid/chloroform solution (3%:97% by vol.) [30] with a concentration of 0.42 mg/mL, and compressed at a rate < 0.01 (Å^2/monomer)/s. The PBLG molecule, due to its α-helical conformation, resembles a rod-like structure that is approximately 150 Å in length and 13 Å in diameter [30, 31]. On water these rods lie down parallel to the interface [31].

X-ray experiments were carried out using the Harvard/BNL liquid surface spectrometer [27] on Beamline X22B at the National Synchrotron Light Source ($\lambda = 1.55$ Å). For both XR and XOSDS, the center of the detector (NaI scintillator) slits lies in the incident plane ($2\theta = 0$). For XR, the reflected intensity at $\beta = \alpha$ (or $q_{xy} = 0$) is measured as a function of $q_z = (4\pi/\lambda)\sin(\alpha)$, while XOSDS was measured as a function of β at fixed α. For both measurements background was eliminated through subtraction of intensities from identical scans taken with 2θ offsets of $\pm 0.3°$. The results were normalized to the incident intensity and analyzed in terms of the theoretical predictions for the difference $\Delta I/I_0 \equiv [I(2\theta = 0) - (1/2)\{I(+0.3°) + I(-0.3°)\}]/I_0$ [20]. The rectangular detector slits, located $L = 621$ mm from the sample center, of (height H) × (width W) give an angular resolution of $\delta\beta = H/L$ and $\delta(2\theta) = W/L$. The slit sizes in mm were (H, W) = (2.5, 3.0) for XR, (1.1, 3.0) for β-scans on water, and (1.0, 3.0) for β-scans on PBLG films.
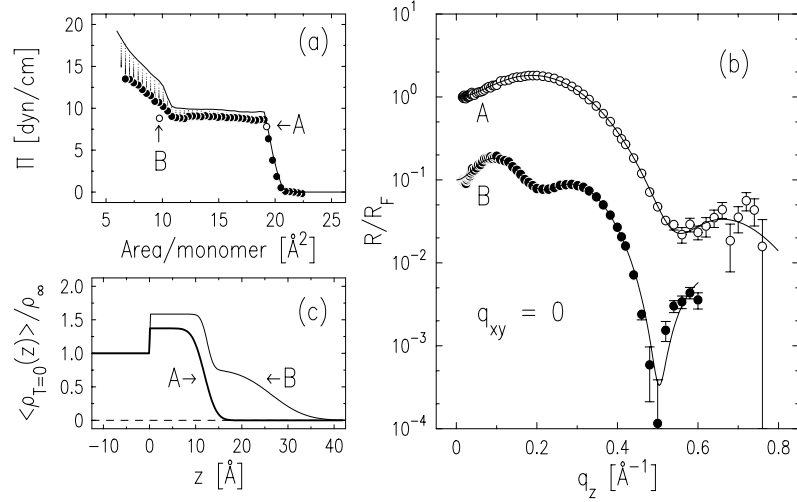
Figure A.2: (a) Typical Π-A isotherms taken on PBLG films at $T = 23$ °C, showing a continuous scan (—) and a relaxation scan (●), in which the film is relaxed at given A until $\Delta\Pi$ over 5 min. is < 0.05 dyn/cm. (b) Normalized reflectivity, R/R_F, measured for PBLG films at points A and B in (a). The fits (—) are based on Eq. (A.1), detector resolutions, and the average local electron densities $<\rho_{T=0}(z)>$ in (c), where $q_{max} = 0.5$ Å^{-1} is assumed.

A.3 Results and Discussion

In Fig. A.1, we show $\Delta I/I_0$ for β-scans taken on the bare water surface. The local density profile $\rho_{T=0}(\mathbf{r}) = <\rho_{T=0}(z)>$ at any point on the simple water/gas interface is a step function, so that $\Phi_0(q_z) = 1$ [13]. The solid lines in Fig. A.1 are calculated values of $\Delta I/I_0$ using the known temperature, surface tension and $q_{max} = \pi/(1.4$ Å$) = 2.25$ Å^{-1} as obtained previously by Schwartz et al. for water [13]. The calculation involves *no adjustable parameters*. The theory agrees excellently with the measurements for both the specular and off-specular data. Conservative estimates of uncertainties in the experimentally determined parameters (T, γ, $\delta\beta$, $\delta(2\theta)$, etc.) lead to errors in the shown curves that are much smaller than the size of the symbols for the data.

The validity of the formula Eq. (A.1) was tested again for a less simple interfacial structure using the PBLG LM on water. Fig. A.2(a) shows typical Π-A isotherms, suggesting a monolayer-bilayer transition, with the plateau indicating coexistence of the

two phases [31]. Specular reflectivity R, given by the convolution of Eq. (A.1) with the detector resolution function centered at $\beta = \alpha$, can be used to obtain the structure factor $\Phi_0(q_z)$ of the film coated surface. The XR data measured on a PBLG film at points A = (19.2 Å^2/mon., 7.8 dyn/cm) and B = (9.7 Å^2/mon., 8.8 dyn/cm) in the isotherm are shown as R/R_F in Fig. A.2(b). The solid curves in Fig. A.2(b) are fits based on a box model [28] for $<\rho_{T=0}(z)>$. Assuming that the smallest capillary wavelength is on the order of the PBLG rod diameter $d \sim 12.6$ Å, we take the value for $q_{max} \sim 2\pi/d = 0.5$ Å^{-1}. The fact that the results are not sensitive to the precise value of q_{max} is discussed elsewhere [20, 21]. The profiles $<\rho_{T=0}(z)>$ plotted in Fig. A.2(c) correspond to a best fit. The film is clearly a monolayer at A and an incomplete bilayer at B, with each layer thickness being close to the PBLG rod diameter.

Measured differences $\Delta I/I_0$ vs. β from the PBLG film on water are shown in Fig. A.3(a) for the monolayer at A and in Fig. A.3(b) for the bilayer at B. The solid lines correspond to the theoretically predicted $\Delta I/I_0$ using Eq. (A.1), the known physical and experimental parameters (T, γ, $\delta\beta$, $\delta(2\theta)$ etc.), and the XR-based average local density profile $<\rho_{T=0}(z)>$. The very good agreement between data and theory shown in Fig. A.3(a) justifies the assumption that all of the surface diffuse scattering is TDS from the capillary fluctuations and that the *monolayer* is homogeneous. By contrast, Fig. A.3(b) shows that the measured scattering from the PBLG *bilayer* at B exceeds the values predicted on the assumption of a homogeneous bilayer by up to a factor of two. In view of the fact that the structure factor $\Phi_0(q_z)$ was obtained by fitting the XR, the data near $\beta = \alpha$ agree with the model; however, the off-specular intensity is consistently higher than predicted. This is more clearly evident in Fig. A.4, showing the ratio of the data to the solid curves in Fig. A.3(b).

In case of lateral density or non-capillary height fluctuations at the interface, $d\sigma/d\Omega$ has another term beyond Eq. (A.1) that corresponds to scattering due to non-zero $\delta\rho_{T=0}(\boldsymbol{r}) = \rho_{T=0}(\boldsymbol{r}) - <\rho_{T=0}(z)>$. Both the lower density in the second layer and the
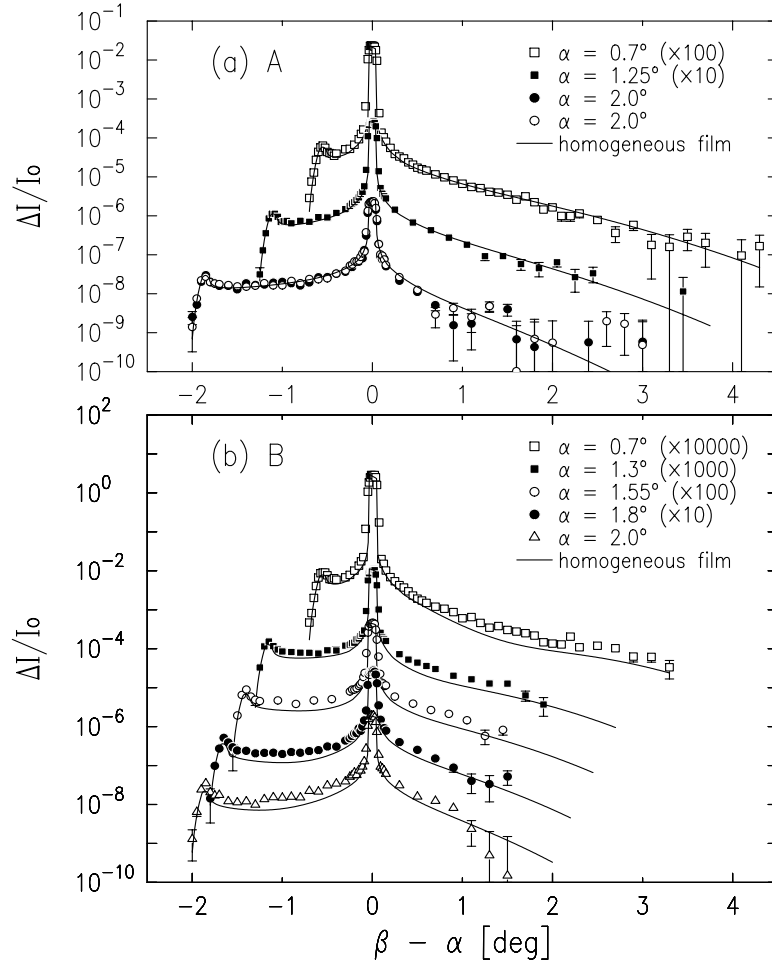
Figure A.3: Measured $\Delta I/I_0$ vs. $(\beta - \alpha)$ for PBLG (a) monolayer at A and (b) bilayer at B in Fig. A.2(a). The solid curves (—) theoretically expected for *homogeneous* PBLG films are based on Eq. (A.1), detector resolutions, and $<\rho_{T=0}(z)>$ in Fig. A.2(c).

diffuseness of the layer/gas interface evident in $<\rho_{T=0}(z)>$ for the PBLG bilayer (Fig. A.2(c)), are suggestive of greater density fluctuations in the newly formed second layer than in the first layer. Therefore, it is reasonable to assume that the extra scattering comes mostly from microscopic inhomogeneities in the second layer. Examples of possible microscopic origins include: (i) a distribution in the heights of molecular centers in the second layer, (ii) deviations in the orientation of molecular axes from being parallel to the interface, and (iii) molecular density variations within the second layer.

Figure A.4: The ratio of measured $\Delta I/I_0$ to the homogeneous contribution in Fig. A.3(b) for PBLG bilayer at B. The fits (—) in (a) are based on an inhomogeneous model Eq. (A.2) with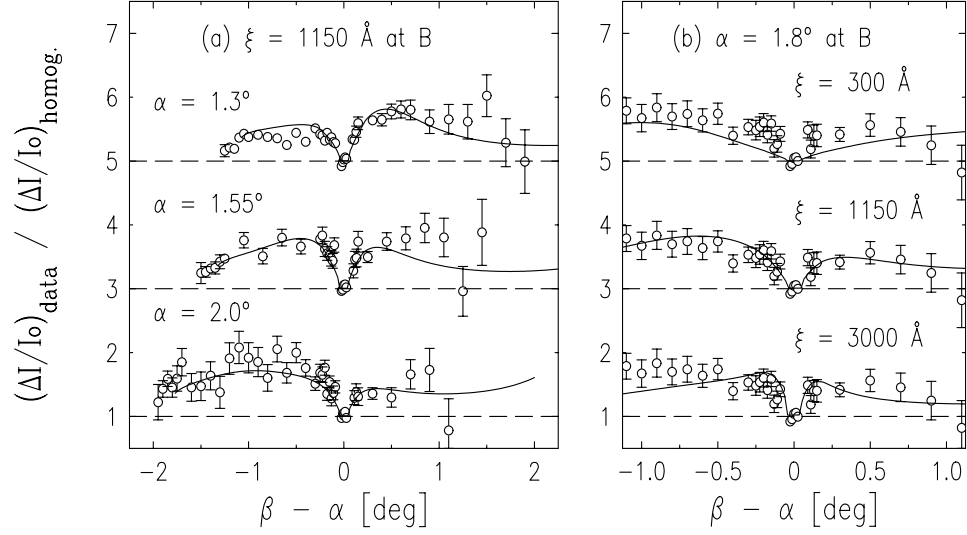 roughness $\sigma_2 = 2.2$ Å and correlation length $\xi = 1150$ Å for the second layer/gas interfacial height fluctuations. The solid curves in (b) correspond to the $\Delta I/I_0$ ratio calculated for three different values of ξ.

Since the present experimental data cannot distinguish between these, we analyze the excess scattering by modeling the second-layer inhomogeneity as follows. The local electron density *within* the second layer is assumed to be constant at $\rho_2 = \rho_\infty \cdot \phi_2$, but the height $h_2(r_{xy})$ of the second layer/gas interface fluctuates about $<h_2(0)> = 0$ over the surface, where $h_2(r_{xy})$ is assumed to be laterally isotropic [32] and defined in a frame (r_{xy}, z') in which capillary waves are absent (i.e. z' = z - h(r_{xy})). If the two height distributions $\{h(r_{xy})\}$ and $\{h_2(r_{xy})\}$ are statistically independent, then, in the limit that $c_2(r_{xy}) \equiv$ $<h_2(r_{xy})h_2(0)> << 1/q_z^2$, it can be shown that the second term in the total $d\sigma/d\Omega$ is given by the convolution of the capillary (h) and the non-capillary (h_2) fluctuations in reciprocal space:

$$\frac{1}{A_0}\left(\frac{d\sigma}{d\Omega}\right)_1 \cong \frac{N\phi_2^2 e^{-\sigma_2^2 q_z^2}}{2\pi} \int_{q'_{xy}<q_{max}} d^2\vec{q}'_{xy} \frac{\eta}{q'^2_{xy}}\left(\frac{q'_{xy}}{q_{max}}\right)^\eta C_2\left(\vec{q}_{xy} - \vec{q}'_{xy}\right) \qquad (A.2)$$

194

where $\sigma_2^2 = <h_2^2(0)>$ and $C_2(\vec{q}_{xy})$ is the 2D F.T. of $c_2(r_{xy})$ [33]. Assuming a simple exponentially decaying correlation function $c_2(r_{xy}) = \sigma_2^2\exp(-r_{xy}/\xi)$, so that $C_2(q) = 2\pi\sigma_2^2\xi^2[1 + \xi^2q^2]^{-3/2}$, the difference between the measured and the theoretical $\Delta I/I_0$ for a homogeneous PBLG bilayer at various sets of (α, β) has been simultaneously fitted to the convolution of Eq. (A.2) with the resolution function. In the fitting, the relative second-layer density was fixed at the XR-based value of $\phi_2 = 0.80$, and only the roughness σ_2 and the correlation length ξ were allowed to vary. The best fit is obtained with $\xi = 1150$ Å (400 Å $< \xi <$ 3200 Å) and $\sigma_2 = 2.2$ Å (1.7 Å $< \sigma_2 <$ 3.1 Å). The ratio between the $\Delta I/I_0$ calculated from the best-fit to the excess scattering and the homogeneous contribution is plotted as the solid lines in Fig. A.4(a) at various α. The ratio is unity at $\beta = \alpha$ and increases above unity as β moves away from α. The inverse width of the "valley" centered at $\beta = \alpha$ is a measure of correlation length ξ. This is demonstrated in Fig. A.4(b), in which the ratios at three different values of ξ are plotted at $\alpha = 1.8°$. From the above analysis, we estimate the correlation length associated with the second-layer inhomogeneity to be on the order of $\xi \sim 1000$ Å, which is about 80 times the rod diameter or about 7-8 times the rod length of typical PBLG molecules.

A.4 Summary

We have proposed a sum rule that establishes the absolute magnitude of the capillary wave contribution to the differential cross section Eq. (A.1) for low-angle x-ray scattering from liquid surfaces. Validity of the sum rule is demonstrated by the excellent agreement between measurements on a bare water surface ($\Phi_0(q_z) = 1$) and a PBLG monolayer ($\Phi_0(q_z) \neq 1$) and intensities $\Delta I/I_0$ calculated by numerical convolution of Eq. (A.1) with the slit-defined resolution function. Analysis of excess diffuse scattering from a PBLG film compressed beyond the elastic limit of the monolayer established the possibility for quantitative characterization of non-capillary inhomogeneities on liquid

surfaces. On the basis of the analysis leading to Fig. A.4 surface fluctuations with 2D correlation lengths between ~100 Å and 1 μm can readily be studied.

References for Appendix A

[1] H. L. Swinney and D. L. Henry, *Phys. Rev. A* **8,** 2586 (1973).

[2] H. Z. Cummins, A. P. Levanyuk and (Ed.), *Light Scattering Near Phase Transitions* (North-Holland, Amsterdam, 1983).

[3] H. Chen, R. J. Comstock and J. B. Cohen, *Ann. Rev. Mater. Sci.* **9,** 51 (1979).

[4] P. S. Pershan, *Structure of Liquid Crystal Phases* (World Scientific, Singapore, 1988).

[5] H. Dosch, *Critical phenomena at surfaces and interfaces: evanescent x-ray and neutron scattering* (Springer Verlag, Berlin, 1992).

[6] H. Dosch, *Appl. Phys. A* **61,** 475 (1995).

[7] S. Dietrich and H. Wagner, *Z. Phys. B* **56,** 207 (1984).

[8] D. R. Nelson, in *Phase Transitions and Critical Phenomena*, Vol. 7, edited by C. Domb and J. L. Lebowitz (Academic, New York, 1983), pp. 1.

[9] D. R. Nelson and B. I. Halperin, *Phys. Rev. B* **19,** 2457 (1979).

[10] S. K. Sinha, E. B. Sirota, S. Garoff and H. B. Stanley, *Phys. Rev. B* **38,** 2297 (1988).

[11] S. Dietrich and A. Haase, *Phys. Rep.* **260,** 1 (1995).

[12] J. Daillant, K. Quinn, C. Gourier and F. Rieutord, *J. Chem. Soc., Faraday Trans.* **92,** 505 (1996).

[13] D. K. Schwartz, M. L. Schlossman, E. H. Kawamoto, G. J. Kellogg, P. S. Pershan and B. M. Ocko, *Phys. Rev. A* **41,** 5687 (1990).

[14] M. K. Sanyal, S. K. Sinha, K. G. Huang and B. M. Ocko, *Phys. Rev. Let.* **66,** 628 (1991).

[15] W. Zhao, X. Zhao, J. Sokolov, M. H. Rafailovich, M. K. Sanyal, S. K. Sinha, B. H. Cao, M. W. Kim and B. B. Sauer, *J. Chem. Phys.* **97,** 8536 (1992).

[16] L. Bourdieu, J. Daillant, D. Chatenay, A. Braslau and D. Colson, *Phys. Rev. Lett.* **72,** 1502 (1994).

[17] Z. Li, W. Zhao, J. Quinn, M. H. Rafailovich, J. Sokolov, R. B. Lennox, A. Eisenberg, X. Z. Wu, M. W. Kim, S. K. Sinha and M. Tolan, *Langmuir* **11,** 4785 (1995).

[18] P. Fontaine, J. Daillant, P. Guenoun, M. Alba, A. Braslau, J. W. Mays, J.-M. Petit and F. Rieutord, *J. Phys. II (France)* **7,** 401 (1997).

[19] C. Gourier, J. Daillant, A. Braslau, M. Alba, K. Quinn, D. Luzet, C. Blot, D. Chatenary, G. Grubel, J.-F. Legrand and G. Vignaud, *Phys. Rev. Lett.* **78,** 3157 (1997).

[20] H. Tostmann, E. DiMasi, P. S. Pershan, B. M. Ocko, O. G. Shpyrko and M. Deutsch, *Phys. Rev. B* **59,** 783 (1999).

[21] M. P. Gelfand and M. E. Fisher, *Physica A* **166,** 1 (1990).

[22] A. Braslau, P. S. Pershan, G. Swislow, B. M. Ocko and J. Als-Nielsen, *Phys. Rev. A* **38,** 2457 (1988).

[23] J. Daillant, L. Bosio, B. Harzallah and J. J. Benattar, *J. Phys. II (France)* **1,** 149 (1991).

[24] Li et al. (ref. [17]) have previously used a scattering geometry similar to OSDX to separate the capillary-wave TDS from small-angle diffraction originating from inter-particle correlations of micelles at the air-water interface.

[25] J. K. Basu and M. K. Sanyal, *Phys. Rev. Lett.* **79,** 4617 (1997).

[26] Eq. (A.1) is based on a kinematic approximation. In order to partially account for the surface enhancement effect observed when α or $\beta \sim \alpha_c$, the transmission factors for the single water-vapor interface have been included in Eq. (A.1) and used for all of our analysis. The small effect that the presence of multiple interfaces has on the surface enhancement for the LM is negligible.

[27] D. K. Schwartz, M. L. Schlossman and P. S. Pershan, *J. Chem. Phys.* **96,** 2356 (1992).

[28] M. Fukuto, K. Penanen, R. K. Heilmann, P. S. Pershan and D. Vaknin, *J. Chem. Phys.* **107,** 5531 (1997).

[29] Purchased from Sigma Chemical Co. MW: 26,000 (vis), 17,300 (LALLS).

[30] S. M. Yu, V. Conticello, G. Zhang, C. Kayser, M. J. Fournier, T. L. Mason and D. A. Tirrel, *Nature* **389,** 167 (1997).

[31] P. Lavigne, P. Tancrede, F. Lamarche, M. Grandbois and C. Salesse, *Thin Solid Films* **242,** 229 (1994).

[32] The range of $(\beta - \alpha)$ in the present measurements is not large enough to probe the expected correlation lengths associated with rod-induced anisotropy in the pair correlations.

[33] An equivalent model would replace the height-height correlation function and the Gaussian prefactor (see Eq. (A.2)) by a lateral density-density correlation function with a different prefactor.

Appendix B
Surface Diffuse Scattering from a Dense Layer

B.1 Introduction

Liquid surfaces are characterized by the presence of capillary waves (CWs), i.e., thermally excited fluctuations of liquid interfacial heights $h(r_{xy})$ against surface tension γ. The most dominating term $(\gamma/2)|\nabla h(r_{xy})|^2$ in the interfacial energy density and the two-dimensional nature of the interface lead to a logarithmic dependence of height-height correlation functions on the in-plane distance r_{xy} for $2\pi/q_{max}$ (~ molecular size) $<< r_{xy} <<$ $2\pi/q_{min}$ (~ mm for a gravitational cutoff). Because of this, thermal diffuse scattering (TDS) from liquid surfaces displays an algebraic singularity at the specular condition q_{xy} = 0 [1, 2], where q_{xy} is the projection of the wave vector transfer $\mathbf{q}$ onto the surface (x-y plane; see Fig. 5.1 for scattering geometry). It has been shown recently that so long as η = $(k_B T/2\pi\gamma)q_z^2 < 2$, the TDS from a homogeneous liquid surface can be described well by the following normalized form of differential cross section [3-5]:

$$\frac{1}{A_0}\left(\frac{d\sigma}{d\Omega}\right)_{hmg} \approx \frac{1}{16\pi^2}\left(\frac{q_c}{2}\right)^4 \frac{|\Phi_0(q_z)|^2}{q_z^2 \sin(\alpha)} \frac{2\pi\eta}{q_{xy}^2}\left(\frac{q_{xy}}{q_{max}}\right)^{\eta},$$

(B.1)

where q_z is the component of $\mathbf{q}$ along the surface normal (z-axis), q_c is the critical wave vector for total reflection, and A_0 is the cross-sectional area of the incident beam. The surface structure factor $|\Phi_0(q_z)|^2$ can be expressed as

$$|\Phi_0(q_z)|^2 = \left|\int_{-\infty}^{+\infty} dz \frac{d}{dz}\left[\frac{\langle\rho_{T=0}(z)\rangle}{\rho_\infty}\right]e^{-iq_z z}\right|^2,$$

(B.2)

and ρ_∞ is the electron density for the bulk subphase. The factor $<\rho_{T=0}(z)>$ above is an average "intrinsic" electron density profile and describes the local profile that applies to all points on the surface if the surface is laterally homogeneous (apart from CWs).

The above form of $d\sigma/d\Omega$ is based on the Born (or "kinematic") approximation (BA), which neglects the effects of refraction and multiple scattering. As such, it becomes quantitatively less accurate as the incident angle α and/or the output angle β (see Fig. 5.1 or A.1) approaches the critical angle $\alpha_c = q_c/2k_0 = (2/k_0)\sqrt{\pi r_e \rho_\infty}$. The range of angles over which it is valid depends on the local interfacial profile $<\rho_{T=0}(z)>$. For example, in the case of the free surface of a pure liquid (e.g., H_2O [3], In [4]) or a homogeneous Langmuir film whose density is comparable to the water subphase (e.g. PBLG monolayer [3]), Eq. (B.1) has been shown to agree with the β-scan data in the incidence plane for angles α/α_c, $\beta/\alpha_c > 4 \sim 5$. In fact, if the effect of refraction is partially taken into account by multiplying the above expression by the transmission factors $T_F(\alpha)T_F(\beta)$ for sharp gas/bulk interface [1], the theory agrees with the data even for the values of β that are close to α_c [3].

In general, if a high-density layer is present on the surface such that $\rho_1/\rho_\infty = \phi_1 > 1$, the applicability of the BA expression requires that the scattering angles be large compared with $\sqrt{\phi_1}\,\alpha_c$. If $\phi_1 \gg 1$, the refraction and multiple scattering effects at small angles are enhanced, and non-negligible deviations between the actual scattering amplitude and the BA expression can persist up to larger angles than the case of a low-density layer. For example, for a monolayer formed by gold nanoclusters on water (see Chapter 5), the layer density can be as high as $\phi_1 \sim 6$ (or $\sqrt{\phi_1} \sim 2.5$). In such cases, an alternative expression that is more accurate than Eqs. (B.1)-(B.2) is needed to analyze diffuse scattering data in a relatively wide range of small angles.

A reasonable extension of the normalized $(d\sigma/d\Omega)_{hmg}$ to the case of a homogeneous and conformal surface containing a high-density layer is to keep the form in Eq. (B.1) but to replace the structure factor in Eq. (B.2) by

$$\left|\Phi_0(q_z)\right|^2 = \frac{R_{T=0}(q_z)}{R_F(q_z)}, \tag{B.3}$$

where $R_F(q_z)$ is the Fresnel reflectivity from an ideally sharp and flat gas/bulk interface. The factor $R_{T=0}(q_z)$ refers to the reflectivity from the intrinsic profile $<\rho_{T=0}(z)>$ that would be obtained if the CWs were absent (i.e., $h(r_{xy}) = 0$). For $q_z >> \sqrt{\phi_1}\, q_c$, Eq. (B.3) converges to the BA result Eq. (B.2). For smaller q_z, $R_{T=0}(q_z)$ can be calculated more exactly by using the Parratt formalism [6, 7], which is based on a division of $<\rho_{T=0}(z)>$ into constant-density slabs and the application of the exact boundary conditions at each slab/slab interface.

The aim of this appendix is to demonstrate the advantages and quantitative accuracy of the new form of $(d\sigma/d\Omega)_{hmg}$ given by Eq. (B.1) and (B.3). For simplicity, we consider a case where the intrinsic profile $<\rho_{T=0}(z)>$ consists of a step-function layer of constant density ϕ_1 and thickness d (see Fig. B.1). For this simple two-interface case, the use of a distorted-wave Born approximation (DWBA) method allows one to obtain a general expression for diffuse scattering cross section $(d\sigma/d\Omega)_{diff}$ arising from interfacial roughness such that refraction effects are taken into account. We first provide a brief outline of the DWBA approach in Sec. B.2. In Sec. B.3, we make quantitative comparisons between the DWBA result and other approximations for $(d\sigma/d\Omega)_{diff}$ in the limit $q_z^2<h^2(0)> << 1$. In Sec. B.4, we show the new form of $(d\sigma/d\Omega)_{hmg}$ that can be applied to liquid surfaces even when a high density layer $\phi_1 >> 1$ is present. In Sec. B.5, the effect of $\phi_1 >> 1$ on the surface enhancement peak at $\beta = \alpha_c$ is discussed.

B.2 DWBA for the 1-Layer, 2-Interface Case

Sinha *et al*. [1] utilized a DWBA method to obtain a general expression for $(d\sigma/d\Omega)_{diff}$ for the case of a single interface with no surface layer. Daillant *et al*. [8] later used an equivalent approach to evaluate $(d\sigma/d\Omega)_{diff}$ in the presence of multiple interfaces. In the following we provide a brief summary that describes how the DWBA method used
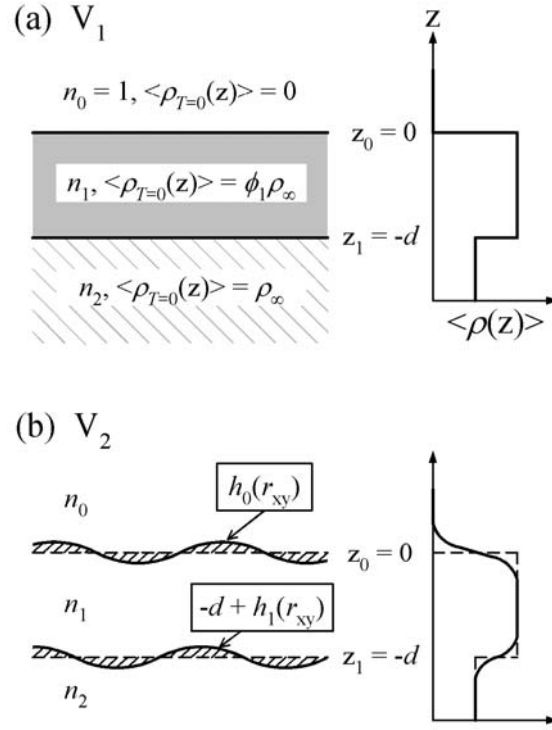
Figure B.1: Schematic illustrations of (a) unperturbed and (b) perturbed cases of a 1-layer, 2-interface surface, where the surface normal (z-axis) is vertical. The top medium with refractive index $n_0 = 1$ corresponds to the gas above the surface, the middle medium with n_1 to the single surface layer, and the bottom medium with n_2 to the bulk subphase. The figures on the right represent the average electron density profile $\langle \rho(z) \rangle$.

by Sinha *et al.* can be extended to the one-layer, two-interface case.

The local electric field at a point **r** in space is given by solutions to the wave equation:

$$\nabla^2 \psi + [k_0^2 - V]\psi = 0. \tag{B.4}$$

For a surface consisting of one layer and two interfaces, the potential V can be divided into two terms:

$$V = V_1 + V_2, \tag{B.5}$$

where an unperturbed potential V_1 (see Fig. B.1(a)) represents the case of sharp interfaces:

$$V_1 = \begin{cases} 0 & \text{for } z > 0 \\ k_0^2\left(1 - n_1^2\right) & \text{for } -d < z < 0 \\ k_0^2\left(1 - n_2^2\right) & \text{for } z < -d \end{cases} \tag{B.6}$$

The refractive index n_i in medium i is in general a complex number. However, if the absorption can be neglected, it is real and related to electron density ρ_i in the medium by $n_i = 1 - 2\pi r_e \rho_i / k_0^2$. The perturbation term V_2 (see Fig. B.1(b)) due to fluctuations of interfacial heights $h_i(r_{xy})$ can be expressed as:

$$V_2 = \begin{cases} k_0^2\left(1 - n_1^2\right) & \text{for } 0 < z < h_0\left(r_{xy}\right) \\ -k_0^2\left(1 - n_1^2\right) & \text{for } h_0\left(r_{xy}\right) < z < 0 \\ k_0^2\left(n_1^2 - n_2^2\right) & \text{for } -d < z < -d + h_1\left(r_{xy}\right) \\ -k_0^2\left(n_1^2 - n_2^2\right) & \text{for } -d + h_1\left(r_{xy}\right) < z < -d \\ 0 & \text{otherwise} \end{cases} \tag{B.7}$$

where we assume $<h_i^2(r_{xy})>^{1/2} << d$. Note that V_2 is nonzero only in the vicinity of each interface, as indicated by the shaded regions in Fig. B.1(b).

For $V = V_1$, the eigen-solutions for Eq. (B.4) are given by simple superpositions of plane-waves. For an incident beam striking the surface at angle $\alpha = \alpha_0$ from the above, a set of solutions that satisfy the boundary conditions at each interface is given by

$$\frac{\psi_1(\vec{r})}{E_0} = \begin{cases} \left[e^{ik_{z,0}(\alpha)z} + r_0(\alpha)e^{-ik_{z,0}(\alpha)z} \right] e^{i\vec{k}_{xy}(\alpha)\cdot\vec{r}_{xy}} & \text{for } z > 0 \\ \left[t_1(\alpha)e^{ik_{z,1}(\alpha)z} + r_1(\alpha)e^{-ik_{z,1}(\alpha)[z+2d]} \right] e^{i\vec{k}_{xy}(\alpha)\cdot\vec{r}_{xy}} & \text{for } -d < z < 0 \\ t_2(\alpha)e^{ik_{z,1}(\alpha)[z+d]} e^{i\vec{k}_{xy}(\alpha)\cdot\vec{r}_{xy}} & \text{for } z < -d \end{cases}$$
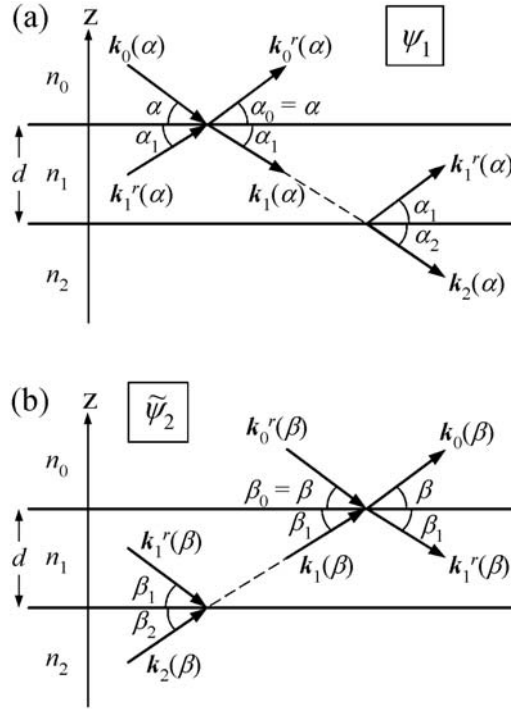
$$\tag{B.8}$$

Figure B.2: Schematic illustrations of (a) the regular and (b) the time-reversed eigen-states for scattering from an unperturbed 1-layer, 2-interface surface ($V = V_1$).

where $k_{z,i}(\alpha) = -k_0 n_i \sin(\alpha_i)$ and $k_{xy} = k_0 \cos(\alpha)$. The eigen-function ψ_1 is referred to as the "regular state" and describes the situation where the incident beam leads ultimately to a specular reflection above the surface and a transmitted wave into the bulk subphase, as illustrated in Fig. B.2(a). The one-layer reflection and transmission coefficients $r_i(\alpha)$ and $t_i(\alpha)$ in each medium ($V = V_1$) can be expressed as

$$r_0(\alpha) = \frac{r_{01}(\alpha) + r_{12}(\alpha)e^{-2ik_{z,1}(\alpha)d}}{1 + r_{01}(\alpha)r_{12}(\alpha)e^{-2ik_{z,1}(\alpha)d}}$$

$$t_1(\alpha) = \frac{t_{01}(\alpha)}{1 + r_{01}(\alpha)r_{12}(\alpha)e^{-2ik_{z,1}(\alpha)d}}$$

$$r_1(\alpha) = \frac{t_{01}(\alpha)r_{12}(\alpha)}{1 + r_{01}(\alpha)r_{12}(\alpha)e^{-2ik_{z,1}(\alpha)d}}$$

$$t_2(\alpha) = \frac{t_{01}(\alpha)t_{12}(\alpha)e^{-ik_{z,1}(\alpha)d}}{1 + r_{01}(\alpha)r_{12}(\alpha)e^{-2ik_{z,1}(\alpha)d}}$$

(B.9)

where the single-interface reflection and transmission coefficients are given by

$$r_{ij}(\alpha) = \frac{n_i \sin(\alpha_i) - n_j \sin(\alpha_j)}{n_i \sin(\alpha_i) + n_j \sin(\alpha_j)}$$

$$t_{ij}(\alpha) = \frac{2n_i \sin(\alpha_i)}{n_i \sin(\alpha_i) + n_j \sin(\alpha_j)}$$

(B.10)

These coefficients are the exact field amplitudes for sharp interfaces and can be obtained by applying the Parratt formalism [6].

Another set of eigen-solutions that also satisfy the boundary conditions for $V = V_1$ is given by the "time-reversed state" [1]:

$$\frac{\tilde{\psi}_2(\vec{r})}{E_0} = \begin{cases} \left[e^{ik_{z,0}(\beta)z} + r_0^*(\beta)e^{-ik_{z,0}(\beta)z} \right] e^{i\vec{k}_{xy}(\beta)\cdot\vec{r}_{xy}} & \text{for } z > 0 \\ \left[t_1^*(\beta)e^{ik_{z,1}(\beta)z} + r_1^*(\beta)e^{-ik_{z,1}(\beta)[z+2d]} \right] e^{i\vec{k}_{xy}(\beta)\cdot\vec{r}_{xy}} & \text{for } -d < z < 0 \\ t_2^*(\beta)e^{ik_{z,1}(\beta)[z+d]} e^{i\vec{k}_{xy}(\beta)\cdot\vec{r}_{xy}} & \text{for } z < -d \end{cases}$$

(B.11)

This state describes a situation where two waves, one hitting the surface from the above and the other coming up from the bulk subphase, combine to produce an outgoing wave above the surface at output angle $\beta = \beta_0$ (see Fig. B.2(b)).

Under the DWBA, the diffuse scattering from the surface arises from nonzero transition probability between the two states ψ_1 and $\tilde{\psi}_2$ due to the presence of the perturbation V_2. In particular, diffuse scattering cross section is given by [1]

$$\left(\frac{d\sigma}{d\Omega}\right)_{diff} = \frac{\langle B^*B \rangle - |\langle B \rangle|^2}{16\pi^2 |E_0|^4},$$

(B.12)

where

$$B \equiv \langle \tilde{\psi}_2 | V_2 | \psi_1 \rangle.$$

(B.13)

In principle, the matrix element B can be evaluated by directly substituting Eqs. (B.8) and (B.11) into Eq. (B.13), which leads to a relatively large number of terms. The calculation is simplified somewhat by the following approximation based on the continuity of the eigen-states ψ_i across each interface. It can be shown that the power-series expansion of the difference between ψ_i above and below each interface has a leading term that is proportional to $[\delta z]^2$ where $\delta z = z - z_i$. By representing the field near the top interface $(z \sim z_0 = 0)$ with that above the surface $(i = 0)$ and representing the field near the bottom interface $(z \sim z_1 = -d)$ with that of the bulk subphase $(i = 2)$, ψ_i can be approximated as

$$\frac{\psi_1(\vec{r})}{E_0} \approx \begin{cases} \left[e^{ik_{z,0}(\alpha)z} + r_0(\alpha)e^{-ik_{z,0}(\alpha)z} \right] e^{i\vec{k}_{xy}(\alpha)\cdot\vec{r}_{xy}} & \text{for } z \sim 0 \\ t_2(\alpha)e^{ik_{z,1}(\alpha)[z+d]} e^{i\vec{k}_{xy}(\alpha)\cdot\vec{r}_{xy}} & \text{for } z \sim -d \end{cases} \tag{B.14}$$

(similarly for ψ_2). This approximation reduces the number of terms contained in B considerably and is appropriate if $q_z^2 \langle h_i^2(0)\rangle \ll 1$, a condition that is likely to hold for small q_z where the BA expression is quantitatively less reliable.

Using the above approximation, it can be shown that the DWBA expression for $(d\sigma/d\Omega)_{\text{diff}}$ for the case where fluctuations at the two interfaces are *perfectly conformal*, i.e., $h_1(r_{xy}) = h_0(r_{xy}) = h(r_{xy})$, is given by

$$\left(\frac{d\sigma}{d\Omega}\right)_{diff} = \left|1 - n_1^2\right|^2 \left\{ \left[1 + |r_0(\beta)|^2 |r_0(\alpha)|^2\right] \Sigma_+(q_z, q_z) + 2\,\mathrm{Re}[r_0(\beta)r_0(\alpha)\Sigma_-(q_z, q_z)] \right.$$

$$+ \left[|r_0(\beta)|^2 + |r_0(\alpha)|^2\right] \Sigma_+(q_z', q_z') + 2\,\mathrm{Re}[r_0^*(\beta)r_0(\alpha)\Sigma_-(q_z', q_z')]$$

$$+ 2\,\mathrm{Re}\left[\left[r_0^*(\alpha) + |r_0(\beta)|^2 r_0(\alpha)\right]\Sigma_+(q_z, q_z')\right]$$

$$+ \left. 2\,\mathrm{Re}\left[\left[r_0^*(\beta) + |r_0(\alpha)|^2 r_0(\beta)\right]\Sigma_-(q_z, q_z')\right]\right\}$$

$$+ \left|n_1^2 - n_2^2\right|^2 |t_2(\beta)|^2 |t_2(\alpha)|^2 \Sigma_+(q_z^t, q_z^t)$$

$$+ 2\,\mathrm{Re}\left\{\left(1 - n_1^2\right)\left(n_1^2 - n_2^2\right)^* t_2^*(\beta)t_2^*(\alpha)\left[\Sigma_+(q_z, q_z^t) + r_0(\beta)r_0(\alpha)\Sigma_-(q_z, q_z^t)\right.\right.$$

$$\left.\left. + r_0(\alpha)\Sigma_+(q_z', q_z^t) + r_0(\beta)\Sigma_+(q_z', q_z^t)\right]\right\}$$

(B.15)

where

$$q_z = k_0\left[\sin(\beta) + \sin(\alpha)\right]$$
$$q_z' \equiv k_0\left[\sin(\beta) - \sin(\alpha)\right]$$
$$q_z^t \equiv k_0 n_2\left[\sin(\beta_2) + \sin(\alpha_2)\right] = k_0\left[\sqrt{\sin^2(\beta) - \sin^2(\alpha_c)} + \sqrt{\sin^2(\alpha) - \sin^2(\alpha_c)}\right]$$

(B.16)

The factors $\Sigma_\pm$ are defined as

$$\Sigma_\pm(p_z, p_z') \equiv \pm A \frac{k_0^4}{16\pi^2} \frac{e^{-\frac{1}{2}\left[p_z^2 + \left(p_z'^*\right)^2\right]\sigma^2}}{p_z p_z'^*} \int_A d^2 r_{xy} e^{-i\vec{q}_{xy}\cdot\vec{r}_{xy}}\left[e^{\pm p_z p_z'^*\langle h(\vec{r}_{xy})h(0)\rangle} - 1\right]$$

(B.17)

where $\sigma^2 = \langle h^2(0)\rangle$ represents the conformal mean-square roughness. The expression in Eq. (B.15) is equivalent to the results obtained by Daillant *et al.* [8].

The DWBA expression for $(d\sigma/d\Omega)_{diff}$ in Eq. (B.15) takes into account the refraction effects and is therefore more quantitatively accurate at small q_z than the BA result. However, it is clear that even when the surface structure is relatively simple, the

207

expression is complicated and contains many integration terms. In the following, the above DWBA result is compared with other approximate expressions that are simpler and more physically intuitive.

B.3 Approximate Expressions for the Conformal 1-Layer, 2-Interface Case at Small q_z

The BA is quantitatively valid when the scattering amplitudes are small, i.e., at large q_z. The main objective of the present discussion is to obtain a more quantitatively accurate description of the surface scattering at small angles where the BA fails. In this section, we compare the magnitudes of $(d\sigma/d\Omega)_{\text{diff}}$ based on various approximation methods in the limit $q_z^2\sigma^2 \ll 1$ ($\sigma^2 = <h^2(0)>$), where an improvement upon the BA result is needed. In this small q_z limit, $(d\sigma/d\Omega)_{\text{diff}}$ has the following form in all cases:

$$\frac{1}{A}\left(\frac{d\sigma}{d\Omega}\right)_{diff} \approx \frac{1}{16\pi^2}\left(\frac{q_c}{2}\right)^4 F(q_z)\int_A d^2r_{xy}e^{-i\vec{q}_{xy}\cdot\vec{r}_{xy}}\left\langle h(r_{xy})h(0)\right\rangle. \tag{B.18}$$

The factor $F(q_z)$ contains the information about the local intrinsic profile $<\rho_{\Gamma=0}(z)>$ and the conformal roughness σ. The expression for $F(q_z)$ depends on the approximation method used and is the quantity to be directly compared. In what follows, we assume the same intrinsic profile as considered earlier, i.e., a step-function surface layer of relative density ϕ_1 and thickness d.

On the basis of the discussion in the preceding section, the factor $F(q_z)$ under the DWBA is given by

$$F_{DWBA}(q_z) = \phi_1^2 \left\{ \left| 1 + r_0(\beta) r_0(\alpha) \right|^2 e^{-q_z^2 \sigma^2} + \left| r_0(\beta) + r_0(\alpha) \right|^2 e^{-q_z'^2 \sigma^2} \right.$$

$$\left. + 2\operatorname{Re}\left[\left[r_0(\beta) + r_0(\alpha) \right] \left[1 + r_0^*(\beta) r_0^*(\alpha) \right] \right] e^{-\frac{1}{2}\left[q_z^2 + q_z'^2 \right] \sigma^2} \right\}$$

$$+ (1 - \phi_1)^2 \left| t_2(\beta) \right|^2 \left| t_2(\alpha) \right|^2 e^{-\operatorname{Re}\left[\left(q_z^t \right)^2 \right] \sigma^2}$$

$$+ 2\phi_1 (1 - \phi_1) \operatorname{Re}\left\{ t_2^*(\beta) t_2^*(\alpha) \left[1 + r_0(\beta) r_0(\alpha) \right] e^{-\frac{1}{2}\left(q_z^{t*} \right)^2 \sigma^2} \right\} e^{-\frac{1}{2} q_z^2 \sigma^2}$$

$$+ 2\phi_1 (1 - \phi_1) \operatorname{Re}\left\{ t_2^*(\beta) t_2^*(\alpha) \left[r_0(\beta) + r_0(\alpha) \right] e^{-\frac{1}{2}\left(q_z^{t*} \right)^2 \sigma^2} \right\} e^{-\frac{1}{2} q_z'^2 \sigma^2}$$

$$(B.19)$$

If α, $\beta \gg \alpha_c$, the magnitudes of the reflection coefficients are much less than unity. Therefore, in that limit, the above approaches the following form given by setting $r_0(\alpha) = 0$ and $r_0(\beta) = 0$:

$$F_{DWBA, r=0}(q_z) = \left| \phi_1 e^{-\frac{1}{2} q_z^2 \sigma^2} + (1 - \phi_1) t_2(\beta) t_2(\alpha) e^{-\frac{1}{2}\left(q_z^t \right)^2 \sigma^2} \right|^2, \qquad (B.20)$$

where Eq. (B.16) shows that $q_z^t \approx q_z$ for α, $\beta \gg \alpha_c$. In the limit of α, $\beta \gg \sqrt{\phi_1}\, \alpha_c$, Eq. (B.9) shows that the product of the transmission coefficients reduces to:

$$t_2(\beta) t_2(\alpha) \approx e^{-ik_0 n_1 [\sin(\beta_1) + \sin(\alpha_1)] d} \approx e^{-iq_z d}. \qquad (B.21)$$

Therefore, at large q_z, the DWBA result approaches the BA expression, which is given by

$$F_{BA}(q_z) = \left| \Phi_0(q_z) \right|^2 e^{-q_z^2 \sigma^2}$$

$$= \left| \phi_1 + (1 - \phi_1) e^{-iq_z d} \right|^2 e^{-q_z^2 \sigma^2} \qquad (B.22)$$

$$= \left[1 + 4\phi_1 (1 - \phi_1) \sin^2 \left(\tfrac{1}{2} q_z d \right) \right] e^{-q_z^2 \sigma^2}$$

where the BA definition of the factor $\left| \Phi_0(q_z) \right|^2$ (see Eq. (B.2)) has been used.

As noted earlier, the factor $\left| \Phi_0(q_z) \right|^2$ corresponds to the normalized reflectivity $R(q_z)/R_F(q_z)$ that would result from the intrinsic profile if there were no surface roughness

$(\sigma = 0)$. Therefore, it is reasonable to improve upon Eq. (B.22) by utilizing correction methods that apply to specular reflectivity at small q_z. One approach is given by the "qq_t" correction [1] to the BA case, which replaces q_z^2 in F_{BA} with a product $q_z q_z^t$:

$$F_{qq_t}(q_z) = F_{BA}\left(\sqrt{q_z q_z^t}\right) = \left|\Phi_0\left(\sqrt{q_z q_z^t}\right)\right|^2 e^{-q_z q_z^t \sigma^2} . \tag{B.23}$$

Sinha *et al*. [1] has demonstrated that this correction provides a quantitatively accurate description of specular reflectivity at small q_z in the case of a single interface or a low-density surface structure.

Another approach is to employ the Parratt method [6, 7] to calculate the reflectivity that originates from the intrinsic profile. For the one-layer, two-interface case, this correction leads to:

$$F_{Parratt}(q_z) = \frac{|r_0(\theta)|^2}{R_F(q_z)} e^{-q_z^2 \sigma^2} = \frac{|r_0(\theta)|^2}{|r_{02}(\theta)|^2} e^{-q_z^2 \sigma^2} \tag{B.24}$$

where $\theta = \sin^{-1}(q_z/2k_0)$, $R_F = |r_{02}|^2$ (for the ideal gas/bulk interface without a layer), and the reflection coefficients are given by Eqs. (B.9)-(B.10).

The factors $F(q_z)$ for scattering in the incidence plane have been calculated using the various approximation methods described above. The results are compared as a function of the output angle β for the incident angle fixed at $\alpha = 1°$ in Fig. B.3 and for $\alpha = 2°$ in Fig. B.4. In the calculations the layer and roughness parameters have been set at $\phi_1 = 6$, $d = 25$ Å, and $\sigma = 3$ Å, which are close to the typical values for gold nanocluster monolayers on water (described in Chapter 5). The figures show that in the presence of such a high-density surface layer, both the BA result and its "qq_t"-corrected form deviate substantially from the more precise DWBA result at small α and β. On the other hand, the correction based on the Parratt method agrees much better with the DWBA form, except where $\beta \sim \alpha_c$.

The small deviation between F_{DWBA} and F_{parratt} at small β is partly due to the fact

210

$\alpha = 1$ deg, $d = 25$ Å, $\phi_1 = 6.0$, $\sigma = 3.0$ Å
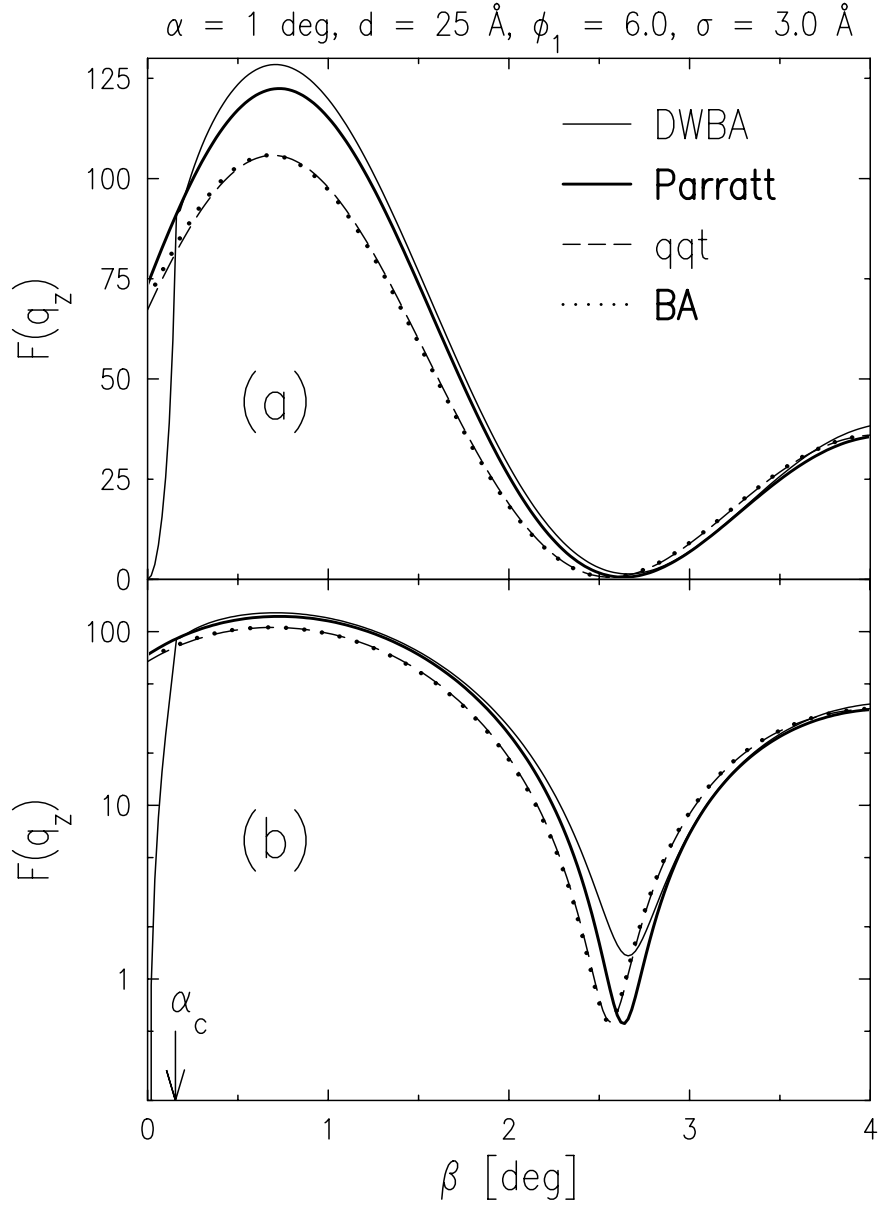
Figure B.3: Comparison between different forms of surface structure factor $F(q_z)$ as a function of output angle β with the incident angle fixed at $\alpha = 1°$ [$q_z/k_0 = \sin(\alpha) + \sin(\beta)$]. The curves have been calculated for a single surface layer of thickness $d = 25$ Å and relative electron density $\phi_1 = 6.0$ and a conformal root-mean-square roughness of $\sigma = 3.0$ Å. (a) A linear plot, and (b) a semi-log plot. The critical angle for total reflection $\alpha_c = 0.154°$ corresponds to the case of water subphase with x-ray wavelength $\lambda = 1.55$ Å.
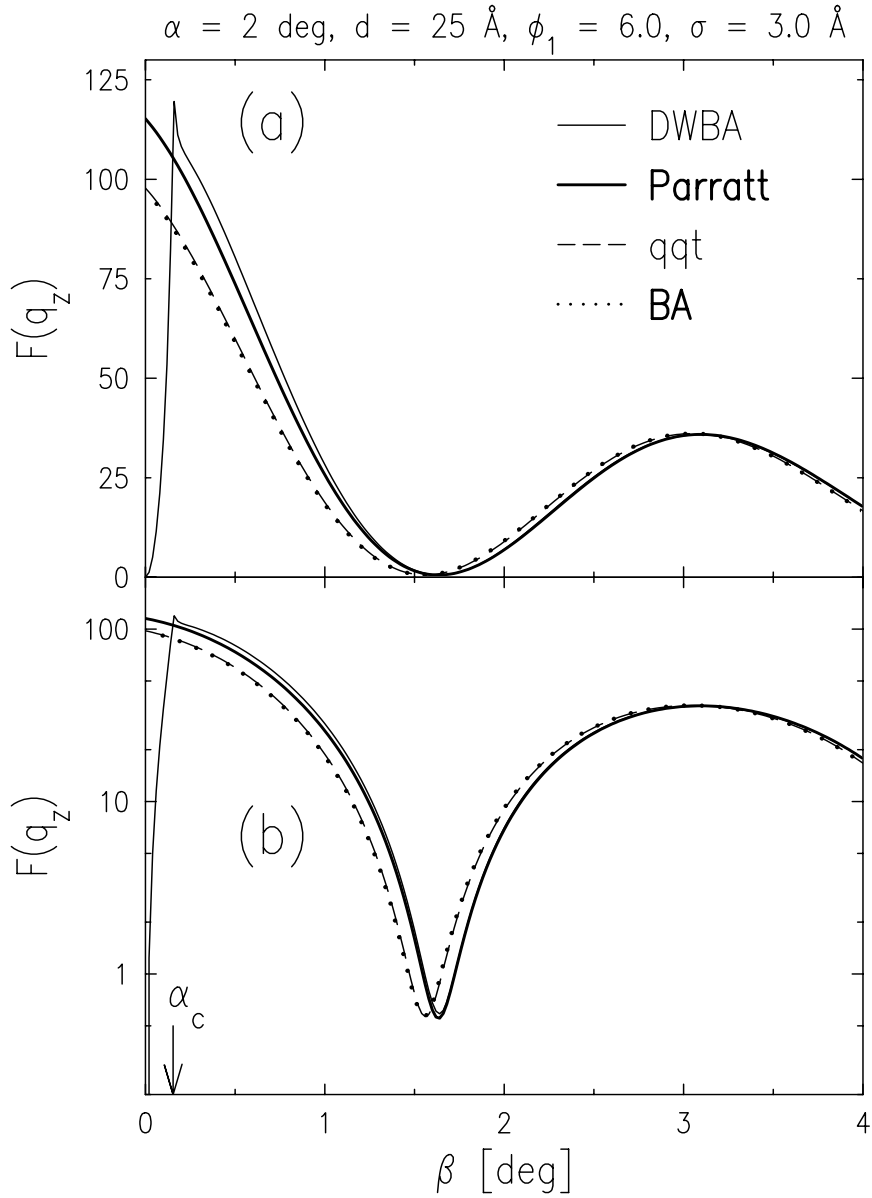
Figure B.4: Comparison between different forms of surface structure factor $F(q_z)$ as a function of output angle β with the incident angle fixed at $\alpha = 2°$ [$q_z/k_0 = \sin(\alpha) + \sin(\beta)$]. The curves have been calculated for a single surface layer of thickness $d = 25$ Å and relative electron density $\phi_1 = 6.0$ and a conformal root-mean-square roughness of $\sigma = 3.0$ Å. (a) A linear plot, and (b) a semi-log plot. The critical angle for total reflection $\alpha_c = 0.154°$ corresponds to the case of water subphase with x-ray wavelength $\lambda = 1.55$ Å.

that the Parratt formalism, which describes specular reflection, fails to account for the surface enhancement peak ("Yoneda" peak) at $\beta \sim \alpha_c$. This peak arises from the invariance of the wave equation under time reversal ($k \rightarrow -k$) and the fact that the field amplitudes of transmitted waves near the surface reaches a maximum (twice the incident field for a simple gas/bulk interface) at α or $\beta = \alpha_c$ [1]. The dependence of this peak on the layer density ϕ_l is discussed in Sec. B.5.

B.4 Scattering from a Homogeneous and Conformal Liquid Surface

The comparisons shown in Figs. B.3 and B.4 suggest that the normalized scattering cross section for a homogeneous and conformal liquid surface should be modified as

$$\frac{1}{A_0}\left(\frac{d\sigma}{d\Omega}\right)_{hmg} \approx \frac{1}{16\pi^2}\left(\frac{q_c}{2}\right)^4 \frac{R_{T=0}(q_z)/R_F(q_z)}{q_z^2 \sin(\alpha)} \frac{2\pi\eta}{q_{xy}^2}\left(\frac{q_{xy}}{q_{\max}}\right)^\eta . \qquad (B.25)$$

The reflectivity $R_{T=0}(q_z)$ arising from the intrinsic profile $<\rho_{T=0}(z)>$ can be calculated using the Parratt method at small q_z and switching to the BA expression in Eq. (B.2) at large q_z. The above expression is quantitatively accurate even when the surface contains a highly dense structure with $\phi_s = \rho_s/\rho_\infty \gg 1$ as long as α/α_c, $\beta/\alpha_c > 4 \sim 5$; that is, the scattering angles need only be large compared with α_c instead of $\sqrt{\phi_s}\,\alpha_c$. The advantage of this expression is that it retains the simple and physically intuitive form based on the BA while providing a better approximation of the more exact DWBA form at small α, β.

B.5 Reduction of the Surface Enhancement Peak by a Dense Layer

The ratios between F_{DWBA} and $F_{Parratt}$ have been calculated at various values of ϕ_l for the conformal one-layer, two-interface case. The results at small β are shown in Fig. B.5(a) for $\alpha = 1°$ and in Fig. B.5(b) for $\alpha = 2°$. The figure demonstrates that the presence of a highly dense surface layer leads to a reduction in the intensity of the surface
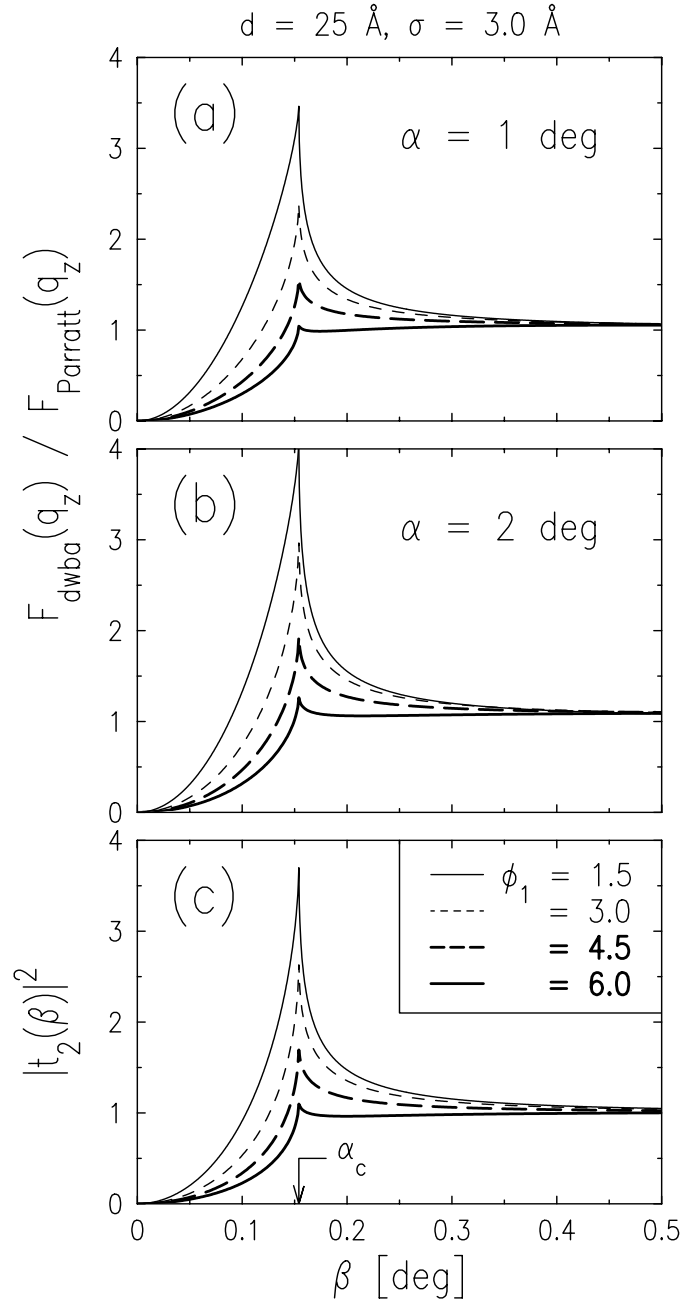
213

Figure B.5: The ratio $F_{\rm dwba}/F_{\rm parratt}$ between the DWBA and the Parratt forms of the surface structure factors, as a function of output angle β with the incident angle fixed at: (a) $\alpha = 1°$, and (b) $\alpha = 2°$. (c) The transmission factor $|t_2(\beta)|^2$. The curves have been calculated for a single surface layer of thickness $d = 25$ Å and a conformal root-mean-square roughness of $\sigma = 3.0$ Å. The four curves shown in each panel correspond (from top to bottom) to the relative electron density of $\phi_1 = 1.5$, 3.0, 4.5, and 6.0 for the surface layer. The critical angle for total reflection $\alpha_c = 0.154°$ corresponds to the case of water subphase with x-ray wavelength $\lambda = 1.55$ Å.

enhancement peak at $\beta = \alpha_c$. Fig. B.5(c) plots the transmission factor $|t(\beta)|^2 = |t_2(\beta)|^2$ for the waves below the layer/bulk interface (see Eq. (B.9)), which displays a similar dependence on ϕ_l as the ratio $F_{DWBA}/F_{Parratt}$ does. These observations indicate that the primary contribution to the surface enhancement peak comes from the factor $|t_2(\beta)|^2$.

The suppression of the surface enhancement peak due to the presence of a dense surface layer originates from a tunneling effect. For $V = V_1$, the substitution of a plane-wave solution of form $\psi(\mathbf{r}) = \psi_z(z)\exp(-i\mathbf{k}_{xy}\cdot\mathbf{r}_{xy})$ into the wave equation in Eq. (B.4) results in an one-dimensional wave-equation [9]:

$$\psi_z''(z) + (1/4)[q_z^2 - q_c^2\phi(z)]\psi_z(z) = 0, \tag{B.26}$$

where $q_z^2 = 4(k_0^2 - k_{xy}^2) = 4k_0^2\sin^2(\beta)$ and $\phi(z)$ is equal to zero for $z > 0$, ϕ_l within the layer, and unity for $z < -d$. The factor $q_c^2\phi(z)$ is equivalent to a finite potential wall for $z < 0$. Therefore, if $q_z < \sqrt{\phi_l}\,q_c$ or $\beta < \sqrt{\phi_l}\,\alpha_c$, the propagation of waves across the layer occurs only through tunneling, i.e., via exponentially decaying evanescent waves. If the layer density ϕ_l increases, the rise in the height of the potential wall reduces the amplitude $t_2(\beta)$ of waves transmitted below the layer/bulk interface for a given $\beta < \sqrt{\phi_l}\,\alpha_c$. This explains the reduction of the surface enhancement peak with increasing layer density. It is clear from this interpretation that an increase in the layer thickness d at fixed $\phi_l > 1$ also reduces the surface enhancement peak.

References for Appendix B

[1] S. K. Sinha, E. B. Sirota, S. Garoff and H. B. Stanley, *Phys. Rev. B* **38,** 2297 (1988).

[2] M. K. Sanyal, S. K. Sinha, K. G. Huang and B. M. Ocko, *Phys. Rev. Lett.* **66,** 628 (1991).

[3] M. Fukuto, R. K. Heilmann, P. S. Pershan, J. A. Griffiths, S. M. Yu and D. A. Tirrell, *Phys. Rev. Lett.* **81,** 3455 (1998).

[4] H. Tostmann, E. DiMasi, P. S. Pershan, B. M. Ocko, O. G. Shpyrko and M. Deutsch, *Phys. Rev. B* **59,** 783 (1999).

[5] P. S. Pershan, *Colloids and Surfaces* **A171,** 149 (2000).

[6] L. G. Parratt, *Phys. Rev.* **95,** 359 (1954).

[7] J. Lekner, *Theory of Reflection* (Martin Nijhoff, Dordrecht, 1987).

[8] J. Daillant and O. Belorgey, *J. Chem. Phys.* **97,** 5824 (1992).

[9] P. S. Pershan, *Faraday Discuss. Chem. Soc.* **89,** 231 (1990).